PHOTO-ELECTROCHEMICAL APPLICATION OF NOVEL CARBON - METAL OXIDES NANOCOMPOSITES FOR THE DEGRADATION OF SELECTED ORGANIC POLLUTANTS IN WATER: EXPERIMENTAL AND COMPUTATIONAL STUDIES

by

Eseoghene Helen UMUKORO

Dissertation in fulfilment of the requirement for the degree

PHILOSOPHIAE DOCTOR

in

CHEMISTRY

in the

FACULTY OF SCIENCE

of the

UNIVERSITY OF JOHANNESBURG

Supervisor : Prof O. A. AROTIBA

Co-supervisor : Prof J. C. NGILA

March 2018

DECLARATION

I hereby declare that this dissertation, which I herewith submit for the research qualification.

PHILOSOPHIAE DOCTOR DEGREE IN CHEMISTRY

To the University of Johannesburg, Department of Applied Chemistry, is apart from the recognised assistance of my supervisors, my own work and has not previously been submitted by me to another institution to obtain a research diploma or degree.

_____ on this ____ day of _____

(Candidate)

_____ on this ____ day of _____

(Supervisor)

_____ on this ____ day of _____

(Co-supervisor)

_____ on this ____ day of _____

(Co-supervisor)

DEDICATION

This work is dedicated to God who has been everything to me in life, and also to my late mother and hero, Janet Enuoyibo, who loved me unconditionally and sacrificed everything within her power for me to be the woman I am today.

ACKNOWLEDGEMENTS

I would like to extend my sincere thanks to the following people and organisations for their contributions towards the success of this work:

- I would like to expresee my profound gratitude to my supervisors, Prof. O. A. Arotiba and Prof J.C. Ngila, for their supervision, godly counsel and advice, kind assistance, encouragement and guidance throughout this work.
- My sincere gratitude goes to Prof. Ponnadurai Ramasama for hosting me in his Computational Chemsitry Research Laboratory for the period of three months at the University of Mauritius. Thank you for giving me the foundation of computational chemistry which has instilled in me the motivation to take my research to another level, and thereby contributing to the body of knowledge in science.
- I want to thank the Department of Applied Chemistry and the Electrochemistry Research Group; both staff and students.
- Water Research Commision, National Research Foundation and L'Oreal-UNESCO for Women in Science for funding this research work. Faculty of Science, University of Johannesburg, South Africa and Obafemi Awolowo University, Ile-Ife, Nigeria for financial assistance.
- My sincere gratitude goes to every member of my family who stood by me during this period of my study: Mr Malomo Umukoro, Ms Portia Umukoro, Mr Believe Umukoro, Mr and Mrs Gbile Akanni, Mrs Sola Ariba, Mr Adejare Adedibu, Mr and Mrs Charles Aideyan, Mr Oghenevwogaga Agbroko, Prof and Mrs L.O. Kehinde, Prof Adesegun Fatusi, Mr Folu Ijagbulu, Ms Fiyinfolu Falodun and Ms Soton Bestman for their prayers, love and encouragement.
- I am grateful to every member of the Men of Issachar Vision as well as Peace House Discipleship Centre, University of Johannesburg for their love and support.
- Many thanks to Prof M.S Akanni, Prof O.I. Asubiojo, Prof S.R.A Adewusi, Prof C.A. Obafemi, Prof G.O Egharevba, Prof A.O Ogunfowokan, Prof E.A Oluyemi, Prof A. Akinlua, Prof M. Aderogba, Dr. A.S Adekunle, Dr. J. A. O. Oyekunle and other members of staff, Department of Chemistry, Obafemi Awolowo University.
- Thanks to my friends; Dr. L.O Olasunkanmi, Dr Gbenga Peleyeju, Mr Azeez Idris.
- Above all, I am eternally grateful to God Almighty for His grace and mercy upon my life through out this period and forever.

LISTS OF PRESENTATIONS AND PUBLICATIONS

Most of the results from this study have been presented in local and international conferences and some of them have been published and submitted for publication in peer reviewed journals. Integral part of this thesis constituted the application that led to the award of 2016 L'Oreal-UNESCO for Women in Science.

Conference Presentations:

1. **Eseoghene H. Umukoro**, Neeraj Kumar, J. Catherine Ngila, Omotayo A. Arotiba, *Fabrication of an expanded graphite supported p-n MoS_2-SnO_2 heterojunction composite photo-electrode for enhanced photo-electrocatalytic degradation of pharmaceutical pollutants* (ORAL), 68th Annual Meeting of the International Society of Electrochemistry, Providence, Rhode Island, USA, 27th, August – 1st September, 2017.
2. **Eseoghene. H. Umukoro,** Moses. G. Peleyeju, J.Catherine. Ngila, Omotayo. A. Arotiba, *Electrochemical and Photo-assisted Electrochemical Oxidation of Organic Pollutants in Waste Water at Novel Tungsten Trioxide-Exfoliated Graphite Composite Electrode* (POSTER)6th Inter-Faculty Postgraduate Symposium, University of Johannesburg, Johannesburg, South Africa, 14th October, 2016
3. **Eseoghene. H. Umukoro,** Moses. G. Peleyeju, J.Catherine. Ngila, Omotayo. A. Arotiba, *Electrochemical and Photo-assisted Electrochemical Oxidation of Organic Pollutants in Waste Water at Novel Tungsten Trioxide-Exfoliated Graphite Composite Electrode* (POSTER), 67th Annual Meeting of the International Society of Electrochemistry, The Hague, The Netherlands, 21-26th, August, 2016.
4. **Eseoghene. H. Umukoro**, Moses. G. Peleyeju, Omotayo. A. Arotiba, J.Catherine Ngila, *Photocatalytic degradation of acid blue 74 in water using Ag-Ag_2O-ZnO nanostructures anchored on graphene oxide* (POSTER), 16th WaterNet/WARFSA/GWA-SA Symposium, Mauritius, 29th – 31st, October, 2015.
5. **Eseoghene. H. Umukoro**, Moses. G. Peleyeju, J. Catherine Ngila, Omotayo. A. Arotiba, *Photoelectrochemical application of silver oxide-zinc oxide nanocomposite doped reduced graphene oxide (Ag_2O-ZnO-rGO) mixed electrode for water treatment* (POSTER), 3rd Conference on "Emerging Frontiers for Sustainable Water" (Africa, India and United Kingdom), Johannesburg, South Africa, 3rd -5th, August, 2015.
6. **Eseoghene. H. Umukoro**, Moses. G. Peleyeju, J. Catherine Ngila, Omotayo. A.

Arotiba, *Photoelectrochemical application of silver oxide-zinc oxide nanocomposite doped reduced graphene oxide (Ag_2O-ZnO-rGO) mixed electrode for water treatment* (POSTER), 3rd Internation Symposium on Electrochemistry (SACI), MAPET, Cape Town (Belville), South Africa, 26 -28th, May, 2015.

Publications directly from thesis:

1. **Eseoghene Umukoro**, Moses G. Peleyeju, J. Catherine Ngila, Omotayo A. Arotiba, Photocatalytic degradation of acid blue 74 in water using Ag-Ag_2O-ZnO nanostructures anchored on graphene oxide, *Solid State Sciences*, 51 (2016) 66-73
2. **Eseoghene H. Umukoro**, Moses G. Peleyeju, J. Catherine Ngila, Omotayo A. Arotiba, Photoelectrochemical degradation of orange II dye in waste water at silver-zinc oxide-reduced graphene oxide nanocomposite photoanode, *Royal Society of Chemistry Advances* RSC Adv., 6(2016) 52868-52877
3. **Eseoghene H. Umukoro**, Moses G. Peleyeju, J. Catherine Ngila, Omotayo A. Arotiba, Towards wastewater treatment: Photo-assisted electrochemical degradation of 2-nitrophenol and orange II dye at a tungsten trioxide-exfoliated graphite composite. *Chemical Engineering Journal*, 317 (2017) 290-301
4. **Eseoghene H. Umukoro**, Siphosetu Madyibi, Moses G. Peleyeju, Luthando Tshwenya, Catherine Ngila, Omotayo A. Arotiba, Photocatalytic application of Pd-ZnO-exfoliated graphite nanocomposite for the enhanced removal of acid orange 7 dye in water, *Solid State Sciences*, 74 (2017) 118-124
5. **Eseoghene H. Umukoro**, Moses G. Peleyeju, Idris O. Azeez, Jane C. Ngila, Nonhlangabezo Mabuba, Lydia Rhyman, Ponnadurai Ramasami, Omotayo A. Arotiba, Photo-electrocatalytic application of palladium decorated zinc oxide-expanded graphite electrode for the removal of 4-nitrophenol: Experimental and computational study, *Royal Society of Chemistry Advances RSC Adv.*, 8(2018) 10255-10266
6. **Eseoghene H. Umukoro**, Neeraj Kumar, Moses G. Peleyeju, J. Catherine Ngila, Omotayo A. Arotiba, Expanded graphite supported p-n MoS_2-SnO_2 heterojunction composite photo-electrode for enhanced photo-electrocatalytic degradation of a pharmaceutical pollutant (Submitted to *Journal of Electroanalytical Chemistry*)

Other Publications during the PhD programme

1. Moses G. Peleyeju, **Eseoghene H. Umukoro**, Jonathan. O. Babalola, Omotayo A. Arotiba, Electrochemical degradation of an anthraquinonic dye on an expanded

graphite-diamond composite electrode, *Electrocatalysis*, 7(2016) 132-139

2. Moses G. Peleyeju, Azeez O. Idris, **Eseoghene H. Umukoro**, Jonathan O. Babalola, Omotayo A. Arotiba, Electrochemical detection of 2,4-dichlorophenol on a ternary composite electrode of diamond, graphene and polyaniline, *ChemElectroChem*, 4:5(2017) 1074-1080 http://dx.doi.org/10.1002/celc.201600621
3. Moses G. Peleyeju, **Eseoghene H. Umukoro**, Jonathan. O. Babalola, Omotayo A. Arotiba, Oxidation of sulfamethoxazole at a TiO_2-exfoliated graphite anode via photoelectrocatalytic process, *Royal Society of Chemistry Advances* RSC Adv., 7(2017) 40571-40580
4. **Eseoghene H Umukoro,** John A Oyekunle, Omotayo O Arotiba, Abonlale Adekunle, Removal Equilibrium, Kinetics and Thermodynamics of Cd (II) and Pb (II) from Synthetic Wastewater Using Plantain Peel Charcoal, *Toxicological Reports* (under review)

ABSTRACT

In the search for novel photo-electrode material, the photocatalytic properties of selected materials were studied before their applications for photoelectrochemical degradation of organic pollutants. In this research work, carbon materials such as reduced graphene oxide (RGO) and exfoliated/expanded graphite (EG) were used to form carbon-metal oxides nanocomposite materials. The materials were characterised using UV-Vis diffuse reflectance spectroscopy, X-ray diffraction (XRD), transmission electron microscopy (TEM), scanning electronic microscopy (SEM), energy dispersive X-ray spectrometry (EDX), Fourier transformed infrared spectroscopy (FTIR) and Raman spectroscopy, cyclic voltammetry, linear sweep voltammetry and chronoamperometry response. Furthermore, the materials were employed for photocatalytic, electrocatalytic and photo-electrocatalytic degradation of organic pollutants in water.

In this regard, a nanocomposite consisting of silver, silver oxide (Ag_2O), zinc oxide (ZnO) and graphene oxide (GO) was synthesised, characterised and photocatalytically applied in the degradation of organic pollutants in water treatment process. The Ag-Ag_2O-ZnO nanostructure was synthesised and calcined at 400 ºC. It was functionalised using 3-aminopropyl triethoxysilane and anchored on carboxylated graphene oxide via the formation of an amide bond to give the Ag-Ag_2O-ZnO/GO nanocomposite. The as-prepared Ag-Ag_2O-ZnO/GO nanocomposite was investigated as a photocatalyst for the photocatalytic degradation of acid blue 74 dye under visible light irradiation in synthetic wastewater containing the dye. The results showed that Ag-Ag_2O-ZnO/GO nanocomposite has a higher photocatalytic activity (90% removal with a kinetic rate constant of 10.69×10^{-3} min^{-1}) than Ag-Ag_2O-ZnO (85% removal) and ZnO (75% removal) respectively.

Due to the high photocatalytic activity of the Ag-Ag_2O-ZnO/GO nanocomposite, a photoanode consisting of a composite of silver (Ag), zinc oxide oxide (ZnO) and reduced graphene oxide (rGO) was photoelectrochemically applied in the degradation and possible mineralisation of organic pollutants in water treatment process. The ZnO and Ag-ZnO nanoparticles were synthesised. The nanoparticles were used to dope reduced graphene oxide by dispersion in methanol, sonicated and dried. The obtained Ag-ZnO-rGO nanocomposite was compressed and fabricated into an electrode. The Ag-ZnO-rGO as a photoanode material was used for the photoelectrochemical degradation of orange II dye as target organic pollutant in 0.1 M Na_2SO_4 solution at a current density of 15 $mAcm^{-2}$. The

results revealed that the photoelectrochemical process was pH and current density dependent and that Ag-ZnO-rGO electrode has a higher photoelectrochemical performance, following the pseudo-first order kinetics with an apparent rate constant of 12.26×10^{-3} min^{-1} (93% removal efficiency) than ZnO-rGO electrode (87% removal efficiency) and rGO (73% removal efficiency) respectively. The degree of mineralisation of the dye was determined using total organic carbon (TOC) which gave better removal efficiency for Ag-ZnO-rGO electrode (67.9%) in comparison with ZnO-rGO (58.7%) and rGO (45.3%) electrodes, respectively.

In order to test the electrochemical and photoelectrochemical properties of exfoliated graphite-based nanocomposite, the degradation of organics in water treatment by electrochemical and photo-assisted electrochemical processes was carried out using a photo-electrode consisting of tungsten trioxide (WO_3) and exfoliated graphite (EG). The WO_3–EG, as photo-electrode material, was investigated for the degradation of 2-nitrophenol and orange II dye as model organic pollutants in a 0.1 M Na_2SO_4 solution, using a 10 $mAcm^{-2}$ current density. The removal efficiency of the dye and 2-nitrophenol was monitored using a UV-Visible spectrophotometer and the mineralisation level was investigated using a TOC analyser. The results showed that the WO_3-EG nanocomposite electrode gave a better degradation kinetics and higher removal efficiency (82% for 2-nitrophenol and 95% for orange II dye), and a higher degree of mineralisation (69% for 2-nitrophenol and 67% for orange II dye) in comparison to the EG electrode. Also, the WO_3-EG nanocomposite electrode exhibited better degradation kinetics for the 2-nitrophenol and orange II dye. Furthermore, efforts were made to evaluate the degradation intermediates which indicated the formation of carboxylic acids that were further degraded by hydroxyl radicals.

Furthermore, in order to explore the photo-electrocatalytic properties of other materials, the photocatalytic activities of a nanocomposite consisting of palladium (Pd), zinc oxide (ZnO) and exfoliated graphite (EG) was utilised for the removal of acid orange 7 dye as a model organic pollutant. Results obtained showed that Pd-ZnO-EG composite displayed a better photocatalytic performance, giving better removal efficiency of 87 % in comparison with ZnO and Pd-ZnO which gave 3 and 25 % percentage removal respectively.

Thus, Pd-ZnO-EG photoelectrode was constructed using a Pd-ZnO-EG nanocomposite. Cyclic voltammetry and chronoamperometry response measurements were carried out on

the electrode. The Pd-ZnO-EG electrode was employed in the photoelectrocatalytic removal of 4-nitrophenol as a target water pollutant at a neutral pH and current density of 7 $mAcm^{-2}$. The results of the optical studies revealed that the Pd-ZnO-EG material absorbed strongly in the visible light region. The Pd-ZnO-EG electrode showed improved photoelectrocatalytic activity (with degradation kinetics having a rate constant of 18.52×10^{-3} min^{-1}) in relation to ZnO-EG and EG electrodes for the removal of the 4-nitrophenol. Density functional theory method was used to model the oxidative degradation of 4-nitrophenol by hydroxyl radical which generate hydroquinone, benzoquinone, 4-nitrocatechol, 4-nitroresorcinol and the opening of the 4-nitrophenol ring. Furthermore, the hydroxyl radical was regenerated and it then further oxidised the ring structure and initiated a new degradation process.

Finally, a photoanode consisting of a p-n MoS_2-SnO_2 heterojunction anchored on expanded graphite (EG) was fabricated and employed in the photo-electrocatalytic degradation of ciprofloxacin, a pharmaceutical pollutant in water, 0.1 M Na_2SO_4 solution using a current density of 0.010 Acm^{-2}. Photoelectrochemical studies were carried out with cyclic and linear sweep voltammetry and chronoamperometry. The removal efficiency of photo-electrocatalytic cell was determined on a UV-Visible spectrophotometer and the extent of mineralisation was measured by a total organic carbon analyser. The results revealed that the SnO_2 particles are nanosheets while the MoS_2 particles are hierarchical microspheres having nanosheets of MoS_2, and they were anchored on the interlayers of the EG sheets. Also, the p-n MoS_2-SnO_2 heterojunction anchored on expanded graphite (EG) was found to be photoactive and displayed a better removal efficiency and mineralisation in comparison to EG, SnO_2-EG and MoS_2-EG electrodes. Also, the MoS_2-SnO_2/EG displayed a better degradation kinetics which followed the pseudo-first order model. This could probably be attributed to the formation of the MoS_2-SnO_2 p-n heterojunction in the MoS_2-SnO_2/EG nanocomposite which enhanced the light harvesting ability of the material resulting in its improved photo-electrocatalytic performance. Thus, these nanocomposite materials could be beneficial for wastewater treatment processes where the removal of organics is very important.

The scientific and technological demonstrations in this study could be employed for wastewater treatment process. Furthermore, the high degradation efficiencies obtained showed that AOPs are cost effective and efficient water treatment methods which could help in reducing health problems that are linked to polluted and contaminated water.

TABLE OF CONTENTS

Section ***Page***

LIST OF FIGURES

Figure ***Description*** ***Page***

LIST OF TABLES

LIST OF ABBREVIATIONS

Ag/AgCl	Silver/silver chloride electrode
AOPs	Advanced oxidation processes
BPA	Bisphenol A
BET	Brunauer Emmett Teller
B3LYP	Becke 3-parameter exchange with Lee, Yang, Parr Correlation
BLYP	Becke correlation functional with Lee, Yang, Parr correlation
Si/BDD	Silicon-boron-doped diamond
CA	Chronoamperometry
CB	Conduction band
CP	Chronopotentiometry
CV	Cyclic voltammetry
DCAA	Dichloroacetic acid
DMF	Dimethylformamide
LSV	Linear sweep voltammetry
DFT	Density functional theory
DRS	Diffuse reflectance spectral
EDC	Endocrine disrupting chemical
EDX	Energy dispersive X-ray spectroscopy
EG	Exfoliated graphite

Eg	Band gap
EP	Epoxy resin
FTIR	Fourier Transform Infra-Red
FTO	Fluorine doped tin oxide
GCE	Glassy carbon electrode
GICs	Graphite intercalation compounds
GO	Graphene oxide
HF	Hartree-Fock
IC	Inorganic carbon
ITO	Indium doped tin oxide
JPCDS	Joint Committee on Powder Diffraction Standards
LDA	Local density approximation
LSDA	Local spin density approximation
MEO	Mediated electrochemical oxidation
NP	Nitrophenols
pHzpc	point of zero charge
POPs	persistent organic pollutants
SCE	saturated calomel electrode
SEM	Scanning electron microscopy
TC	Total carbon

TEM	Transmission electron spectroscopy
Ti	Titanium
TOC	Total organic carbon
USEPA	United States Environmental Protection Agency
UV	Ultra Violet
UV-Vis	Ultra Violet-Visible spectroscopy
XRD	X-Ray diffractometry

CHAPTER 1

INTRODUCTION

1.1 BACKGROUND, PROBLEM STATEMENT AND MOTIVATION

Water is very essential in the life of every living thing on earth. It is used for growing crops, household needs, industrial processes and the sustenance of natural cycles [1]. Water is necessary for the ecosystems to survive as well as the plants and animals living it. In return, the ecosystems aid in balancing the quality and quantity of water [1]. According to Schutte and Focke [2], the human population is projected to increase twice its present number by 2050, and this would make the accessibility to clean and quality water a world challenge. The reason for this crisis is due to the fact that a large percentage of the world's water is salty (97 %), 2% of the water is captured in the form of ice while the available 1% is unevenly distributed, thus making water a scarce commodity [3].

As population and industrial operations are increasing, the demand for water keeps increasing, thus the demand on fresh water from water bodies such as lakes, rivers, etc to sustain industries, agriculture and household needs has gone high in the last century [4]. Furthermore, it was reported that the demand for fresh water by household uses is half that of industrial activities [4]. As industrialisation, economic growth and urbanisation are increasing, the scarcity of water has been worsened. This is due to the large volumes of toxic wastewaters or effluents that are generated and released into the environment. The wastewaters are generated as a result of anthropogenic activities such as household uses and industries such as agriculture, pharmaceuticals, dyes, crude oil refinery, pesticides, dyes and mining [5]. These generated wastewaters are discharged into the environment where they pollute surface water and underground water [6]. Thus, the limited water resources are threatened by water pollution.

The availability of the limited clean water which is essential for good health in any community and a necessary condition for the operations of many industries has become a global challenge in most developing regions of the world, and the intake of contaminated and polluted water, especially in rural areas, has led to avoidable deaths [7, 8]. There are several types of water pollutants and these include as organic, inorganic and microbial pollutants. One of the major water pollutants are organic pollutants. The discharge of organic waste into water bodies is on the increase and these organic wastes pose a lot of health and environmental risk to living organism [7, 8]. Some of these organic wastes are

dyes, phenols, nitro-substituted phenols, chloro-substituted phenols, polychlorinated biphenyl compounds, phthalates, pharmaceuticals, etc. The presence of these organic pollutants in water or wastewater is not only hazardous to human and aquatic lives [9], some of these pollutants are recalcitrant during treatment by the conventional water treatment methods. Hence, it is of utmost importance to eradicate these contaminants and pollutants from wastewater.

Several traditional methods have been employed for the removal of these pollutants. However, some of these contaminants and pollutants remain after the use of these methods [10, 11]. Conventionally, the removal of pollutants from effluents or wastewaters is usually carried out by biological, physical and chemical processes such as phytoremediation, oxidation and reduction, filtration, chemical precipitation and coagulation, use of ion exchange resin, ultrafiltration, solvent extraction, reverse osmosis, and electrodialysis [6]. The disadvantages of most of these conventional methods are time consumption, high capital cost equipments and their maintenance, membrane fouling, partial removal of the pollutants, high cost of operation and conversion of the pollutants into more toxic substances than the initial pollutants [12, 13]. Thus, there is need for the development and use of effective, economical and environmental friendly method for the removal of these pollutants.

Recently, advanced oxidation processes (AOPs) have emerged to be efficient and effective methods for the treatment of wastewaters [14]. They are utilised for the removal of organic pollutants during water treatment due to the generation and use of hydroxyl radicals as oxidising species which initiate other reactions for the degradation and possibly mineralisation of organic pollutants [15]. These AOPs are generally grouped into photochemical and non-photochemical processes. The non-photochemical processes include electrochemical oxidation and use of Fenton (Fe^{2+}/H_2O_2) reagent, ozonation/hydrogen peroxide (O_2/H_2O_2), ferrate (K_2FeO_4, Fe(VI)), zero-valent iron and oxidation in sub- and supercritical water, etc [14], while the photochemical processes include heterogeneous photocatalysis, photo-Fenton, UV/ozonolysis, UV/periodate, UV/H_2O_2, etc [14]. Since hydroxyl radical (•OH) is the oxidising species used in these processes for the breaking down of organic pollutants, they are generally considered environmentally friendly for water treatment processes. These processes are cheap with relatively high effectiveness and efficiency for water treatment.

Electrochemical oxidation is one of the AOPs in which hydrogen peroxide and hydroxyl radicals are produced at the anode surface [16]. However, the efficiency of the process depends largely on the type of materials used. Conducting materials like fluorine doped tin oxide (FTO) and indium doped tin oxide (ITO) used in the preparation of electrodes are expensive and exhibit low conductivity while titanium sheet which is highly conducting is expensive. Hence, there is a quest for cheap and good conducting materials for electrodes. [18].

Furthermore, limitations linked to electrochemical oxidation include mass transfer of the pollutant in solution to the electrode surface and oxygen evolution as a side reaction resulting from the utilisation of high voltage in the degradation process. Thus, there is need to minimise these limitations by combining electrochemical oxidation with other AOPs like photocatalytic degradation giving rise to a process called photoelectrochemical or photo-electrocatalytic process [17]. This process results in the production of more hydroxyl radicals for the oxidation or degradation of the organic pollutants.

Understanding the kinetics and mechanisms of the reactions could provide insight into the degradation products of the reactions since some products could be more toxic than the degraded organic pollutants. The application of first principle computational approaches has been identified as effective tools in electrochemistry. Computational modelling has been used to predict and explain reactions and synthesis of materials with enhanced catalytic performance especially in electrochemical processes [19, 20]. Thus, there is a need for computational modelling of the reaction kinetics and mechanisms, and consequently, the determination of the degradation products

1.2 JUSTIFICATION

Carbonaceous materials such as graphene and exfoliated graphite (EG) possess high electrical conductivity and good electron transport capacity, low cost to life ratio, compressibility, high temperature resistance. In addition, it has high thermal conductivity, good mechanical property, low density, large surface area, and can bear very high current density [18, 21]. Also, they exhibit good anodic potential windows and their oxygen evolution overpotential is high. These attributes make them attractive materials for photo-electrodes for the degradation of organic pollutants in water treatment processes. The porous nature of carbon materials can aid the incorporation of photocatalyst or semiconductors in the carbon materials to form carbon-based composite substrates for the

fabrication of photo-electrodes used in photo-electrocatalytic process for water treatment. Due to the high electron transport nature of these carbon materials, photo-generated holes and electrons of the photocatalyst can be transferred to the graphene/exfoliated graphite. As a result, the recombination process which is a setback in photocatalysis would become minimal. Thus more hydroxyl radicals for the breaking down of the organics would be produced. Moreover, since the porous nature of the exfoliated graphite enhances the trapping of photocatalyst, it reduces losses in recovery process [18, 21-23]. Also, the recombination rate of the generated electron-hole pairs can be reduced by the utilisation of electrical energy to drive away the electrons from the electrolyte-semiconductor interface.

As a result of time consuming and sometimes cost ineffective nature of experimental investigations of electrochemical reactions, quantum chemical calculations have been employed to complement and corroborate experimental determinations of the reaction products and degradation mechanisms of organic pollutants [20, 24]. Quantum chemical parameters such as molecular geometry, activation energy, reaction energy etc. which have been calculated at several levels of theory were correlated with experimental determinations of reaction mechanisms, products, oxidation and reduction behaviours of compounds, etc. so as to establish a relationship between these electrochemical reactions and quantum chemical descriptors [20, 24-28]. In this work, carbonaceous materials such as reduced graphene oxide (RGO) and exfoliated/expanded graphite (EG) were used to form carbon-metal oxides electrode materials which were employed for the photo-electrocatalytic degradation of organic pollutants

1.3 RESEARCH HYPOTHESIS

Carbon-metal oxides nanocomposite materials are good photo-electrode materials for the degradation/removal and possibly minerisation of organic pollutants in water treatment process.

1.4 AIM OF THE STUDY

The aim of this work is to develop novel photo-electrodes using carbon-metal oxides nanocomposite materials for the degradation /removal and possibly mineralisation of organic pollutants in water; while unravelling the reaction kinetics, mechanisms and degradation products of selected reactions using computational approaches.

1.5 SPECIFIC OBJECTIVES OF THE STUDY

The specific objectives of this work are as follows:

1. The design and production/fabrication of good photo-electrocatalytic materials for removal of organic pollutants.
2. Synthesis of carbon materials such as graphene/reduced graphene oxide (RGO) and exfoliated/expanded graphite (EG) and fabrication of electrodes.
3. The use of RGO and EG as conducting platform for the immobilisation of metal oxides and semiconductor photocatalysts such as ZnO, WO_3, SnO2, MoS_2 Ag-Ag_2O.
4. Characterisation of the synthesised materials by Raman spectroscopy, XRD, UV, FTIR, nitrogen adsorption and desorption analysis, TEM, SEM, EDS, CV, LSV and photocurrent response measurements.
5. Application of the electrodes in the electrochemical and photo-electrochemical / photo-electrocatalytic degradation of selected organic pollutants.
6. Determination of the reaction kinetics, mechanisms and degradation products of selected reactions using theoretical quantum chemical computations based on density functional theory (DFT).

1.6 THESIS OUTLINE

This thesis is divided into 10 chapters.

- Chapter 2 entails the literature review of selected organic pollutants and methods used for their removal in water treatment, an overview of advance oxidation processes with emphasis on electrochemical, photocatalytic, and photo-electrocatalytic techniques.
- Chapter 3 discusses the materials and general methodology used in this work. The different characterisations techniques used are discussed as well.
- Chapter 4 presents the search for good photo-electrode material by conducting a photocatalytic study; photocatalytic degradation of acid blue 74 in water using Ag-Ag_2O-ZnO nanostuctures anchored on graphene oxide.
- Chapter 5 entails photoelectrochemical degradation of orange II dye in wastewater at silver-zinc oxide/reduced graphene oxide nanocomposite photoanode.
- Chapter 6 entails towards wastewater treatment: Photo-assisted electrochemical degradation of nitrophenol and orange II dye at a tungsten trioxide-exfoliated graphite composite electrode

- Chapter 7 entails the search the search for good photo-electrode material by conducting a photocatalysis study; photocatalytic application of Pd-ZnO-exfoliated graphite nanocomposite for the enhanced removal of acid orange 7 dye in water
- Chapter 8 presents photo-electrocatalytic application of palladium decorated zinc oxide-expanded graphite electrode for the removal of 4-nitrophenol: Experimental and computational study
- Chapter 9 explores expanded graphite supported p-n MoS_2-SnO_2 heterojunction nanocomposite electrode for enhanced photo-electrocatalytic degradation of a pharmaceutical pollutant.
- Chapter 10 presents the conclusion and recommendations as well as and future work

1.7 REFERENCES

[1] M.W. Rosegrant, X. Cai, S.A. Cline, Global water outlook to 2025, Averting an impending crisis. IWMI, Colombo, Sri Lanka, (2002).

[2] C.F. Schutte, W. Focke, Evaluation of nanotechnology for application in water and wastewater treatment and related aspects in south Africa, Water Research Commission2007.

[3] A. Smith, An Answer to the World's Water Crisis?, Chemistry International, (2009).

[4] R. Kingsford, J.E. Watson, C. Lundquist, O. Venter, L. Hughes, E. Johnston, J. Atherton, M. Gawel, D.A. Keith, B. Mackey, Major conservation policy issues for biodiversity in Oceania, Conservation Biology, 23 (2009) 834-840.

[5] Y. Huang, Y.E. Miao, T. Liu, Electrospun fibrous membranes for efficient heavy metal removal, Journal of Applied Polymer Science, 131 (2014).

[6] J. Su, Y. Zhang, S. Xu, S. Wang, H. Ding, S. Pan, G. Wang, G. Li, H. Zhao, Highly efficient and recyclable triple-shelled $Ag@Fe_3O_4@SiO_2@TiO_2$ photocatalysts for degradation of organic pollutants and reduction of hexavalent chromium ions, Nanoscale, 6 (2014) 5181-5192.

[7] J. Davey, A. Schäfer, Ultrafiltration to Supply Drinking Water in International Development: A Review of Opportunities, Appropriate Technologies for Environmental Protection in the Developing World, Springer 2009, pp. 151-168.

[8] R.P. Schwarzenbach, B.I. Escher, K. Fenner, T.B. Hofstetter, C.A. Johnson, U. Von Gunten, B. Wehrli, The challenge of micropollutants in aquatic systems, Science, 313 (2006) 1072-1077.

[9] J. Méndez-Hernández, F. Ramírez-Vives, M. Solís-Oba, A. Solís-Oba, A. Sobrino-Figueroa, O. Loera, Detoxification and mineralization of Acid Blue 74: study of an alternative secondary treatment to improve the enzymatic decolourization, World Journal of Microbiology and Biotechnology, 29 (2013) 805-814.

[10] R. Chaiyont, C. Badoe, C. Ponce de León, J.L. Nava, F.J. Recio, I. Sires, P. Herrasti, F.C. Walsh, Decolorization of Methyl Orange Dye at IrO_2-SnO_2-Sb_2O_5 Coated Titanium Anodes, Chemical Engineering & Technology, 36 (2013) 123-129.

[11] A.K. Verma, R.R. Dash, P. Bhunia, A review on chemical coagulation/flocculation technologies for removal of colour from textile wastewaters, Journal of Environmental Management, 93 (2012) 154-168.

[12] R. Gaikwad, V. Sapkal, R. Sapkal, Ion exchange system design for removal of heavy metals from acid mine drainage wastewater, Acta Montanistica Slovaca, 15 (2010) 298.

[13] S. Rengaraj, Y. Kim, C.K. Joo, K. Choi, J. Yi, Batch adsorptive removal of copper ions in aqueous solutions by ion exchange resins: 1200H and IRN97H, Korean Journal of Chemical Engineering, 21 (2004) 187-194.

[14] M.I. Litter, Introduction to photochemical advanced oxidation processes for water treatment, Environmental Photochemistry Part II, Springer 2005, pp. 325-366.

[15] S.H.S. Chan, T. Yeong Wu, J.C. Juan, C.Y. Teh, Recent developments of metal oxide semiconductors as photocatalysts in advanced oxidation processes (AOPs) for treatment of dye waste-water, Journal of Chemical Technology and Biotechnology, 86 (2011) 1130-1158.

[16] E. Kusmierek, E. Chrzescijanska, Application of TiO_2–RuO_2/Ti electrodes modified with WO_3 in electro-and photoelectrochemical oxidation of Acid Orange 7 dye, Journal of Photochemistry and Photobiology A: Chemistry, 302 (2015) 59-68.

[17] E. Brillas, C.A. Martínez-Huitle, Decontamination of wastewaters containing synthetic organic dyes by electrochemical methods. An updated review, Applied Catalysis B: Environmental, 166 (2015) 603-643.

[18] B. Ntsendwana, S. Sampath, B. Mamba, O. Arotiba, Photoelectrochemical oxidation of p-nitrophenol on an expanded graphite–TiO_2 electrode, Photochemical & Photobiological Sciences, 12 (2013) 1091-1102.

[19] F. Calle-Vallejo, M.T. Koper, First-principles computational electrochemistry: Achievements and challenges, Electrochimica Acta, 84 (2012) 3-11.

[20] V.-M. Guérin, R. Zouzelka, H. Bibova-Lipsova, J. Jirkovsky, J. Rathousky, T. Pauporté, Experimental and DFT study of the degradation of 4-chlorophenol on hierarchical micro-/nanostructured oxide films, Applied Catalysis B: Environmental, 168 (2015) 132-140.

[21] X. Yu, Y. Zhang, X. Cheng, Preparation and photoelectrochemical performance of expanded graphite/TiO 2 composite, Electrochimica Acta, 137 (2014) 668-675.

[22] B. Ntsendwana, B.B. Mamba, S. Sampath, O.A. Arotiba, Synthesis, characterisation and application of an exfoliated graphite–diamond composite electrode in the electrochemical degradation of trichloroethylene, RSC Advances, 3 (2013) 24473-24483.

[23] M. Peleyeju, E. Umukoro, J. Babalola, O. Arotiba, Electrochemical Degradation of an Anthraquinonic Dye on an Expanded Graphite-Diamond Composite Electrode, Electrocatalysis, 7 (2016) 132-139.

[24] W. Han, C. Zhong, L. Liang, Y. Sun, Y. Guan, L. Wang, X. Sun, J. Li, Electrochemical degradation of triazole fungicides in aqueous solution using TiO_2-NTs/SnO_2-Sb/PbO_2 anode: Experimental and DFT studies, Electrochimica Acta, 130 (2014) 179-186.

[25] V.S. Padalkar, P. Ramasami, N. Sekar, A combined experimental and DFT-TDDFT study of the excited-state intramolecular proton transfer (ESIPT) of 2-(2′-hydroxyphenyl) imidazole derivatives, Journal of fluorescence, 23 (2013) 839-851.

[26] İ.H. Taşdemir, Electrochemistry and determination of cefdinir by voltammetric and computational approaches, Journal of Food & Drug Analysis, 22 (2014).

[27] W. Wang, S. Wang, X. Xie, V. Ramani, Density functional theory study of hydroxide-ion induced degradation of imidazolium cations, International Journal of Hydrogen Energy, 39 (2014) 14355-14361.

[28] U. Warde, L. Rhyman, P. Ramasami, N. Sekar, DFT Studies of the Photophysical Properties of Fluorescent and Semiconductor Polycyclic Benzimidazole Derivatives, Journal of fluorescence, 25 (2015) 685-694.

CHAPTER 2

LITERATURE REVIEW

2.1 INTRODUCTION

This chapter provides an overview of water pollution and types of pollutants. Also, it discusses selected pollutants and associated problems of the pollutants in water. A general overview of advance oxidation processes is discussed with emphasis on electrochemical oxidation, photocatalysis and photo-electrocatalytic oxidation. Furthermore, a brief review on quantum chemistry including the models and methods of computational chemistry with emphasis on density functional theory are presented.

2.2 WATER POLLUTION AND TYPES OF POLLUTANTS

Access to quality water is one major way of ensuring food security, good health of the society and good working conditions for many industries. However, there are problems arising from pollution and contamination of water bodies and the environment which have increasingly attracted a global attention in recent years [1]. Water pollution refers to the introduction of foreign bodies or chemicals that are toxic and hazardous to the human health into water bodies. The introduction of these toxic substances into the environment due to increased urbanisation and industrialisation has made surface and ground water resources to be limited. Consequently, the availability of clean and quality water has become a general challenge [2]. Access to the limited water resources is one of the greatest problems that has plagued the human race and the ecosystems as population is increasing, and it has remained a global concern [3, 4]. In developing regions of the world, accessing clean and safe water is a major problem due to water pollution, and the intake of polluted water has been reported to have adverse effects on the health of the population which had invariably led to deaths that are avoidable [5, 6]. Also, the release of these toxic substances or chemicals into the environment can lead to their transformation into more chronic compounds as a result of some chemical processes which they can undergo in the environment. Consequently, the exposure of human and aquatic lives to these chronic substances can result to carcinogenic problems, reproduction-related issues and disruption of the endocrine systems of some organisms [7]. This makes the removal of these pollutants from wastewater as well as water purification processes paramount.

The main source of water pollutants is anthropogenic activities. These activities lead to the production of organic wastes (pesticides, dyes, crude oil, drugs, etc); inorganic wastes (heavy metals) and microbial wastes [6, 8]. Pollutants produced by humans and other organisms, agricultural substances such as fertilizers applied to agricultural field, discharge from inefficient sewage treatment plants and heavy metals entering into water bodies are on the increase [9]. This could primarily be as a result of increased urbanization and industrialization around the world, and secondly, because many developing nations cannot afford the available state-of-the-art technology for wastewater treatment [10, 11]. For instance, pesticides and fertilizers used in agriculture by farmers for the protection and growth of crops could pose danger. They can mix with run-off rain water and flow into rivers, thereby, affecting aquatic organisms. The organic and inorganic pollutants are the major cause of concern, since they are persistent, non-biodegradable and bio-accumulate in the food chain [1]. Some of these pollutants are toxic chemicals that are utilised during manufacturing processes in the industries. They are potentially hazardous to human and aquatic lives when they are released indiscriminately into the environment and water bodies [12]. Some of these substances cannot be recycled probably due to poor industrial waste management systems. Thus, they are released into the environment either through rivers, streams, and other water bodies, which are perhaps major sources of potable water to humans and livestock [13]. These substances invariably find their ways into both surface and ground water, and as a result, could affect the health of human and other organisms adversely [14].

2.2.1 INORGANIC POLLUTANTS

These are pollutants or toxic compounds that do not possess elemental carbon in their structures. They are released into the environment through different sources. These include heavy metal ions (lead, cadmium, zinc, mercury, arsenic, chromium, etc), anions (sulphides, phosphates, fluoride, chloride, etc.) and gases (carbon dioxide, suphur dioxide and so on) [15]. Generally, some heavy metals are required in trace or very minute quantity in living organisms, but they have been found to be toxic and carcinogenic in nature when they are present in large quantity or in excess. Thus, they pose serious hazards to human and aquatic organisms when they are discharged into water bodies and the environment [16]. The presence of heavy metals in the environment is caused by industrial waste discharge and weathering which results in their accumulation in the food chain. They are known to be persistently stable in the environment and they are non-biodegradable or

broken down into less harmful products [17]. They have the ability to bioaccumulate in humans through the food chain thereby causing severe health problems such as kidney failure, liver diseases, etc. Several techniques have been used for the treatment of heavy metals polluted effluents such as adsorption, membrane separation, phytoremediation, reverse osmosis, flocculation and coagulation, solvent extraction, chemical precipitation, ion-exchange, ultrafiltration, electrodialysis, etc, but there are several limitations with these methods [9, 18].

2.2.2 ORGANIC POLLUTANTS

Organic pollutants constitute a wide range of toxic organic chemicals that are released into the environment. There is a rise in the level of organic pollutants in industrial effluents and sewage, and consequently, an increase in concentration in the environment and water bodies. This is due to the increased production for domestic and industrial usage. They have become a global concern because they constitute a major threat to the environment and humans even at minute quantities. They have been reported to be mutagenic and carcinogenic [19]. Some of these pollutants tend to prevail in the environment for a long period of time and thus, they are known as persistent organic pollutants. Their persistence could be as a result of their continual release into the environment or due to their very long half-life periods. They have the capability to bioaccumulate in the food chain because they can be easily absorbed into the tissues of animals and plants [20]. Industrial effluents from agricultural, pharmaceutical, dyes, petrochemical and textiles industries contain these persistent organic pollutants. Examples include pesticides, insectides, herbicides, dyes, polychlorinated biphenyls (PCBs), polybrominated diphenyl ethers (PBDEs) and phenols [21]. Several health problems are associated with these persistent organic pollutants and these include cancers, breakdown of the immune system as well as nervous and reproductive systems disorders [22]. They are recalcitrant in nature and thus, difficult to treat or remove from water using the conventional wastewater treatment techniques [23]. A selected few of these persistent organic pollutants are discussed below.

2.2.2.1 Dyes

Dyes are coloured organic substances that are used for colouring various things such as clothes, paint, food and medicine [24]. Also, they are employed in the colouring of paper, leather, hair etc. using liquid in which they are either partially or completely soluble. Dyes consist of aromatic and ionising component which enable them to be attracted to the

substances to which they are used to colour. The structures of dyes can be modified, making it less difficult for the production of new dyes having different colours, and they are difficult to remove when employed on the substances [25]. Most textiles are coloured using fibre reactive dyes which usually form a covalent bond with the textile or fabrics. However, other dyes such as mordant dyes need pre-treatment before they are applied and they are precipitated as insoluble salt, making them resistant to fading either by sunlight or chemical attacks. Generally, dyes are classified based on their chemical structure (nitro, phthalocyanin, anthraquinone, indigoid, hydroxy ketone and amino, azo, quinolin, xanthenes, diphenylmethane , carotenoid, etc) or application (vat, sulphur dye, reactive, mordant, direct, acid and basic) [25, 26]. About 15% of the total dyes synthesised in the world are lost during the production and applications of these dyes and they are released in wastewaters which are discharged into the environment [27]. When these dyes are released into the ecosystem, they cause eutrophication and perturbation to aquatic organisms [27]. These dyes have been found as a notable class of organic water pollutants, and dye-containing effluents from industries (especially textile, leather and paint) constitute a major environmental and health challenge [28]. It has been documented that some of these dyes are toxic and cancer-causing agents, and consequently, can cause health problems such as dermatitis, allergies, and tumours [28-31]. Also, the intravenous administration of indigo carmine has led to cardiac arrest [32]. Some organic dyes in water are very difficult to remove during water treatment by the conventional treatment methods and systems [33-35]. The water quality degradation, health risk and recalcitrant behaviours posed by organic dyes during conventional water treatment necessitate the need to develop alternative (and complementary) methods for their removal. Examples of these azo dyes are orange II dye (also known as acid orange 7) and acid blue 74 (known as indigo carmine, is widely utilised as additive in pharmaceutical and food industries). The structures of orange II dye and acid blue 74 are present in Figure 1.

Several conventional methods have been utilised for the treatment of dye-containing effluents and these methods include precipitation, reverse osmosis, chemical oxidation, adsorption, aerobic and anaerobic treatment. The main setbacks of these conventional methods include sludge formation, high operational cost, waste disposal and time consumption [36-38].

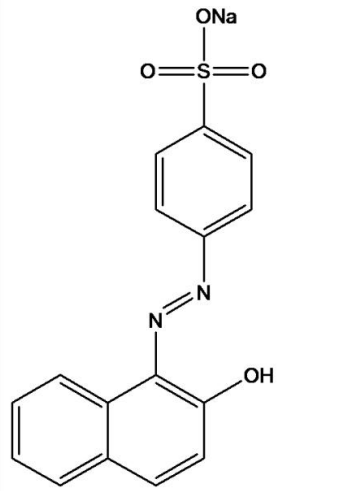

Orange II dye or Acid orange 7

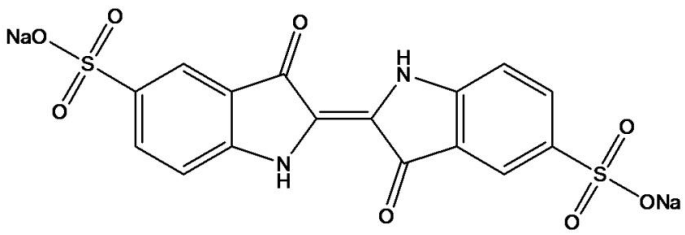

Acid blue 74 dye or Indigo carmine

Figure 2.1: Structures of selected dyes.

2.2.2.2 Nitrophenol

Phenol and its nitro derivatives have been widely used in industries involved in the manufacturing of explosives, herbicides, textiles, pesticides, pharmaceutical, dyes, paints, paper, etc. [39]. They are released into the aquatic environment through human activities. Also, nitrophenols are produced and found in rain water when aromatic compounds react with ozone and nitrogen oxides in the troposphere. Also, they are formed by photodegradation of pesticides which contains the moiety of nitrophenols [40]. Examples are 2- nitrophenol, 3-nitrophenol, 4-nitropheol and 4,5-dinitrophenol. Their toxicity is linked to the nitro groups which are normally reduced to nitro, nitroso and hydroxylamine derivatives [41]. They are persistent and bio-refractory organic pollutants that have been listed as some of the persistent organic pollutants that are toxic and of priority by United States Environmental Protection Agencies (USEPA), especially 2-nitrophenol and 4-nitrophenol which are stable, biorefractory in nature, toxic and mutagenic to living organisms. Furthermore, the release of wastewaters containing these compounds from industries could pose potential hazards to humans and the environment in general [42].

Consequently, there is need for proper treatment of these industrial wastewaters before being released into water bodies. Nevertheless, the removal of nitrophenols by the conventional methods is ineffective and difficult due to their recalcitrant nature [35, 42-44].

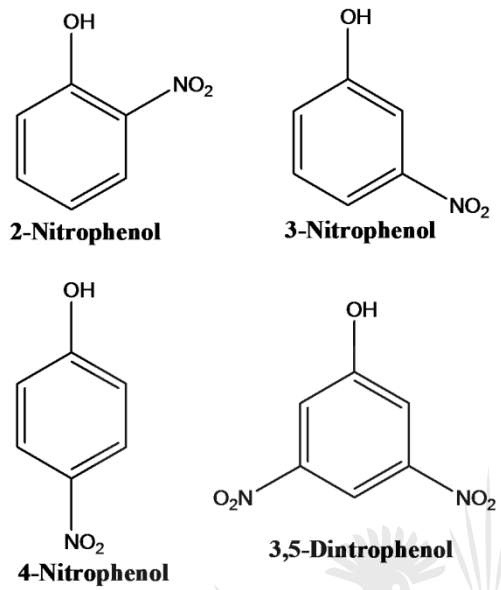

Figure 2.2: Structure of nitrophenols

2.2.2.3 Pharmaceutical pollutants

Thousands of tons of wastewaters containing pharmaceutical pollutants are being generated annually, and these are emptied into water bodies with little or no proper treatment, making the complexity of wastewater pollution a major challenge especially in developing countries [10, 11]. Specifically, antibiotics can cause problems to the ecosystem due to their capacity to persist in the environment [45-47]. Recently, the persistence of pharmaceutical products, especially antibiotics in water bodies even after treatment, has been reported [48]. This persistence can be attributed to the poor efficiency of the conventional wastewater treatment methods as a result of the recalcitrant nature of these pharmaceuticals. Also, they have attracted global scientific concerns because of their potential capacity to promote the spread of microorganisms having genes that are resistant to antibiotics. Consequently, they can cause serious threats to aquatic and human lives [48, 49]. These challenges thus necessitate the need for adequate and effective treatment techniques for the removal of pharmaceuticals. Example of such antibiotics is

ciprofloxacin which is used for the treatment of bacterial infections, and its wide occurrence in the aquatic environment has necessitated the search for effective techniques for its removal [50-52]. The structure of ciprofloxacin is given in Fig.4

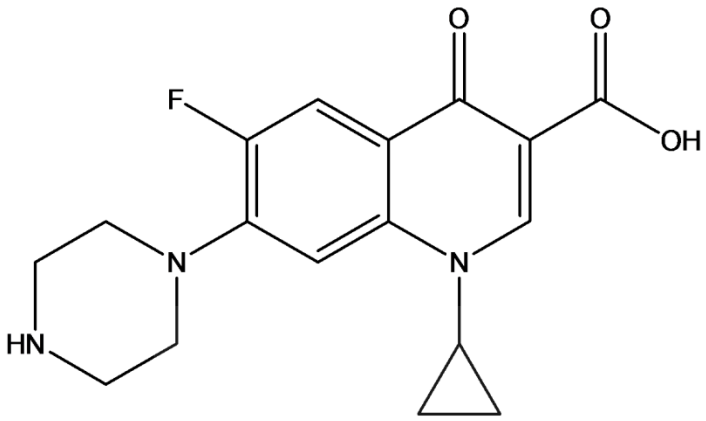

.

Figure 2.3: Typical structure of antibiotics, ciprofloxacin

2.3 CHALLENGES OF CONVENTIONAL METHODS IN WATER TREATMENT

Several methods have been investigated to treat wastewater from industries and they are generally classified into physical (adsorption), chemical (ozonation and chlorination), and biological (biodegradation). Chemical methods are mostly employed for treating these pollutants [27, 53]. The conventional wastewater treatment methods have proven to be ineffective and not sufficient for the purification of industrial wastewater. Hence other methods such as flocculation and coagulation, reverse osmosis, adsorption, active sludge, etc., have been employed, but the drawbacks that are associated with these methods involve creating pollutant-containing phase that are more concentrated. In addition, conventional methods such as activated carbon, ion exchange, membrane filtration, etc tend to generate additional wastes during water purification process and this requires extra cost [54]. These methods, in some cases, do not adequately get the desired level of purity stipulated by law or for use [55]. Also, the use of bacteria beds leads to wastewater composition fluctuations [27].

2.4 ADVANCE OXIDATION PROCESSES

Advanced oxidation processes (AOPs) have been discovered as a favourable and promising approach for environmental remediation, and are now becoming widely utilised in degrading organic pollutants in water treatment processes. AOPs involve the production of hydroxyl radical which is a non-selective oxidising agent and other powerful oxidants for the degradation of recalcitrant organics. The hydroxyl radical generated initiates series of reactions which break down the molecules of the organic pollutants into less harmful products in a process known as mineralisation [39, 56]. AOPs have been reported to have good results in developed countries and are currently being used in developing countries [55]. These AOPs are generally grouped into photochemical and non-photochemical processes. The non-photochemical processes include electrochemical oxidation, use of Fenton ($Fe^{2+/}H_2O_2$) reagent, ozonation/hydrogen peroxide (O_2/H_2O_2), ferrate (K_2FeO_4, Fe(VI)), zero-valent iron, oxidation in sub- and supercritical water, etc [55], while the photochemical processes include heterogeneous photocatalysis, photo-Fenton, UV/ozonolysis, UV/periodate, UV/H_2O_2, etc [55]. In this work, heterogeneous photocatalysis, electrochemical oxidation and the combination of both processes will be explored in detail.

2.4.1 Electrochemical oxidation

Electrochemical oxidation is an alternative approach for treating organic pollutants in wastewaters [57, 58]. It involves the oxidation of the organic pollutants in an electrolytic cell by either direct anodic oxidation (transfer of electron) at the surface of the electrode, resulting in poor decontamination efficiency or chemical reaction initiated by hydroxyl radicals electrochemically generated from water discharged at the electrode denoted as M. This could be in the form of chemically adsorbed active oxygen (metal oxide anode, MO, having oxygen in its lattice) or the active oxygen is physically adsorbed (M(•OH)) [59]. Due to the existence of the species resulting from the oxidation of the water discharged on the surface of the electrode, two main views have been proposed for electrochemical oxidation [57-60]. They are known as electrochemical conversion and electrochemical combustion methods.

Electrochemical conversion method involves the selective transformation of refractory organic pollutants into simple compounds that can be biodegraded such as carboxylic acids using the chemisorbed MO. On the other hand, electrochemical combustion method

involves the conversion of organic pollutants into dehydrogenated or hydroxylated substances by the physisorbed M(•OH) to the extent of mineralisation to carbon dioxide and inorganic ions. Moreover, the production of the oxidising agents and the oxidation of pollutants are dependent on the electrochemical cell potential difference. The oxidation of water and pollutants as well as anodic activities are maintained and promoted concurrently by using a high potential difference of the cell. On the other hand, the application of a low cell potential difference leads to oxygen evolution avoidance but there is loss of activity of the anode due to the adsorption of intermediates that are formed from direct anodic oxidation on the electrode surface. This renders this electrochemical procedure less practicable in water remediation process [57].

2.4.1.1 Model of electrochemical oxidation or direct electrochemical oxidation

According to Comninellis [60], there is selective oxidation of organic pollutants which takes place with the higher oxide, MO, formed by the electrode as a result of chemically adsorbed active oxygen in the metal lattice while combustion results from the accumulation of the M(•OH) radicals on the surface of the electrode (physisorbed active oxygen) [60]. Nevertheless, there was a modification of this model after diamond electrodes like boron-doped diamond (BDD) were used as electrodes [57, 61]. As a result, the behavioural patterns of these anodes were explained using the concept of active and non-active electrodes. The active anodes have low oxygen overpotentials, with chemically adsorbed active oxygen as the main oxidant responsible for the electrochemical conversion of the organic pollutants into carboxylic acids. Examples include RuO_2, IrO_2 and Pt anodes. For the non-active electrodes, there is high oxygen overpotential and the electrochemical combustion is done by the M(•OH) radicals resulting to mineralisation of the organics to carbon dioxide. Examples of non-active anodes include BDD, SnO_2 and PbO_2 anodes. This proposed model assumes water oxidation which leads to the formation M(•OH) radical is the first step in the two types of anodes, M. As shown in equation 2.1.

$$M + H_2O \rightarrow M(HO\bullet) + H^+ + e^- \qquad [2.1]$$

The chemical and electrochemical activities of the M(•OH) radicals depend on the type of electrode material used. It is assumed that the active anode surface strongly interacts with the hydroxyl radical to form the higher oxide MO according to equation 2.2.

$$M(HO\bullet) \rightarrow MO + H^+ + e^- \quad [2.2]$$

This reaction takes place when a active metal oxide anode has higher oxidation states. MO/M is the redox couple that mediates in the oxidation of the organic pollutant as presented in equation 2.3.

$$MO + R \rightarrow M + RO \quad [2.3]$$

And this reaction tends to compete with the side reaction of oxygen evolution which results from the decomposition of the higher oxide as shown in equation 2.4.

$$MO \rightarrow M + \frac{1}{2}O_2 \quad [2.4]$$

On the other hand, the surface of a non-active anode reacts weakly with the •OH radical such that the organic pollutant reacts directly with the M(•OH) to form less harmful substances like carbon dioxide and water as given in equation 2.5

$$M(HO\bullet) + R \rightarrow M + mCO_2 + nH_2O + H^+ + e^- \quad [2.5]$$

Where R is a fraction of the organic pollutant with m number of carbon atoms and does not have any heteroatom, but needs an oxygen atom in order to be converted completely into carbon dioxide. The mineralisation reaction is in competition with the side reactions of this radical leading to oxygen evolution either directly or by indirect reaction to form hydrogen peroxide as presented in equations 2.6 and 2.7 [57, 58, 60]

$$M(HO\bullet) \rightarrow M + \frac{1}{2}O_2 + H^+ + e^- \quad [2.6]$$

$$M(HO\bullet) \rightarrow \frac{1}{2}H_2O_2 \quad [2.7]$$

For a non-active electrode, there is no direct anodic reaction of the electrode with the organic pollutants. Also, there is no active adsorption site available for the pollutants from solution for catalytic activities on the electrode. It serves as an inert platform and electron sink, allowing the oxidation of water. It is the hydroxyl radical generated that mediates the oxidation of the organic pollutants. This model of active and non-active anode assumes

that the chemical (oxidation rate of organic pollutant) and electrochemical (overpotential for oxygen evolution) nature of the M(•OH) is linked to the degree of interaction of M–•OH. Hence a weak interaction commensurate to a lower anodic activity for the oxidation of the organic pollutants but a faster kinetics of reaction with the M(•OH) [60, 61]. The electrochemical generation of M(•OH) as the initiating oxidant renders electrochemical oxidation as an electrochemical advanced oxidation process (EAOP). Various reactive oxygen species (ROS) were produced in the reactions such as M(•OH) and H_2O_2, but M(•OH) is the strongest oxidising agent of the organic pollutants, even though its life time is short and acts during the supply of direct current to the electrode [57, 58].

2.4.1.2 Indirect or mediated electrochemical oxidation

Indirect electrochemical oxidation method involves the use of electrochemically generated strong oxidants for the treatment or destruction of organic pollutants. It involves the use of electrochemical oxidation with active chlorine or the chlorine mediated oxidation in which chloride ion present in the solution is oxidised to give the active chlorine species and the organic pollutant is oxidised in the bulk solution [58, 62]. These active oxidising species are chlorine, hypochorite and chlorite, chlorate, perchlorate, etc [57-59]. Another indirect electrochemical oxidation is the electro-Fenton process in which the organic pollutants can be decontaminated by hydroxyl radical (•OH) generated from Fenton's reaction taking place between Fe^{2+} and H_2O_2 which are generated from oxygen reduction at the cathode [63].

For the electrochemical oxidation with active chlorine, chlorine and hypochlorite are generally employed to treat effluents and drinking water [57, 64, 65]. The advantages of this method include fast destruction of pollutants, cost effectiveness and avoidance of dangerous chlorine [57, 64]. However, there are limitations to this method such as electrogeneration of chloroform as well as perchlorate and chlorite as by-products which have high hazardous effects on humans [57, 64, 66].

2.4.2 Electrode materials

In determining the degree of decontamination or removal of organic pollutants, the type of electrode material used in the electrochemical oxidation of the pollutants is one of the key factors to consider [57]. An electrode can be said to be a conductor or semiconductor that makes direct contact with the electrolyte solution, and the output and input of the process is

also determined by the electrode. The common materials used as electrodes are the noble metals such as silver, gold, platinum, etc.), semiconductors such as metal oxides, and different types of carbonaceous materials [67]. For an electrode to be suitable for electrochemical oxidation of organic pollutants, it should be made of material that possesses high electrical conductivity, good mechanical property, low cost/life ratio, non-/low toxicity, and good catalytic activity. It must be physically and chemically stable and resistant to corrosion. In addition, it must have a high oxygen evolution overpotential which determines the extent of oxygen evolution as a side reaction in the electrochemical oxidation of the organic pollutants from wastewater.

2.4.2.1 Metal electrodes

Silver, gold and platinum metals have been employed as electrode materials. These noble metals have displayed wide range of anodic potential window and favourable electron transfer kinetics. However, due to their low hydrogen evolution overpotential, their cathodic potential window range is restricted. Also, due to the tendency to form surface oxides, high background current may be produced which invariably can cause the electrode reaction kinetics of the electrodes to be affected [67, 68]. Silver electrode has been reported to be good and employed for the manufacturing of chemically modified electrodes in electrochemical processes. Gold and platinum have been found to be chemically stable and manufactured easily. Other metals employed as electrode materials are nickel and copper which have been reported to be used for the sensing of amino acids and carbohydrates [67, 69, 70]. Moreover, nickel–titanium and platinum–ruthenium electrodes have bifunctional catalytic mechanisms and have been employed in fuel cells preparations[67].

Platinum and titanium-supported platinum electrodes have been reported to be effective in the decolourisation of dyes wastewaters by electrochemical oxidation processes. However, due to their very high cost, they have proved to be non-practicable for industrial operations for organic pollutants removal. Thus, the use of different materials for doping platinum electrodes has been explored for the electrochemical degradation of organic pollutants such as dyes [57, 71, 72]. The removal efficiencies for TOC, COD and colour have be observed to be majorly current density, stirring, temperature and pH dependent [57, 72]. Platinum is an active electrode which was observed to give a good decolourisation, but a poor mineralisation when used to treat dyes solutions [71]. This is an indication that platinum

electrode is efficient in colour removal by electrochemical oxidation, but not effective in decontamination of organic pollutants like dyes [57]. Nevertheless, the efficiency of electrochemical oxidation of platinum electrode can be enhanced by using sodium chloride as a supporting electrolyte or the addition of a particular quantity of sodium chloride to the supporting electrolyte of choice in degrading the pollutants, thus making active chlorine the main oxidising and/or additional oxidising agent in the solution [72]. This fast decolorisation and low decontamination capability of platinum electrode for organic pollutants can be due to Pt(•OH) which aided the oxidation process, but the concurrent formation of PtO higher oxide reduced the efficiency of the material [57, 72]. Comparing platinum electrode with others such as lead oxide (PbO_2) and silicon-boron-doped diamond (Si/BDD) electrodes for the electrochemical degradation of Alizarin Red dye, it was observed that the non-active Si/BDD and PbO_2 electrodes were more efficient than the active platinum electrode [57, 71, 73].

2.4.2.2 Metal oxide electrodes

In the review of Brillas and Martinez-Huitle, several groups have applied varieties of electrode materials such as undoped and doped lead oxide (PbO_2) for the electrochemical degradation of dyes [57]. Due to the high oxygen evolution overpotential of PbO_2 electrode, the electrochemical oxidation rate of organic pollutants on PbO_2 electrode is very high compared to the traditional electrodes. Thus, it has been explored extensively for the removal of dye from aqueous solution as revealed by Carvalho et al. [57, 74]. The decontamination efficiency of PbO_2 and BDD electrodes for the electrochemical oxidation of Auramin-O was investigated [75]. BBD electrode was found to have higher oxidation rate and current efficieny than PbO_2. Due to the high oxygen overpotential of PbO_2, it displayed a higher mineralisation, but consumed more power in the oxidation process. This suggested that the ability of the electrodes to oxidise organic pollutants depends largely on the physically adsorbed PbO_2(•OH) and BDD(•OH) radicals that are electro-generated on the electrodes [57, 75]. Furthermore, it was reported that PbO_2 electrode undergoes surface corrosion and ionisation to produce Pb^{2+} which is toxic to humans, and such constitutes a secondary pollution even though it possesses high oxygen evolution overpotential [57]

2.4.2.3 Carbon electrodes

Carbonaceous materials have been widely employed as electrode in electrochemical processes. This is due to the unique properties of the carbon such as chemical inertness and

low resistivity. Also, electron exchange can be enhanced on these electrodes by their surface renewal. Carbonaceous materials possess rich surface chemistry, low background current, wide range of potential window and low cost. Thus, they are used extensively as electrodes. Examples of carbon electrodes used include diamond and doped diamond, glassy carbon electrode (GCE), activated carbon, carbon fibre, carbon paste, graphene (graphene oxide/reduced graphene oxide), exfoliated or expanded graphite (EG) and carbon-based composites electrodes. They possess the sp^2 bonding and the six-member aromatic ring in their structure [67]. However, the electrochemical properties of these electrodes differ from one another due to the different relative densities of their basal and edge planes [67]. In this work, emphasis is laid on graphene and exfoliated or expanded graphite.

Glassy Carbon electrodes

Glassy carbon material consists of carbon substrate which combines graphite ceramic and glassy. It is utilised in many electrochemical applications due to its unique properties and structure such as chemical inertness and impermeability to gases [76]. It has mechanical stability, resistance to acidity, electrochemical properties and very low porosity. Generally, the electrode is pre-treated for reproducibility by cyclic voltametric scanning over a wide range of potential window. It can also be treated mechanically by polishing the surface on a micro-fabric cloth with ~1 micron, having an alumina slurry, and then sonicated in a solvent so as to remove the alumina paste. The electrochemical properties can be tuned by modification of glassy carbon electrode with different materials, thereby increasing its applicability. It is used in environmental remediation such electrochemical sensing and electrochemical degradation of organic pollutants as well as other electrochemical processes such as energy and biomedical applications by its modification with other materials such as metal nanoparticles, semiconductors, conducting polymers, etc. Since glassy carbon electrode is hard and difficult to shape as well as being expensive, there is need for the development of other carbon materials that are cheap and efficient as electrodes.

Graphene

Graphene is a carbonaceous material with a two-dimensional structure where the carbons are arranged in a polar honeycomb lattice. The carbon atoms are linked together by sp^2 in hexagonal arrangement. It is a semiconductor with a zero band gap [77]. There are two

major categories of methods for graphene preparation. The first category involves the bottom-up methods which are largely based on the transformation of the molecularly building blocks into two-dimensional networks that are covalently bonded via chemical reactions like epitaxial growth, and the chemical vapour deposition which can give high quality graphene with small amount of defects. However, large scale productions of graphene using these methods are limited and expensive to realise. The second category is the top-down methods that involve graphite exfoliation in liquid which is more cost effective [78].

Graphene has attracted interests since its first discovery in 2004 [79, 80]. The bands in the electronic structure of graphene tend to overlap in two Dirac points in the first Brillouin zone, and it can withstand current density that is millions of times greater than what copper can withstand. It is resistant to gas permeation and has a very high transmittance value [78, 81]. It has been reviewed that the Dirac cone of its band structure encourages the mobility of both holes and electrons [82]. Graphene possesses special characteristic features such as high surface area, high mechanical and thermal stabilities, high thermal conductivity and outstanding electron mobility [82, 83]. The high charge carrier mobility and its band structure that are its unique properties present it a potential candidate for optoelectronic processes and applications. This has made graphene-based materials attractive in water application, optical, photocatalytic, gas sensing and biosensing and nano-electronics applications. [84-86]. It is seen as nanoscale building blocks for preparing graphene-based composites because of its special features [78]. The π-π conjugation network of graphene and its extraordinary conductive nature renders it a good electron acceptor, thus, making it an electron sink for photogenerated electrons when combined with semiconductors for optoelectronic processes [78].

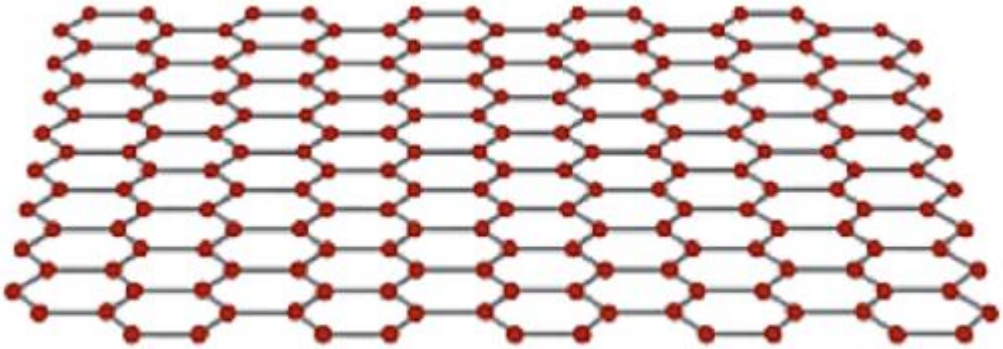

Figure 2.4: An ideal structure of graphene

A monodisperse composite of $CoFe_2O_4$ on reduced graphene oxide (rGO) was synthesised using a solvothermal reaction by Wu et al [87]. The composite was highly active and magnetic with a high specific surface area. It was utilised for the photocatalytic degradation of methylene on a heterogeneous Fenton-like reaction. An excellent photocatalytic performance was recorded using the rGO/$CoFe_2O_4$ composite when compared to the bare $CoFe_2O_4$. A ternary photocatalyst consisting of Au loaded on C_3N_4/graphene was reported for the photocatalytic ability for the treatment of ciprofloxacin and methylene blue under visible light. It was synthesised using a sonication-photodeposition method in which the carbon nitride was immobilised on the graphene and the Au was then deposited on the composite. The results revealed that the surface plasma resonance nature of the gold nanaoparticles and the electron acceptor ability enhanced the visible light absorption and the separation of the photogenerated electron-hole pairs of the composite. This invariably improved the photocatalytic performance of the Au-C_3N_4/graphene composite [88]. Noble metal-doped graphene photocatalysts such as palladium-graphene, silver-graphene and Au-graphene nanocomposites have been documented as catalysts for alcohol oxidation and photocatalytic oxidation of dyes [84, 89, 90]. The photo-electrochemical and photocatalytic performance of CdS-graphene nanocomposite under visible light was reported to be excellent when tested for the degradation of different dyes [91]. For energy application, CeO_2 and WO_3 immobilised on graphene have been utilised for photocapacitive applications. The performances of these nanocomposites were greatly improved by the presence graphene in the CeO_2-graphene

and WO_3-graphene. This can be attributed to its high surface area, good conductivity and charge carrier mobility and transport nature [85, 92]

Expanded or exfoliated graphite

Exfoliated graphite (EG), a carbonaceous material, is graphite in which most part of its carbon layers are separated to a large extent. This process which could be thermal, mechanical or chemical, leading to the carbon layers separation is called exfoliation [93, 94]. It is prepared when graphite intercalation compounds (GICs) are subjected to high temperature heating and there is vaporisation of intercalates which leads to the tearing of the carbon layers. Even though all the carbon layers do not get separated, the separation takes place between adjacent layers of carbons. There is decrease in density, but increased volume in exfoliated graphite because of the porosity resulting from the carbon layers separation. This also leads to increase in specific surface area when there is separation through the whole graphite plane [94]. Generally, graphite flakes possess a graphite c-axis that is perpendicular to the plane of its flakes and these graphite flakes tend to be long in the direction of the c-axis after expansion to give exfoliated or expanded graphite [93, 94]. It can be re-compressed without a binder and this re-compressing process leads to the interlocking of the carbon layers in EG [95].

Exfoliated graphite possesses low density, dielectric, mechanical and thermal properties, large surface area, compressibility, high temperature resistance, high electrical conductivity and good electron transport capacity. Moreover, the porous nature of the exfoliated graphite enhances the trapping of photocatalyst. Consequently, it will help in immobilising the powdered photocatalysts and hence it reduces losses in recovery process [96-99]. Also, it is utilised manufacturing thermal shielding, adsorption, vibration damping and electromagnetic interference shielding materials, high temperature gaskets, supports for catalysts and seals [94]. EG material is an attractive material for electrode. It can be constructed into various shapes and sizes of electrode without using a binder. Like glassy carbon electrode, its surface can be polished easily so as to renew it. In addition, EG has been reported for its electrocatalytic property which made it viable for electrochemical sensing and electrochemical oxidation of pollutants [96, 98, 100]. EG/TiO_2 has been documented for its photoelectrocchemical degradation of phenol, nitrophenol and dyes, showing excellence performance [97, 99]. The main setback of EG is that it has lower

oxygen evolution over-potential which leads to a decrease in current efficiency, thus causing partial oxidation of organic pollutants [101].

2.4.3 Heterogeneous photocatalysis

Recently, heterogeneous photocatalytic degradation has been found as a promising route for oxidation of persistent organic pollutants leading to the production of less harmful substances. The process involves the absorption of ultraviolet or visible radiations by a solid, usually a semiconductor, direct or indirectly from an energy source. When a semiconductor absorbs a photon of energy greater than its band gap, an electron is excited to the conduction band thereby creating a hole in the valence band. The generation of the electrons could lead to oxidation-reduction reactions on the surface of the semiconductor. The hole reacts with a reductant to give an oxidized product while the electron reacts with an oxidant to give a reduced product. They migrate to the surface of the semiconductor where they either react with adsorbed species or recombine with the dissipation of the energy absorbed [55]. In both reactions, hydroxyl radicals are produced as follows;

In the oxidative reactions due to photocatalytic effect:

$$hv + MO \rightarrow MO\ (h^+ + e^-) \quad [2.8]$$

Where MO is metal oxide

$$h^+ + H_2O \rightarrow H^+ + \bullet OH \quad [2.9]$$

$$2\ h^+ + 2\ H_2O \rightarrow 2\ H^+ + H_2O_2 \quad [2.11]$$

$$H_2O_2 \rightarrow HO\bullet + \bullet OH \quad [2.12]$$

The reductive reaction due to photocatalytic effect:

$$e^- + O_2 \rightarrow \bullet O_2^- \quad [2.13]$$

$$\bullet O_2^- + H^+ \rightarrow HO_2\bullet \quad [2.14]$$

$$\bullet O_2^- + HO_2\bullet + H^+ \rightarrow H_2O_2 + O_2 \quad [2.15]$$

$$HOOH \rightarrow HO\bullet + \bullet OH \quad [2.16]$$

The migrated holes and electrons on the surface of the semiconductor produce a reduction-oxidation platform for the photocatalytic degradation of organic pollutants such as dyes. The photogenerated holes react with water molecules to form a proton and hydroxyl radical (•OH). The dissolved oxygen molecules in the wastewater react with the photogenerated electrons in the conduction band to give a superoxide oxygen radical ($•O_2^-$) which further react with a proton to give hydroperoxide radical ($H_2O•$). These radicals then react with the pollutants repeatedly to mineralise them into less harmful substances like CO_2, H_2O and N_2 [102]. The process depends largely on the in-situ generation of hydroxyl radicals which are strong oxidising agents for the conversion of a wide range of toxic organic substances into harmful products like CO_2 and H_2O. The destruction of these refractory organic pollutants is dependent on the semiconductor photocatalyst, oxidising species, and source of radiation (UV or visible light). Since solar light is abundant from the sun, it is an indication that sunlight is an economical and ecological light source [54, 89]. Nevertheless, there are some setbacks associated with these metal oxide semiconductors like slow electron transfer rate, recombination of the photogenerated holes and electrons, and narrow light absorption range [82].

Owing to the recalcitrant nature of dye to water treatment with conventional methods, photocatalysis have been developed as a means of dye removal in water. Galindo et al. reported the use of acid blue 74 (also known as indigo carmine) as a case study for photochemical and photocatalytic degradation of an indigoid dye [103]. Titania-based photocatalysts such as TiO_2 impregnated on activated carbon [104] and sol-gel prepared SiC-TiO_2 photocatalyst[105] have been used for the degradation of indigo carmine. Also, multi-elements doped ZrO_2 photocatalyst [106], autoclaved cellular concrete that is impregnatd with iron III oxide [107] and Nd-doped TiO_2 decorated on graphene oxide nanocomposite photocatalyst have been reported [108]. Yang et al fabricated a p-type Cu_2O nanowires on the surface of n-type TiO_2 nanotubes arrays as photocatalyst and employed it for the degradation of 4-nitrophenol under simulated solar light. The material displayed better performance than the unmodified TiO_2. The enhanced photocatalytic performance was due to the presence of the p-type Cu_2O nanowire which aid the charge separation at the p-n heterojunction interface [109].

2.4.3.1 Zinc oxide (ZnO) photocatalyst

ZnO has been reported as a suitable photocatalyst for the degradation of organic pollutants in water treatment because of its availability, low cost, good optoelectronic nature, chemical inertness, non-toxicity, and photochemical and catalytic properties [110-114]. It is an n-type semiconductor with a wide band gap of 3.37 eV and a high exciton bound energy of 60 meV at room temperature [115]. The position of the valence band of ZnO renders the photogenerated holes strong oxidizing species to decompose most organic substances [110, 116]. ZnO is reportedly utilised for the decomposition of several dyes in solutions [110, 117-119], pesticides [120] and other organic pollutants found in the environment [110, 121]. ZnO has been found as a good alternative to TiO_2, however, it undergoes photocorrosion and it is susceptible to facile dissolution of extremely high or low pH which has limited its photoatalytic applications [110]. Like other photocatalysts, there are some limitations associated with ZnO such as the recombination of the photogenerated holes and electrons, and narrow light absorption range [82]. In order to solve these problems, several materials have been employed to dope this semiconductor [112]. Several studies have been conducted for the utilisation of ZnO under visible light irradiation for the degradation of some organic substances in aqueous solution. For example, the successful synthesis of ZnO–reduced graphene oxide (RGO)–carbon nanotube (CNT) composites using a microwave method was reported [122]. The photocatalytic ability of the material was tested on methylene blue degradation and the results showed that the phototcatalytic performance was enhanced by the presence of graphene and carbon nanotubes in the composite which helped to reduce the charge carriers recombination rate [122]. Saravanan et al reported the synthesis of a ternary $ZnO/Ag/Mn_2O_3$ nanocomposite using a facile and cheap route and it was used for visible light photocatalytic degradation of textile effluents. The ternary $ZnO/Ag/Mn_2O_3$ nanocomposite was found to display excellent catalytic degradation of the industrial textile effluent in comparison to the bare ZnO [123].

A gelatin-assisted hydrothermal method was used by Feng et al for the preparation of ZnO nanocrystals supported on reduced graphene oxide (RGO) sheets. The RGO was used as a support and controller of the various shapes such as nanospheres, nanocrystals and nanorods of the ZnO by varying the amount of the RGO. The results showed that ZnO nanoparticles were evenly distributed on the RGO nanosheets. The ZnO–RGO composite was used as photocatalyst for the degradation of methylene blue using visible light and

ultraviolet irradiation. The performance was greatly improved by the RGO using both irradiations and kinetic rate constants tripled with the use of RGO [124].

2.4.3.2 Silver oxide (Ag_2O) photocatalyst

Ag_2O is a p-type semiconductor with a narrow band gap of 1.46 eV and it is a suitable catalyst for industrial applications because of its cost effectiveness, ease of preparation, non-toxicity and high efficiency [125-127]. On the contrary, its instability and photosensitive nature tend to limits its applications in photocatalytic processes under visible light irradiation [125, 128]. However, the self-stabilising mechanism of Ag_2O for photosensitive materials by the use of Ag to enhance the structural stability of Ag_2O has been reported [125, 129]. In the same vein, Liu et al reviewed the efficiency and stable visible light photocatalysis of Ag/AgI, Ag/Ag/Br and Ag/AgCl aided by this self-stabilisation means [125], the results obtained showed that Ag-based photocatalyst materials can be remarkably improved by the presence of metallic silver (Ag). Thus, the absorption of light in the visible spectrum by metal oxide such as ZnO and TiO_2 can be improved by surface plasmon resonance effect of Ag due to the formation of Ag-Ag_2O as a result of photodecomposition [125, 130, 131]

The formation of a p-n heterojunction between Ag_2O and other metal oxides semiconductors such as ZnO and TiO_2 can help to enhance interfacial electron transport, and consequently, minimize the electron-hole pair recombination of those semiconductors. In addition, Ag_2O can act as a photosensitizer under solar light due to its lower band gap compared to higher band gap semiconductor of those metal oxides (ZnO and TiO_2) and thus improving the their photocatalytic performance under visible light [111, 126]. The introduction of metallic Ag into ZnO has been found to improve its visible light absorption as a result of surface plasmon resonance effect of Ag. In addition, Ag can act as an electron sink for the photogenerated electrons [132]. This allows the production of more hydroxyl radicals by the holes and eventually enhances the photocatalytic process [114]. The efficient removal of iodide ions under visible light using Ag_2O-Ag/TiO_2 composite has been investigated [131]. The ultrasonic fabrication of AgBr/Ag/Ag_2O/GO composite was carried out and its photocatalytic property was studied on organic dyes. The obtained results showed that the composite gave a better photocatalytic performance on the oxidation of methyl orange and rhodamine B when compared to the use of the graphene oxide, (GO) and AgBr using simulated solar irradiation [133]. A 3-dimensional p-n

heterojunction Ag_2O-TiO_2 was synthesised using a p-type Ag_2O and an n-type TiO_2 for the photocatatlytic degradation of methyl orange under ultraviolet irradiation. The results revealed that the presence of the heterojunction microsphere gave an enhanced photocatalytic performance of four times higher than that of the n-type TiO_2 photocatalyst [134].

2.4.3.3 Tungsten trioxide (WO_3) photocatalyst

Tungsten oxide (WO_3) is an n-type semiconductor having a band gap around 2.8 eV. It exists in various phases such as monoclinic II (ε-WO_3), monoclinic I (γ-WO_3), tetragonal (α-WO_3), orthorhombic (β-WO_3), triclinic (δ-WO_3) [135]. These phases exist and undergo transition at various temperatures as follows; monoclinic II (ε-WO_3, < - 43 ^oC) to triclinic (δ-WO_3, - 43 to 17 ^oC) to monoclinic I (γ-WO_3, 17 to 330 ^oC) to orthorhombic (β-WO_3, 33 to 740 ^oC) to tetragonal (α-WO_3, >740 ^oC). The transition phases are reversible except the monoclinic I (γ-WO_3) phase which tends to be stable at room temperature [135].

WO_3 has recovery ability from photocorrosion, stable physicochemical properties and visible light sensitivity which makes it a good photocatalyst [136]. It is an inexpensive photocatalyst with different applications such as in gas sensing, energy renewal and storage, electrochromic devices and photocatalysis [85, 137-139]. Its small band gap helps WO_3 to be responsive in the visible light region up to 480 nm, and also absorbs about 12% of solar spectrum. In addition, it is resistant to corrosion in acidic aqueous media [135, 140]. WO_3 has been employed for the photocatalytic degradation of organic pollutants, however, it exhibits a lower efficiency of light energy conversion due to its low reduction potential in comparison to TiO_2 [141]. The synthesis and characterisation of AgI/WO_3 nanocomposite was carried out and its photocatalytic effect was tested for the degradation tetracycline, giving an enhanced photocatalytic performance [142]. In addition, deposition of WO_3 thin films on platinum gauze substrate was used for the fabrication of photoelectrode for the degradation of orange II dye [143]. Furthermore, bismuth tungstate was synthesised and co-doped using samarium and nitrogen. The composite was found to be efficient and possesses excellent photocatalytic ability under visible light [144]. The photocatalytic effect of silver doped WO_3 was evaluated on the oxidation of methylene blue under visible light. The Ag-WO_3 was found to display a higher photocatalytic capability than the pure WO_3 material [145]. A low temperature hydrothermal method was used to prepare Nb-doped WO_3 nanowires and the photocatalytic performance was

investigated on the removal of methylene blue in solution under simulated solar light. It is shown that pristine WO_3 tends to aggregate while the Nb-WO_3 nanocomposite displayed narrow band gaps with increase in the Nb ions. Furthermore, the Nb-WO_3 exhibited a better photocatalytic activity compared to the pure WO_3 [146].

2.4.3.4 Tin oxide (SnO_2) photocatalyst

SnO_2 is an n-type semiconductor having a band gap, Eg = 3.6 eV [147, 148]. It has been utilised as electrode materials in transistors [147, 149], lithium batteries [150, 151], solar cells [152], sensors [147, 153] and supercapacitors [154], as well as in photocatalysis [148]. This is due to its peculiar properties such as its high chemical and electrochemical stability, gas sensitivity and photoelectronic nature [148, 153]. Generally, the properties of nanocrystalline SnO_2 are different from those of the amorphous or crystalline SnO_2. These properties are dependent on the crystal structures, morphologies and grain sizes. The unique properties of SnO_2 are of scientific interests that render it useful in several applications like gas sensors, electrochromic devices, glass coatings, heat mirrors, nanofiltration membranes. However, like other semiconductor with wide band gap, it is linked with setbacks such as electron-hole recombination and narrow visible light absorption range. Thus, there is need to improve its photoactive performance for effective application by doping or using a p-type semiconductor to form a p-n heterojunction material with n-type SnO_2 that could aid the separation of the photo-excited holes and electrons [155]. Wu et al [148] reported a biomolecule-assisted hydrothermal method for the preparation of SnO_2 nanocrystals. The photocatalytic effect of the nanocrystals was tested on the degradation of Rhodamine B, and the results showed that the degradation efficiency was up to 100% in 150 min. The excellent photocatalytic performance of the SnO_2 nanocrystals was ascribed to its small sizes of less than 10 nm.

Spheres-like nanoparticles of SnO_2 were prepared using a microwave synthesis technique and evaluated for its photocatalytic properties by Rhodamine B under UV-light. It was discovered that the SnO_2 having nanorods on its surface gave a higher photocatalytic capability [156]. Ag-SnO_2 nanocomposites having sphere shape was synthesised using *Saccharum officinarum* stem extract and employed as photocatalyst as well as antioxidant and antibacterial agents. Its photocatalytic property was tested for the degradation of 4-nitrophenol, methyl violet 6B, Rose Bengal and methylene blue, while its antimicrobial ability was investigated against *Escherichia coli*, *Bacillus subtilis* and *Pseudomonas*

aeruginosa [157]. SnO_2-based electrode was fabricated and used for the removal of pesticide atrazine by electrochemical and photo-assisted electrochemical oxidation processes. The obtained results demonstrated an excellent removal efficiency of the SnO_2-based electrode. The obtained COD removal was dependent on the amount of SnO_2 present in the composite electrode [158].

2.4.3.5 Molydenum disulphide (MoS_2) photocatalyst

MoS_2 is a 2D material consisting of molybdenum atoms inserted between sulphur atoms that are hexagonally packed. It is a p-type material having a band gap, Eg of 1.9 eV. It has attracted scientific interest due to its high charge carrier mobility, high surface area, excellent optical, magnetic, electrocatalytic and mechanical properties [159-163]. As a result of its advantageous properties, it has been employed for several electrochemical processes such as solar cells, phototransistors, sensors, hydrogen evolution and supercapacitors [160, 161, 164, 165]. Its high specific surface area and adsorption capability has made it a good candidate for photocatalytic processes [155]. A p-type MoS_2 can be used for the enhancement of an n-type semiconductor by the formation of a p-n heterojunction which can aid charge carrier separation. In addition, the low band gap and excellent visible light absorption nature of MoS_2, could improve the photoactivity of such semiconductor with wider band gaps [166]. Zhao et al fabricated a p-n heterojunction n-$BiVO_4$@p-MoS_2 composite with a core-shell structure. The composite was utilised for the photocatalytic oxidation of crystal violet dye and reduction of Cr^{6+}. The composite photocatalyst displayed an enhanced photocatalytic oxidation and reduction processes which were ascribed to the reduced charge carrier recombination, high surface area and adsorption ability of the material. Also, the core-shell structure aided the effective transfer of photogenerated electrons at the interface of $BiVO_4/MoS_2$ [155]. Ke et al reported the synthesis of $Bi_2O_3/Bi_2S_3/MoS_2$ p-n heterojunction having layered p-type MoS_2 and n-type Bi_2O_3 for excellent photocatalytic water oxidation and the degradation of organic pollutants [166]. MoS_2 nanosheet was used to coat TiO_2 nanobelts as photocatalyst and was employed for the degradation of Rhodamine B and hydrogen production. The materials showed high surface area, adsorption ability and displayed excellent photocatalytic activity [167].

2.4.4 Photoelectrocatalytic degradation

Photoelectrocatalytic oxidation is the electrochemical application of photocatalytic oxidation which results to a higher efficiency for wastewater treatment. It involves the fabrication of a photoelectrode by the immobilisation of a photoactive/semiconductor material on a conducting material, and the concurrent application of visible light and bias potential. This results in the generation of oxidising agents such as hydroxyl radicals by the semiconductor and conducting substrates for the break-down of the pollutants [57, 168]. In other words, a constant bias anodic potential is applied to semiconductor-based anode which is exposed to ultraviolet or visible light irradiation. The electrochemical cell utilised in photoelectrocatalytic is a photoreactor made of quartz glass that allows UV or visible light to pass through it to get to the electrode surface. The photogenerated electrons are driven continuously from the anode to the cathode with the aid of an external electrical circuit. This results in the production of more holes and •OH when compared with heterogeneous photocatalysis where there are some degree of electron-hole recombination [57, 63]. The advantage of photoelectrocatalytic process over photocatalytic degradation can be attributed to the inhibition of the photogenerated hole and electron pairs recombination by the external electric field. For example, Guaraldo et al reported the use of Ti/TiO_2 thin film electrodes for the degradation of indigo carmine and the results showed that the anatase form of the electrode gave an excellent photoelectroactivity in the removal of indigo carmine [169]. The photoelectrocatalytic efficiency of $Ti/TiO_2/WO_3$ electrode was investigated for the treatment of indigo carmine. It displayed improved performance and the degradation products obtained are 2-amino-α-oxo-5-sulfo-benzeneacetic acid, 2,3-dioxo-14-indole-5-sulfonic acid and 2-amine-5-sulfo-benzoic acid [170]. Several works on the photocatalytic and photoelectrocatalytic degradation of orange II dye have been documented [171-175]. The immobilisation of TiO_2 on PbO_2 as electrode for photo-assisted degradation of orange II dye was conducted at different initial pH values by Li et al [176]. An enhanced photoelectrocatalytic degradation of orange II dye using TiO_2/reduced graphene oxide as electrode was reported in literatures [177]. Ag-ZnO photocatalyst were coated on fluorine doped tin oxide as photo-electrode for the degradation of methyl orange, 4-nitrophenol and methylene blue. The result showed that the material has excellent visible light absorption behaviour both as a photocatalyt and as electrode. Also, the presence of the Ag enhanced the light absorption and reduced the recombination rate of the photogenerated electron and hole pairs [178]. The modification of nano-TiO2 with platinum on a rotating disk electrode as working electrode was

investigated by Su et al [179]. The electrode was employed for the photo-electrocatalytic degradation of 4-nitrophenol using hydrodynamic differential pulse voltammetry. The results revealed that hydroquinone was produced as an intermediate compound by the direct oxidation of the 4-nitrophenol by the hydroxyl radicals produced [179]. TiO_2-expanded graphite was prepared by a sol-gel method and used to fabricate electrode which was utilised for the photoelectrochemical degradation of 4-nitrophenol [97]. The material was able to withstand high current density and it gave a better removal efficiency for the photoelectrochemical degradation when compared with electrochemical degradation and photolysis of the 4-nitrophenol. An n-ZnO/p-Cu_2O/n-TNA ternary heterojunction electrode was fabricated and its photoelectrochemical property was tested on the degradation of tetracycline. The electrode was found to be efficient with excellent photoelectrocatalytic performance [180]. It was reported that the use of Pt/Ti electrode for the photo-electrocatalytic oxidation of antibiotic, berberine, gave better removal efficiency and mineralisation when compared to electrochemical and photocatalytic processes [181]. Smirnova et al studied the photoelectrochemical properties of titanium films modified with silver and gold nanoparticles and then employed the composite for the degradation of tetracycline hydrochloride [182].

2.5 Quantum Chemistry

Quantum chemistry is an area of chemistry that uses quantum mechanics principles to solve chemical problems such as reaction mechanisms, reaction kinetics, thermodynamics, molecular structures, and so on. The models of quantum mechanics consider an electron as a wave instead of a particle, and tend to give Schrodinger wave equations approximate solutions, thereby providing explanations to the behavioural patterns of chemical systems by predicting some important properties of an electronic system. The Schrodinger wave equation (SWE) is the fundamental formula used to obtain most of the molecular quantum chemical parameters, and it written as follows [183-186]:

$$\hat{H}\,\psi = E\,\psi \qquad [2.17]$$

Where $\hat{H}$ is known as the Hamiltonian, E is the energy, and Ψ is regarded as the wave function of the system. Mathematically, this equation is known as the Eigen-equations, wherein E and Ψ are referred to as Eigen-value and Eigen-function respectively.

The Hamiltonian expression, $\hat{H}$ for a given system having *i* number of particles is given as:

$$\hat{H} = -\sum_i^{particles} \frac{\nabla_i^2}{2m_i} + \sum_{i<j}^{particles} \sum \frac{q_i q_j}{r_{ij}} \quad [2.18]$$

Where the first term of equation [2.18] is the Laplacian operator, $\frac{\nabla_i^2}{2m_i}$.

mi, *qi*, and *rij* are the mass *mi*, charge *qi*, and distance between particles *i* and *j*, respectively. The first term on the right side of the equation deals with the kinetic energy of the wave-like nature of the particle while the second term on the right side of the equation deals with the energy resulting from Coulombic attraction/repulsion between particles. Due to the complexity of the Hamiltonian, it is not mostly utilised in recent software of computational chemistry [183]. A basis set is a set of mathematical functions used in the description of the shape of orbitals in an atom/molecule [184-186]. They are sets of fundamental functions that can be added together to produce the necessary features needed for quantum chemical calculations. These mathematical functions help to give description of the angular and radial distributions of electron density [184, 187]. Generally, some of these calculations are carried out by the use of basis sets that are already in existence. The accuracy of any quantum chemical calculation is usually dependent on the type basis sets applied in the calculation [185, 186]. Also, the larger the basis set, the more accurate and time consuming the calculation will be [188]. The most commonly used split-valence basis set are the Pople type basis sets like 3-21G, 6-21G, 4-31G, 6-31G, and 6-311G. In other to improve the accuracy of these Pople basis sets, features like polarization and diffuse functions are introduced to it. Examples of the polarization functions are 6-31G* or 6-31G(d) which means that a set of d-orbital primitives has been added to atoms apart from hydrogen, while the 6-31G** or 6-31G(d,p) implies that a set of *p* primitives was added to hydrogen plus the addition of the d-orbital primitives on the higher atoms. These functions tend to allow the wave function to be flexible and change shape, hence they are known as polarization functions [185, 188]. They are often used because of their high accuracy of calculated vibrational frequencies and geometries [185, 186]. Examples of the diffuse functions are 6–31+G* or 6–31++G* where a single plus sign signifies that diffuse functions have been added to atoms apart from hydrogen and the second plus sign suggests diffuse functions are utilised for all atoms and these include hydrogen. They describe the shape of the wave function far from the nucleus and they are employed for anions which generally have larger electron density distribution [183, 185, 186, 188].

2.5.1 Methods and models of computational chemistry

Quantum mechanics can be utilised for the prediction of any exact property of a single atom or molecule. One of its assertions is the description of microscopic systems by wave functions which characterise the physical properties of the system completely, and that each physical property has a quantum mechanical operator that corresponds to it. The application of the quantum mechanical operator to a wave function can help in the prediction of the probability that the system will display particular values that are associated to that property [186, 188]. Nonetheless, the quantum mechanical equations have just be been solved only for one-electron systems. The successful usage of quantum mechanics in solving chemical challenges depends on the utilisation of correct approximation to get the appropriate quantum chemical parameters as well as how close is the predicted data to the obtained experimental results [188]. Getting a good approximate solution to the correct Schrodinger wave equation of a system under investigation will determine how successful a quantum chemical calculation will be. The development and implementation of several approximation methods in different sophisticated computer software codes have aided speedy calculations of quantum chemical parameters. One major problem in computational chemistry is choosing an appropriate level of theory or method for solving a certain problem, and ease in the evaluation of the quality of the results obtained [183]. The introduction of theoretical quantum chemical models into computer software programs, coupled with the advancement of computer algorithms and hardware, has enormously improved the application of computational chemistry in solving chemical challenges.

The use of quantum chemical parameters in predicting electrochemical reactions and reaction pathways has been explored due to the advancement in computer hardware and software technologies. The various methods developed include the ab initio, semi-empirical, molecular mechanics, etc., but the emphasis of this thesis will be on the density functional theory (DFT) method.

2.5.2 Density functional theory (DFT) methods

In recent years, DFT has been widely used because it takes less computational time compared to other methods with almost the same accuracy [183, 185, 186, 188]. Thus, DFT has been found as one of the most promising computational approach to model the electronic structure of matter which includes atoms, molecules, solids, nuclei, and quantum

and classical fluids [189]. In this approach, the electron density is used to derive the ground-state properties of the system and this takes less computational time since the integrals for Coulombic repulsion can be done using the electron density (a three-dimensional function). This is an indication that the DFT calculations scale only as N3 which makes it even faster than the HF calculations which scale as N4. The type of functions used is what determines the accuracy of a DFT calculation and that better DFT functions can produce results that have similar accuracy similar with the results of an MP2 calculation [186]. The original approach of the DFT which was developed by Hohenberg and Kohn [189] gives the ground state properties of the many-electron system based on the electron density instead of a many-body wave function that is utilised by the HF theory. Every ground-state property such as the ground-state energy is a function of the electron density. However, the simple method employed for DFT calculations which still retains the exact nature of the original DFT concept was later given by Kohn and Sham [190]. Moreover, it was found that the type of functions and basis set utilised in a DFT calculation determines its speed and accuracy. There are different functional used in DFT with their advantages and disadvantages. They were constructed from fundamental quantum mechanics as well as by the parameterisation of functions to give the best reproducible experimental results [185, 186]. Among them are those that are based on only the electron exchange (without correlation terms) that is, the X-alpha (Xα) functionals. Some of these functionals give the simplest approximation to the complete problem and they are constructed based on the local density approximation (LDA) or local spin density approximation (LSDA) in case of high-spin systems [183]. They are the fastest method, but give less accurate geometries. An example of LDA is Vosko, Wilks and Nusair (VWN) functional. The gradient corrected functional give more accurate geometries make use of the electron density and its gradient and these include Becke correlation functional with Lee, Yang, Parr exchange (BLYP). But the hybrids functional/calculations which is a combination of HF and DFT methods give more accurate geometries. They are the more recent calculations and these include Becke 3-parameter exchange with Lee, Yang, Parr correlation (B3LYP), Becke 3-parameter exchange with Perdew and Wang correlation, Becke 3-parameter exchange with Perdew correlation (B3P86), etc. [183, 185, 186, 188].

Quantum chemical calculations based on DFT have been employed to complement and corroborate experimental electrochemical determinations of reaction products and degradation mechanisms of organic pollutants [191, 192]. For example, DFT studies have been used to predict electrochemical degradation of triazole fungicide as a model organic

pollutant in water on TiO_2-NTs/SnO_2-Sb/PbO_2 electrode and the results corroborated the experimental data [192] . DFT study have been reportedly carried out for the degradation of 4-chlorophenol on hierarchical ZnO with nanoporos and nanowire structures which were immobilised on a substrate [193]. The OH radical attack on the 4-chlorophenol was modelled which led to the generation of benzoquinone, hydroquinone, 4-chlorocatechol and the opening of the ring, while the OH radical was re-generated after the breaking down of the 4-cholorophenol molecule.

2.6 REFERENCES

[1] J. Su, Y. Zhang, S. Xu, S. Wang, H. Ding, S. Pan, G. Wang, G. Li, H. Zhao, Highly efficient and recyclable triple-shelled $Ag@Fe_3O_4@SiO_2@TiO_2$ photocatalysts for degradation of organic pollutants and reduction of hexavalent chromium ions, Nanoscale, 6 (2014) 5181-5192.

[2] M.H. Daniel, A.A. Montebelo, M.C. Bernardes, J.P. Ometto, P.B. De Camargo, A.V. Krusche, M.V. Ballester, R.L. Victoria, L.A. Martinelli, Effects of urban sewage on dissolved oxygen, dissolved inorganic and organic carbon, and electrical conductivity of small streams along a gradient of urbanization in the Piracicaba river basin, Water, Air, and Soil Pollution, 136 (2002) 189-206.

[3] R.P. Schwarzenbach, T. Egli, T.B. Hofstetter, U. von Gunten, B. Wehrli, Global water pollution and human health, Annual Review of Environment and Resources, 35 (2010) 109-136.

[4] R.P. Schwarzenbach, B.I. Escher, K. Fenner, T.B. Hofstetter, C.A. Johnson, U. Von Gunten, B. Wehrli, The challenge of micropollutants in aquatic systems, Science, 313 (2006) 1072-1077.

[5] K. Hayward, Drinking water contaminant hit-list for US EPA, Water, 21 (1998).

[6] S.H. Safe, Polychlorinated biphenyls (PCBs): environmental impact, biochemical and toxic responses, and implications for risk assessment, Critical reviews in toxicology, 24 (1994) 87-149.

[7] X.-J. Kong, D. Li, L.-Q. Cao, X.-M. Zhang, Y. Zhao, Y. Lv, J. Zhang, Evaluation of municipal sewage treatment systems for pollutant removal efficiency by measuring levels of micropollutants, Chemosphere, 72 (2008) 59-66.

[8] J. Wyatt, E. Linton, The industrial potencial of microbial nitrile biochemistry, Cyanide Compounds in Biology, 140 (1988) 32-48.

[9] Y. Huang, Y.E. Miao, T. Liu, Electrospun fibrous membranes for efficient heavy metal removal, Journal of Applied Polymer Science, 131 (2014).

[10] A.S. Giri, A.K. Golder, Ciprofloxacin degradation from aqueous solution by Fenton oxidation: reaction kinetics and degradation mechanisms, RSC Advances, 4 (2014) 6738-6745.

[11] D.J. Larsson, C. de Pedro, N. Paxeus, Effluent from drug manufactures contains extremely high levels of pharmaceuticals, Journal of hazardous materials, 148 (2007) 751-755.

[12] C. Blaise, G. Forget, S. Trottier, Toxicity screening of aqueous samples using a cost-effective 72-h exposure Selenastrum capricornutum assay, Environmental Toxicology, 15 (2000) 352-359.

[13] T. Tadesse, Solid and Hazardous Waste Management, Ethiopia Public Health Training Initiative: Addis Ababa, Ethiopia, (2004).

[14] C.A. Basha, N. Bhadrinarayana, N. Anantharaman, K.M.S. Begum, Heavy metal removal from copper smelting effluent using electrochemical cylindrical flow reactor, Journal of Hazardous Materials, 152 (2008) 71-78.

[15] M. Morales, P. Martı, A. Llopis, L. Campos, S. Sagrado, An environmental study by factor analysis of surface seawaters in the Gulf of Valencia (Western Mediterranean), Analytica Chimica Acta, 394 (1999) 109-117.

[16] N. Zahra, Lead removal from water by low cost adsorbents: a review, Pakistan Journal of Analytical & Environmental Chemistry, 13 (2012) 8.

[17] M.E. Argun, S. Dursun, C. Ozdemir, M. Karatas, Heavy metal adsorption by modified oak sawdust: Thermodynamics and kinetics, Journal of hazardous materials, 141 (2007) 77-85.

[18] K.K. Krishnani, X. Meng, C. Christodoulatos, V.M. Boddu, Biosorption mechanism of nine different heavy metals onto biomatrix from rice husk, Journal of Hazardous Materials, 153 (2008) 1222-1234.

[19] I. Dror, D. Baram, B. Berkowitz, Use of nanosized catalysts for transformation of chloro-organic pollutants, Environmental science & technology, 39 (2005) 1283-1290.

[20] E. Deribe, B.O. Rosseland, R. Borgstrøm, B. Salbu, Z. Gebremariam, E. Dadebo, H.R. Norli, O.M. Eklo, Bioaccumulation of persistent organic pollutants (POPs) in fish species from Lake Koka, Ethiopia: the influence of lipid content and trophic position, Science of the Total Environment, 410 (2011) 136-145.

[21] U. Černigoj, P. Trebše, U.L. Štangar, Photodegradation of organic pollutants in aqueous solutions catalyzed by immobilized titanium dioxide: novel routes towards higher efficiency: dissertation, U. Černigoj 2007.

[22] Q. Qing Li, A. Loganath, Y. Seng Chong, J. Tan, J. Philip Obbard, Persistent organic pollutants and adverse health effects in humans, Journal of Toxicology and Environmental Health, Part A, 69 (2006) 1987-2005.

[23] H. Choi, E. Stathatos, D.D. Dionysiou, Photocatalytic TiO_2 films and membranes for the development of efficient wastewater treatment and reuse systems, Desalination, 202 (2007) 199-206.

[24] B. Padhi, Pollution due to synthetic dyes toxicity & carcinogenicity studies and remediation, International Journal of Environmental Sciences, 3 (2012) 940.

[25] A. Zahrim, N. Hilal, Treatment of highly concentrated dye solution by coagulation/flocculation–sand filtration and nanofiltration, Water resources and industry, 3 (2013) 23-34.

[26] Z. Carmen, S. Daniela, Textile organic dyes–characteristics, polluting effects and separation/elimination procedures from industrial effluents–a critical overview, Organic Pollutants Ten Years After the Stockholm Convention-Environmental and Analytical Update, InTech, 2012.

[27] H. Lachheb, E. Puzenat, A. Houas, M. Ksibi, E. Elaloui, C. Guillard, J.-M. Herrmann, Photocatalytic degradation of various types of dyes (Alizarin S, Crocein Orange G, Methyl Red, Congo Red, Methylene Blue) in water by UV-irradiated titania, Applied Catalysis B: Environmental, 39 (2002) 75-90.

[28] J. Méndez-Hernández, F. Ramírez-Vives, M. Solís-Oba, A. Solís-Oba, A. Sobrino-Figueroa, O. Loera, Detoxification and mineralization of Acid Blue 74: study of an

alternative secondary treatment to improve the enzymatic decolourization, World Journal of Microbiology and Biotechnology, 29 (2013) 805-814.

[29] N. Nasuha, H. Zurainan, H. Maarof, N. Zubir, N. Amri, Effect of cationic and anionic dye adsorption from aqueous solution by using chemically modified papaya seed, International Conference on Environment Science and Engineering, 2011, pp. 50-54.

[30] M. Rafatullah, O. Sulaiman, R. Hashim, A. Ahmad, Adsorption of methylene blue on low-cost adsorbents: a review, Journal of hazardous materials, 177 (2010) 70-80.

[31] A.S. Raymundo, R. Zanarotto, M. Belisário, M.d.G. Pereira, J.N. Ribeiro, A.V.F.N. Ribeiro, Evaluation of sugar-cane bagasse as bioadsorbent in the textile wastewater treatment contaminated with carcinogenic congo red dye, Brazilian Archives of Biology and Technology, 53 (2010) 931-938.

[32] W.-J. Lee, H.-S. Jang, Cardiac arrest from intravenous indigo carmine during laparoscopic surgery-A case report, Korean journal of anesthesiology, 62 (2012) 87-90.

[33] O. Ama, N. Mabuba, O. Arotiba, Synthesis, Characterization, and Application of Exfoliated Graphite/Zirconium Nanocomposite Electrode for the Photoelectrochemical Degradation of Organic Dye in Water, Electrocatalysis, (2015) 1-8.

[34] R. Chaiyont, C. Badoe, C. Ponce de León, J.L. Nava, F.J. Recio, I. Sires, P. Herrasti, F.C. Walsh, Decolorization of Methyl Orange Dye at IrO_2-SnO_2-Sb_2O_5 Coated Titanium Anodes, Chemical Engineering & Technology, 36 (2013) 123-129.

[35] A.K. Verma, R.R. Dash, P. Bhunia, A review on chemical coagulation/flocculation technologies for removal of colour from textile wastewaters, Journal of Environmental Management, 93 (2012) 154-168.

[36] M.H. Entezari, Z.S. Al-Hoseini, Sono-sorption as a new method for the removal of methylene blue from aqueous solution, Ultrasonics sonochemistry, 14 (2007) 599-604.

[37] M.S. Lucas, J.A. Peres, Decolorization of the azo dye Reactive Black 5 by Fenton and photo-Fenton oxidation, Dyes and Pigments, 71 (2006) 236-244.

[38] Z. Shan, W. Wang, X. Lin, H. Ding, F. Huang, Photocatalytic degradation of organic dyes on visible-light responsive photocatalyst $PbBiO_2Br$, Journal of Solid State Chemistry, 181 (2008) 1361-1366.

[39] A. Shokri, Degradation of 2-nitrophenol from petrochemical wastewater by ozone, Russian Journal of Applied Chemistry, 88 (2015) 2038-2043.

[40] Y. Lei, P. Mulchandani, W. Chen, A. Mulchandani, Direct determination of p-nitrophenyl substituent organophosphorus nerve agents using a recombinant Pseudomonas putida JS444-modified Clark oxygen electrode, Journal of agricultural and food chemistry, 53 (2005) 524-527.

[41] D.-P. Zhang, W.-L. Wu, H.-Y. Long, Y.-C. Liu, Z.-S. Yang, Voltammetric Behavior of o-Nitrophenol and Damage to DNA, International journal of molecular sciences, 9 (2008) 316-326.

[42] S. Ammar, N. Oturan, M.A. Oturan, Electrochemical oxidation of 2-nitrophenol in aqueous medium by electro-Fenton technology, Journal of Environmental Engineering and Management, 17 (2007) 89.

[43] P. Gharbani, M. Khosravi, S. Tabatabaii, K. Zare, S. Dastmalchi, A. Mehrizad, Degradation of trace aqueous 4-chloro-2-nitrophenol occurring in pharmaceutical industrial wastewater by ozone, International Journal of Environmental Science & Technology, 7 (2010) 377-384.

[44] A. Karimi-Jashni, R.M. Narbaitz, Impact of pH on the adsorption and desorption kinetics of 2-nitrophenol on activated carbons, Water Research, 31 (1997) 3039-3044.

[45] I. Cesarino, R.P. Simões, F.C. Lavarda, A. Batagin-Neto, Electrochemical oxidation of sulfamethazine on a glassy carbon electrode modified with graphene and gold nanoparticles, Electrochimica Acta, 192 (2016) 8-14.

[46] A. El-Ghenymy, P.L. Cabot, F. Centellas, J.A. Garrido, R.M. Rodríguez, C. Arias, E. Brillas, Electrochemical incineration of the antimicrobial sulfamethazine at a boron-doped diamond anode, Electrochimica Acta, 90 (2013) 254-264.

[47] M. Pérez-Moya, M. Graells, G. Castells, J. Amigó, E. Ortega, G. Buhigas, L.M. Pérez, H.D. Mansilla, Characterization of the degradation performance of the sulfamethazine antibiotic by photo-Fenton process, Water Research, 44 (2010) 2533-2540.

[48] Y. Ji, C. Ferronato, A. Salvador, X. Yang, J.-M. Chovelon, Degradation of ciprofloxacin and sulfamethoxazole by ferrous-activated persulfate: implications for remediation of groundwater contaminated by antibiotics, Science of the total environment, 472 (2014) 800-808.

[49] K. Kümmerer, Antibiotics in the aquatic environment–a review–part I, Chemosphere, 75 (2009) 417-434.

[50] M. El-Kemary, H. El-Shamy, I. El-Mehasseb, Photocatalytic degradation of ciprofloxacin drug in water using ZnO nanoparticles, Journal of Luminescence, 130 (2010) 2327-2331.

[51] P. Huo, Z. Lu, H. Wang, J. Pan, H. Li, X. Wu, W. Huang, Y. Yan, Enhanced photodegradation of antibiotics solution under visible light with Fe^{2+}/Fe^{3+} immobilized on TiO_2/fly-ash cenospheres by using ions imprinting technology, Chemical engineering journal, 172 (2011) 615-622.

[52] W. Shi, Y. Yan, X. Yan, Microwave-assisted synthesis of nano-scale $BiVO_4$ photocatalysts and their excellent visible-light-driven photocatalytic activity for the degradation of ciprofloxacin, Chemical engineering journal, 215 (2013) 740-746.

[53] T. Madrakian, A. Afkhami, H. Mahmood-Kashani, M. Ahmadi, Adsorption of some cationic and anionic dyes on magnetite nanoparticles-modified activated carbon from aqueous solutions: equilibrium and kinetics study, Journal of the Iranian Chemical Society, 10 (2013) 481-489.

[54] S. Ahmed, M. Rasul, W.N. Martens, R. Brown, M. Hashib, Heterogeneous photocatalytic degradation of phenols in wastewater: a review on current status and developments, Desalination, 261 (2010) 3-18.

[55] M.I. Litter, Introduction to photochemical advanced oxidation processes for water treatment, Environmental Photochemistry Part II, Springer 2005, pp. 325-366.

[56] P. Gharbani, S. Tabatabaii, A. Mehrizad, Removal of Congo red from textile wastewater by ozonation, International Journal of Environmental Science & Technology, 5 (2008) 495-500.

[57] E. Brillas, C.A. Martínez-Huitle, Decontamination of wastewaters containing synthetic organic dyes by electrochemical methods. An updated review, Applied Catalysis B: Environmental, 166 (2015) 603-643.

[58] C.A. Martinez-Huitle, S. Ferro, Electrochemical oxidation of organic pollutants for the wastewater treatment: direct and indirect processes, Chemical Society Reviews, 35 (2006) 1324-1340.

[59] C.A. Martínez-Huitle, E. Brillas, Decontamination of wastewaters containing synthetic organic dyes by electrochemical methods: a general review, Applied Catalysis B: Environmental, 87 (2009) 105-145.

[60] C. Comninellis, G. Chen, Electrochemistry for the Environment, Springer 2010.

[61] B. Marselli, J. Garcia-Gomez, P.-A. Michaud, M. Rodrigo, C. Comninellis, Electrogeneration of hydroxyl radicals on boron-doped diamond electrodes, Journal of the Electrochemical Society, 150 (2003) D79-D83.

[62] A.M.S. Solano, C.K.C. de Araújo, J.V. de Melo, J.M. Peralta-Hernandez, D.R. da Silva, C.A. Martínez-Huitle, Decontamination of real textile industrial effluent by strong oxidant species electrogenerated on diamond electrode: viability and disadvantages of this electrochemical technology, Applied Catalysis B: Environmental, 130 (2013) 112-120.

[63] E. Brillas, I. Sirés, M.A. Oturan, Electro-Fenton process and related electrochemical technologies based on Fenton's reaction chemistry, Chemical reviews, 109 (2009) 6570-6631.

[64] C.A. Martínez-Huitle, E. Brillas, Electrochemical alternatives for drinking water disinfection, Angewandte Chemie International Edition, 47 (2008) 1998-2005.

[65] M.A. Tarr, Chemical degradation methods for wastes and pollutants: environmental and industrial applications, CRC Press 2003.

[66] M.H. Bergmann, J. Rollin, Product and by-product formation in laboratory studies on disinfection electrolysis of water using boron-doped diamond anodes, Catalysis Today, 124 (2007) 198-203.

[67] G. Li, P. Miao, Theoretical background of electrochemical analysis, Electrochemical analysis of proteins and cells, Springer 2013, pp. 5-18.

[68] D.C. Johnson, W.R. LaCourse, Liquid chromatography with pulsed electrochemical detection at gold and platinum electrodes, Analytical Chemistry, 62 (1990) 589A-597A.

[69] C. Fan, G. Li, Y. Zhuang, J. Zhu, D. Zhu, Iodide modified silver electrode and its application to the electroanalysis of hemoglobin, Electroanalysis, 12 (2000) 205-208.

[70] A. Gutés, C. Carraro, R. Maboudian, Nonenzymatic glucose sensing based on deposited palladium nanoparticles on epoxy-silver electrodes, Electrochimica acta, 56 (2011) 5855-5859.

[71] M.B. Ferreira, J.H.B. Rocha, J.V. de Melo, C.A. Martinez-Huitle, M.A.Q. Alfaro, Use of a dual arrangement of flow cells for electrochemical decontamination of aqueous solutions containing synthetic dyes, Electrocatalysis, 4 (2013) 274-282.

[72] A.S. Solano, J. Rocha, N. Fernandes, D. Da Silva, C. Martinez-Huitle, Direct and indirect electrochemical oxidation process for decolourisation treatment of synthetic wastewaters containing dye, Oxidation Communications, 34 (2011) 218-229.

[73] S. Ammar, R. Abdelhedi, C. Flox, C. Arias, E. Brillas, Electrochemical degradation of the dye indigo carmine at boron-doped diamond anode for wastewaters remediation, Environmental Chemistry Letters, 4 (2006) 229-233.

[74] D. Carvalho, J. Bezerra Rocha, N. Fernandes, D. Da Silva, C. Martínez-Huitle, Application of electrochemical oxidation as alternative for removing methyl green dye from aqueous solutions, Latin American applied research, 41 (2011) 127-133.

[75] E. Hmani, Y. Samet, R. Abdelhédi, Electrochemical degradation of auramine-O dye at boron-doped diamond and lead dioxide electrodes, Diamond and Related Materials, 30 (2012) 1-8.

[76] C. Vedhi, G. Selvanathan, P. Arumugam, P. Manisankar, Electrochemical sensors of heavy metals using novel polymer-modified glassy carbon electrodes, Ionics, 15 (2009) 377.

[77] J. Byun, Emerging frontiers of graphene in biomedicine, J. Microbiol. Biotechnol, 25 (2015) 145-151.

[78] M. Yi, Z. Shen, A review on mechanical exfoliation for the scalable production of graphene, Journal of Materials Chemistry A, 3 (2015) 11700-11715.

[79] K. Novoselov, D. Jiang, F. Schedin, T. Booth, V. Khotkevich, S. Morozov, A. Geim, Two-dimensional atomic crystals, Proceedings of the National Academy of Sciences of the United States of America, 102 (2005) 10451-10453.

[80] K.S. Novoselov, A.K. Geim, S.V. Morozov, D. Jiang, Y. Zhang, S.V. Dubonos, I.V. Grigorieva, A.A. Firsov, Electric field effect in atomically thin carbon films, science, 306 (2004) 666-669.

[81] J. Moser, A. Barreiro, A. Bachtold, Current-induced cleaning of graphene, Applied Physics Letters, 91 (2007) 163513.

[82] F. Chen, F. Yan, Q. Chen, Y. Wang, L. Han, Z. Chen, S. Fang, Fabrication of Fe_3O_4@ SiO_2@ TiO_2 nanoparticles supported by graphene oxide sheets for the repeated adsorption and photocatalytic degradation of rhodamine B under UV irradiation, Dalton Transactions, 43 (2014) 13537-13544.

[83] P. Wang, Y. Tang, Z. Dong, Z. Chen, T.-T. Lim, Ag–AgBr/TiO_2/RGO nanocomposite for visible-light photocatalytic degradation of penicillin G, Journal of Materials Chemistry A, 1 (2013) 4718-4727.

[84] M.E. Khan, M.M. Khan, M.H. Cho, Green synthesis, photocatalytic and photoelectrochemical performance of an Au–Graphene nanocomposite, RSC Advances, 5 (2015) 26897-26904.

[85] M.E. Khan, M.M. Khan, M.H. Cho, Fabrication of WO_3 nanorods on graphene nanosheets for improved visible light-induced photocapacitive and photocatalytic performance, RSC Advances, 6 (2016) 20824-20833.

[86] Y. Wang, H. Chang, H. Wu, H. Liu, Bioinspired prospects of graphene: from biosensing to energy, Journal of Materials Chemistry B, 1 (2013) 3521-3534.

[87] Q. Wu, H. Zhang, L. Zhou, C. Bao, H. Zhu, Y. Zhang, Synthesis and application of rGO/$CoFe_2O_4$ composite for catalytic degradation of methylene blue on heterogeneous Fenton-like oxidation, Journal of the Taiwan Institute of Chemical Engineers, 67 (2016) 484-494.

[88] J. Xue, S. Ma, Y. Zhou, Q. Wang, Au-loaded porous graphitic C_3N_4/graphene layered composite as a ternary plasmonic photocatalyst and its visible-light photocatalytic performance, Rsc Advances, 5 (2015) 88249-88257.

[89] R. Goslich, R. Dillert, D. Bahnemann, Solar water treatment: principles and reactors, Water Science and Technology, 35 (1997) 137-148.

[90] M.E. Khan, M.M. Khan, M.H. Cho, Biogenic synthesis of a Ag–graphene nanocomposite with efficient photocatalytic degradation, electrical conductivity and photoelectrochemical performance, New Journal of Chemistry, 39 (2015) 8121-8129.

[91] M.E. Khan, M.M. Khan, M.H. Cho, CdS-graphene nanocomposite for efficient visible-light-driven photocatalytic and photoelectrochemical applications, Journal of colloid and interface science, 482 (2016) 221-232.

[92] M.E. Khan, M.M. Khan, M.H. Cho, Ce3+-ion, surface oxygen vacancy, and visible light-induced photocatalytic dye degradation and photocapacitive performance of CeO_2-graphene nanostructures, Scientific Reports, 7 (2017).

[93] D. Chung, Exfoliation of graphite, Journal of materials science, 22 (1987) 4190-4198.

[94] D. Chung, A review of exfoliated graphite, Journal of materials science, 51 (2016) 554-568.

[95] M. Dowell, R. Howard, Tensile and compressive properties of flexible graphite foils, Carbon, 24 (1986) 311-323.

[96] B. Ntsendwana, B.B. Mamba, S. Sampath, O.A. Arotiba, Synthesis, characterisation and application of an exfoliated graphite–diamond composite electrode in the electrochemical degradation of trichloroethylene, RSC Advances, 3 (2013) 24473-24483.

[97] B. Ntsendwana, S. Sampath, B. Mamba, O. Arotiba, Photoelectrochemical oxidation of p-nitrophenol on an expanded graphite–TiO_2 electrode, Photochemical & Photobiological Sciences, 12 (2013) 1091-1102.

[98] M. Peleyeju, E. Umukoro, J. Babalola, O. Arotiba, Electrochemical Degradation of an Anthraquinonic Dye on an Expanded Graphite-Diamond Composite Electrode, Electrocatalysis, 7 (2016) 132-139.

[99] X. Yu, Y. Zhang, X. Cheng, Preparation and photoelectrochemical performance of expanded graphite/TiO_2 composite, Electrochimica Acta, 137 (2014) 668-675.

[100] T. Ndlovu, O.A. Arotiba, S. Sampath, R.W. Krause, B.B. Mamba, Electrochemical detection and removal of lead in water using poly (propylene imine) modified re-compressed exfoliated graphite electrodes, Journal of Applied Electrochemistry, 41 (2011) 1389-1396.

[101] W. Yun-Hai, C. Qing-Yun, L. Guo, L. Xiang-Lin, Anodic materials with high energy efficiency for electrochemical oxidation of toxic organics in waste water, Industrial waste, InTech 2012.

[102] S.H.S. Chan, T. Yeong Wu, J.C. Juan, C.Y. Teh, Recent developments of metal oxide semiconductors as photocatalysts in advanced oxidation processes (AOPs) for treatment of dye waste-water, Journal of Chemical Technology and Biotechnology, 86 (2011) 1130-1158.

[103] C. Galindo, P. Jacques, A. Kalt, Photochemical and photocatalytic degradation of an indigoid dye: a case study of acid blue 74 (AB74), Journal of Photochemistry and Photobiology A: Chemistry, 141 (2001) 47-56.

[104] A. Subramani, K. Byrappa, S. Ananda, K. Rai, C. Ranganathaiah, M. Yoshimura, Photocatalytic degradation of indigo carmine dye using TiO_2 impregnated activated carbon, Bulletin of materials science, 30 (2007).

[105] C. Gómez-Solís, I. Juárez-Ramírez, E. Moctezuma, L.M. Torres-Martínez, Photodegradation of indigo carmine and methylene blue dyes in aqueous solution by SiC–TiO_2 catalysts prepared by sol–gel, Journal of hazardous materials, 217 (2012) 194-199.

[106] E. Agorku, A. Kuvarega, B. Mamba, A. Pandey, A. Mishra, Enhanced visible-light photocatalytic activity of multi-elements-doped ZrO_2 for degradation of indigo carmine, Journal of Rare Earths, 33 (2015) 498-506.

[107] F. De Andrade, G. De Lima, R. Augusti, M. Coelho, J. Ardisson, O. Romero, A versatile approach to treat aqueous residues of textile industry: the photocatalytic degradation of Indigo Carmine dye employing the autoclaved cellular concrete/Fe_2O_3 system, Chemical Engineering Journal, 180 (2012) 25-31.

[108] S.O.-B. Oppong, W.W. Anku, S.K. Shukla, E.S. Agorku, P.P. Govender, Photocatalytic degradation of indigo carmine using Nd-doped TiO_2-decorated graphene oxide nanocomposites, Journal of Sol-Gel Science and Technology, 80 (2016) 38-49.

[109] L. Yang, S. Luo, Y. Li, Y. Xiao, Q. Kang, Q. Cai, High efficient photocatalytic degradation of p-nitrophenol on a unique Cu2O/TiO2 pn heterojunction network catalyst, Environmental science & technology, 44 (2010) 7641-7646.

[110] A. Di Paola, E. García-López, G. Marcì, L. Palmisano, A survey of photocatalytic materials for environmental remediation, Journal of hazardous materials, 211 (2012) 3-29.

[111] S. Ma, J. Xue, Y. Zhou, Z. Zhang, Photochemical synthesis of ZnO/Ag_2O heterostructures with enhanced ultraviolet and visible photocatalytic activity, Journal of Materials Chemistry A, 2 (2014) 7272-7280.

[112] S. Naghizadeh-Alamdari, A. Habibi-Yangjeh, M. Pirhashemi, One-pot ultrasonic-assisted method for preparation of Ag/AgCl sensitized ZnO nanostructures as visible-light-driven photocatalysts, Solid State Sciences, 40 (2015) 111-120.

[113] M. Pudukudy, Z. Yaakob, Simple chemical synthesis of novel ZnO nanostructures: role of counter ions, Solid State Sciences, 30 (2014) 78-88.

[114] J. Qin, R. Li, C. Lu, Y. Jiang, H. Tang, X. Yang, Ag/ZnO/graphene oxide heterostructure for the removal of rhodamine B by the synergistic adsorption–degradation effects, Ceramics International, 41 (2015) 4231-4237.

[115] D. An, Y. Li, X. Lian, Y. Zou, G. Deng, Synthesis of porous ZnO structure for gas sensor and photocatalytic applications, Colloids and Surfaces A: Physicochemical and Engineering Aspects, 447 (2014) 81-87.

[116] M. Miyauchi, A. Nakajima, T. Watanabe, K. Hashimoto, Photocatalysis and photoinduced hydrophilicity of various metal oxide thin films, Chemistry of Materials, 14 (2002) 2812-2816.

[117] C. Lu, Y. Wu, F. Mai, W. Chung, C. Wu, W. Lin, C. Chen, Degradation efficiencies and mechanisms of the ZnO-mediated photocatalytic degradation of Basic Blue 11 under visible light irradiation, Journal of Molecular Catalysis A: Chemical, 310 (2009) 159-165.

[118] N. Sobana, M. Swaminathan, Combination effect of ZnO and activated carbon for solar assisted photocatalytic degradation of Direct Blue 53, Solar energy materials and solar cells, 91 (2007) 727-734.

[119] S. Su, S. Lu, W. Xu, Photocatalytic degradation of reactive brilliant blue X-BR in aqueous solution using quantum-sized ZnO, Materials research bulletin, 43 (2008) 2172-2178.

[120] S. Navarro, J. Fenoll, N. Vela, E. Ruiz, G. Navarro, Photocatalytic degradation of eight pesticides in leaching water by use of ZnO under natural sunlight, Journal of hazardous materials, 172 (2009) 1303-1310.

[121] V. Kandavelu, H. Kastien, K.R. Thampi, Photocatalytic degradation of isothiazolin-3-ones in water and emulsion paints containing nanocrystalline TiO_2 and ZnO catalysts, Applied Catalysis B: Environmental, 48 (2004) 101-111.

[122] T. Lv, L. Pan, X. Liu, Z. Sun, Enhanced photocatalytic degradation of methylene blue by ZnO–reduced graphene oxide–carbon nanotube composites synthesized via microwave-assisted reaction, Catalysis Science & Technology, 2 (2012) 2297-2301.

[123] R. Saravanan, M.M. Khan, V.K. Gupta, E. Mosquera, F. Gracia, V. Narayanan, A. Stephen, ZnO/Ag/Mn_2O_3 nanocomposite for visible light-induced industrial textile effluent degradation, uric acid and ascorbic acid sensing and antimicrobial activity, RSC Advances, 5 (2015) 34645-34651.

[124] Y. Feng, N. Feng, Y. Wei, G. Zhang, An in situ gelatin-assisted hydrothermal synthesis of ZnO–reduced graphene oxide composites with enhanced photocatalytic performance under ultraviolet and visible light, RSC Advances, 4 (2014) 7933-7943.

[125] C. Liu, C. Cao, X. Luo, S. Luo, Ag-bridged Ag_2O nanowire network/TiO_2 nanotube array p–n heterojunction as a highly efficient and stable visible light photocatalyst, Journal of hazardous materials, 285 (2015) 319-324.

[126] D. Sarkar, C.K. Ghosh, S. Mukherjee, K.K. Chattopadhyay, Three dimensional Ag_2O/TiO_2 type-II (p–n) nanoheterojunctions for superior photocatalytic activity, ACS applied materials & interfaces, 5 (2012) 331-337.

[127] Y. Xu, M.A. Schoonen, The absolute energy positions of conduction and valence bands of selected semiconducting minerals, American Mineralogist, 85 (2000) 543-556.

[128] X. Wang, S. Li, H. Yu, J. Yu, S. Liu, Ag_2O as a New Visible-Light Photocatalyst: Self-Stability and High Photocatalytic Activity, Chemistry-A European Journal, 17 (2011) 7777-7780.

[129] G. Wang, X. Ma, B. Huang, H. Cheng, Z. Wang, J. Zhan, X. Qin, X. Zhang, Y. Dai, Controlled synthesis of Ag_2O microcrystals with facet-dependent photocatalytic activities, Journal of Materials Chemistry, 22 (2012) 21189-21194.

[130] F. Chen, Z. Liu, Y. Liu, P. Fang, Y. Dai, Enhanced adsorption and photocatalytic degradation of high-concentration methylene blue on Ag_2O-modified TiO_2-based nanosheet, Chemical Engineering Journal, 221 (2013) 283-291.

[131] S. Liu, N. Wang, Y. Zhang, Y. Li, Z. Han, P. Na, Efficient removal of radioactive iodide ions from water by three-dimensional Ag_2O–Ag/TiO_2 composites under visible light irradiation, Journal of hazardous materials, 284 (2015) 171-181.

[132] Y. Cai, H. Fan, M. Xu, Q. Li, Rapid photocatalytic activity and honeycomb Ag/ZnO heterostructures via solution combustion synthesis, Colloids and Surfaces A: Physicochemical and Engineering Aspects, 436 (2013) 787-795.

[133] J. Xie, L. Li, Y. Guan, H. Lu, C. Han, D. Zhao, C. Tian, Q. Yin, AgBr/Ag/Ag_2O/GO composite: Ultrasonic fabrication, characterization and visible-driven photocatalytic property, Materials Letters, 120 (2014) 54-57.

[134] D. Sarkar, C.K. Ghosh, S. Mukherjee, K.K. Chattopadhyay, Three dimensional Ag_2O/TiO_2 type-II (p–n) nanoheterojunctions for superior photocatalytic activity, (2012).

[135] N. Asim, M. Badeiei, K. Ghoreishi, N. Ludin, M.R.F. Zonooz, K. Sopian, New Developments in photocatalysts modification: case study of WO_3, Advances in Fluid Mechanics and Heat & Mass Transfer, (2012) 110-116.

[136] Y. Hunge, M. Mahadik, V. Mohite, S. Kumbhar, N. Deshpande, K. Rajpure, A. Moholkar, P. Patil, C. Bhosale, Photoelectrocatalytic degradation of methyl blue using sprayed WO_3 thin films, Journal of Materials Science: Materials in Electronics, 27 (2016) 1629-1635.

[137] S. Bai, Y. Ma, R. Luo, A. Chen, D. Li, Room temperature triethylamine sensing properties of polyaniline–WO_3 nanocomposites with p–n heterojunctions, RSC Advances, 6 (2016) 2687-2694.

[138] L. Yin, D. Chen, M. Feng, L. Ge, D. Yang, Z. Song, B. Fan, R. Zhang, G. Shao, Hierarchical Fe_2O_3@WO_3 nanostructures with ultrahigh specific surface areas: microwave-assisted synthesis and enhanced H 2 S-sensing performance, RSC Advances, 5 (2015) 328-337.

[139] J. Zhou, Y. Wei, G. Luo, J. Zheng, C. Xu, Electrochromic properties of vertically aligned Ni-doped WO_3 nanostructure films and their application in complementary electrochromic devices, Journal of Materials Chemistry C, 4 (2016) 1613-1622.

[140] I. Vamvasakis, I. Georgaki, D. Vernardou, G. Kenanakis, N. Katsarakis, Synthesis of WO_3 catalytic powders: evaluation of photocatalytic activity under NUV/visible light irradiation and alkaline reaction pH, Journal of Sol-Gel Science and Technology, 76 (2015) 120-128.

[141] Y. Wicaksana, S. Liu, J. Scott, R. Amal, Tungsten trioxide as a visible light photocatalyst for volatile organic carbon removal, Molecules, 19 (2014) 17747-17762.

[142] T. Wang, W. Quan, D. Jiang, L. Chen, D. Li, S. Meng, M. Chen, Synthesis of redox-mediator-free direct Z-scheme AgI/WO_3 nanocomposite photocatalysts for the degradation of tetracycline with enhanced photocatalytic activity, Chemical Engineering Journal, 300 (2016) 280-290.

[143] J. Luo, J. Yartym, M. Hepel, Photoelectrochemical degradation of Orange II textile dye on nanostructured WO_3 film electrodes, J New Mat Elect Syst, 5 (2002) 315-321.

[144] F. Wang, W. Li, S. Gu, H. Li, X. Wu, X. Liu, Samarium and Nitrogen Co-Doped Bi_2WO_6 Photocatalysts: Synergistic Effect of Sm^{3+}/Sm^{2+} Redox Centers and N-Doped Level for Enhancing Visible-Light Photocatalytic Activity, Chemistry-A European Journal, 22 (2016) 12859-12867.

[145] S.M. Harshulkhan, K. Janaki, G. Velraj, R.S. Ganapthy, M. Nagarajan, Effect of Ag doping on structural, optical and photocatalytic activity of tungsten oxide (WO_3) nanoparticles, Journal of Materials Science: Materials in Electronics, 27 (2016) 4744-4751.

[146] W. Mu, X. Xie, X. Li, R. Zhang, Q. Yu, K. Lv, H. Wei, Y. Jian, Characterizations of Nb-doped WO_3 nanomaterials and their enhanced photocatalytic performance, Rsc Advances, 4 (2014) 36064-36070.

[147] Q. Kuang, C. Lao, Z.L. Wang, Z. Xie, L. Zheng, High-sensitivity humidity sensor based on a single SnO_2 nanowire, Journal of the American Chemical Society, 129 (2007) 6070-6071.

[148] S. Wu, H. Cao, S. Yin, X. Liu, X. Zhang, Amino acid-assisted hydrothermal synthesis and photocatalysis of SnO_2 nanocrystals, The Journal of Physical Chemistry C, 113 (2009) 17893-17898.

[149] E.N. Dattoli, Q. Wan, W. Guo, Y. Chen, X. Pan, W. Lu, Fully transparent thin-film transistor devices based on SnO_2 nanowires, Nano letters, 7 (2007) 2463-2469.

[150] P. Lian, X. Zhu, S. Liang, Z. Li, W. Yang, H. Wang, High reversible capacity of SnO_2/graphene nanocomposite as an anode material for lithium-ion batteries, Electrochimica Acta, 56 (2011) 4532-4539.

[151] L. Yu, D. Cai, H. Wang, M.-M. Titirici, Hydrothermal synthesis of SnO_2 and SnO_2@C nanorods and their application as anode materials in lithium-ion batteries, RSC Advances, 3 (2013) 17281-17286.

[152] M. Moreno, A. Varela, L. Otero-Díaz, Cation nonstoichiometry in tin-monoxide-phase Sn 1− δ O with tweed microstructure, Physical Review B, 56 (1997) 5186.

[153] D. Zhang, Y.e. Sun, P. Li, Y. Zhang, Facile fabrication of MoS_2-modified SnO_2 hybrid nanocomposite for ultrasensitive humidity sensing, ACS applied materials & interfaces, 8 (2016) 14142-14149.

[154] J. Yan, E. Khoo, A. Sumboja, P.S. Lee, Facile coating of manganese oxide on tin oxide nanowires with high-performance capacitive behavior, ACS nano, 4 (2010) 4247-4255.

[155] W. Zhao, Y. Liu, Z. Wei, S. Yang, H. He, C. Sun, Fabrication of a novel p–n heterojunction photocatalyst n-$BiVO_4$@ p-MoS_2 with core–shell structure and its excellent visible-light photocatalytic reduction and oxidation activities, Applied Catalysis B: Environmental, 185 (2016) 242-252.

[156] Z. He, J. Zhou, Synthesis, characterization, and activity of tin oxide nanoparticles: influence of solvothermal time on photocatalytic degradation of rhodamine B, Modern Research in Catalysis, 2 (2013) 13.

[157] T. Sinha, M. Ahmaruzzaman, P.P. Adhikari, R. Bora, Green and Environmentally Sustainable Fabrication of Ag-SnO2 Nanocomposite and Its Multifunctional Efficacy As Photocatalyst and Antibacterial and Antioxidant Agent, ACS Sustainable Chemistry & Engineering, (2017).

[158] G.R. Malpass, D.W. Miwa, S.A. Machado, A.J. Motheo, SnO_2-based materials for pesticide degradation, Journal of hazardous materials, 180 (2010) 145-151.

[159] S.K. Balasingam, J.S. Lee, Y. Jun, Few-layered $MoSe_2$ nanosheets as an advanced electrode material for supercapacitors, Dalton Transactions, 44 (2015) 15491-15498.

[160] S.K. Balasingam, A. Thirumurugan, J.S. Lee, Y. Jun, Amorphous MoS_x thin-film-coated carbon fiber paper as a 3D electrode for long cycle life symmetric supercapacitors, Nanoscale, 8 (2016) 11787-11791.

[161] L. Hao, W. Gao, Y. Liu, Y. Liu, Z. Han, Q. Xue, J. Zhu, Self-powered broadband, high-detectivity and ultrafast photodetectors based on Pd-MoS_2/Si heterojunctions, Physical Chemistry Chemical Physics, 18 (2016) 1131-1139.

[162] Q. Ji, Y. Zhang, T. Gao, Y. Zhang, D. Ma, M. Liu, Y. Chen, X. Qiao, P.-H. Tan, M. Kan, Epitaxial monolayer MoS_2 on mica with novel photoluminescence, Nano letters, 13 (2013) 3870-3877.

[163] Y. Yoon, K. Ganapathi, S. Salahuddin, How good can monolayer MoS_2 transistors be?, Nano letters, 11 (2011) 3768-3773.

[164] R. Bose, S.K. Balasingam, S. Shin, Z. Jin, D.H. Kwon, Y. Jun, Y.-S. Min, Importance of hydrophilic pretreatment in the hydrothermal growth of amorphous molybdenum sulfide for hydrogen evolution catalysis, Langmuir, 31 (2015) 5220-5227.

[165] H. Xu, J. Wu, Q. Feng, N. Mao, C. Wang, J. Zhang, High responsivity and gate tunable graphene-MoS_2 hybrid phototransistor, Small, 10 (2014) 2300-2306.

[166] J. Ke, J. Liu, H. Sun, H. Zhang, X. Duan, P. Liang, X. Li, M.O. Tade, S. Liu, S. Wang, Facile assembly of Bi_2O_3/Bi_2S_3/MoS_2 np heterojunction with layered n-Bi_2O_3 and p-MoS_2 for enhanced photocatalytic water oxidation and pollutant degradation, Applied Catalysis B: Environmental, 200 (2017) 47-55.

[167] W. Zhou, Z. Yin, Y. Du, X. Huang, Z. Zeng, Z. Fan, H. Liu, J. Wang, H. Zhang, Synthesis of few-layer MoS_2 nanosheet-coated TiO_2 nanobelt heterostructures for enhanced photocatalytic activities, small, 9 (2013) 140-147.

[168] E.H. Umukoro, M.G. Peleyeju, J.C. Ngila, O.A. Arotiba, Towards wastewater treatment: Photo-assisted electrochemical degradation of 2-nitrophenol and orange II dye at a tungsten trioxide-exfoliated graphite composite electrode, Chemical Engineering Journal, 317 (2017) 290-301.

[169] T. Guaraldo, S.H. Pulcinelli, M.B. Zanoni, Influence of particle size on the photoactivity of Ti/TiO_2 thin film electrodes, and enhanced photoelectrocatalytic degradation of indigo carmine dye, Journal of Photochemistry and Photobiology A: Chemistry, 217 (2011) 259-266.

[170] T.T. Guaraldo, T.B. Zanoni, S.I. de Torresi, V.R. Gonçales, G.J. Zocolo, D.P. Oliveira, M.V.B. Zanoni, On the application of nanostructured electrodes prepared by $Ti/TiO_2/WO_3$ "template": A case study of removing toxicity of indigo using visible irradiation, Chemosphere, 91 (2013) 586-593.

[171] S. Anandan, G.-J. Lee, P.-K. Chen, C. Fan, J.J. Wu, Removal of orange II dye in water by visible light assisted photocatalytic ozonation using Bi_2O_3 and Au/Bi_2O_3 nanorods, Industrial & Engineering Chemistry Research, 49 (2010) 9729-9737.

[172] Y. Bessekhouad, N. Chaoui, M. Trzpit, N. Ghazzal, D. Robert, J. Weber, UV–vis versus visible degradation of Acid Orange II in a coupled CdS/TiO_2 semiconductors suspension, Journal of Photochemistry and Photobiology A: Chemistry, 183 (2006) 218-224.

[173] P. Ji, J. Zhang, F. Chen, M. Anpo, Study of adsorption and degradation of acid orange 7 on the surface of CeO_2 under visible light irradiation, Applied Catalysis B: Environmental, 85 (2009) 148-154.

[174] M. Rauf, M. Meetani, S. Hisaindee, An overview on the photocatalytic degradation of azo dyes in the presence of TiO_2 doped with selective transition metals, Desalination, 276 (2011) 13-27.

[175] V. Stengl, S. Bakardjieva, Molybdenum-doped anatase and its extraordinary photocatalytic activity in the degradation of orange II in the UV and vis regions, The Journal of Physical Chemistry C, 114 (2010) 19308-19317.

[176] G. Li, J. Qu, X. Zhang, H. Liu, H. Liu, Electrochemically assisted photocatalytic degradation of Orange II: influence of initial pH values, Journal of Molecular Catalysis A: Chemical, 259 (2006) 238-244.

[177] D. Wang, X. Li, J. Chen, X. Tao, Enhanced photoelectrocatalytic activity of reduced graphene oxide/TiO_2 composite films for dye degradation, Chemical engineering journal, 198 (2012) 547-554.

[178] S.A. Ansari, M.M. Khan, M.O. Ansari, J. Lee, M.H. Cho, Biogenic synthesis, photocatalytic, and photoelectrochemical performance of Ag–ZnO nanocomposite, The Journal of Physical Chemistry C, 117 (2013) 27023-27030.

[179] B. Su, Y. Ma, Y. Du, C. Wang, Study of photoelectrocatalytic degradation behavior of p-nitrophenol with nano-TiO_2 modified film at a rotating ring–disk electrode, Electrochemistry Communications, 11 (2009) 1154-1157.

[180] J. Li, S. Lv, Y. Liu, J. Bai, B. Zhou, X. Hu, Photoeletrocatalytic activity of an n-ZnO/p-Cu_2O/n-TNA ternary heterojunction electrode for tetracycline degradation, Journal of hazardous materials, 262 (2013) 482-488.

[181] S. Xiao, Y. Song, Z. Tian, X. Tu, X. Hu, L. Ruixia, Enhanced mineralization of antibiotic berberine by the photoelectrochemical process in presence of chlorides and its optimization by response surface methodology, Environmental Earth Sciences, 73 (2015) 4947-4955.

[182] N. Smirnova, V. Vorobets, O. Linnik, E. Manuilov, G. Kolbasov, A. Eremenko, Photoelectrochemical and photocatalytic properties of mesoporous TiO_2 films modified with silver and gold nanoparticles, Surface and Interface Analysis, 42 (2010) 1205-1208.

[183] F. Jensen, Introduction to computational chemistry. 2007, West Sussex, England: John Wiley & Sons Ltd, 30-34.

[184] H. Kiyak, Synthesis, Characterization and Computational Studies of Oxomolybdenum Compounds with Nitrogen Donor Ligands., Turkey, Izmir Institute of Technology, MSc Thesis (2010).

[185] L.O. Olasunkanmi, Electrochemical, Quantum Chemical Calculation And Molecular Dynamic Simulation Studies On Some Quinoxaline Derivatives As Corrosion Inhibitors For Mild Steel In Acidic Medium, North West University, South Africa, PhD Thesis (2016).

[186] D.C. Young, A Practical Guide for Applying Techniques to Real-World Problems, Wiley–Interscience New York:, 2001.

[187] K. Ramachandran, G. Deepa, K. Namboori, Computational chemistry and molecular modeling: principles and applications, Springer Science & Business Media2008.

[188] C.J. Cramer, Essentials of computational chemistry: theories and models, John Wiley & Sons 2013.

[189] J.C. Cuevas, Introduction to density functional theory, Universität Karlsruhe, Germany, (2010).

[190] W. Kohn, L.J. Sham, Self-consistent equations including exchange and correlation effects, Physical review, 140 (1965) A1133.

[191] F. Calle-Vallejo, M.T. Koper, First-principles computational electrochemistry: Achievements and challenges, Electrochimica Acta, 84 (2012) 3-11.

[192] W. Han, C. Zhong, L. Liang, Y. Sun, Y. Guan, L. Wang, X. Sun, J. Li, Electrochemical degradation of triazole fungicides in aqueous solution using TiO_2-NTs/SnO_2-Sb/PbO_2 anode: experimental and DFT studies, Electrochimica Acta, 130 (2014) 179-186.

[193] V.-M. Guérin, R. Zouzelka, H. Bibova-Lipsova, J. Jirkovsky, J. Rathousky, T. Pauporté, Experimental and DFT study of the degradation of 4-chlorophenol on hierarchical micro-/nanostructured oxide films, Applied Catalysis B: Environmental, 168 (2015) 132-140.

CHAPTER 3

METHODOLOGY

3.1 INTRODUCTION

This chapter provides the experimental procedures that are employed for the achievement of the objectives of this research work. All the major experimental work and characterisation techniques utilised in this research are discussed in this chapter. The result and discussion chapters give detailed experimental methods and procedures employed for the synthesis of the photocatalysts and nanocomposites used for the photocatalytic, electrocatalytic and photoelectrocatalytic degradation processes for this research.

3.2 GENERAL EXPERIMENTAL PROCEDURES

3.2.1 Materials and reagents

Potassium hydroxide, silver nitrate ($AgNO_3$), ascorbic acid, natural graphite flakes, nitric acid, sulphuric acid (98%), sodium nitrate ($NaNO_3$), potassium permanganate ($KMnO_4$), hydrogen peroxide, zinc nitrate hexahydrate ($Zn(NO_3)_2.6H_2O$), Ammonium metatungstate hydrate, absolute ethanol (99.9%), 3-aminopropyltriethoxysilane (APTES), dimethylsulphoxide (DMSO), oxalic acid, hydrobromic acid (HBr) acid blue 74 (Indigo carmine), orange II dye (acid orange 7 dye), sodium sulphate, potassium hexacyanoferrate (II), potassium hexacyanoferrate (III), potassium chloride, sodium hydroxide, 2-nitrophenol, 4-nitrophenol zinc acetate dihydrate ($Zn(CH_3COO)_2.2H_2O$), ammonium hydroxide (NH_4OH), polyethylene glycol, palladium acetate ($Pd(CH_3COO)_2$), Tin (IV) chloride dehydrate, thiourea, ammonium heptamolybdate tetrahydrate, ciprofloxacin and conducting silver paint. All reagents were purchased from Sigma Aldrich, Germany, and were of analytical grade and they were used for the experiments without further purifications.

3.2.2 Synthesis of graphene oxide and reduced graphene oxide

Graphene oxide was prepared by a modified Hummer's method [1] and then reduced to give reduced graphene oxide using ascorbic acid by a method described by Zhang et al. [2]. In brief, 5 g of graphite flakes were added to 2.5 g of sodium nitrate and 115 mL of sulphuric acid. The mixture was mixed and stirred vigorously. The mixture was allowed to

cool in an ice-bath and 15 g of potassium permanganate was added to the mixture over a period of 2 h. The mixture was allowed to cool in an ice-bath to room temperature and then heated to 35 ºC for 30 min. Then, it was poured into 250 mL of de-ionized water in a flask and heated to 70 ºC. The mixture was poured into 1 L of de-ionized water after keeping the temperature constant for about 15 min. A 30 mL volume of 3% hydrogen peroxide was added to remove any unreacted $KMnO_4$ and manganese dioxide in the mixture. Then, it was washed several times by centrifugation and filtration using de-ionized water until a pH of 6 was obtained. The resulting graphite oxide was then ultrasonicated for 2 h to obtain graphene oxide and then dried in an oven at 60 ºC for 48 h.

Furthermore, 5 g of ascorbic acid was added to an aqueous suspension which contained 0.1 g of the prepared graphene oxide in 50 mL of deionised water and sonicated for 30 min. The resultant suspension was stirred at 90 ºC for 48 h. Then, the product –reduced graphene oxide - was filtered and dried at 60 ºC overnight before use.

3.2.3 Synthesis of exfoliated graphite

Natural graphite was synthesised using modified methods in literature [3, 4]. Briefly, natural graphite was sieved using a 300 µm sieve mesh and intercalated by being soaked in concentrated nitric acid and sulphuric acid mixture in a ratio of 1:3 by volume for 48 hours at room temperature. The intercalated material was then washed to pH 7 and air-dried. It was further exfoliated by subjecting it to temperature of 800 ºC in a furnace for about a minute to obtain a puffed up exfoliated graphite material.

3.2.4 Evaluation of photocatalytic activity

The visible light photocatalytic activity of the materials was evaluated for the degradation of dyes which was chosen as target pollutants for a period of 180 to 210 min. An aqueous suspension (100 mL) containing 0.1 g of the photocatalyst nanocomposite and dye (20 mgL^{-1}) was prepared and stirred magnetically in the dark for 30 min to reach an adsorption-desorption equilibrium. Then the suspension was irradiated with a simulated solar light at room temperature. It was used for the photocatalytic degradation and kinetic studies of the target pollutant. At 30 min intervals, aliquots of the suspension were withdrawn, and filtered using a disposable syringe and a 0.4 µm PVDF filter. The concentration of the dye in the supernatant solution was measured using Cary 60 UV-Visible spectrophotometer (Agilent technologies, Australia)

3.2.5 Preparation of the rGO- or EG-composite electrode

A specific amount of the as-prepared photocatalyst (detailed procedures are in the results and discussion chapters) was dispersed in about 10 mL methanol and sonicated for 20 min to obtain a uniform dispersion. An equal amount of the carbon material such as reduced graphene oxide or exfoliated graphite was added to the dispersion and stirred vigorously for another 10 min. Then, the mixture was poured into a dish and dried in the oven at 90 ºC for about 48 h for the complete removal of the methanol to obtain the carbon-based composite which consist of the photocatalyst and the carbon material.

The as-prepared rGO, EG and their composite materials were compressed into pellet of 1.3 cm in diameter using a press machine at a very high pressure. Then the pellets were used to fabricate electrodes with the aid of a glass rod, conduction silver paint, copper wire and epoxy resin. One end of the copper wire in the glass tube was coiled to form a flat surface. The pellet was placed on the surface using the conductive silver paint which enabled the conduction between the copper wire and the composite [4]. It was allowed to dry in the air for about 1 h. The edge of the pellet was covered with epoxy resin so that electron flow is mainly from the basal plane.

3.3 CHARACTERISATION TECHNIQUES

3.3.1 Transmission electron microscopy (TEM)

TEM (JEOL TEM) analysis of samples makes use of electron beams in the electron microscope to illuminate the sample. It is this electron interaction with the sample that results in image production. The images produced have very high resolution because the wavelength of electrons is 100000 times shorter than that of visible light. Also its operation is done at high voltages of about 200 kV to 400 kV. Since the electron beam interacts with the sample while passing through the entire thickness of the sample, the TEM image tends to be a projection of the entire sample such as the surface and the internal structures of the sample The samples were placed in absolute ethanol and sonicated for 10 min and placed on a copper grid that is coated with carbon. Samples were left to dry under a beam of light and dipped in chloroform before introduction into the TEM instrument. This image analysis of the samples was carried out to determine structural morphology of the samples.

3.3.2 Scanning electron microscopy (SEM)

SEM gives information about the surface morphology and size of materials. It uses high energy electrons to interact with the surface of the materials by producing different signals. The data produced are collected for a particular area of the surface of the material under investigation and a 3D image is generated which gives variations of the properties [5]. Due to its electron usage, the material must be conductive electrically or coated with a material that is conductive in nature such as gold or carbon so as to increase its conductivity. In this characterisation technique, the electron beam is generated and focused into a small spot using a condenser lens and then with the aid of an objective lens, the beam is refocused where the electrons are deflected over the sample surface at regulated speeds to produce the images. The chamber of the microscope is held in vacuum in order to prevent the collision between the beam of electrons and the gas molecules, leading to microscope resolution reduction [6]. These electrons possess kinetic energy which is dissipated as signals when they interact with the sample/material under investigation [6, 7]. In this work, SEM was utilised to detect the surface morphology of the samples from the prepared materials.

3.3.3 Energy dispersive X-ray (EDX) spectroscopy

This is a qualitative and quantitative analytical technique based on measuring the interactions of high energy electrons with the surface of samples. The high energy elelctron is utilised to excite ground state electrons from the surface of the sample. These electrons in the excited state further emit the energy to fill the vacant ground state. The energy lost in this process is in form of X-ray phonons having a fixed wavelength. The X-ray phonons data is acquired by the x-ray analyser and the relationship between the intensity of the emitted x-rays and their corresponding energies gives an EDS spectrum [174]. There is a relationship between the emitted x-rays and the difference in energy levels of electrons in different shells of a particular element which is a characteristic feature of the atomic structure of the elements [8, 9]. Hence, the elemental composition of sample materials can be analysed. The intensity specific X-ray photons obtained is proportional to the quantity of specific elements in the chemical composition of the sample material. In this research, EDX analyses were carried out in conjunction with scanning electron microscopy.

3.3.4 Raman spectroscopy

Raman spectroscopy is a very important analysis technique in the field of carbon research. It is non-destructive tool commonly used for structural characterisation of graphitic materials, particularly for distinguishing ordered and disordered crystal structures of carbon [8]. Raman spectroscopy is a technique that is based on inelastic scattering of monochromatic light, usually from a laser source in the visible region. That is, when the monochromatic light interacts with the sample, there is a shift in frequency of the photons in the monochromatic light. These photons are absorbed and re-emitted by the sample, making the frequency of the photons to change downwards or upwards after re-emission when compared with the original monochromatic photons frequency. This phenomenon is known as the Raman Effect. This shift gives information on the vibrational, rotational and other low frequency transitions in the molecules of the sample being analysed. The obtained positions of the Raman peaks are regarded as fingerprint or characteristics of different materials. Raman spectroscopy is an analysis technique that is very sensitive to changes in the atomic structure of carbons and it has been found to be very important in understanding the vibration properties and the microstructure of graphitic crystals in ordered and disordered graphite or carbon materials. When used for most carbon materials, it exhibits the G and D bands around 1360 cm^{-1} and 1580 cm^{-1} respectively and the ratio the intensity of the D band to the G band is sometimes used as a measure of the crystallite size in graphitic materials [8]. However, for nanoparticles, this Raman band tends to shift to a higher frequency and broadened peak when there is decreased particle size and diameter. In this work, Perkin Elmer Raman microscope (Raman micro 200, USA) with 50 x objective and 514.5 nm air cooled having Ar^{+} Laser with intensity of the laser is 1.3 mW was utilised.

3.3.5 X-ray diffractometry (XRD)

XRD provides information on the phase composition and crystallographic of given materials. It could give single and multiple phases as well as detecting impurities in the materials, texture analysis, determine crystallographic structure, lattice properties and crystallite sizes. –In this analysis, an atom produces a beam of incident x-rays to diffract into specific directions. The angles and the intensities of this beam are measured, and based on its intensity a crystal phase is formed or not. The samples analysed were placed on a borosilicate glass stub and exposed to x-rays from a Cu-Kα radiation source (Bruker

D6). The diffraction angle (2-theta) was set in the range of 0.4-2 and 10-80 nm for low angle and full scan, respectively.

The crystallite size is determined using the Debye-Scherrer equation:

$$D = \frac{K\lambda}{\beta \cos\theta} \qquad [3.1]$$

Where K is known as a dimensionless constant, 2θ is the diffraction angle, λ is the wavelength of the X-ray radiation, and β is the full width half-maximum (FWHM) of the diffraction peak. The crystallite size is measured by the broadening of a particular planar reflection from within the crystal unit cell. It is inversely proportionally to the FWHM of the individual peak, thus, the more narrow the peak, the larger the crystallite size. In this work, X-ray diffraction analyses of the samples were carried out to determine the phase and the crystallinity of the materials.

3.3.6 Fourier transform infrared spectroscopy

It is a technique used for molecular characterisation. It is carried out based on the atom vibrations in a molecule. It involves the determination of the functional groups present in the materials. Here molecules absorb light in the infrared region of the electromagnetic spectrum. The radiation is passed through a sample and the fraction of incident radiation absorbed is determined at a specific energy. The energy where the absorption peak appears is related to the vibration frequency of a part of the molecule of the material [10]. In other words, the absorbed light corresponds to the organic functional group or bond present in the molecules. These chemical bonds tend to stretch, contract and bend. The frequency range typically measured for samples are between wave numbers 4000 cm^{-1} - 400 cm^{-1}. This implies that functional groups tend to adsorb infrared radiation in a specific wavenumber range regardless of the structure of the rest of the molecule. The correlation of the band wavenumber position with the chemical structure is then used to identify a functional group in a sample. FTIR spectra were obtained with Perkin Elmer Series 100 spectrum.

3.3.7 UV-Visible spectrophotometry

UV-Visible spectrophotometry involves the investigation of absorption properties of various materials such as chromophores in the UV-Visible region from 180 nm-800 nm.

The bonding and non-bonding molecular oritals tend to absorb electromagnetic radiations (*hv*) at certain wavelength and get excited when a beam of light is passed through any chromophore. This leads to absorption bands that are characteristic features of that molecule [11]. It is employed for the qualitative and quantitative analysis of materials. The wavelength of absorption provides qualitative information on the structure of the molecule in the material while the extent is related to the amount of the molecule absorbing the radiations. The quantitative calculation of the absorbance is based on the Lambert-Beer Law:

$$A = \varepsilon cL \qquad [3.2]$$

Here, A is the absorbance estimated as $A = \log_{10}(I_0/I)$ in which I_0 is the intensity of the incident light, I is the intensity of the emitted light., A is the molar absorbance c is the concentration in molarity of the sample/compound in the solution, and L is the path length of light in the sample. Due to the linear relationship existing between the absorbance and the substance concentration, the concentration of unknown material can be evaluated using the UV-Visible spectroscopy. In this work, Cary 60 UV-Visible spectrophotometer (Agilent technologies, USA) was used to monitor the concentration of the pollutants in the degradation processes.

3.3.8 Diffuse reflectance spectroscopy (DRS)

Diffuse reflectance spectroscopy (DRS) is a technique used for the analysis of powdered materials. It involves the characterisation of the absorption maxima of the solid nanoparticles such as semiconductors. The absorbed light results in electronic transitions in the material which makes light to be absorbed or re-emitted by the material, and thus help to elucidate the structure of the material. Semiconductor crystallites with diameters in a few nanometers range show a 3D size effect in their electronic structure. The material under investigation is mixed with potassium bromide which does not absorb radiations, and and the mixture is employed for the estimation of the band-gap energy and the absorption [12]. The diffuse reflectance of the sample is dependent on its particle size as well as its refractive index [13]. In this work, UV-Visible diffuse reflectance spectroscopy was employed in determining the band gap (Eg) based on the equation;

$$Eg = 1239/\lambda_{edge} \qquad [3.3]$$

Where λ_{edge} is the wavelength of the absorption edge [14]. The spectra from the UV absorbance were done at a wavelength of 200–800 nm with Shimadzu UV-2450 (Japan).

3.3.9 Brunauer, Emmet and Teller (BET) analysis

BET analysis (Micromeritics 3000) on the samples was carried out to determine their specific surface areas and textural characteristics. The specific surface area of a powder is often determined by physical adsorption of a gas on the surface of a solid and also by calculating the amount of adsorbate gas corresponding to the monomolecular layer on the surface. Determination of surface and textural properties is usually carried out at the temperature of liquid nitrogen. The corresponding amount of N_2 gas adsorbed is measured by volumetric continuous flow procedure. Thus, in this work, the materials (ZnO and Pd-ZnO-EG) were analysed for their surface areas, pore volumes and sizes

3.4 ELECTROCHEMICAL TECHNIQUES

The electrochemical measurements are usually done in an electrochemical set-up which consists of a working electrode, a reference electrode, and a counter electrode as shown in Figure 3.1. The reaction under investigation takes place at the working electrode. There are various materials that have been used as working electrode and these include gold, platinum, silver and carbon substrates such as graphite, graphene, glassy carbon and diamond. The efficiency of an electrochemical analysis is dependent on the surface area and shape of the fabricated working electrode. The reference electrode is utilised to regulate the potential applied to the working electrode since the potential of the reference electrode is stable and known, while the counter electrode is employed for measurement of current response of the working electrode and this help in the stability of the electrochemical process that is taking place at the working electrode. There are several kinds of reference electrodes used in electrochemical techniques and examples include the silver/silver chloride electrode (Ag/AgCl) and the saturated calomel electrode (SCE). The counter electrode is usually a conductive material which does not react with the solution. An example is a platinum foil or wire.

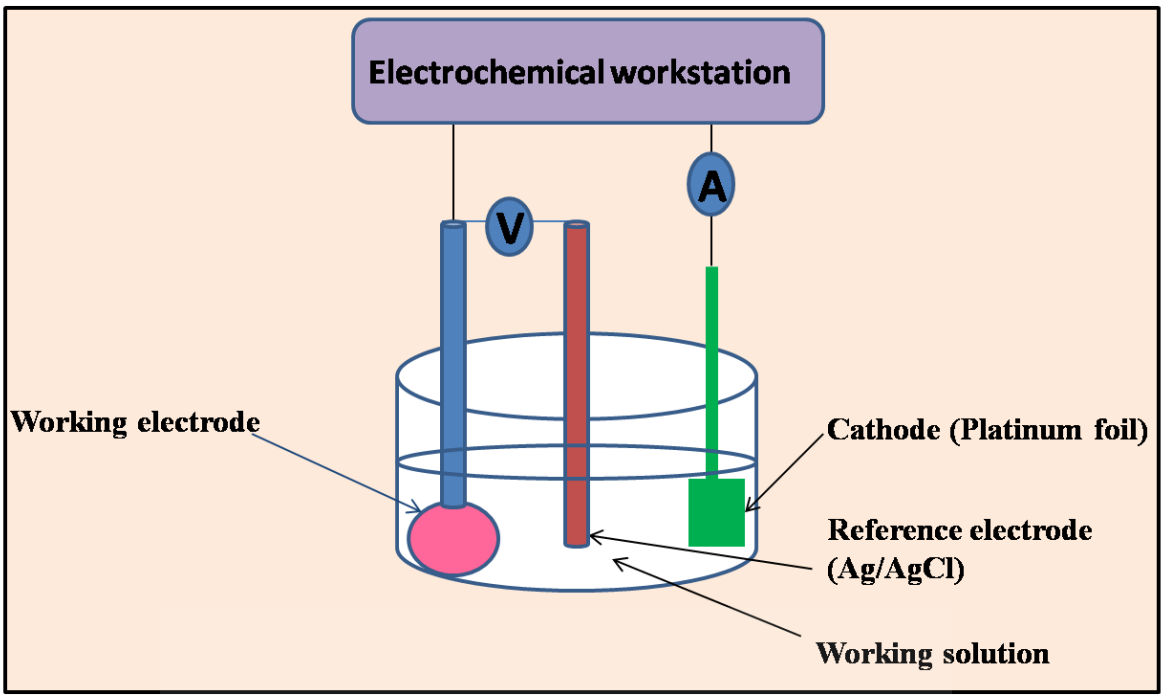

Figure 3.1: Schematic schematic representation of a three electrode system.

The electrodes are put in a solution known as an electrochemical probe and an electrolyte is added to make sure it is conductive enough for the electrochemical process. When a potential is applied, there is a flow of current from the working electrode to the counter electrode and this is measured by the potentiostat. Several electrochemical techniques need to be carried out to gain knowledge of the electrochemical activity of a working electrode and include cyclic voltammetry, electrochemical impedance spectroscopy, square wave voltammetry, etc. However, for this work, cyclic voltammetry, chronopotentiometry, chronoamperometry, and linear sweep voltammetry are discussed.

3.4.1 Cyclic voltammetry

Cyclic voltammetry (CV) could provide information on the kinetics of electron transfer, thermodynamics of redox process as well as adsorption processes. It is the most widely used technique in electrochemical measurements. This technique can be used to study the reversibility, kinetics, formal oxidation as well as reduction potentials of a system [15-19].

In a typical cyclic voltammetry analysis, the potential of an electrode is usually cycled from an initial potential, E_i to a final potential, E_f and then back to the initial potential E_i. The oxidation process normally occurs in the forward part of the cyclic voltammetry if the scanning is carried out from a negative to a positive potential, while the oxidation occurs in

the reverse part of the cyclic voltammetry, with the potential going from a positive to a negative potential. Nevertheless, if the potential is being scanned from positive to negative, the reduction process would take place in the forward part of the cyclic voltammetry scan while the oxidation process occurs in the reverse scan. Parameters such as the anodic (E_{pa}) and cathodic peak potentials (E_{pc}), denoted as and, respectively as well as anodic (I_{pa}) and cathodic peak currents (I_{pc}) are usually investigated using cyclic voltammograms for the analysis of a reversible reaction properties as well as those of an electroactive material. Cyclic voltammetric processes could be reversible, quasi-reversible or irreversible A schematic diagram of a typical CV is shown in Fig. 3.2 with the parameters.

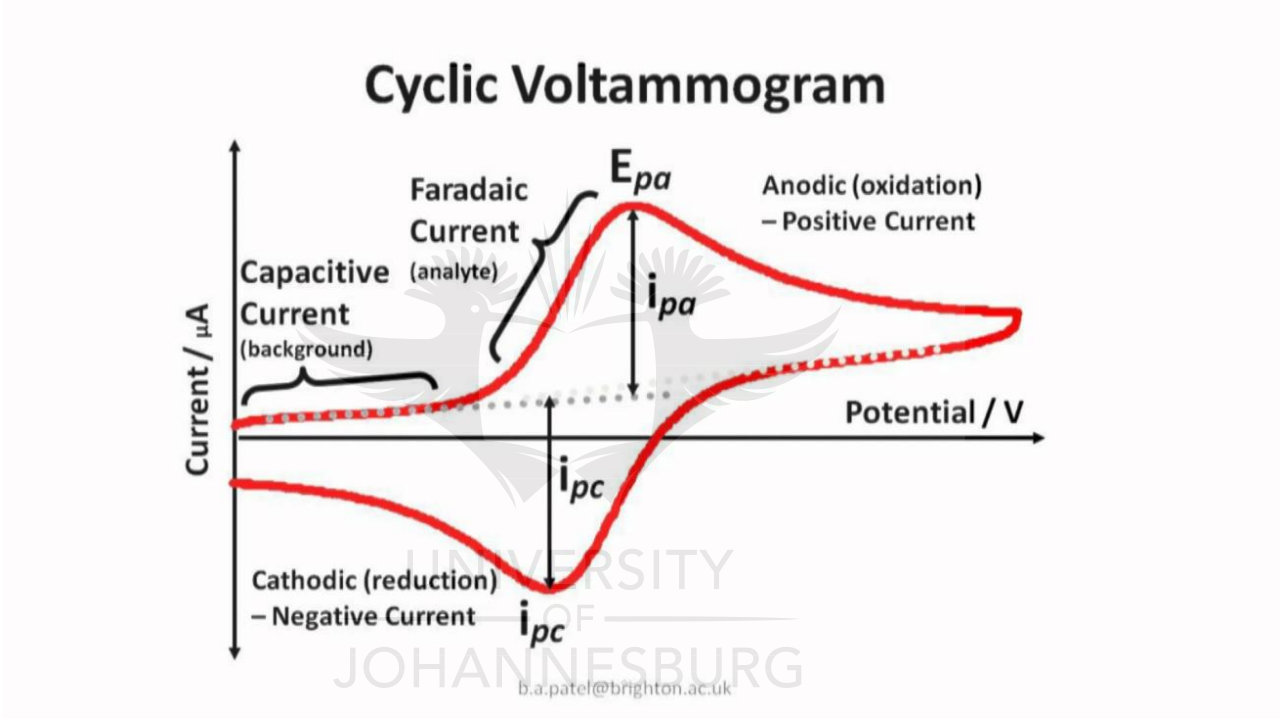

Figure 3.2: Schematic illustration of typical cyclic voltammogram

Reversible process is based on the assumption that the concentrations of the oxidised (Ox) and the reduced species (Re) are in a state of equilibrium with a rapid transfer of electrons, thus obeying the Nernst equation.

$$Ox + ne^{-} \leftrightarrow \mathrm{Re} \qquad [3.4]$$

In this case, the electroactive species are stable and as a result the values of I_{pc} and I_{pa} are the same. Also, they are proportional to the concentrations of the active species. For a reversible process, the half-wave potential ($E_{1/2}$) is equal to the formal potential ($E^{o'}$) which is related to the standard potential (E^{o}) as given by the equation [3.5]:

$$E_{1/2} = E^{\circ'} = E^{\circ} + \frac{RT}{2F}\ln\frac{[Ox]}{[\mathrm{Re}]} \qquad [3.5]$$

Where F is the Faraday constant (96,485C mol^{-1}), F is the Faraday constant (96,485C mol^{-1}), R is the gas constant (8.314 J mol^{-1} K^{-1}), [Ox] is the concentration of the oxidised species (mol L^{-1}), and [Re] is the concentration of reduced species (mol L^{-1}). The formal redox potential, $E^{o'}$ can be estimated using equation [3.6]:

$$E^{\circ\prime} = \frac{E_{pa} + E_{pc}}{2} \qquad [3.6]$$

Where E_{pc} is the cathodic peak potential and E_{pa} is the anodic peak potential. The number of electrons transferred, *n*, in a reversible process can be calculated using equation [3.7] as a criterion for Nernstian behaviour.

$$\Delta E = E - E = 2.03\frac{RT}{nF} = \frac{0.059V}{n} \qquad [3.7]$$

It implies that for a reversible one-electron process, the peak-to-peak separation assumes different values which are dependent on the temperature [20]. Thus, when the value of ΔEp is estimated, a deviation of about 10 – 20 mV from the theoretical value does not affect the criterion for reversibility, particularly when high scan rates are used. This is because the presence of solution resistance will tend to shift the forward and backward peaks system, and increase the relative value of ΔE if compensation is not adequately made for it by the electrochemical instrumentation [20]. At room temperature, the peak current of a reversible process is given by the Randles-Sevcik equation [20]:

$$i_p = (2.69x10^5)n^{3/2}AC(Dv)^{1/2} \qquad [3.8]$$

Where i_p is the peak current, n is the number of electrons, A is the area of electrode in cm^2, C is the concentration in mol cm^{-3}, D is the diffusion coefficient given in cm^2 s^{-1} and v is scan rate (V s^{-1}).

The plot of the peak current versus the square root of the scan rate (I_p as the y-axis and $v^{½}$ as the x-axis) which is known as the Randles- Sevcik plot, gives a straight line passing through the origin. The slope of this linear plot can be employed for the estimation of the concentration of the analyte if the diffusion coefficient, *D,* is known. Other variables can

be calculated using the Randles-Sevcik equation. If the peak current (I_p) at a particular scan rate (v) is measured, and the area of the electrode (A), the diffusion coefficient (D) and the concentration (C) of the analyte under investigation are given, the number of electrons (n) taking part in the redox change can be estimated. In the same vein, if the number of electrons (n) is known, then the diffusion coefficient (D) of the species as well as other variables can be calculated. In addition, the plot of the log of peak current against the log of scan rate will give a linear plot where the slope differentiates between the diffusion controlled peaks, adsorption controlled peaks or a mixture of both. A slope of 0.5 means that the process is diffusion controlled peak while a slope of 1 is for an adsorption peak. Also, when an intermediate value of the slope (0.5-1) is obtained, it indicates that there is a mixed mechanism (diffusion-adsorption) [21].

Quasi-reversible process is an intermediate process between a reversible and an irreversible system. In quasi-reversible process, the c current generated is influenced by mass transport and charge transfer kinetics [22]. It occurs when the Nernst equilibrium at the surface of the electrode cannot be maintained by the relative rate of electron transfer with respect to that of mass transport. For quasi-reversible process, I_p increases as $v^{1/2}$ increases but it does not occur in linearly and $\Delta E > 59/n$ mV increases as v is increasing.

Irreversible process is a process where there is either a forward oxidation or reduction peak but a weak reverse peak could be observed in some cases. This is as a result of the slow electron exchange or slow chemical reactions at the surface of the electrode [23]. Generally, Nernst equation is not followed in this process because the rate of electron transfer is not adequate for the maintenance of the surface equilibrium, and consequently, the oxidised [O] and reduced [R] species are not at equilibrium. Thus in this research, cyclic voltammetry was employed to study the electrochemical behaviour of some analytes with respect to the electrode materials.

3.4.2 Chronoamperometry

This technique involves the stepping of the potential of the working electrode and the current which results from the faradic processes that take place at the electrode due to potential step is monitored with respect to time [24]. During chronoamperometric measurements, the potential is stepped from E_1, where there is no flow of current; where the oxidation or reduction of the electrochemically active species does not take place to E_2

where the current is attributed to the electrode reaction as presented in Fig. 3.3. This current-time dependence can be monitored (Fig. 3.3b) using the Cottrell equation [24]:

$$i(t) = \frac{nFAcD^{1/2}}{\pi^{1/2} t^{1/2}} = kt^{-1/2} \qquad [3.9]$$

Where F is the Faraday constant; A is the area of electrode, C is the solution concentration, t is time, and D is the diffusion coefficient of solution, n is the number of electrons involved in the reaction and k is the rate constant.

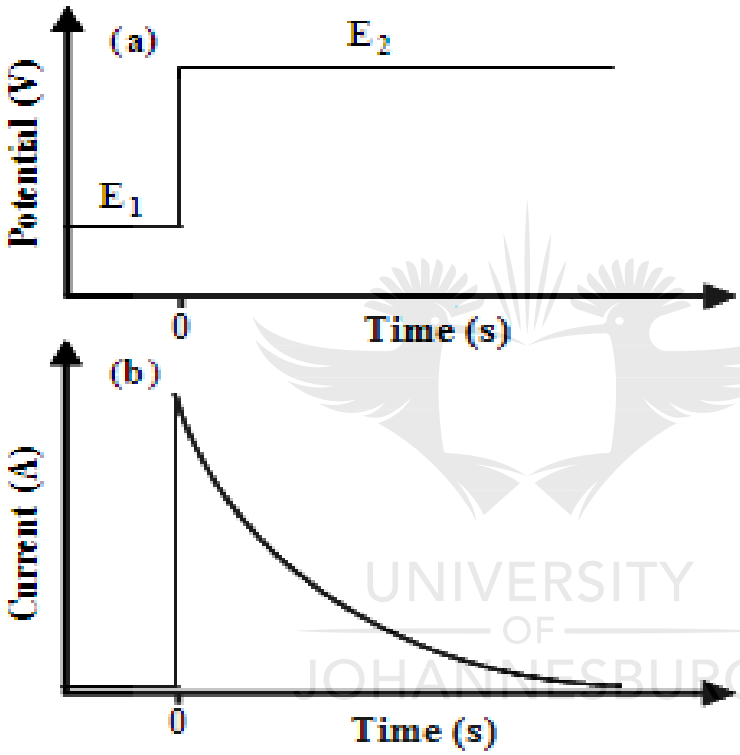

Figure 3.3: Typical chronoamperometric (a) potential-time waveform and (b) resultant current-time response.

The current time curve is a representation of the change in concentration gradient at the vicinity of the surface. It is a slow expansion of the diffusion layer that is linked with the reduction of the reactant as time increases. As a result, there is a decay of current with time. This process provides a very good signal to noise ratio because the current is integrated over longer time intervals. Also, it is mostly used for bulk electrolysis where the current is monitored over a long period of time. Hence, in this work, chronoamperometry was used for bulk electrolysis of the selected pollutants.

3.4.3 Chronopotentiometry

Chronopotentiometry requires the application of a constant current to the working electrode and the generated potential is measured with respect to time. The first plateau that appears is the potential that is needed to oxidise the substrate which have the lowest standard potential (that is, the flat part of the curve for the period of time that the anode has charged). The potential will be constant for the oxidation potential of the substrate pending when the concentration at the surface of the electrode moves to zero. Then the potential will increase in order to oxidize the next most easily oxidizable species in solution as presented in Fig. 3.4 [24].

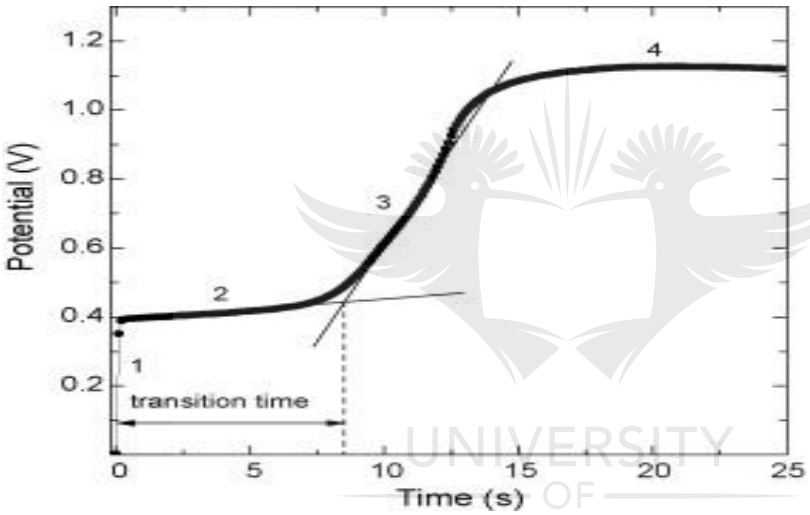

Figure 3.4: Potential-time response curve of a chronopotentiometric experiment.

For the same electrochemical reaction, the square root of electrolysis time (τ) will vary with the bulk concentration of the electroactive species when the excitation current step is allowed to be constant. The transition time is the time needed to complete the oxidation of the substrate on the surface of the microelectrode. The theoretical relationship between the applied current, i and the electrolysis time, τ is given by the Sand equation [24]:

$$i\tau^{1/2} = \frac{nFAc\pi^{1/2}D^{1/2}}{2} \qquad [3.10]$$

In equation [3.10], F is the Faraday's constant, n is the number of electrons transferred in the electrochemical reaction, D is diffusion coefficient A is the electrode area, and C is the

bulk concentration of electroactive species. In this type of measurements, the electrolysis time (τ) does not depend on the form of diffusion to the surface of the electrode, since the Sand equation is applicable for spherical and planar electrodes. Also, the ohmic drop due to solution resistance is also constant when a constant current is applied. Thus, the ohmic distortion can be corrected by a constant potential offset. Nevertheless, when a constant potential is applied like in the chronoamperometry, the current is generated, and therefore, the ohmic drop tends to vary with potential and this makes the correction to be complicated. In this research, chronopotentiometry was utilised for monitoring the bulk electrolysis of the selected pollutants.

3.4.4 Linear sweep voltammetry

This is a cyclic voltammetry that does not involve a vertex potential and a reverse scan. It involves the scanning or increasing the potential of a working electrode (which could a planar, cylindrical or spherical electrode) linearly with time at particular rates and the current is measured. A voltammogram is obtained from the plot of current as a function of potential [25].

Generally for a LSV experiment, the scan is initiated from the left hand side of the plot of the current-voltage in which there is no flow of current. There is a flow of current as the potential/voltage is swept more to the right, to a more reductive value. This current flow continues until it gets to a peak before it starts to drop. For instance, for the electrochemical reduction of iron (III) ion to iron (II) ion, there is a faster electron transfer rate when compared to the voltage sweep rate. Thus, there is an equilibrium which is established on the surface of the electrode that is the same with equilibrium that is predicted by Nernst equation that the concentration is related to the voltage/potential as shown in equation [3.11];

$$E = E^{\circ} + \frac{RT}{2F} \ln \frac{[Ox]}{[\mathrm{Re}]} \qquad [3.11]$$

It assumes that the concentrations of the oxidised (Ox) and the reduced species (Re) are in a state of equilibrium with a rapid transfer of electrons.

$$Ox + ne^{-} \leftrightarrow \mathrm{Re} \qquad [3.12]$$

Where E is is the applied potential, E^o is the standard potential, F is the Faraday constant (96,485C mol^{-1}), R is the gas constant (8.314 J mol^{-1} K^{-1}), [O] is the concentration of the oxidised species (mol L^{-1}), and [R] is the concentration of reduced species (mol L^{-1}). Sweeping the potential from V_1 to V_2 will lead to shifts in the equilibrium positions of the reactant species at the surface of the electrode, and there is a flow of current as the equilibrium is altered. There is an increase in current as the voltage sweep is increased from the initial value and the equilibrium position is shifting, thereby causing a conversion of more reactant species. The current further gets to the peak, and when the diffusion goes above the electrode at some point, it makes the reactant flux to the electrode too slow to satisfy the Nernst equation. In this case, there is drop in current just like the case of potential step measurement, and this current drop resembles that which is predicted by the Cottrell equation as stated in section 3.4.2. Altering the scan rates leads to changes in the current response as shown in Figure 3.5 which presents voltammograms using different scan rates for a solution containing iron (III) ion [25].

$$Fe^{3+} + e^- \leftrightarrow Fe^{2+} \qquad [3.13]$$

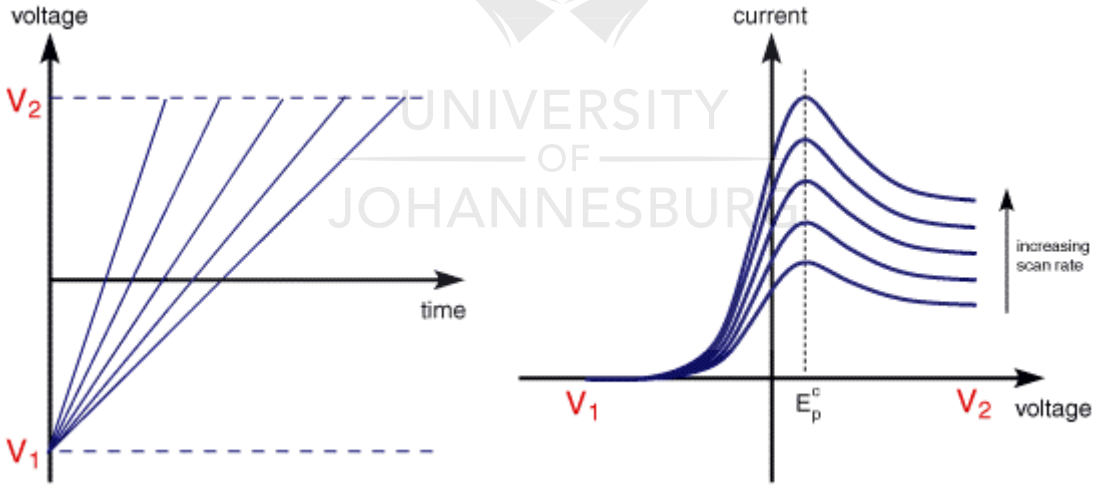

Figure 3.5: Typical linear sweep voltammograms at various scan rates

It is shown that as the scan rate increases, the recording of the linear sweep voltammograms will be taking a longer period of time. Thus, there will be a difference in the sizes for the diffusion layer above the surface of the electrode which depends on the value of the voltage/potential scan rate applied. The diffusion layer tends to grow further from the electrode for a slow voltage/potential scan when compared to a faster scan. As a

result, flux of the reactant species to the surface of the electrode is relatively smaller at slow scan rates compared to that at faster scan rates. This implies that the lower magnitude of current is obtained for lower scan rates and higher magnitude of current at higher scan rates because the current is generally proportional to the flux of the reactant species to the electrode.

3.4.5 Photoelectrochemical experiments

The photoelectrochemical experiments were conducted in a photo-reactor with an approximate volume of 100 mL which consists of quartz window for easy penetration of light. The light source was Oriel LCA-100 Solar Simulator having a 100 W xenon lamp and AM1.5G filter which produces a power beam of 100 $mWcm^{-2}$ (1.0 sun equivalence), at a distance of 8 cm from the reactor. A potentiostat/galvanostatic with a voltage range of 1 V- 3 V and a current density range of 1 mA–15 mA was utilised as the source of power supply for the electrochemical degradation of the target pollutants in 0.1 M sodium sulphate as the supporting electrolyte. The electrodes (1.3 cm in diameter) were used as working electrodes, Ag/AgCl (3.0M KCl) as reference electrodes and platinum foil as a counter electrode. Aliquots of the solution were collected at certain intervals from the photoreactor with the aid of a disposable syringe and filtered over a period of time. The electrodes were fixed vertically facing the incident light of the simulator. For the electrochemical degradation of the pollutants, only current density/potential was applied without the use of light.

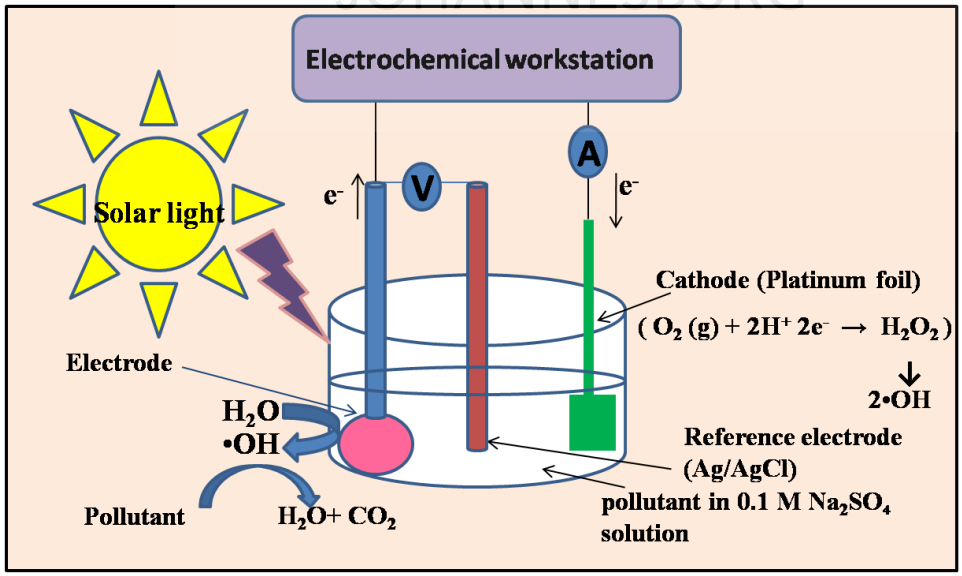

Figure 3.6: Schematic presentation of a photoelectrochemical setup.

3.5 TOTAL ORGANIC CONTENT (TOC) ANALYSER

Total Organic Carbon (TOC) analyser (Shimadzu TOC 5000 A) was used in this work to measure the extent of mineralisation of the pollutants during the degradation processes. It involves the total measure of the concentration of all the organic carbon atoms that are covalently bonded in the organic matter in water which consists of thousands of components. These include dissolved macromolecules, macroscopic particles, colloids, and specific organic compounds. It is estimated in parts per million (ppm or mgL^{-1}), although it can be expressed in lower measurements like parts per billion (ppb or μgL^{-1}) or parts per trillion (ppt). Suince it is a sum measurement, it does not identify specific organic contaminants. However, it can detect the presence of all the molecules having carbon atoms and as such, it helps to identify the presence of any organic contaminants irrespective of the molecular composition.

Generally, there are two types of carbons that are present in water samples. These are the total organic carbon (TOC) and the inorganic carbon (IC). Organic carbons are the carbon atoms which form bonds with hydrogen or oxygen to give organic compounds. The two forms of carbons are known as the total carbon (TC) and the relationship between them is given as:

$$TOC = TC - IC \qquad [3.14]$$

TOC analyzer makes use of a carrier gas (oxygen) which flows through the total carbon (TC) combustion tube that is packed with catalyst and kept at 680 °C. After the acidification of the sample under investigation, sparge gas is bubbled through the sample in order to eliminate the inorganic carbon component. The carrier gas contains the combustion products which come from the total carbon combustion tube and it flows through the inorganic carbon reaction vessel, dehumidifier, halogen scrubber and then it gets to the sample cell of the non-dispersive infrared (NDIR) detector which measures the carbon dioxide content [26, 27]. The output signal which is the analog of the NDIR detector is displayed as peaks. The peak area is proportional to the total carbon concentration of the sample. Generally, the estimated total carbon is known as the TOC which represents the non-purgeable organic carbon and refers to organic carbon present in a sample in a non-volatile form. The total carbon in an organic sample could be easily measured from the calibration curve that is prepared with standard solutions of known

carbon content since the peak areas are proportional to the concentration of the total carbon.

3.6 REFERENCES

[1] H.L. Poh, F. Šaněk, A. Ambrosi, G. Zhao, Z. Sofer, M. Pumera, Graphenes prepared by Staudenmaier, Hofmann and Hummers methods with consequent thermal exfoliation exhibit very different electrochemical properties, Nanoscale, 4 (2012) 3515-3522.

[2] J. Zhang, H. Yang, G. Shen, P. Cheng, J. Zhang, S. Guo, Reduction of graphene oxide via L-ascorbic acid, Chemical Communications, 46 (2010) 1112-1114.

[3] T. Ndlovu, B.B. Mamba, S. Sampath, R.W. Krause, O.A. Arotiba, Voltammetric detection of arsenic on a bismuth modified exfoliated graphite electrode, Electrochimica Acta, 128 (2014) 48-53.

[4] B. Ntsendwana, B.B. Mamba, S. Sampath, O.A. Arotiba, Synthesis, characterisation and application of an exfoliated graphite–diamond composite electrode in the electrochemical degradation of trichloroethylene, RSC Advances, 3 (2013) 24473-24483.

[5] J.I. Goldstein, Scanning electron microscopy and x-ray microanalysis, (1979).

[6] R.F. Egerton, Physical principles of electron microscopy, Springer2005.

[7] L. Reimer, Electron scattering and diffusion, Scanning Electron Microscopy, Springer1998, pp. 57-134.

[8] G.D. Christian, J.E. O'Reilly, Instrumental analysis, (1988).

[9] P. Franklyn, J, Preparation and characterisation of novel titanium-tungsten oxides, University of Cambridge, Certificate postgraduate studies in chemistry dissertation (2005).

[10] B. Stuart, B. George, P. McIntyre, Modern infrared spectroscopy applied to soil humic substances chemistry, Science of the Total Environment, 117 (1996) 41-52.

[11] L.D. Field, S. Sternhell, J.R. Kalman, Organic structures from spectra, John Wiley & Sons2012.

[12] A. Murphy, Band-gap determination from diffuse reflectance measurements of semiconductor films, and application to photoelectrochemical water-splitting, Solar Energy Materials and Solar Cells, 91 (2007) 1326-1337.

[13] J.D. Lindberg, D.G. Snyder, Determination of the optical absorption coefficient of powdered materials whose particle size distribution and refractive indices are unknown, Applied optics, 12 (1973) 573-578.

[14] W. Weng, M. Ma, P. Du, G. Zhao, G. Shen, J. Wang, G. Han, Superhydrophilic Fe doped titanium dioxide thin films prepared by a spray pyrolysis deposition, Surface and Coatings Technology, 198 (2005) 340-344.

[15] A.J. Bard, L.R. Faulkner, J. Leddy, C.G. Zoski, Electrochemical methods: fundamentals and applications, wiley New York1980.

[16] M.J. Brown, J. Raymond, D. Homa, C. Kennedy, T. Sinks, Association between children's blood lead levels, lead service lines, and water disinfection, Washington, DC, 1998–2006, Environmental research, 111 (2011) 67-74.

[17] D.B. Hibbert, Introduction to electrochemistry, Introduction to electrochemistry, Springer1993, pp. 1-10.

[18] A.E. Kaifer, M. Gómez-Kaifer, Supramolecular electrochemistry, John Wiley & Sons2008.

[19] J. Randles, A cathode ray polarograph, Transactions of the Faraday Society, 44 (1948) 322-327.

[20] P. Zanello, Inorganic electrochemistry: theory, practice and application, Royal Society of Chemistry2007.

[21] D.K. Gosser, Cyclic voltammetry: simulation and analysis of reaction mechanisms, VCH New York1993.

[22] J. Wang, Analytical electrochemistry, John Wiley & Sons2006.

[23] P. Kissinger, W.R. Heineman, Laboratory Techniques in Electroanalytical Chemistry, revised and expanded, CRC press1996.

[24] H.H. Girault, Analytical and physical electrochemistry, CRC Press2004.

[25] P. Andricacos, H. Cheh, The application of linear sweep voltammetry to a rotating disk electrode for the reversible deposition of an insoluble species, Journal of The Electrochemical Society, 127 (1980) 2153-2157.

[26] I. Bisutti, I. Hilke, M. Raessler, Determination of total organic carbon–an overview of current methods, TrAC Trends in Analytical Chemistry, 23 (2004) 716-726.

[27] J.N.G. Paniz, É.M. Flores, V.L. Dressler, A.F. Martins, Flow injection turbidimetric determination of total organic carbon with a gas–liquid transfer microreactor, Analytica chimica acta, 445 (2001) 139-144.

CHAPTER 4

PHOTOCATALYTIC DEGRADATION OF ACID BLUE 74 IN WATER USING Ag-Ag_2O-ZnO NANOSTRUCTURES ANCHORED ON GRAPHENE OXIDE[1]

4.1 INTRODUCTION

Access to clean water has been a challenge in most developing regions of the world. The intake of contaminated or polluted water, especially in rural areas, has led to many avoidable deaths [1, 2]. Organic dyes are a notable class of organic water pollutants, and dye-containing effluents from industries (especially textile) constitute a major environmental and health challenge [3]. Some organic dyes in water are very difficult to remove during water treatment by the conventional treatment methods and systems [4-6]. The water quality degradation, health risk and recalcitrant behaviors posed by organic dyes during conventional water treatment necessitate the need to develop alternative (and complementary) methods for their removal. In recent years, advanced oxidation processes (AOPs) have emerged to be efficient and effective methods for the treatment of dye wastewaters [7]. They are utilized for the removal of organic pollutants during water treatment due to the generation and use of hydroxyl radicals as oxidizing species which initiate other reactions for the degradation and possibly mineralization of organic pollutants such as dyes [8].

Among the AOPs, heterogeneous photocatalysis has attracted attention as a promising technique for solving environmental problems especially in the degradation of organic pollutants in water treatment [9]. Heterogeneous photocatalysis is a process that occurs when a semiconductor absorbs a photon of energy greater than its band gap (the region between the electron-fill valance band and the empty conduction band of a semiconductor), and an electron is excited to the conduction band thereby creating a hole in the valence band. The generation of the electrons could lead to oxidation and reduction reactions on the surface of the semiconductor. In both reactions, hydroxyl radicals are produced and these radicals react with the molecules of the organic pollutants repeatedly to degrade and possibly mineralize them into less toxic and simpler substances such as N_2, CO_2 and H_2O [8].

[1] This chapter has been published in: Umukoro, E. H.; Peleyeju, G.; Ngila, J. C.; Arotiba, O. A. Photocatalytic Degradation of Acid Blue 74 in Water Using Ag-Ag_2O-ZnO Nanostuctures Anchored on Graphene Oxide. *Solid State Sciences*. **2016**, 51, 66-73

ZnO has been reported as a suitable photocatalyst for the degradation of organic pollutants in water treatment because of its availability, low cost, good optoelectronic nature, chemical inertness, non-toxicity, and photochemical and catalytic properties [9-13]. It is an n-type semiconductor with a wide band gap of 3.37 eV and a high exciton bound energy of 60 meV at room temperature [14]. However, there are some limitations associated with ZnO such as the recombination of the photogenerated holes and electrons, and narrow light absorption range [15]. In order to solve these problems, several materials such as silver compounds have been employed to dope this semiconductor [11].

Ag_2O is a p-type semiconductor with a narrow band gap of 1.46 eV and it is a suitable catalyst for industrial applications because of its cost effectiveness, ease of preparation, non-toxicity and high efficiency [16-18]. The formation of a p-n heterojunction between Ag_2O and ZnO can help to enhance interfacial electron transport, and consequently, minimize the electron-hole pair recombination. In addition, Ag_2O can act as a photosensitizer under solar light due to its lower band gap compared to ZnO and thus improving the photocatalytic performance of ZnO under visible light [9, 17]. The introduction of metallic Ag into ZnO has been found to improve its visible light absorption as a result of surface plasmon resonance effect of Ag. In addition, Ag can act as an electron sink for the photogenerated electrons [19]. This allows the production of more hydroxyl radicals by the holes and eventually enhances the photocatalytic process [13].

Graphene composes of sp^2-bonded carbon atoms having a two dimensional planar honeycomb lattice with unique properties such as high surface area, high mechanical and thermal stabilities, high thermal conductivity and outstanding electron mobility [15, 20]. It has been reviewed that the Dirac cone of its band structure encourages the mobility of both holes and electrons [15]. As a result, the photogenerated electrons and holes from ZnO can be transferred to the graphene, thus, reducing the rate of recombination of the electron-hole pairs and improving the photocatalytic performance of ZnO.

Owing to the unique properties (especially excitation and electron mobility) of ZnO, Ag, Ag_2O and graphene highighted above, it is envisaged that a composite of these materials may enhance the photoactivity of ZnO. To the best of our knowledge, $Ag/Ag_2O/ZnO$/graphene oxide nanocomposites have not been reported for the photocatalytic degradation of pollutants such as dyes. Thus, in this work,

$Ag/Ag_2O/ZnO$/graphene oxide nanocomposites was synthesized, characterized and applied photocatalytically for the degradation of acid blue 74 in water treatment.

4.2 EXPERIMENTAL PROCEDURE

4.2.1 Materials and apparatus

Natural graphite flakes, sulphuric acid (98%), sodium nitrate, potassium permanganate ($KMnO_4$), hydrogen peroxide (H_2O_2), zinc nitrate hexahydrate ($Zn(NO_3).6H_2O$), silver nitrate ($AgNO_3$), potassium hydroxide (KOH), Acid blue 74 (Indigo carmine), 3-aminopropyltriethoxysilane (APTES), dimethylsulphoxide (DMSO), ethanol, oxalic acid, and hydrobromic acid (HBr) were purchased from Sigma Aldrich, Germany, and they were of analytical grade without further purifications.

The ZnO, graphene oxide and the composites were characterized using x-ray diffractometer (Rigagu Ultima IV, Japan) at 40 kV and 30 mA with Cu Kα radiation (λ=0.15406) with K-beta filter. It was done with the aid of a scintillation counter ranging from 5-90º at a speed of a 2º /min. The surface morphology of the materials were obtained using transmission electron microscopy (JEOL 2100 HRTEM 200 V, Japan), scanning electron microscopy (SEM) (TESCAN, Vega 3 XMU, Czech Republic) and the surface elemental composition was determined using energy-disperse x-ray spectrometer (EDS) (TESCAN, Czech Republic) attached to the SEM. Spectroscopic studies were carried out using Perkin Elmer FTIR spectrometer (Spectrum 100, USA) and Perkin Elmer Raman microscope (Raman micro 200, USA) to obtain the FTIR and Raman spectra, respectively. All characterizations were carried out in the University of Johannesburg, South Africa.

4.2.2. Preparation of graphene oxide (GO)

Graphene oxide was prepared by a modified Hummer's method [21]. Briefly, 5 g of graphite flakes, 2.5 g of sodium nitrate and 115 mL of surphuric acid were mixed and stirred. The mixture was then cooled using an ice-bath. 15 g of potassium permanganate was added to the mixture for a period of 2 h. The mixture was allowed to cool to room temperature and then heated to 35 ºC for 30 min. It was then poured into a flask which contained 250 mL of de-ionized water and heated to 70 ºC. Maintaining the temperature for about 15 min, the mixture was poured into 1 L of de-ionized water. Then, 30 mL of 3% hydrogen peroxide was added to the mixture to remove unreacted $KMnO_4$ and Manganese

dioxide. The mixture was washed several times by centrifugation and filtration using de-ionized water until a pH of 6 was obtained. The obtained graphite oxide was then ultrasonicated for 2 h to give graphene oxide, and then dried in an oven at 60 ºC for 48 h before use.

4.2.3. Preparation of carboxylated graphene oxide (GO-COOH)

Carboxylated GO was prepared as described by Tang et al. [22]. A suspension of 50 mg of GO dispersed in 30 mL de-ionized water was prepared by ultrasonication. Then 5 mL of HBr was added to the mixture and stirred vigorously for 12 h, followed by the addition of 1.5 g of HOOC-COOH and stirring for 4 hours. The mixture was filtered and then dried at 50 ºC for 24 h in a vacuum.

4.2.4. Preparation of Ag-Ag_2O-ZnO composite

The Ag-Ag_2O-ZnO composite was prepared by a modified method described by Li H. et al. [23]. Briefly, 14.87 g of zinc nitrate hexahydrate and 0.149 g of silver nitrate were dissolved in 100 mL of de-ionized water, followed by the drop-wise addition of 3 M KOH under vigorous stirring until the pH of the solution increased to 10. The viscosity of the mixture was found to be increasing with increase in the KOH solution. The mixture was stirred for 2 h at a very high speed and irradiated with 150 W ozone free xenon lamp for 2 hours to reduce Ag^+ to Ag^0 by photochemical decomposition of Ag_2O. The distance between the lamp and the reactor was 10 cm. The obtained precipitate was centrifuged, washed with de-ionized water several times and ethanol. It was further dried in an oven at 60ºC overnight and calcined at 400 ºC for 2 h. The ZnO was prepared in a similar way without the addition of silver nitrate and irradiation respectively.

4.2.5. Amine functionalized Ag-Ag_2O-ZnO

Functionalization was carried out by a modified co-condensation reaction [24, 25] using 3-aminopropyltriethoxysilane. 0.5 g of Ag-Ag_2O-ZnO was dispersed in DMSO (50 mL) by sonication for 1 h. The mixture was then transferred into a round bottom flask which was attached to a reflux condenser. 400 µL of 3-APTES was added to the mixture and refluxed at 120 ºC for 3 h. The resultant nanoparticles was centrifuged at 7500 rpm for about 30 min and washed several times with ethanol so as to remove any unreacted 3-APTES. The product was then dried at 60 ºC overnight before use.

4.2.6. Preparation of Ag-Ag_2O-ZnO/GO nanocomposite

The synthesis of Ag-Ag_2O-ZnO/GO nanocomposite was carried out by the formation of an amide bond between the NH_2 of the amine-functionalized Ag-Ag_2O-ZnO and the COOH of the carboxylated GO [15]. Briefly, 10 mg of GO-COOH was dispersed in 30 mL of de-ionized water that contained 50 mg of EDC.HCL and 32 mg of NHS, followed by sonication for 2 h. 500 mg of Ag-Ag_2O-ZnO-NH_2 was added to the mixture and allowed to react for 24 h under stirring at room temperature. The product obtained was washed with de-ionized water and ethanol by centrifugation and then dried at 60 ºC for 2 h under vacuum before use.

4.2.7. Evaluation of photocatalytic activity

The visible light photocatalytic activity of the materials was evaluated for the degradation of acid blue 74 which was chosen as a target pollutant for a period of 210 min. 100 mL of an aqueous suspension containing 0.1 g of Ag-Ag_2O-ZnO/GO nanocomposite and acid blue 74 (20 mgL^{-1}) was prepared and stirred magnetically in the dark for 30 min to reach an adsorption-desorption equilibrium. Then the suspension was irradiated with a simulated solar light at room temperature. The light was filtered with a dichroic UV filter ($\lambda > 420$ nm). The source of radiation was a New Port Solar Simulator equipped with 150 W ozone free xenon lamp which produces a collimated beam of 33 mm diameter (equivalent to 1.3 sun). This was used to emulate the sun's energy. The distance between the simulator and the reactor is 10 cm so as to produce a beam power equivalent to 1 sun. It was used for the photodegradation and kinetic studies of the target pollutant. At 30 min intervals, 5 mL aliquots of the suspension were withdrawn, and filtered using a disposable syringe and a 0.4 µm PVDF filter. The concentration of the acid blue 74 in the supernatant solution was measured using Cary 60 UV-Visible spectrophotometer (Agilent technologies, Australia) at $\lambda = 610$ nm as a function of degradation.

4.3 RESULTS AND DISCUSSION

4.3.1. Raman spectroscopy

Raman spectroscopy was carried out to show the formation of GO and the structural changes that occurred after the addition of the metal oxides nanostructures. Fig 4.1 (expanded in inset) shows the Raman spectrum of GO before the formation of the

nanocomposite. The Raman spectrum displays two peaks at ~1600 and ~1350 cm^{-1} which corresponds to the G and D bands of GO respectively. The G band is due to the in-plane phonon vibration mode of the sp^2-bonded carbon atoms in graphene while the D band is due to defects or disorder in the hexagonal graphitic sheets resulting from the intercalation of oxygen-containing functional groups or presence of sp^3 bonding [20, 26]. In the Raman spectra of the Ag-Ag_2O-ZnO/GO, the peaks at 370, 450 and 570 cm^{-1} correspond to A_1 (TO), E_2 and E_1 (LO) modes of ZnO structure respectively. In addition, the presence of E_1 (LO) mode is attributed to the local vibration of impurities. This implies that there can be formation of defects in ZnO as the growth time increases [27]. The reduction in intensities of the D and G bands observed in the Raman spectrum of Ag-Ag_2O-ZnO/GO is as a result of the dilution effect upon the addition of Ag-Ag_2O and ZnO nanoparticles on the surface of the graphene sheets of the GO [20].

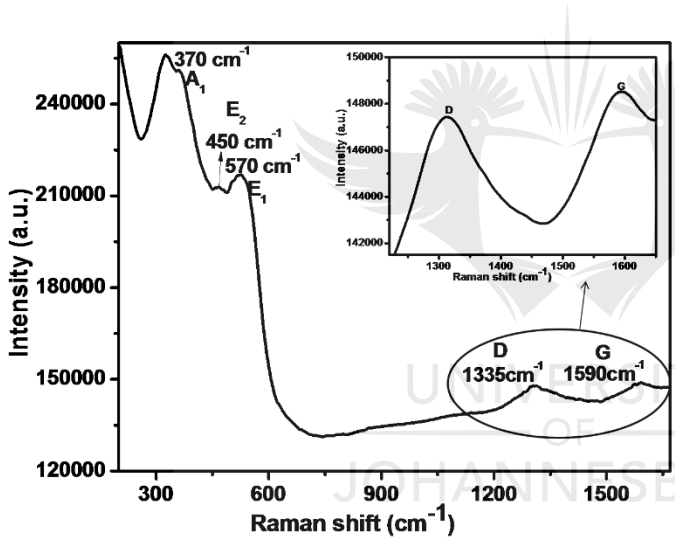

Figure 4.1: Raman spectrum of Ag-Ag_2O-ZnO/GO

4.3.2 XRD Analysis

XRD studies were carried out on the as-prepared materials as presented in Fig 4.2. Fig.4.2a shows the observed diffraction peaks for GO at 2θ = 11º (002) and 42º (100) crystal planes. The diffraction peaks of a typical hexagonal wurzite structure of ZnO (Fig. 2b) were observed at 31.9º (100), 34.6º (002), 36.4º (101), 47.7º (102), 56.7º (110), 63.0º (103), 66.5º (200), 68.1º (112), 69.2º (201), 72.6º (004), 77.1º (202) and 81.5 (104) (JCPDS Card no. 36-1451). The additional peaks of low intensities that are seen in Fig.4.2c at 38.1º (111), 44.2º (200), and 65.5º (220) confirmed the presence of Ag in the as-prepared Ag-

Ag_2O-ZnO composite (JCPDS Card no. 04-0783). Also, the peaks at 38.1º (200) and 55.0º (220) can be assigned to the crystal planes of Ag_2O (JCPDS Card no. 41-1104). Thus, Fig.4.2c confirms the co-existence of Ag and Ag_2O in Ag-Ag_2O-ZnO composite. In Fig.4.2d, the peaks at (100), (002), and (101) crystal planes of ZnO became broadened and reduced in intensities due to little destruction of the crystalline structure of ZnO in the nanocomposite. This destruction is as a result of the distortion caused by the introduction of Ag and GO [28]. The disappearance of GO peaks at 11º (002) and 42º (100) after the addition of Ag-Ag_2O and ZnO nanoparticles was due to the destruction of the regular stack of GO [13]. The reduction in intensity can simply be as a result of dilution from GO and other constituent. The peak at ca 16º, which could not be assigned with certainty, may be due to impurities. GO-COOH commonly shows peaks at 2θ = 25º and 44º [26] and this could be as a result of the presence of some unreacted GO-COOH in the sample.

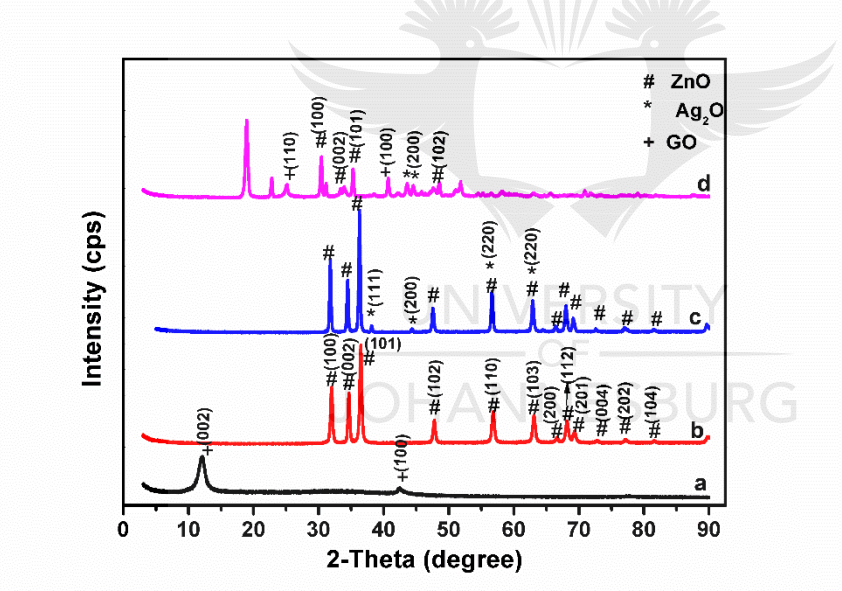

Figure 4.2: XRD patterns of (a) GO, (b) ZnO, (c) Ag-Ag_2O-ZnO, and (d) Ag-Ag_2O-ZnO/GO

4.3.3 FTIR Analysis

FTIR studies were conducted to characterize the functional groups present in the as-prepared materials. The FTIR spectra of GO, GO-COOH, Ag-Ag_2O-ZnO-NH_2 and Ag-Ag_2O-ZnO/GO are presented in Fig.4.3. In Fig.4.3a, the absorption band at 3390 cm^{-1} can be attributed to O-H stretching vibration from the hydroxyl groups in GO and the absorbed

water on the surface of the GO. The bands appearing at 1610 and 1720 cm^{-1} can be assigned to C=C bond stretching vibration and the stretching vibration of C=O bond of carboxyl group in GO respectively. The absorption peak at 1055 cm^{-1} is attributed to C-O stretching vibration which usually occurs around 1260-1000 cm^{-1}. Also, the broad and weak peak at 1228 cm^{-1} can be associated to C-O-H bending vibration (1440-1220 cm^{-1}) [22]. Fig.4.3b shows the FTIR spectra of GO-COOH. The strengthening of the peak at 3400 cm^{-1} and the peak broadening at 1700 cm^{-1} indicates the presence of more carboxylic groups [15]. This is also evident by the increase in intensity of the band at 1254 cm^{-1} attributed to C-O-H stretching vibration, suggesting more hydroxyl groups [22]. In the spectra of Ag-Ag_2O-ZnO-NH_2 (Fig.4.3c), the broad peak at 457 cm^{-1} accounts for Zn-O bond and Ag-O bond stretching vibrations. Also, the absorption peaks at 1620 and 1127 cm^{-1} are as a result of N-H bending vibration and C-N stretching vibration of amine. In addition, the absorption band at 878 cm^{-1} is associated with N-H out of plane bending vibration of amine. The broad band observed at 3497 cm^{-1} can be assigned to N-H stretching vibration of primary amine which could be overlapping with the stretching vibration of hydroxyl groups from the absorbed water on the ZnO surface [29]. These suggest that the Ag-Ag_2O-ZnO was successfully functionalized to give Ag-Ag_2O-ZnO-NH_2. Upon the addition of GO to the amine-functionalized nanoparticle, the FTIR spectra reveal the peaks at 3350, 1650, and 1390 cm^{-1} which are assigned to N-H stretching vibration amide, CO-NH stretching vibration of amide and C-N stretching vibration of amide respectively. Thus, the Ag-Ag_2O-ZnO nanoparticles were successfully anchored on the surface of GO by covalent bonding.

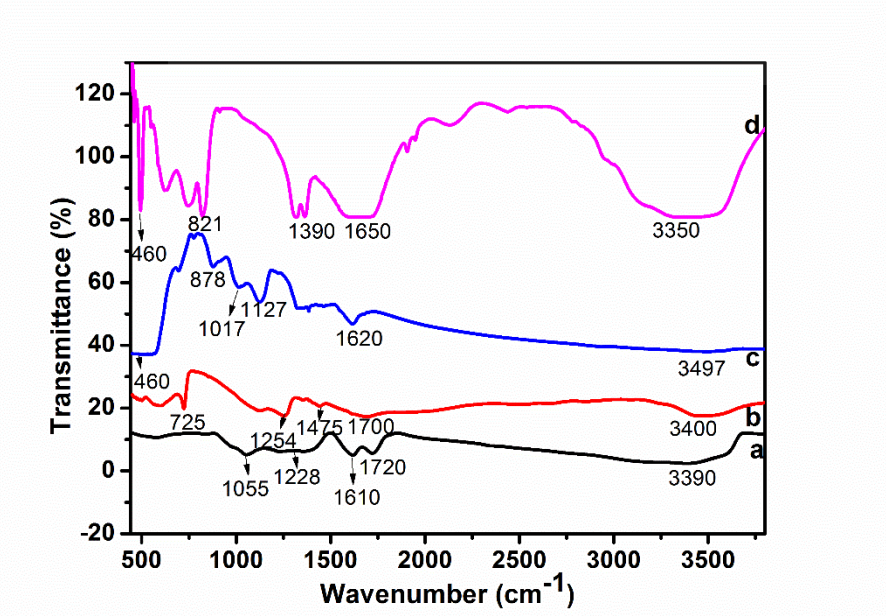

Figure 4.3: FTIR spectra of GO (a), GO-COOH (b), Ag-Ag_2O-ZnO-NH_2 (c), and Ag-Ag_2O-ZnO/GO (d)

4.3.4 SEM-EDX and TEM Analyses

The morphology and hetero-structure of the as-prepared samples were studied using scanning electron microscopy, energy dispersed x-ray spectroscopy and transmission electron microscopy. Fig. 4.4a shows that the as-prepared ZnO are uniformly distributed flower-like structures. In the case of Fig. 4.4b, there is the disappearance of the flower-like morphology, and the appearance of globular structures due to the presence of the Ag-Ag_2O nanoparticles which are evenly fused with the ZnO nanoparticles. Fig. 4.4c shows the SEM result of GO having several layers of sheets. The TEM results showed that the Ag-Ag_2O-ZnO nanoparticles were successfully anchored on the GO sheets (Fig. 4.4d). The TEM result revealed irregular sizes of the as-prepared nanocomposite ranging from 29.66 nm to 42.65 nm. Furthermore, Energy dispersive X-ray spectroscopic study was carried out to establish the elemental composition of the as-prepared Ag-Ag_2O-ZnO/GO. Fig. 4.4e shows the EDX spectrum of the as-prepared Ag-Ag_2O-ZnO/GO composite having C, O, Zn and Ag. The low intensity of Ag shows the presence of a very small percentage of Ag_2O (0.48%) compared to ZnO (36.06 %) and GO (63.46 %) in the Ag-Ag_2O-ZnO/GO nanocomposite (inset of Fig. 4.4e).

a) 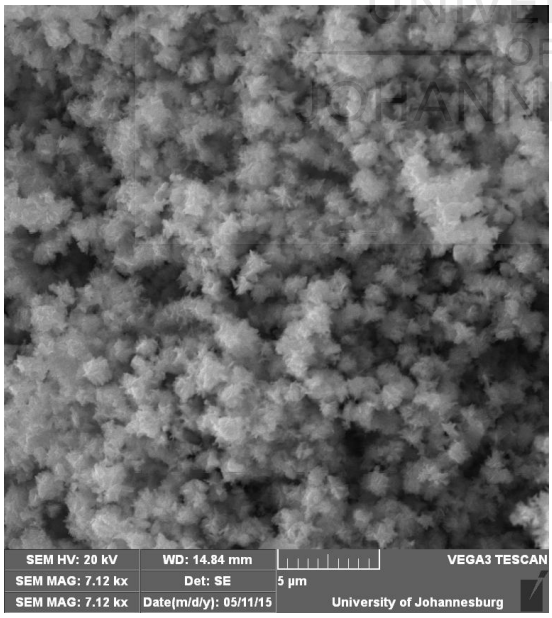

b) 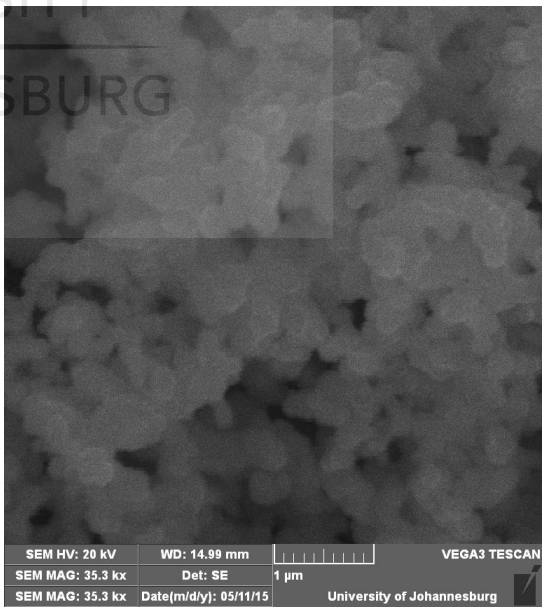

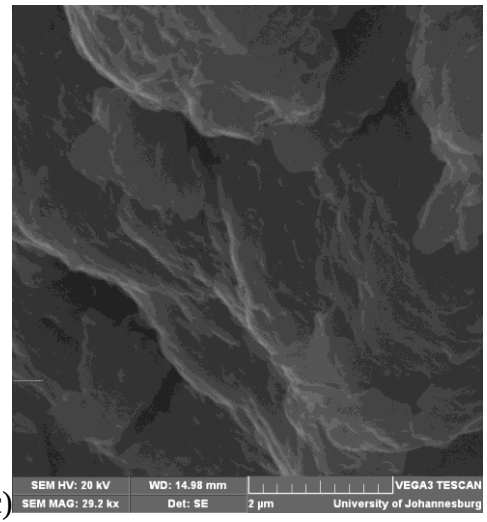

c)

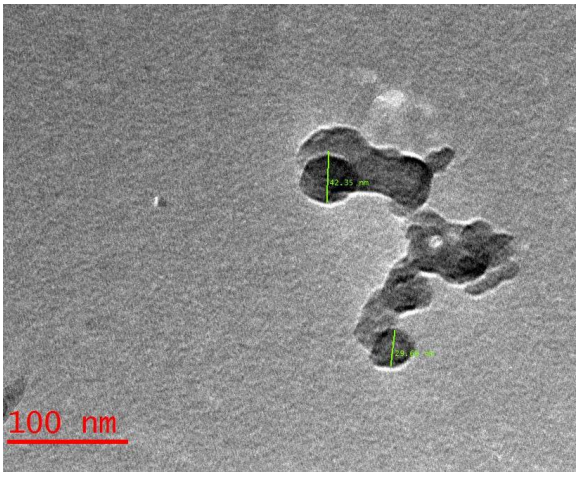

d)

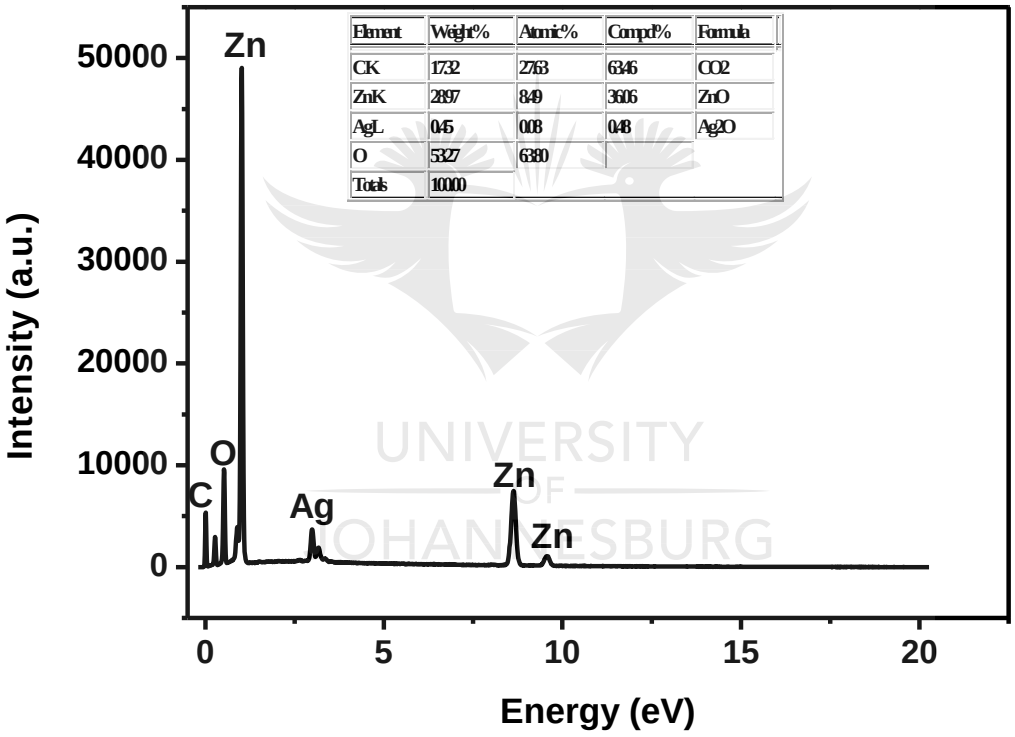

e)

Figure 4.4: SEM images of (a) the as-prepared ZnO; (b) the as-prepared Ag-Ag_2O-ZnO; the as-prepared GO. (d) TEM image of the as-prepared Ag-Ag_2O-ZnO/GO. (e) EDX spectrum and EDX data of the as-prepared Ag-Ag_2O-ZnO/GO nanocomposite (inset)

4.3.5 UV-Vis diffuse reflectance studies

UV-Vis diffuse reflectance analysis was carried out on the samples to study their optical properties (Fig. 4.5). The absorption band of the as-prepared ZnO occurred around wavelength (λ) = 380 nm and the band gap energy (E_g) is about 3.3 eV from the equation [30]:

$$E_g = 1240 / \lambda \qquad [4.1]$$

As seen in Fig. 4.5b, Ag-Ag_2O-ZnO showed a higher absorption of light in the visible region than ZnO. This can be assigned to the surface plasmon resonance (SPR) effects of Ag [20, 31] and the Ag_2O nanoparticles that act as a photosensitizer [32]. In Fig.4.5c, there is a strong visible light absorption from λ = 450-800 nm for the Ag-Ag_2O-ZnO/GO nanocomposite. This is due to the presence of GO which serves as a photosensitizer for the visible light absorption. The enhanced visible light harvesting ability of the Ag-Ag_2O-ZnO/GO can be attributed to the synergistic effects of the SPR effect of Ag and photosensitization of Ag_2O nanoparticles and GO [13], thus, displaying a good capacity for visible light photocatalytic process.

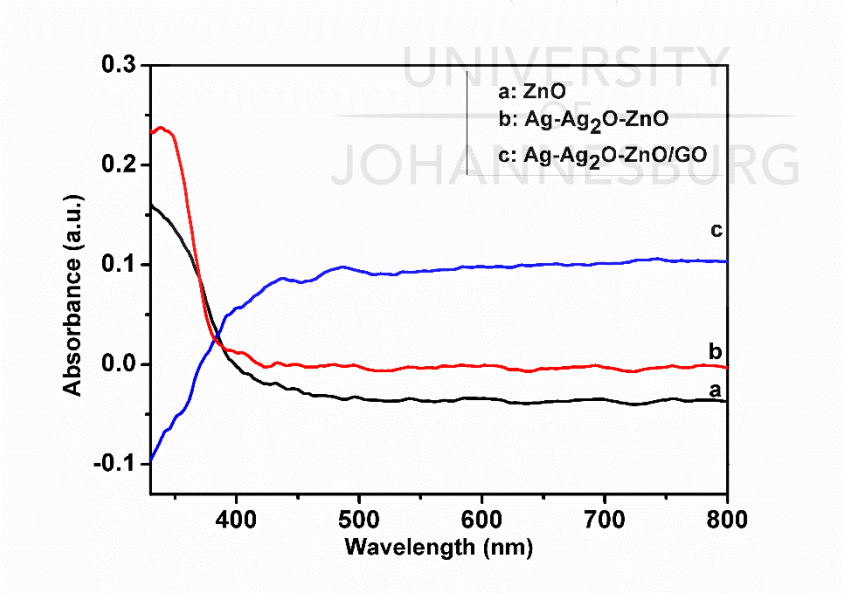

Figure 4.5: UV-Vis diffuse reflectance spectra of (a) ZnO; (b) Ag-Ag_2O-ZnO and (c) Ag-Ag_2O-ZnO/GO

4.3.6 Photocatalytic Activity

The photocatalytic activities of the as-prepared catalysts were evaluated for the degradation of acid blue 74 dye as a model for organic pollutants. The photodegradation process was evaluated in terms of decolourization efficiencies while the photodegradation activity was monitored using 610 nm as the optical absorption peak. The degradation of acid blue 74 dye with an initial concentration of 20 ppm as a function of the irradiation time is shown in Fig. 4.6a. It can be observed that the intensities of the characteristic absorption peaks decreases with increase in time. This suggests the gradual degradation of the acid blue 74 by the photocatalyst. The highest photocatalytic efficiency was displayed by Ag-Ag_2O-ZnO/GO. The percentage removal for the as-prepared ZnO nanocatalyst after 210 min was 75 %. The introduction of Ag-Ag_2O and GO increased the photodegradation efficiency of the ZnO nanocatalyst, giving a percentage removal of 85 % (Ag-Ag_2O-ZnO) and 90 % (Ag-Ag_2O-ZnO/GO) respectively. The kinetics of the photocatalytic degradation of the dye was studied using the pseudo-first order kinetics:

$$\ln C_o / C_t = kt \qquad [4.2]$$

where C_o / C_t is the normalized concentration of the dye, t is the reaction time, and k is the apparent reaction rate constant. The k_{app} values for the as-prepared catalysts are as follows: Ag-Ag_2O-ZnO/GO (10.69×10^{-3} min^{-1}) > Ag-Ag_2O-ZnO (9.48×10^{-3} min^{-1}) > ZnO (6.87×10^{-3} min^{-1}). Fig. 6b and 6c show the normalized concentration plots and kinetics of the degradation of acid blue 74 dye under visible light irradiation respectively.

The high visible light photocatalytic performance of the Ag-Ag_2O-ZnO/GO can be assigned to: (i) the surface plasmon resonance of Ag [20], (ii) minimized electron-hole pair recombination by enhanced interfacial electron transport due to the p-n heterojunction between Ag_2O and ZnO [9, 17], (iii) the outstanding electron mobility of graphene which enhanced the transfer of photogenerated electrons and holes from ZnO to the graphene, thus, minimizing the rate of recombination of the electron-hole pairs [15, 20].

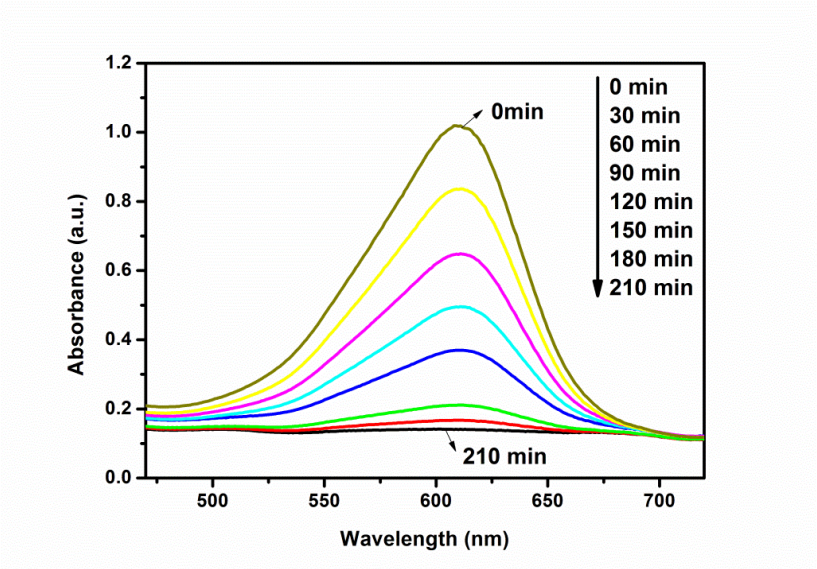

a)

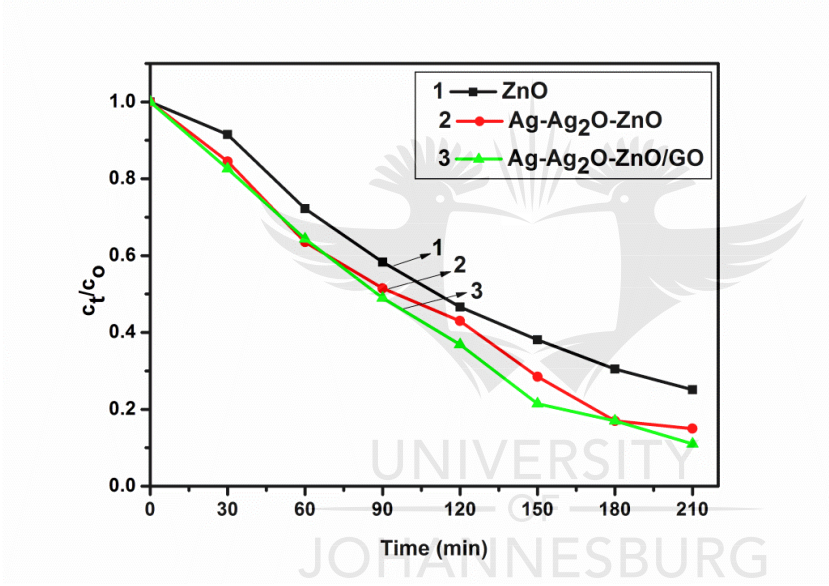

b)

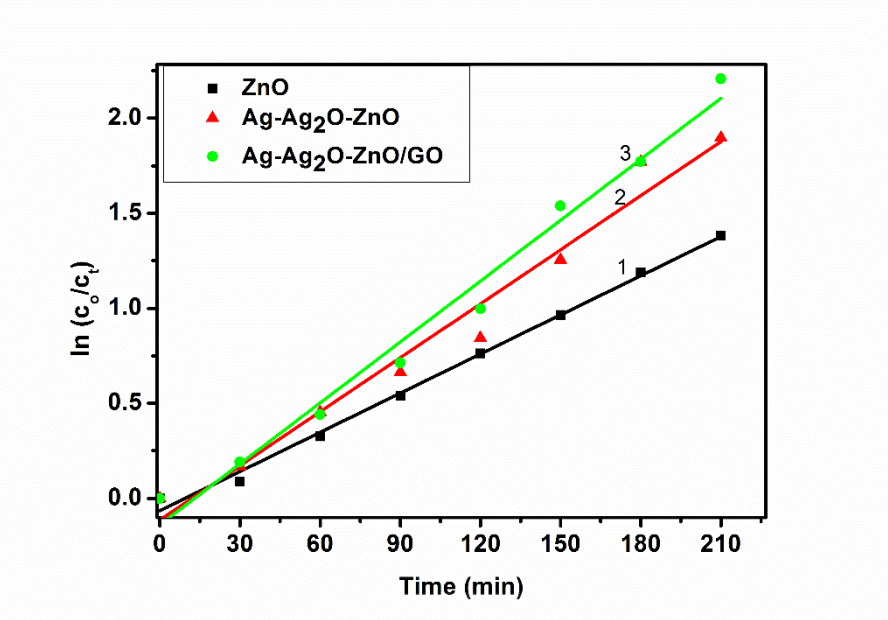

c)

Figure 4.6: (a) UV-Vis degradation profile of 20 ppm of acid blue 74 dye using Ag-Ag_2O-ZnO/GO. (b) Photocatalytic degradation plots of acid blue 74 dye using (1) ZnO, (2) Ag-Ag_2O-ZnO and (3) Ag-Ag_2O-ZnO/GO. (c) Kinetics of the degradation of acid blue 74 dye under visible light irradiation with (1) ZnO, (2) Ag-Ag_2O-ZnO and (3) Ag-Ag_2O-ZnO/GO

4.3.7 Proposed photocatalytic activity mechanism

The possible mechanism of the photocatalytic activity resulting from the absorption of visible light by Ag-Ag_2O-ZnO/GO is shown in Fig.4.7a and the pertinent reactions involved in the formation of the •OH radicals are presented in Eqns [4.3] – [4.13].

$hv + ZnO \rightarrow ZnO\ (h^+ + e^-)$ [4.3]

$hv + Ag_2O \rightarrow Ag_2O\ (h^+ + e^-)$ [4.4]

$h^+ + H_2O \rightarrow H^+ + \bullet OH$ [4.5]

$2\ h^+ + 2\ H_2O \rightarrow 2\ H^+ + H_2O_2$ [4.6]

$H_2O_2 \rightarrow 2\ \bullet OH$ [4.7]

$e^- + O_2 \rightarrow \bullet O_2^-$ [4.8]

$$\bullet O_2^- + H^+ \rightarrow HO_2\bullet \quad [4.9]$$

$$\bullet O_2^- + HO_2\bullet + H^+ \rightarrow H_2O_2 + O_2 \quad [4.10]$$

$$H_2O_2 \rightarrow 2\ \bullet OH \quad [4.11]$$

$$\bullet OH + \text{Acid blue 74 (dye)} \rightarrow CO_2 + H_2O \quad [4.12]$$

$$h^+ + \text{Acid blue 74 (dye)} \rightarrow CO_2 + H_2O \quad [4.13]$$

The photogenerated holes and electrons migrate to the surface of the semiconductors to produce a redox environment for the photocatalytic degradation of the dye. The photogenerated holes react with water molecules to form a proton and hydroxyl radical (•OH). The oxygen molecules in the waste water react with the photogenerated electrons in the conduction band to give a superoxide oxygen radical ($\bullet O_2^-$) which then reacts with a proton to give hydroperoxide radical ($H_2O\bullet$). These radicals further react with the dye molecules repeatedly to mineralized them into less toxic and simple substances like CO_2 and H_2O [8, 33].

Generally, the Fermi levels of n-type ZnO and p-type Ag_2O are different and when these semiconductors are attached, there is the formation of a p-n heterojunction at the interface which causes electrons to flow from the n-type area to the p-type area until equilibrium is established as seen in Fig. 4.7b. Thus, there is a positive charge on the n-type ZnO and a negative charge on the p-type Ag_2O and consequently forming an opposing electric field or a potential difference at the junction [34]. In the process of photocatalytic degradation, the generated electrons flow to the conduction band of the positively charged n-type ZnO while the generated holes flow to the valence band of the negatively charged p-type Ag2O as a result of the electric field that is established at the p-n heterojunction between the Ag2O and ZnO. Hence there is the enhancement of charged separation and reduced recombination rate. In addition, the presence of Ag nanoparticles helped in the charge separation and reduced recombination of the electron-hole pairs by the formation of Schottky barriers conduction band for trapping electrons [32, 35].

a)

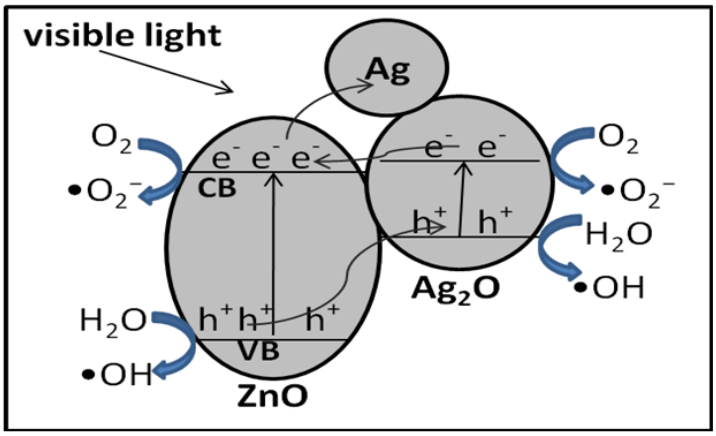

b)

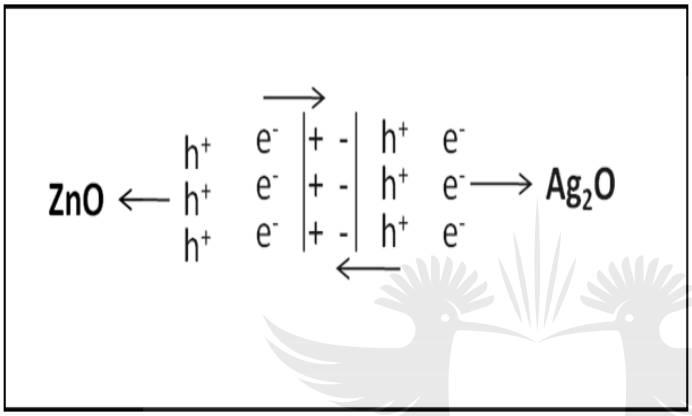

Figure 4.7: (a) Possible mechanisms for photocatalytic activity of Ag-Ag_2O-ZnO/GO for the degradation of acid blue 74 dye. b) Movement of electrons and holes between the n-type ZnO and p-type Ag_2O

4.4 SUB CONCLUSION

ZnO, Ag-Ag_2O-ZnO and Ag-Ag_2O-ZnO/GO nanocomposites were synthesized using co-precipitation method and calcined at 400 ºC. The materials were characterized using various spectroscopic and microscopic techniques. The TEM results showed the formation of nanocomposites. The Ag-Ag_2O improved the absorption capacity of ZnO for visible light due to the surface plasmon resonance effect of Ag, and the ability of Ag_2O to act as a photosensitizer. In addition, the Ag acted as electron sink for the photogenerated electrons while the GO aided in the transfer of photogenerated holes and electrons, thus, reducing the recombination of the electron-hole pairs. The synergistic effect of Ag-Ag_2O and GO in the ZnO nanocomposite is evident from the enhanced photocatalytic performance

displayed by Ag-Ag_2O-ZnO/GO compared to Ag-Ag_2O-ZnO and ZnO respectively. Thus, Ag-Ag_2O-ZnO/GO photocatalyst lends itself to application in water treatment where the removal of organics is very important.

4.5 REFERENCES

[1] J. Davey, A. Schäfer, Ultrafiltration to Supply Drinking Water in International Development: A Review of Opportunities, Appropriate Technologies for Environmental Protection in the Developing World, Springer 2009, pp. 151-168.

[2] R.P. Schwarzenbach, B.I. Escher, K. Fenner, T.B. Hofstetter, C.A. Johnson, U. Von Gunten, B. Wehrli, The challenge of micropollutants in aquatic systems, Science, 313 (2006) 1072-1077.

[3] J. Méndez-Hernández, F. Ramírez-Vives, M. Solís-Oba, A. Solís-Oba, A. Sobrino-Figueroa, O. Loera, Detoxification and mineralization of Acid Blue 74: study of an alternative secondary treatment to improve the enzymatic decolourization, World Journal of Microbiology and Biotechnology, 29 (2013) 805-814.

[4] O. Ama, N. Mabuba, O. Arotiba, Synthesis, Characterization, and Application of Exfoliated Graphite/Zirconium Nanocomposite Electrode for the Photoelectrochemical Degradation of Organic Dye in Water, Electrocatalysis, (2015) 1-8.

[5] R. Chaiyont, C. Badoe, C. Ponce de León, J.L. Nava, F.J. Recio, I. Sires, P. Herrasti, F.C. Walsh, Decolorization of Methyl Orange Dye at IrO_2-SnO_2-Sb_2O_5 Coated Titanium Anodes, Chemical Engineering & Technology, 36 (2013) 123-129.

[6] A.K. Verma, R.R. Dash, P. Bhunia, A review on chemical coagulation/flocculation technologies for removal of colour from textile wastewaters, Journal of Environmental Management, 93 (2012) 154-168.

[7] M.I. Litter, Introduction to photochemical advanced oxidation processes for water treatment, Environmental Photochemistry Part II, Springer 2005, pp. 325-366.

[8] S.H.S. Chan, T. Yeong Wu, J.C. Juan, C.Y. Teh, Recent developments of metal oxide semiconductors as photocatalysts in advanced oxidation processes (AOPs) for treatment of dye waste-water, Journal of Chemical Technology and Biotechnology, 86 (2011) 1130-1158.

[9] S. Ma, J. Xue, Y. Zhou, Z. Zhang, Photochemical synthesis of ZnO/Ag_2O heterostructures with enhanced ultraviolet and visible photocatalytic activity, Journal of Materials Chemistry A, 2 (2014) 7272-7280.

[10] A. Di Paola, E. García-López, G. Marcì, L. Palmisano, A survey of photocatalytic materials for environmental remediation, Journal of Hazardous Materials, 211 (2012) 3-29.

[11] S. Naghizadeh-Alamdari, A. Habibi-Yangjeh, M. Pirhashemi, One-pot ultrasonic-assisted method for preparation of Ag/AgCl sensitized ZnO nanostructures as visible-light-driven photocatalysts, Solid State Sciences, 40 (2015) 111-120.

[12] M. Pudukudy, Z. Yaakob, Simple chemical synthesis of novel ZnO nanostructures: role of counter ions, Solid State Sciences, 30 (2014) 78-88.

[13] J. Qin, R. Li, C. Lu, Y. Jiang, H. Tang, X. Yang, Ag/ZnO/graphene oxide heterostructure for the removal of rhodamine B by the synergistic adsorption–degradation effects, Ceramics International, 41 (2015) 4231-4237.

[14] D. An, Y. Li, X. Lian, Y. Zou, G. Deng, Synthesis of porous ZnO structure for gas sensor and photocatalytic applications, Colloids and Surfaces A: Physicochemical and Engineering Aspects, 447 (2014) 81-87.

[15] F. Chen, F. Yan, Q. Chen, Y. Wang, L. Han, Z. Chen, S. Fang, Fabrication of Fe_3O_4@SiO_2@TiO_2 nanoparticles supported by graphene oxide sheets for the repeated adsorption and photocatalytic degradation of rhodamine B under UV irradiation, Dalton Transactions, 43 (2014) 13537-13544.

[16] C. Liu, C. Cao, X. Luo, S. Luo, Ag-bridged Ag_2O nanowire network/TiO_2 nanotube array p–n heterojunction as a highly efficient and stable visible light photocatalyst, Journal of Hazardous Materials, 285 (2015) 319-324.

[17] D. Sarkar, C.K. Ghosh, S. Mukherjee, K.K. Chattopadhyay, Three dimensional Ag_2O/TiO_2 type-II (p–n) nanoheterojunctions for superior photocatalytic activity, ACS Applied Materials & Interfaces, 5 (2012) 331-337.

[18] Y. Xu, M.A. Schoonen, The absolute energy positions of conduction and valence bands of selected semiconducting minerals, American Mineralogist, 85 (2000) 543-556.

[19] Y. Cai, H. Fan, M. Xu, Q. Li, Rapid photocatalytic activity and honeycomb Ag/ZnO heterostructures via solution combustion synthesis, Colloids and Surfaces A: Physicochemical and Engineering Aspects, 436 (2013) 787-795.

[20] P. Wang, Y. Tang, Z. Dong, Z. Chen, T.T. Lim, Ag–AgBr/TiO_2/RGO nanocomposite for visible-light photocatalytic degradation of penicillin G, Journal of Materials Chemistry A, 1 (2013) 4718-4727.

[21] H.L. Poh, F. Šaněk, A. Ambrosi, G. Zhao, Z. Sofer, M. Pumera, Graphenes prepared by Staudenmaier, Hofmann and Hummers methods with consequent thermal exfoliation exhibit very different electrochemical properties, Nanoscale, 4 (2012) 3515-3522.

[22] M. Tang, X. Xu, T. Wu, S. Zhang, X. Li, Y. Li, Polyacrylamide grafting of modified graphene oxides by in situ free radical polymerization, Materials Research Bulletin, 60 (2014) 576-583.

[23] H. Li, Z. Lei, C. Liu, Z. Zhang, B. Lu, Photocatalytic degradation of lignin on synthesized Ag–AgCl/ZnO nanorods under solar light and preliminary trials for methane fermentation, Bioresource Technology, 175 (2015) 494-501.

[24] Y. Guo, H. Wang, C. He, L. Qiu, X. Cao, Uniform carbon-coated ZnO nanorods: microwave-assisted preparation, cytotoxicity, and photocatalytic activity, Langmuir, 25 (2009) 4678-4684.

[25] P. Patra, S. Mitra, N. Debnath, P. Pramanik, A. Goswami, Ciprofloxacin conjugated zinc oxide nanoparticle: A camouflage towards multidrug resistant bacteria, Bulletin of Materials Science, 37 (2014) 199-206.

[26] K.-W. Park, J.H. Jung, Spectroscopic and electrochemical characteristics of a carboxylated graphene–ZnO composites, Journal of Power Sources, 199 (2012) 379-385.

[27] F.D. Nayeri, S. Darbari, E.A. Soleimani, S. Mohajerzadeh, Surface structure and field emission properties of cost effectively synthesized zinc oxide nanowire/multiwalled carbon nanotube heterojunction arrays, Journal of Physics D: Applied Physics, 45 (2012) 285101.

[28] A.I. Uddin, D.-T. Phan, G.-S. Chung, Low temperature acetylene gas sensor based on Ag nanoparticles-loaded ZnO-reduced graphene oxide hybrid, Sensors and Actuators B: Chemical, 207 (2015) 362-369.

[29] Y. Zhang, H. Wu, X. Huang, J. Zhang, S. Guo, Effect of substrate (ZnO) morphology on enzyme immobilization and its catalytic activity, Nanoscale Research Letters, 6 (2011) 1-7.

[30] J. Li, S. Lv, Y. Liu, J. Bai, B. Zhou, X. Hu, Photoeletrocatalytic activity of an n-ZnO/p-Cu 2 O/n-TNA ternary heterojunction electrode for tetracycline degradation, Journal of Hazardous Materials, 262 (2013) 482-488.

[31] P. Wang, B. Huang, Q. Zhang, X. Zhang, X. Qin, Y. Dai, J. Zhan, J. Yu, H. Liu, Z. Lou, Highly efficient visible light plasmonic photocatalyst Ag@Ag(Br, I), Chemistry-A European Journal, 16 (2010) 10042-10047.

[32] W. Zhou, H. Liu, J. Wang, D. Liu, G. Du, J. Cui, Ag_2O/TiO_2 nanobelts heterostructure with enhanced ultraviolet and visible photocatalytic activity, ACS Applied Materials & Interfaces, 2 (2010) 2385-2392.

[33] H. Hua, Y. Xi, Z. Zhao, X. Xie, C. Hu, H. Liu, Gram-scale wet chemical synthesis of Ag_2O/TiO_2 aggregated sphere heterostructure with high photocatalytic activity, Materials Letters, 91 (2013) 81-83.

[34] Q. Deng, H. Tang, G. Liu, X. Song, G. Xu, Q. Li, D.H. Ng, G. Wang, The fabrication and photocatalytic performances of flower-like Ag nanoparticles/ZnO nanosheets-assembled microspheres, Applied Surface Science, 331 (2015) 50-57.

[35] D. Sriprabha, T. Mohankumar, D. Nataraj, T.D. Thangadurai, Enhanced Methylene Blue Dye Degradation by Newly Synthesized Ag_2O/TiO_2 Heterostructure, Journal of Environmental Nanotechnology, 3 (2014) 105-111.

CHAPTER 5

PHOTOELECTROCHEMICAL DEGRADATION OF ORANGE II DYE IN WASTEWATER AT SILVER-ZINC OXIDE/REDUCED GRAPHENE OXIDE NANOCOMPOSITE PHOTOANODE[1]

5.1 INTRODUCTION

Electrochemical oxidation of aqueous wastes containing biorefractory organics such as phenolic compounds has been recognised as a promising alternative due to ease of automation, high efficiency and environmental compatibility [1-4]. This method involves *in situ* generation of very active hydroxyl radicals which rapidly and non-selectively oxidise a broad range of organic pollutants. The most widely used anode materials include boron doped diamond, ruthenium oxide, activated carbon and single walled carbon nanotubes [5-11]. However, these materials are expensive, difficult to fabricate and their performances are hampered because of the adhesive used during fabrication [12, 13].

The availability of clean water for industrial and domestic use is a well-known global challenge owing to increase in dosage and complexity of water pollutants. The discharge of organic waste into water bodies is on the increase and these organic wastes pose a lot of health and environmental risk to living organism [1, 2]. Dyes are a typical group of organic pollutants which can originate from industrial effluents generated by paints, textiles, leathers, and printing industries. The presence of dye in water or wastewater is not only hazardous to human and aquatic lives [3], some dyes are recalcitrant during treatment by the conventional water treatment methods. This necessitates the need to develop other treatment methods as alternatives and complements to the existing conventional techniques.

Advanced oxidation processes (AOPs) have been reported as alternatives to conventional methods for the removal of organic pollutants in water treatment processes [4]. AOP involves the generation of hydroxyl radicals and other oxidants for the oxidation of organic pollutants [5, 6]. Electrochemical oxidation is a type of advanced oxidation process where the hydroxyl radicals are generated electrochemically usually at the anode [4, 6]. Some of the drawbacks associated with electrochemical oxidation include mass transfer of the

[1] This chapter has been published in: Umukoro, E. H.; Peleyeju, G.; Ngila, J. C.; Arotiba, O. A. Photoelectrochemical degradation of orange II dye in wastewater at a silver-zinc oxide/reduced graphene oxide nanocomposite photoanode. *RSC Advances*, **2016**, 6, 52868-52877

pollutant in solution to the electrode surface and oxygen evolution as a side reaction resulting from the utilisation of high voltage in the degradation process. The oxygen evolution is parasitic to the production of hydroxyl radicals and tends to compete with the oxidation of the organic pollutants Thus, there is need to minimise these drawbacks by combining electrochemical oxidation with heterogeneous photocatalytic degradation where photogenerated electrons react with oxygen molecule (evolution) to give a superoxide oxygen radical ($\bullet O_2^-$) which then react with a proton to give hydroperoxide radical ($H_2O\bullet$). These radicals further reacts with the pollutant molecules repeatedly to mineralized them into less toxic and simple substances like CO_2 and H_2O [4] Heterogeneous photocatalytic degradation involves the absorption of ultraviolet or visible radiations by a semiconductor from an energy source, leading to the generation of electrons and holes [5]. The holes and electrons migrate to the surface of the semiconductor to produce a redox environment for the degradation of organic pollutants such as dyes. The limitations associated with these semiconductors include slow electron transfer rate, recombination of the photogenerated holes and electrons, and narrow light absorption range [7]. It has been reviewed that the recombination rate of the generated electron-hole pairs can be reduced by the utilisation of electrical energy to drive away the electrons from the interface of the electrolyte-semiconductor. Hence it leads to an increase in the generation of hydroxyl radicals, and consequently, an increase in the degradation of the organic pollutants [6, 8].

The combination of electrochemical oxidation and heterogeneous photocatalytic degradation is known as photoelectrochemical process. It is a process whereby a photoactive material is immobilized on a conducting material to form a photoanode and an anodic potential is then applied [6], thus, leading to the generation of hydroxyl radicals by both materials. The photoelectrochemical degradation of P-nitrophenol on expanded graphite-diamond, tetracycline on n-ZnO/p-Cu_2O/n-TNA ternary heterojunction electrode, rhodamine B on TiO_2-coated ZnO:I nanorod array films and $BiFeO_3/TiO_2$ nanotube arrays as composite electrodes have been reported [6, 9-11]. Xiong et al. [12] studied the photocatalytic and photoelectrochemical activities of n-type Cu_2O film for the stability and inactivation of E.coli.

ZnO has been found as an alternative semiconductor to TiO_2 as a result of its low cost, non-toxicity, chemical inertness, good optoelectronic and catalytic properties [13, 14]. However, its wide band gap (3.37eV) limits its utilization of visible light. The absorption of light in the visible spectrum by ZnO can be improved by the introduction of Ag due to

its surface plasmon resonance effect [15, 16]. Moreover, Ag can be incorporated as an electron sink for the generated electrons. Hence it enhances the generation of more hydroxyl radicals by the electrons and holes, and therefore, improves the degradation process of the pollutants [17]. Graphene comprises sp^2-bonded carbon atoms packed tightly into 2-D planar honeycomb lattices with special properties like high surface area, high mechanical stability, high thermal and electrical conductivities, and very good electron mobility [18-20]. The mobility of both holes and electrons can be enhanced by the Dirac cone of the band structure of graphene [7]. Hence the photogenerated electrons and holes from the ZnO can be transported to the graphene. Consequently, the rate of recombination of the electron-hole pairs would be minimized and the efficiency of ZnO in the composite electrode would be enhanced.

It can be hypothesised that the combined properties of Ag, ZnO and reduced graphene (rGO) highlighted above, are beneficial for the photoelectrochemical performance of Ag-ZnO-rGO composite electrode. It was reported that n-ZnO/p-Cu_2O/n-TiO_2 nanotube arrays have been prepared and applied as electrode for the photoelectrocatalytic degradation of tetracycline. The results showed an excellent photoelectrocatalytic activity due to the ternary heterojunction of the material [9]. Photoelectrochemical oxidation of salicylic acid and salicylaldehyde has been carried out on titanium dioxide nanotube arrays, giving over 83 % removal of both organics [21]. The use of Zn-Co-layered double hydroxides nanowalls has been reported as electrocatalyst for the electrochemical oxidation of water [22]. In addition, several materials have been employed in the construction of photoanodes for the photoelectrochemical oxidation of water. These include TiO2 array sheathed with hydroxides of nickel and chromium to form a core/shell array [23], $BiVO_4$, [24] modification of $BiVO_4$ with double hydroxides [25] and semiconductor-chromophore-polyoxometalate [26]. Few studies have been reported on the fabrication and application of Ag/ZnO/rGO as gas sensor [27], while ZnO/rGO/Ag and Ag/ZnO/GO as photocatalysts for dyes removal [17, 28]. However, to the best of the knowledge of the authors, Ag-ZnO-rGO composite electrode has not been employed as a photoanode for the photoelectrochemical degradation of dyes. Thus, in this study, Ag-ZnO nanoparticles were immobilized on reduced graphene oxide, fabricated into an electrode and applied as photoanode in the photoelectrochemical degradation of orange II dye as a target organic pollutant in water treatment process.

5.2 EXPERIMENTAL PROCEDURES

5.2.1 Materials and apparatus

Potassium hydroxide, silver nitrate, ascorbic acid, natural graphite flakes, sulphuric acid (98%), sodium nitrate, potassium permanganate, hydrogen peroxide, zinc nitrate hexahydrat, absolute ethanol (99.9%) and orange II dye. All reagents were purchased from Sigma Aldrich, Germany, and were of analytical grade and they were used without further purifications.

Reduced graphene oxide (rGO), ZnO and the composites were characterised using x-ray diffractometer (Rigagu Ultima IV, Japan) at 40 kV and 30 mA with Cu Kα radiation (λ=0.15406) with K-beta filter. This was carried out using scintillation counter ranging from 5-90º at a speed of a 2º /min. The studies of surface morphology of the as-synthesized materials were done using transmission electron microscopy (JEOL 2100 HRTEM 200V, Japan), scanning electron microscopy (SEM) (TESCAN, Vega 3 XMU, Czech Republic). The surface elemental composition was obtained using energy-disperse x-ray spectrometer (EDS) (TESCAN, Czech Republic) which was attached to the SEM. Spectroscopic studies were carried out using Perkin Elmer FTIR spectrometer (Spectrum 100, USA) and Perkin Elmer Raman microscope (Raman micro 200, USA) to obtain the FTIR and Raman spectra, respectively. Decolourisation of the dye was investigated using UV-Visible spectrophotometer (Cary 60, Agilent technologies, Australia). New Port 9600 Full Spectrum Solar Simulator equipped with 150 W ozone free xenon lamp which produces a collimated beam of 33 mm diameter (equivalent to 1.3 sun) was used as the light source. All characterisation experiments were performed at the University of Johannesburg.

5.2.2 PREPARATION OF REDUCED GRAPHENE OXIDE (RGO)

Graphene oxide was prepared by a modified Hummer's method [29] and then reduced using ascorbic acid by a method described by Zhang et al. [30]. In brief, 5 g of graphite flakes were added to 2.5 g of sodium nitrate and 115 mL of sulphuric acid. The mixture was mixed and stirred vigorously. The mixture was allowed to cool in an ice-bath and 15 g of potassium permanganate was added to the mixture over a period of 2 h. The mixture was allowed to cool in an ice-bath to room temperature and then heated to 35 ºC for 30 min. Then, it was poured into 250 mL of de-ionized water in a flask and heated to 70 ºC. The mixture was poured into 1 L of de-ionized water after keeping the temperature

constant for about 15 min. A 30 mL volume of 3% hydrogen peroxide was added to remove any unreacted $KMnO_4$ and manganese dioxide in the mixture. Then, it was washed several times by centrifugation and filtration using de-ionized water until a pH of 6 was obtained. The resulting graphite oxide was then ultrasonicated for 2 h to obtain graphene oxide and then dried in an oven at 60 ºC for 48 h. Furthermore, 5 g of ascorbic acid was added to an aqueous suspension which contained 0.1 g of the prepared graphene oxide in 50 mL of deionised water and sonicated for 30 min. The resultant suspension was stirred at 90 ºC for 48 h. Then, the product –reduced graphene oxide - was filtered and dried at 60 ºC overnight before use.

5.2.3 Preparation of Ag-ZnO nanoparticles

The Ag-ZnO composite was synthesised using a modified co-precipitation method [31, 32]. In brief, a solution containing 14.87 g of zinc nitrate hexahydrate and 0.149 g of silver nitrate dissolved in 100 mL of de-ionised water was prepared. A 3 M KOH solution was added drop-wise while stirring vigorous until the pH of the solution reached 10. Then, it was further stirred for 2 h at a very high speed. It was observed that the viscosity of the mixture increased with increase in the amount of KOH solution added. The product obtained was centrifuged, and washed with de-ionised water and ethanol several times. Subsequently, it was dried in an oven at 60 ºC for 12 h and calcined at 400 ºC for 2 h. The ZnO was prepared in a similar way without the addition of silver nitrate.

5.2.4 Preparation of Ag-ZnO-rGO composite photoanode

A sample of 100 mg of the as-prepared Ag-ZnO was dispersed in about 10 mL methanol and sonicated for 20 min to obtain a uniform dispersion. 100 mg of rGO was added to the dispersion and stirred vigorously for another 10 min. Then, the mixture was poured into a dish and dried in the oven at 90 ºC for about 48 h for the complete removal of the methanol to obtain the Ag-ZnO-rGO composite. The as-prepared Ag-ZnO-rGO composite was compressed into pellet of 1.3 cm in diameter using a press machine at a very high pressure. Then the pellet was used to fabricate a photoanode with the aid of a glass rod, conduction silver paint, copper wire and epoxy resin. One end of the copper wire in the glass tube was coiled to form a flat surface. The pellet was placed on the surface using the conductive silver paint which enabled the conduction between the copper wire and the composite [33].

It was allowed to dry in the air for about 1 h. The edge of the pellet was covered with epoxy resin so that electron flow is mainly from the basal plane.

5.2.5 Electrochemical and Photoelectrochemical experiments

Electrochemical and photoelectrochemical studies were conducted using $[Fe(CN)_6]^{-3/-4}$ in 0.1 M KCl solution as the redox probe and 0.1 M Na_2SO_4 as the supporting electrolyte on a Autolab (302N) potentiostat/galvanostat electrochemical station with a three- electrode system having Ag-ZnO-rGO (1.3 cm) as working electrode, Ag/AgCl (3.0 M KCl) as the reference electrode and platinum foil as the counter electrode. The degradation experiments were conducted in a 100 mL quartz cell photoreactor which contained the orange II dye solution and the electrodes. The working electrode was positioned to receive the light coming from the source of light. The potentiostat/galvanostatic was utilised as the source of power for the electrochemical degradation of the dye in a 0.1 M sodium sulphate solution as a supporting electrolyte. The source of light was a New Port 9600. The distance between the simulator and the reactor is 10 cm so as to produce a beam power equivalent to 1 sun. In the case of electrochemical oxidation of the dye, only potential was applied. For photocatalytic degradation, only light was utilised, while both potential and light were applied for the photoelectrochemical degradation of the dye. At intervals of 30 min, an aliquot (5 mL) of solution was withdrawn from the cell using a disposable syringe and filtered using a 0.4 µm PVDF membrane filter for a period of 210 min. The degradation was measured using a UV-Vis spectrophotometer (Cary 60, Agilent) at an absorption band of λ = 483 nm, and with the aid of TOC analyzer (Teledyne Tekmar TOC fusion).

5.3 RESULTS AND DISCUSSION

5.3.1 Raman spectroscopy

Raman spectroscopic study was carried out to determine the formation of rGO from GO. Fig 5.1a shows the Raman spectra of (i) GO and (ii) rGO. The Raman spectra display two peaks at ~1600 cm^{-1} and ~1350 cm^{-1} which correspond to the G and D bands respectively. The G band is due to the in-plane phonon vibration mode of the sp^2-bonded carbon atoms in graphene while the D band is due to defects or disorder in the hexagonal graphitic sheets resulting from the intercalation of oxygen-containing functional groups or presence of sp^3 bonding [18, 20]. The higher intensity of the D band in relation to the G band in the rGO

would give a higher D/G intensity ratio compare to the lower D/G intensity ratio in the GO. This indicates the extent of the defects in the graphitic layers [34]. Thus, it can be inferred that the graphene oxide was successfully reduced by the ascorbic acid, leaving few oxygen-containing functional groups that resulted in the defects in the GO.

5.3.2 X-ray diffractometry

XRD analyses were conducted on the as-synthesised rGO, ZnO and Ag-ZnO-rGO and the XRD patterns of the different materials are shown in Fig. 5.1b. In Fig. 5.1b(i), the observed diffraction peak at 2θ = 26.4º is attributed to the 002 crystal plane of rGO (JCPDS Card no. 75-1621). The diffraction peaks of hexagonal wurzite structure of ZnO (JCPDS Card no. 36-1451) were observed at 31.8º (100), 34.6º (002), 36.4º(101), 47.7º (102), 56.7º (110), 63.0º (103), 66.5º (200), 68.1º (112), 69.2º (201) and 72.6º (004). However, there are very low intensity peaks observed in Fig. 5.1b (iv) at 38.1º (111) and 44.2º (200) which indicated the presence of Ag in the as-synthesized Ag-ZnO-rGO composite (JCPDS Card no. 04-0783). Furthermore, the rGO peak at 2θ = 26.4º (002) appeared broadened and lower in intensity in the as-synthesised Ag-ZnO-rGO composite. This could be due to little destruction of the crystalline structure of rGO resulting from the presence of Ag-ZnO nanostructures [17].

The crystallite size of the as-prepared sample was determined using the Debye-Scherrer's equation- $D = K\lambda / \beta \cos\theta$, where D is the crystal size, K is a constant (0.9), λ is the x-ray wavelength, β is the full width of half maximum (FWHM) (radian) and θ is the diffraction angle at the maximum. The average calculated crystalline size of the ZnO was ca 21.8 nm.

5.3.3 UV-Vis diffuse reflectance spectroscopy

UV-Vis diffuse reflectance study was carried out on the samples to determine the effects of Ag and rGO on the optical properties of the as-prepared ZnO nanoparticles (Fig. 5.1c). It can be observed from the UV-Vis spectra that Ag-ZnO displayed a slightly stronger visible light absorption in comparison to ZnO. This is due to the surface plasmon resonance effects of Ag nanoparticles [20, 35]. Figure 5.1c shows that there is an intense visible light absorption from λ = 430-800 nm for the Ag-ZnO-rGO composite resulting from the presence of rGO which serves as a photosensitizer for the visible light absorption. This enhanced visible light harvesting ability of the Ag-ZnO-rGO material can be ascribed to the synergistic effects of the SPR effect of Ag nanoparticles and enhanced visible light

absorption of rGO [17]. Thus, the visible light absorption capacity of the composite is a necessity for its enhanced photoelectrochemical degradation efficiency using solar energy.

5.3.4 Fourier transform infrared spectroscopy

FTIR analyses were performed to investigate the functional groups present in the as-synthesised materials. The FTIR spectra of rGO and Ag-ZnO-rGO are presented in Fig. 5.1d. In Fig. 5.1d(i), the absorption band at 3400 cm^{-1} can be attributed to O-H stretching vibration from the hydroxyl groups in rGO and the absorbed water on the surface of the rGO. The bands at 1620 cm^{-1} and 1720 cm^{-1} can be attributed to C=C bond stretching vibration and the stretching vibration of C=O bond of carboxyl group in rGO respectively. The broad absorption peak at 1150 cm^{-1} is attributed to C-O stretching vibration which usually occurs around 1260-1000 cm^{-1}. In the spectra of Ag-ZnO-rGO (Fig. 5.1d(ii)), the broad peak at 510 cm^{-1} accounts for Zn-O bond stretching vibration. Also, the weak peak at 1224 cm^{-1} can be associated to C-O-H bending vibration (1440-1220 cm^{-1}) [19]. The broad band observed at 3400 cm^{-1} can be assigned to O-H stretching vibration of rGO which probably overlaps with the stretching vibration of hydroxyl groups from the absorbed water on the ZnO surface [27]. These characteristics peaks were used as indications for the successful preparation of the Ag-ZnO-rGO composite.

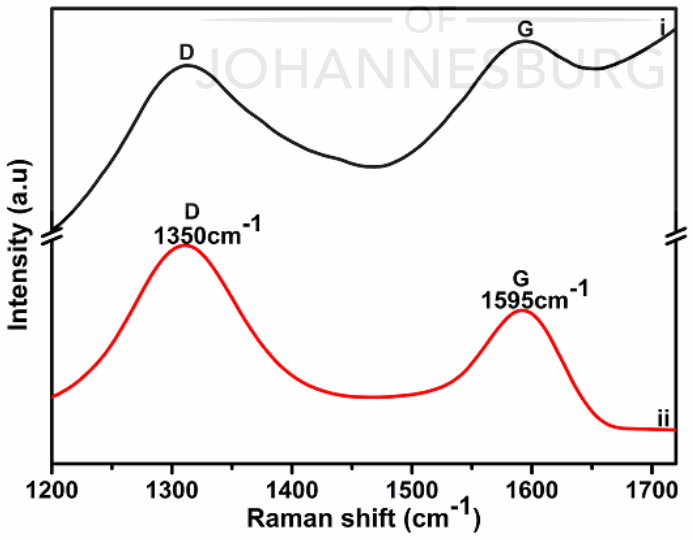

a)

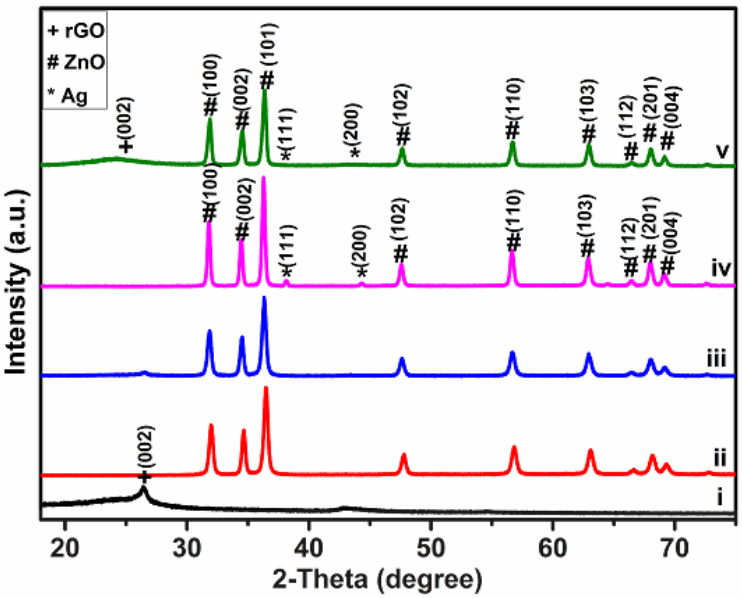

b)

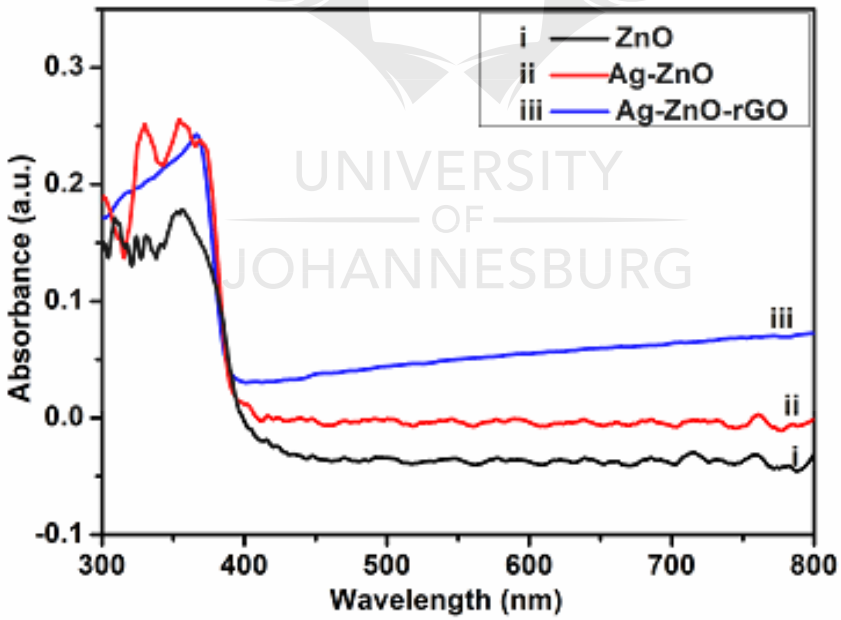

c)

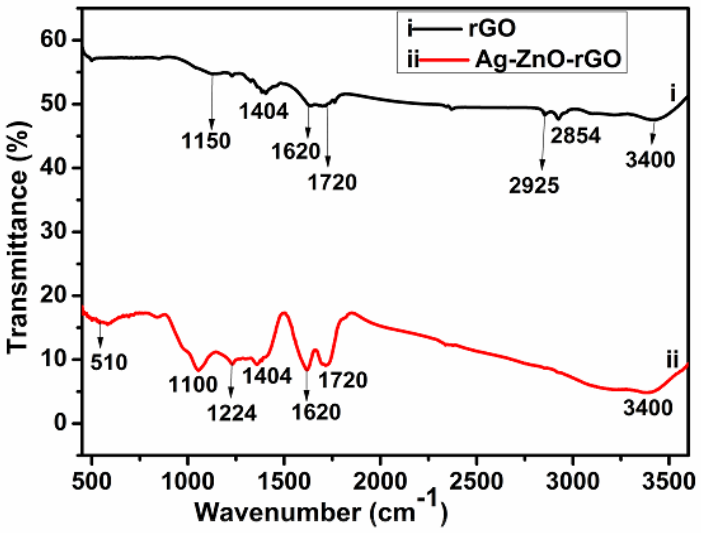

d)

Figure 5.1: (a) Raman spectra of the prepared (i) GO and (ii) rGO; (b) XRD patterns of (i) GO, (ii) ZnO, (iii) ZnO-rGO, (iv) Ag-ZnO and (v) Ag-ZnO-rGO; (c) UV-vis diffuse reflectance spectra of (i) ZnO, (ii) Ag-ZnO, and (iii) Ag-ZnO-rGO; (d) FTIR spectra of (i) rGO and (ii) Ag-ZnO-rGO

5.3.5 Electron microscopy characterisation

The surface morphology of the as-synthesised materials was studied using scanning electron microscopy coupled with energy dispersed x-ray spectroscopy and transmission electron microscopy (Fig 5.2). The as-prepared ZnO nanoparticles are presented in Fig. 5.2a having a uniform flower-like structures. Fig. 5.2b reveals the graphitic sheets of the rGO, while the presence of Ag-ZnO dispersed within and on the layers of the rGO sheets is seen in Fig 5.2c. The presence of silver in the dispersed Ag-ZnO was confirmed by EDS which also shows the presence of Zn, O and C (Fig 5.2d). The very low intensity of Ag confirmed the presence of a very minute percentage of Ag in comparison with ZnO and rGO in the Ag-ZnO-rGO nanocomposite. The TEM image (Fig 5.2e) shows the irregular sizes of the as-prepared nanocomposite ranging from 36.86 nm to 42.65 nm.

a)

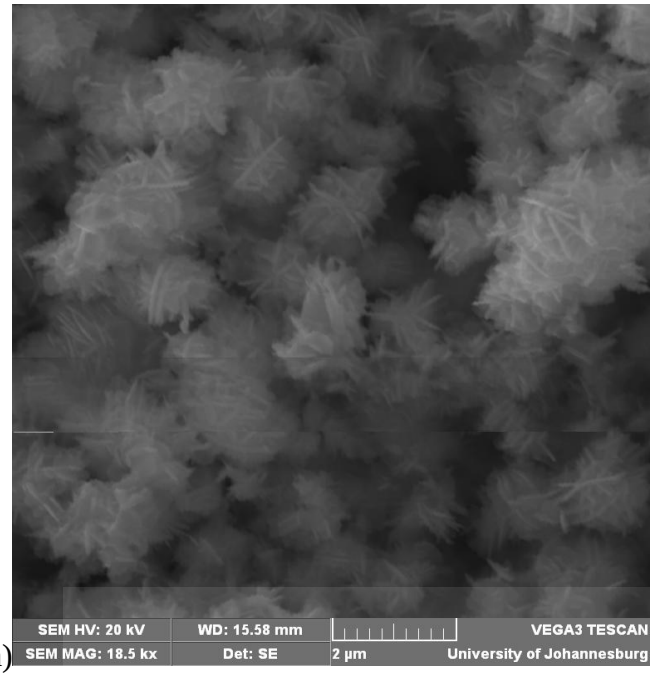

b)

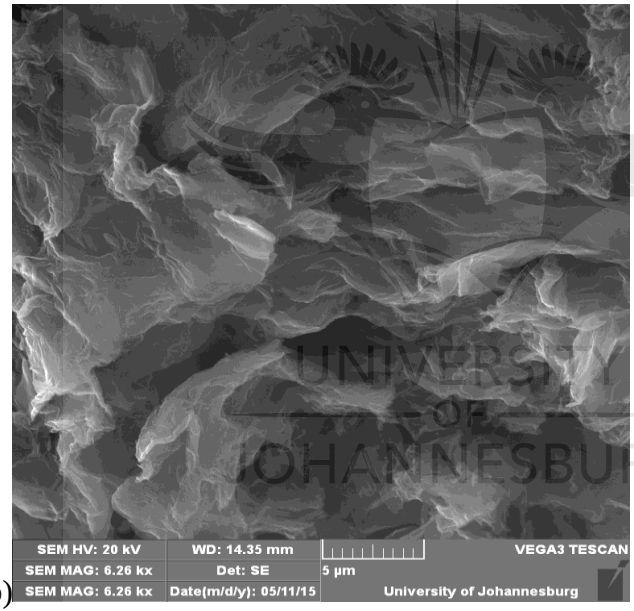

c)

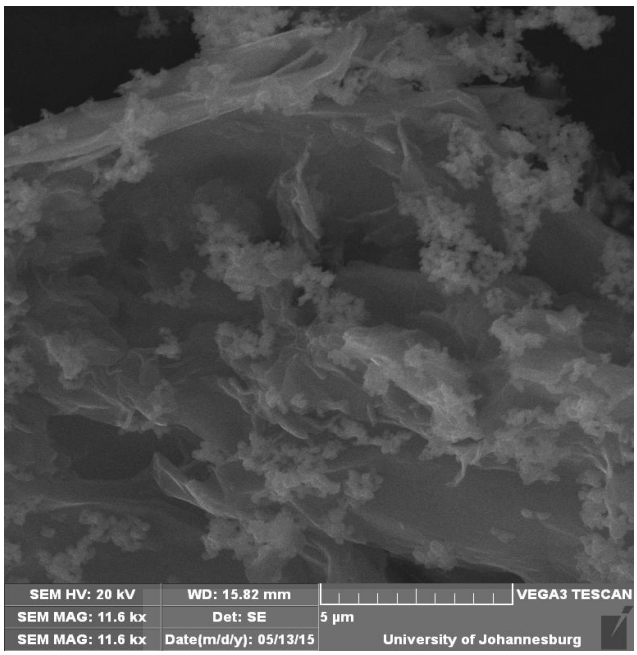

d)

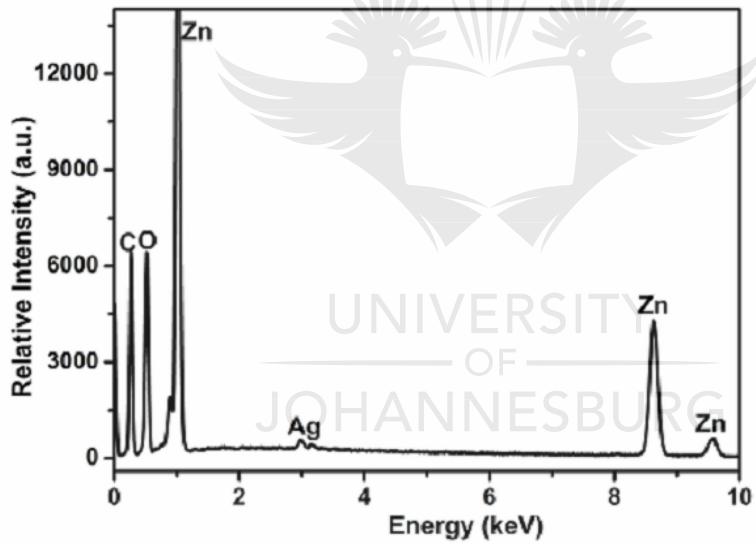

e)

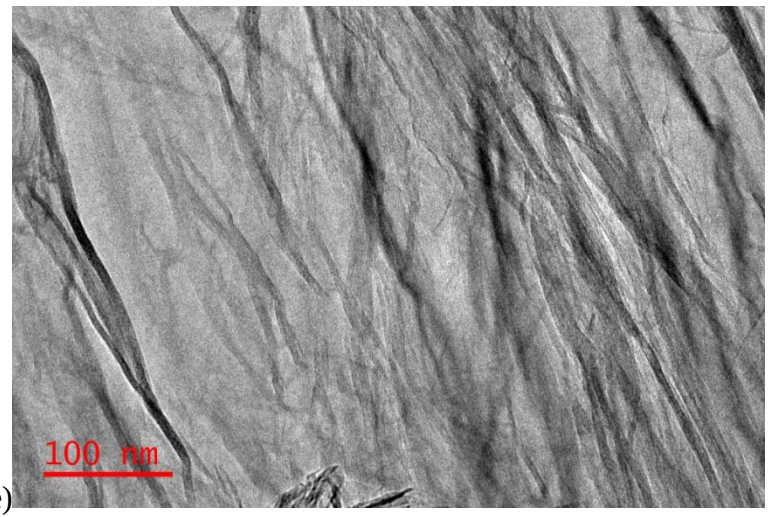

f)

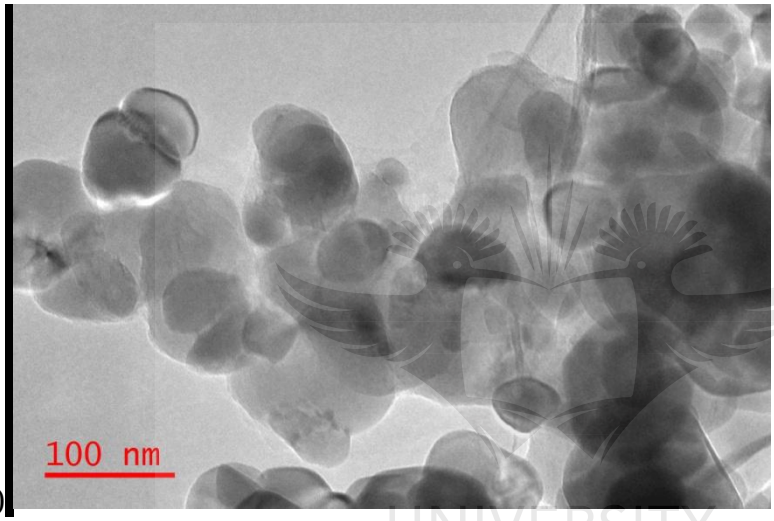

g)

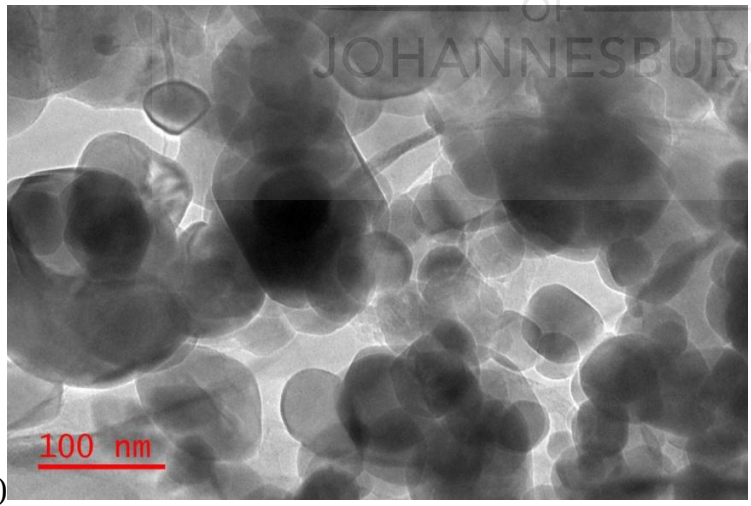

Figure 5.2: (a) SEM images of (a) ZnO nanoparticles; b) reduced graphene oxide (rGO); (c) the as-synthesised Ag-ZnO-rGO material. (d) EDX spectrum of the as-prepared

composite. TEM images of the as-synthesised (e) rGO; (f) ZnO-rGO and (g) Ag-ZnO-rGO material.

5.3.6 Electrochemical and photoelectrochemical characterisation

The electrochemical properties of rGO and Ag-ZnO-rGO electrodes were investigated in $[Fe(CN)_6]^{-3/-4}$ redox probe (Fig. 5.3a). It was observed that Ag-ZnO-rGO electrode exhibited an increase in current in relation to rGO. The faradaic current expected from the redox probe must have been impeded by the oxygen functional groups around the graphene backbone of the rGO. The enhanced current in the Ag-ZnO-rGO resulted from the Ag dopant which increased the conductivity of the electrode. The increase in the current (photocurrent) response of the electrode after illumination suggests that the Ag-ZnO-rGO is photoactive and can thus be used as a photoanode (Fig 5.3b). This photoelectrochemical activity is expected to aid in the production of more hydroxyl radicals responsible for the degradation of organic pollutants in water.

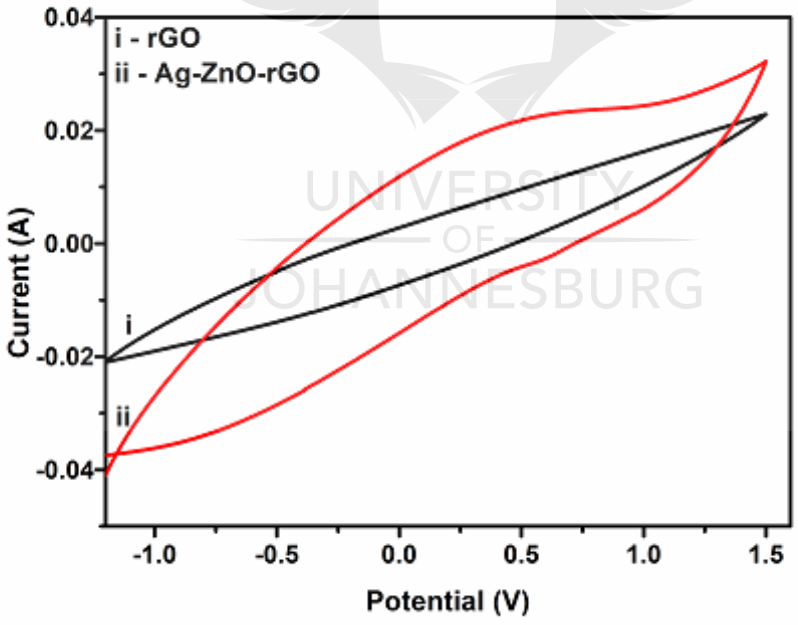

a)

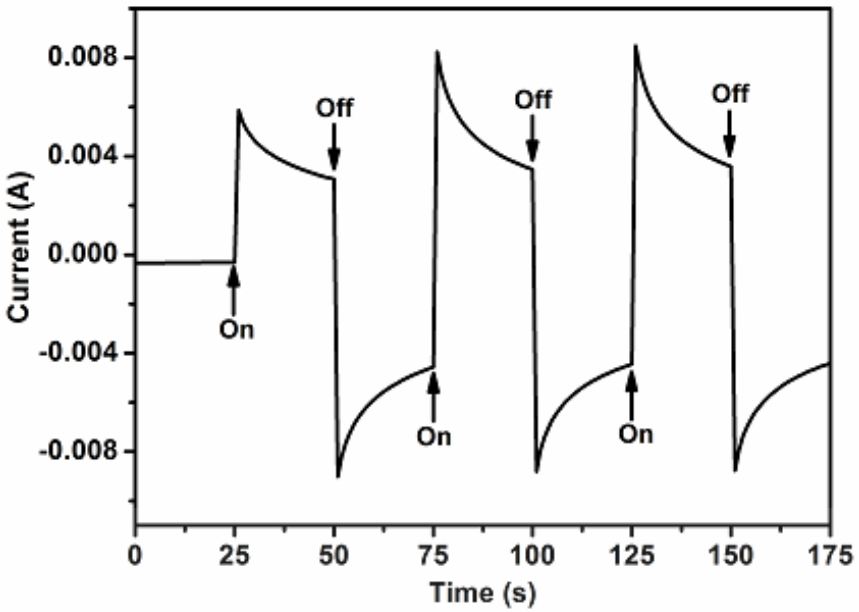

b)

Figure 5.3: (a) Cyclic voltammograms of (a)(i) rGO and (ii) Ag-ZnO-rGO electrodes in 5mM $[Fe(CN)_6]^{-3/-4}$ in 0.1 M KCl at 50 mVs^{-1}; (b) Photoelectrochemical response of Ag-ZnO-rGO electrode in 0.1 M Na2SO4 in the dark (off) and under illumination (on) at 0.3 V.

5.3.7 Photoelectrochemical degradation of the dye

The degradation of orange II dye as a model of organic pollutant was conducted using different electrodes as photoanodes and under different degradation processes such as electrochemical oxidation, photocatalytic degradation and photoelectrochemical oxidation in which a 0.1 M Na_2SO_4 solution was used as the supporting electrolyte (Fig. 5.4). A decline in absorbance at the λmax of 483 nm of the dye was used as the extent of degradation (or decolourisation) in the electrochemical cell (Fig 5.4a). The photoelectrochemical studies of the rGO, ZnO-rGO and Ag-ZnO-rGO electrodes were carried out for the degradation of orange II dye. The percentage removal for the as-prepared rGO electrode after 210 min was 73%. The introduction of ZnO and Ag-ZnO increased the photoelectrochemical oxidation efficiency to a percentage removal of 87 % (ZnO-rGO) and 93 % (Ag-ZnO-rGO) respectively. This is due to the photoactive ability of ZnO and its enhancement of visible light absorption by the surface plasmon resonance

effect of Ag. In addition, Ag can act as an electron sink, reducing the recombination rate of the electron-hole pairs. Consequently, there is an increase in the production of hydroxyl radicals for the degradation process.

Furthermore, Ag-ZnO-rGO electrode was investigated for the degradation of the orange II dye under electrochemical oxidation, photocatalytic degradation and photoelectrochemical oxidation processes. Electrochemical oxidation displayed lower removal efficiency when compared to the photoelectrochemical oxidation. In electrochemical oxidation, the absorbed hydroxyl groups on the electrode surface combine to form hydroxyl radicals for the oxidation of the organic pollutants and they could also combine to give oxygen molecules. Thus, evolution of oxygen can occur at the electrode as a result of the combination of these hydroxyl groups [6]. This leads to competition between the oxygen molecules and the production of hydroxyl radicals, and consequently, could results in low oxidation efficiency. However, the photogenerated electrons in photocatalytic process can be utilized in the reduction of the oxygen molecules to produce superoxide radicals and then generate more hydroxyl radicals in addition to the production of hydroxyl radicals by ZnO when irradiated with light. An enhanced performance was achieved in the photoelectrochemical process giving a removal efficiency of 93 % in comparison to electrochemical oxidation (87%) and photocatalysis (47%) after 210 min. Hence it suggests a synergistic combination of photocatalytic and electrochemical oxidation processes.

Fig. 5.4(b-c) outline the plots of the normalised concentration with time using rGO, ZnO-rGO and Ag-ZnO-rGO electrodes for photoelectrochemical oxidation, and Ag-ZnO-rGO electrode for electrochemical oxidation, photocatalysis and photoelectrochemical oxidation.

The dependence of decolourisation on pH and current density was investigated and presented in Fig. 5.4(e-f). The removal efficiency decreased as the pH of the solution was increased from pH 5 to 10 as shown in Fig.5.4e. The high percentage removal at pH 5 is due to the electrostatic interactions between the negatively-charged orange II dye (pH 2 - 9.6) [36] and the positively-charged surface of the electrode containing ZnO ($pH < pH_{pzc}$ = 6.9-9.8) [37]. Studies at extreme acidic pH of 1-3 and basic pH of 11-14 were not carried out because of the application at a higher scale where it may not be cost effective and realistic to do pH adjustment. The effect of current density is shown in Fig. 5.4f. The

removal efficiency increased as the current density was increased. This is as a result of the production of more hydroxyl radicals as the current was increasing. However, it was observed that the electrode began to leach at current densities higher than 15 $mAcm^{-2}$. Hence a current density of 15 $mAcm^{-2}$ was chosen as the optimal current density. The ability of the Ag-ZnO-rGO photoanode to withstand a current density of 15 $mAcm^{-2}$ is an indication that the electrode possesses high stability to an extent and hence could be utilised in practical applications. The degree of mineralisation of the dye was determined using total organic carbon (TOC) which gave a better removal for Ag-ZnO-rGO electrode (67.9%) in relation to ZnO-rGO (58.7%) and rGO (45.3%) electrodes respectively.

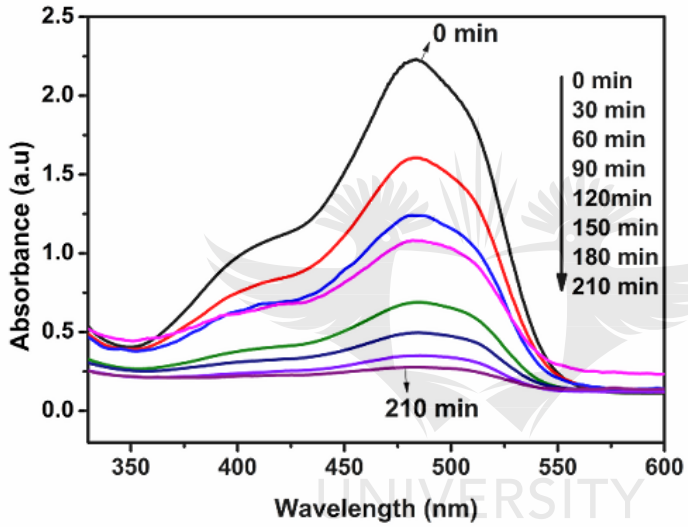

a)

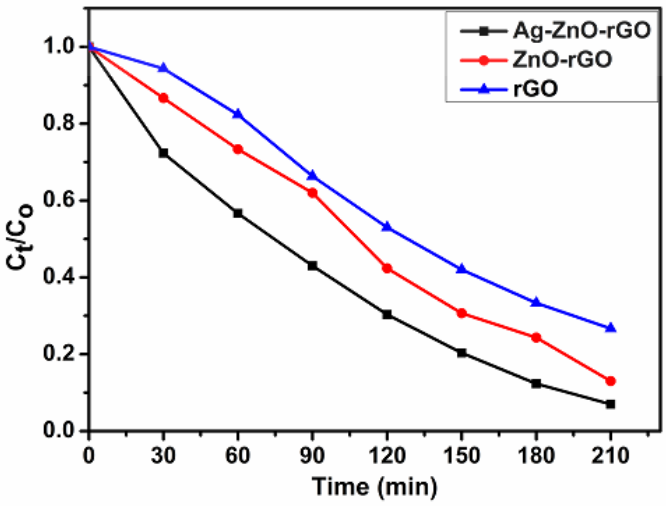

b)

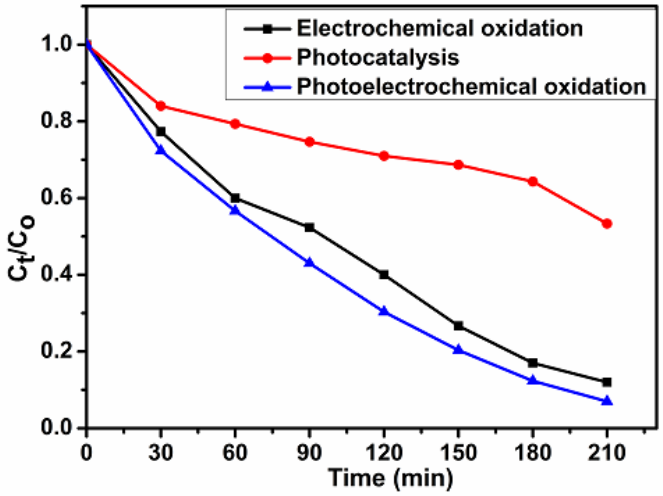

c)

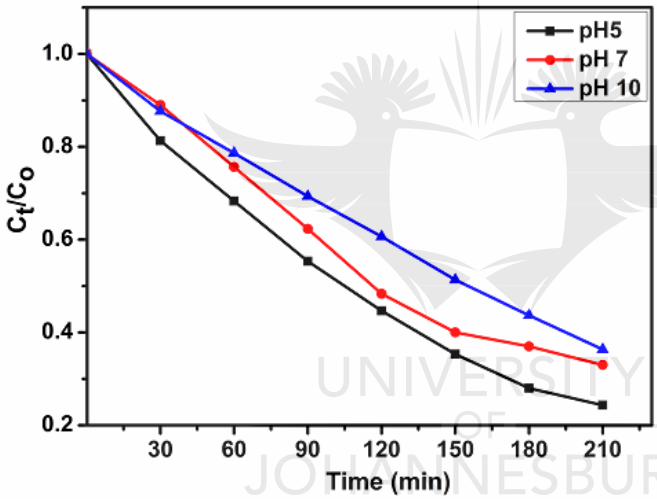

d)

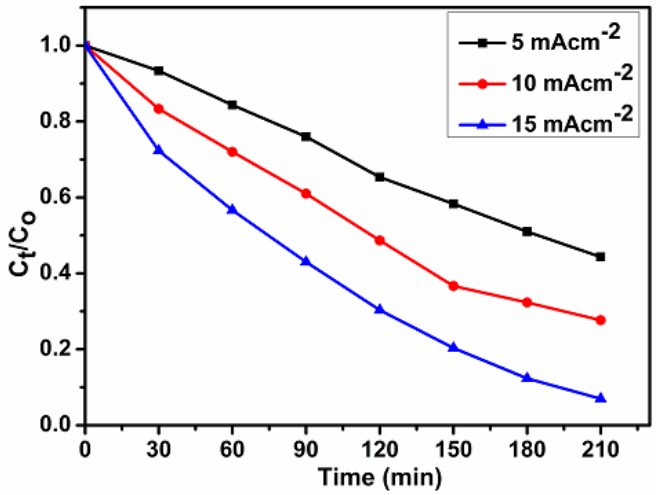

e)

Figure 5.4: (a) UV-Vis spectra for the degradation of orange II dye at Ag-ZnO-rGO electrode using photoelectrochemical oxidation; Normalised decay plots of the photoelectrochemical degradation of orange II dye (b) at rGO, ZnO-rGO and Ag-ZnO-rGO electrodes; (c) using photoelectrochemical oxidation, electrochemical oxidation and photocatalysis at Ag-ZnO-rGO electrode; and effects of (d) pH and (e) current density on the photoelectrochemical degradation of orange II dye.

5.3.8 Degradation kinetics

The kinetics of the degradation of the orange II dye was studied using the pseudo-first order kinetics equation $\ln C_o/C_t = k_{app}t$, where C_o is the initial concentration of the dye and C_t is the concentration at time, t, t is the reaction time, and k is the apparent reaction rate constant. This equation is usually applied for the kinetics of electrochemical degradation of organics [6, 38]. The data obtained for the photoelectrochemical degradation processes using the as-prepared electrodes were fitted into the pseudo-first order kinetics and linear plots of $\ln C_o / C_t$ against t were obtained which suggested that the degradation kinetics is pseudo-first order kinetics. The k_{app} values for the as-prepared electrodes are; 12.26×10^{-3} min^{-1} (Ag-ZnO-rGO) > 9.38×10^{-3} min^{-1} (ZnO-rGO) > 6.63×10^{-3} min^{-1} (rGO) with correlation coefficients (R^2) of 0.9750, 0.9479 and 0.9787 respectively. Fig. 5.5a shows the kinetics of the photoelectrochemical degradation of orange II dye in 0.1 M Na_2SO_4 at pH 5 and 15 $mAcm^{-2}$.

A plausible mechanism for the photoelectrochemical activity as a result of the voltage supply and absorption of visible light by Ag-ZnO-rGO is shown in Fig. 5.5b and the necessary reactions involved in the production of the •OH radicals for the dye degradation are shown in Eqns [5.1] – [5.13].

$$E + H_2O \rightarrow E(\bullet OH) + H^+ + e^- \text{ (at the surface of the electrode)} \qquad [5.1]$$

Where E is the electrode

The nature of material used for the fabrication of the electrode determines whether the activity of the electrode. An active electrode will interact strongly with the generated hydroxyl radical to produce a higher oxide referred to as EO which then oxidises the pollutant, orange II dye.

$$E\ (\bullet OH) \rightarrow EO + H^+ + e^- \quad [5.2]$$

$$EO + \text{orange II dye} \rightarrow E + CO_2 + H_2O \quad [5.3]$$

Or

$$\bullet OH + \text{orange II dye} \rightarrow CO_2 + H_2O \quad [5.4]$$

In addition, the evolution of oxygen as a result of the decomposition of the higher oxide may compete with the oxidation of the organic pollutant, thereby, leading to incomplete oxidation of the organic pollutant [6].

$$EO \rightarrow E + \tfrac{1}{2}\ O_2 \quad [5.5]$$

Upon the absorption of light;

$$hv + ZnO \rightarrow ZnO + h^+ + e^- \quad [5.6]$$

$$h^+ + H_2O \rightarrow H^+ + \bullet OH \quad [5.7]$$

$$e^- + O_2 \rightarrow \bullet O_2^- \quad [5.8]$$

$$\bullet O_2^- + H^+ \rightarrow HO_2\bullet \quad [5.9]$$

$$HO_2\bullet + H_2O \rightarrow H_2O_2 + \bullet OH \quad [5.10]$$

$$H_2O_2 \rightarrow 2\ \bullet OH \quad [5.11]$$

$$\bullet OH + \text{Orange II (dye)} \rightarrow CO_2 + H_2O \quad [5.12]$$

$$h^+ + \text{Orange II (dye)} \rightarrow CO_2 + H_2O \quad [5.13]$$

The photogenerated electrons can be driven from the conduction band of ZnO to the Ag and rGO by the application of a bias potential or electrical energy, and thereby reducing the recombination of the charges within the ZnO [11]. The holes react with water molecules to form a proton and hydroxyl radical (•OH) while the oxygen molecules released in the waste water react with the photogenerated electrons to form a superoxide oxygen radical ($\bullet O_2^-$). The $\bullet O_2^-$ reacts with a proton to form hydroperoxide radical ($H_2O\bullet$) which can react with water to give hydrogen peroxide which in turn generates hydroxyl

radicals. Consequently, these radicals and the holes are involved in reactions with the orange II dye molecules repeatedly to degrade and possibly mineralised them into less toxic substances such as CO_2 and H_2O [4, 39].

The improved photoelectrochemical performance of the Ag-ZnO-rGO can be attributed to: (i) the surface plasmon resonance of Ag [20], (ii) reduced electron-hole pair recombination by enhanced interfacial electron transport between Ag and ZnO [14, 40], (iii) the outstanding electron mobility/conductivity of reduced graphene oxide which enhanced the transfer of photogenerated electrons and holes from ZnO to the graphene, thus, minimizing the rate of recombination of the electron-hole pairs [7, 20].

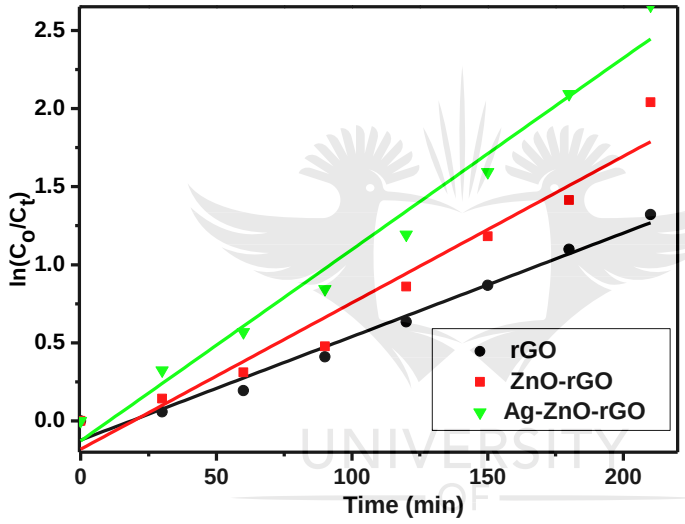

a)

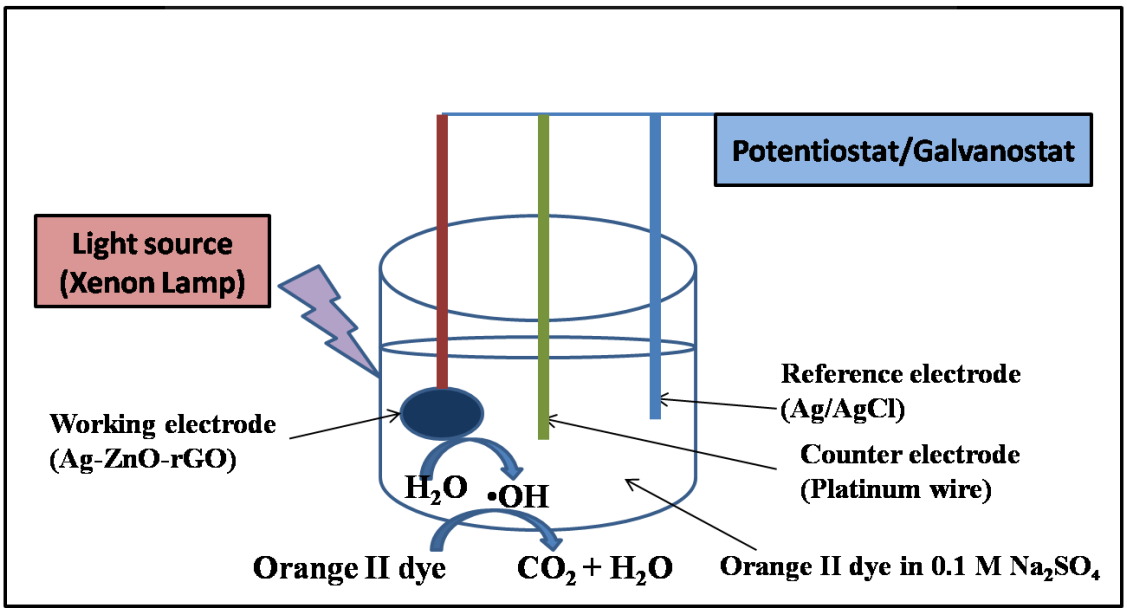

b)

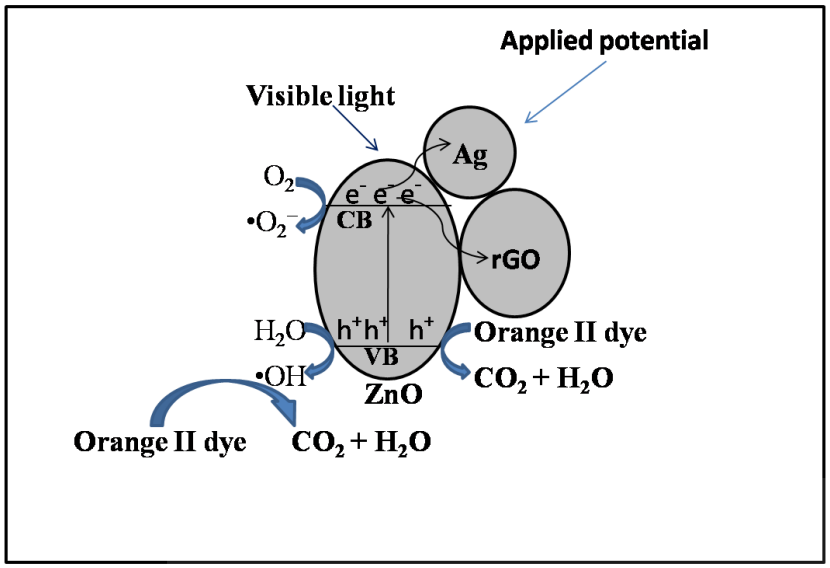

c)

Figure 5.5: (a) Kinetic plots of photoelectrochemical degradation of orange II dye at pH 5 and 15 $mAcm^{-2}$ using rGO, ZnO-rGO and Ag-ZnO-rGO electrodes; (b) photoelectrochemical set-up for the degradation of orange II dye (c) a proposed mechanism for the photoelectrochemical activity of the as-prepared Ag-ZnO-rGO for the degradation of orange II dye.

5.4 SUB CONCLUSION

A novel photoanode of Ag-ZnO-GO nanocomposite was synthesised and characterised using various spectroscopic, electron microscopic and electrochemical techniques. The photoanode was used in the photoelectrochemical degradation of orange II dye with a percentage removal of 93%. The presence of Ag-ZnO improved the photoelectrochemical performance of the photoanode due to the production of hydroxyl radicals upon the irradiation of ZnO by visible light, and the surface plasmon resonance effect of Ag. The degradation kinetics followed a pseudo first order reaction. Hence Ag-ZnO-rGO photoanode can be employed in the photoelectrochemical degradation of dyes in water treatment process.

5.5 REFERENCE

[1] J. Davey, A. Schäfer, Ultrafiltration to Supply Drinking Water in International Development: A Review of Opportunities, Appropriate Technologies for Environmental Protection in the Developing World, Springer2009, pp. 151-168.

[2] R.P. Schwarzenbach, B.I. Escher, K. Fenner, T.B. Hofstetter, C.A. Johnson, U. Von Gunten, B. Wehrli, The challenge of micropollutants in aquatic systems, Science, 313 (2006) 1072-1077.

[3] J. Méndez-Hernández, F. Ramírez-Vives, M. Solís-Oba, A. Solís-Oba, A. Sobrino-Figueroa, O. Loera, Detoxification and mineralization of Acid Blue 74: study of an alternative secondary treatment to improve the enzymatic decolourization, World Journal of Microbiology and Biotechnology, 29 (2013) 805-814.

[4] S.H.S. Chan, T. Yeong Wu, J.C. Juan, C.Y. Teh, Recent developments of metal oxide semiconductors as photocatalysts in advanced oxidation processes (AOPs) for treatment of dye waste-water, Journal of Chemical Technology and Biotechnology, 86 (2011) 1130-1158.

[5] M.I. Litter, Introduction to photochemical advanced oxidation processes for water treatment, Environmental Photochemistry Part II, Springer2005, pp. 325-366.

[6] B. Ntsendwana, S. Sampath, B. Mamba, O. Arotiba, Photoelectrochemical oxidation of p-nitrophenol on an expanded graphite–TiO 2 electrode, Photochemical & Photobiological Sciences, 12 (2013) 1091-1102.

[7] F. Chen, F. Yan, Q. Chen, Y. Wang, L. Han, Z. Chen, S. Fang, Fabrication of Fe 3 O 4@ SiO 2@ TiO 2 nanoparticles supported by graphene oxide sheets for the repeated adsorption and photocatalytic degradation of rhodamine B under UV irradiation, Dalton Transactions, 43 (2014) 13537-13544.

[8] K. Vinodgopal, P.V. Kamat, Electrochemically assisted photocatalysis using nanocrystalline semiconductor thin films, Solar energy materials and solar cells, 38 (1995) 401-410.

[9] J. Li, S. Lv, Y. Liu, J. Bai, B. Zhou, X. Hu, Photoeletrocatalytic activity of an n-ZnO/p-Cu_2O/n-TNA ternary heterojunction electrode for tetracycline degradation, Journal of hazardous materials, 262 (2013) 482-488.

[10] Y. Wang, Y.-Z. Zheng, S. Lu, X. Tao, Y. Che, J.-F. Chen, Visible-Light-Responsive TiO2-Coated ZnO: I Nanorod Array Films with Enhanced Photoelectrochemical and Photocatalytic Performance, ACS applied materials & interfaces, 7 (2015) 6093-6101.

[11] A. Zhu, Q. Zhao, X. Li, Y. Shi, $BiFeO_3/TiO_2$ nanotube arrays composite electrode: Construction, characterization, and enhanced photoelectrochemical properties, ACS applied materials & interfaces, 6 (2013) 671-679.

[12] L. Xiong, T.W. Ng, Y. Yu, D. Xia, H.Y. Yip, G. Li, T. An, H. Zhao, P.K. Wong, N-type Cu_2O Film for Photocatalytic and Photoelectrocatalytic Processes: Its stability and Inactivation of E. coli, Electrochimica Acta, 153 (2015) 583-593.

[13] A. Di Paola, E. García-López, G. Marcì, L. Palmisano, A survey of photocatalytic materials for environmental remediation, Journal of hazardous materials, 211 (2012) 3-29.

[14] S. Ma, J. Xue, Y. Zhou, Z. Zhang, Photochemical synthesis of ZnO/Ag_2O heterostructures with enhanced ultraviolet and visible photocatalytic activity, Journal of Materials Chemistry A, 2 (2014) 7272-7280.

[15] F. Chen, Z. Liu, Y. Liu, P. Fang, Y. Dai, Enhanced adsorption and photocatalytic degradation of high-concentration methylene blue on Ag_2O-modified TiO_2-based nanosheet, Chemical Engineering Journal, 221 (2013) 283-291.

[16] S. Liu, N. Wang, Y. Zhang, Y. Li, Z. Han, P. Na, Efficient removal of radioactive iodide ions from water by three-dimensional Ag_2O–Ag/TiO_2 composites under visible light irradiation, Journal of hazardous materials, 284 (2015) 171-181.

[17] J. Qin, R. Li, C. Lu, Y. Jiang, H. Tang, X. Yang, Ag/ZnO/graphene oxide heterostructure for the removal of rhodamine B by the synergistic adsorption–degradation effects, Ceramics International, 41 (2015) 4231-4237.

[18] K.-W. Park, J.H. Jung, Spectroscopic and electrochemical characteristics of a carboxylated graphene–ZnO composites, Journal of Power Sources, 199 (2012) 379-385.

[19] M. Tang, X. Xu, T. Wu, S. Zhang, X. Li, Y. Li, Polyacrylamide grafting of modified graphene oxides by in situ free radical polymerization, Materials Research Bulletin, 60 (2014) 576-583.

[20] P. Wang, Y. Tang, Z. Dong, Z. Chen, T.-T. Lim, Ag–AgBr/TiO_2/RGO nanocomposite for visible-light photocatalytic degradation of penicillin G, Journal of Materials Chemistry A, 1 (2013) 4718-4727.

[21] M. Tian, B. Adams, J. Wen, R.M. Asmussen, A. Chen, Photoelectrochemical oxidation of salicylic acid and salicylaldehyde on titanium dioxide nanotube arrays, Electrochimica Acta, 54 (2009) 3799-3805.

[22] Y. Li, L. Zhang, X. Xiang, D. Yan, F. Li, Engineering of ZnCo-layered double hydroxide nanowalls toward high-efficiency electrochemical water oxidation, Journal of Materials Chemistry A, 2 (2014) 13250-13258.

[23] W. He, Y. Yang, L. Wang, J. Yang, X. Xiang, D. Yan, F. Li, Photoelectrochemical water oxidation efficiency of a core/shell array photoanode enhanced by a dual suppression strategy, ChemSusChem, 8 (2015) 1568-1576.

[24] W. He, R. Wang, C. Zhou, J. Yang, F. Li, X. Xiang, Controlling the Structure and Photoelectrochemical Performance of $BiVO_4$ Photoanodes Prepared from Electrodeposited Bismuth Precursors: Effect of Zinc Ions as Directing Agent, Industrial & Engineering Chemistry Research, 54 (2015) 10723-10730.

[25] W. He, R. Wang, L. Zhang, J. Zhu, X. Xiang, F. Li, Enhanced photoelectrochemical water oxidation on a $BiVO_4$ photoanode modified with multi-functional layered double hydroxide nanowalls, Journal of Materials Chemistry A, 3 (2015) 17977-17982.

[26] X. Xiang, J. Fielden, W. Rodríguez-Córdoba, Z. Huang, N. Zhang, Z. Luo, D.G. Musaev, T. Lian, C.L. Hill, Electron transfer dynamics in semiconductor–chromophore–polyoxometalate catalyst photoanodes, The Journal of Physical Chemistry C, 117 (2013) 918-926.

[27] A.I. Uddin, D.-T. Phan, G.-S. Chung, Low temperature acetylene gas sensor based on Ag nanoparticles-loaded ZnO-reduced graphene oxide hybrid, Sensors and Actuators B: Chemical, 207 (2015) 362-369.

[28] A. Meng, J. Shao, X. Fan, J. Wang, Z. Li, Rapid synthesis of a flower-like ZnO/rGO/Ag micro/nano-composite with enhanced photocatalytic performance by a one-step microwave method, RSC Advances, 4 (2014) 60300-60305.

[29] H.L. Poh, F. Šaněk, A. Ambrosi, G. Zhao, Z. Sofer, M. Pumera, Graphenes prepared by Staudenmaier, Hofmann and Hummers methods with consequent thermal exfoliation exhibit very different electrochemical properties, Nanoscale, 4 (2012) 3515-3522.

[30] J. Zhang, H. Yang, G. Shen, P. Cheng, J. Zhang, S. Guo, Reduction of graphene oxide via L-ascorbic acid, Chemical Communications, 46 (2010) 1112-1114.

[31] H. Li, Z. Lei, C. Liu, Z. Zhang, B. Lu, Photocatalytic degradation of lignin on synthesized Ag–AgCl/ZnO nanorods under solar light and preliminary trials for methane fermentation, Bioresource technology, 175 (2015) 494-501.

[32] E.H. Umukoro, M.G. Peleyeju, J.C. Ngila, O.A. Arotiba, Photocatalytic degradation of acid blue 74 in water using Ag–Ag_2O–ZnO nanostuctures anchored on graphene oxide, Solid State Sciences, 51 (2016) 66-73.

[33] B. Ntsendwana, B.B. Mamba, S. Sampath, O.A. Arotiba, Synthesis, characterisation and application of an exfoliated graphite–diamond composite electrode in the electrochemical degradation of trichloroethylene, RSC Advances, 3 (2013) 24473-24483.

[34] A.K. Das, M. Srivastav, R.K. Layek, M.E. Uddin, D. Jung, N.H. Kim, J.H. Lee, Iodide-mediated room temperature reduction of graphene oxide: a rapid chemical route for the synthesis of a bifunctional electrocatalyst, Journal of Materials Chemistry A, 2 (2014) 1332-1340.

[35] P. Wang, B. Huang, Q. Zhang, X. Zhang, X. Qin, Y. Dai, J. Zhan, J. Yu, H. Liu, Z. Lou, Highly efficient visible light plasmonic photocatalyst Ag@Ag(Br, I), Chemistry-A European Journal, 16 (2010) 10042-10047.

[36] L. Abramian, H. El-Rassy, Adsorption kinetics and thermodynamics of azo-dye Orange II onto highly porous titania aerogel, Chemical Engineering Journal, 150 (2009) 403-410.

[37] M.A. Chamjangali, S. Boroumand, Synthesis of flower-like Ag-ZnO nanostructure and its application in the photodegradation of methyl orange, Journal of the Brazilian Chemical Society, 24 (2013) 1329-1338.

[38] J. Zhang, M. Li, Z. Feng, J. Chen, C. Li, UV Raman spectroscopic study on TiO_2.I. Phase transformation at the surface and in the bulk, The Journal of Physical Chemistry B, 110 (2006) 927-935.

[39] H. Hua, Y. Xi, Z. Zhao, X. Xie, C. Hu, H. Liu, Gram-scale wet chemical synthesis of Ag_2O/TiO_2 aggregated sphere heterostructure with high photocatalytic activity, Materials Letters, 91 (2013) 81-83.

[40] D. Sarkar, C.K. Ghosh, S. Mukherjee, K.K. Chattopadhyay, Three dimensional Ag_2O/TiO_2 type-II (p–n) nanoheterojunctions for superior photocatalytic activity, ACS applied materials & interfaces, 5 (2012) 331-337.

CHAPTER 6

TOWARDS WASTEWATER TREATMENT: PHOTO-ASSISTED ELECTROCHEMICAL DEGRADATION OF 2-NITROPHENOL AND ORANGE II DYE AT A TUNGSTEN TRIOXIDE-EXFOLIATED GRAPHITE COMPOSITE ELECTRODE[1]

6.1 INTRODUCTION

Phenol and its nitro derivatives have been widely used in industries involved in the manufacturing of explosives, herbicides, textiles, pesticides, dyes, paper, etc. [1]. They are bio-refractory organics that have been listed as one of the persistent organic pollutants that are toxic and of priority by United States Environmental Protection Agencies (USEPA), especially 2-nitrophenol which is toxic and mutagenic to living organisms. Furthermore, the release of wastewaters containing these compounds from industries could pose potential hazards to humans and the environment in general [2]. Consequently, there is need for proper treatment of these industrial wastewaters before being released into water bodies. The removal of organic pollutants such as nitro-phenols and dyes by conventional methods is ineffective and difficult [2-5] due to their recalcitrant nature.

However, advanced oxidation processes (AOPs) have been discovered as a favourable and promising approach for environmental remediation, and it is now becoming widely utilised in degrading organic pollutants (dyes and phenolic compounds) in water treatment processes. AOP involves the production of hydroxyl radical which is a non-selective oxidising agent and other powerful oxidants for the degradation of recalcitrant organics [1, 6]. Generally, electrochemical oxidation is an AOP in which hydrogen peroxide and hydroxyl radicals are produced at the anode surface [7]. The oxidation of the organics occurs by either anodic oxidation which is done directly, giving low efficiency or chemical reactions with hydroxyl radicals that are electrochemically generated [7, 8]. However, there are limitations associated with this process which include mass transfer due to low concentration of the organics, and oxygen evolution as a result of the application of high voltage for the degradation of the organic pollutants [9]. Moreover, this process requires the use of high voltage and long time [7, 8]. Thus, there is necessity for the improvement on electrochemical oxidation by combining it with photocatalysis in which photogenerated

[1] This chapter has been published in: Umukoro, E. H.; Peleyeju, G.; Ngila, J. C.; Arotiba, O. A. Towards wastewater treatment: Photo-assisted electrochemical degradation of 2-nitrophenol and orange II dye at a tungsten trioxide-exfoliated graphite composite. *Chemical Engineering Journal*, **2017**, 317, 290-301.

electrons from a semiconductor photocatalyst can react with evolved oxygen to produce oxygen reactive radicals ($\bullet O_2^-$) that can further react with protons to generate $H_2O\bullet$. The radicals, in turn, undergo reactions with the organic pollutant species [10, 11]. This photo-assisted electrochemical process can be carried out by immobilising a photoactive substance such as a metal oxide semiconductor on a conducting material with the application of a bias potential, accompanied by the generation of OH• species by both substances for the degradation of organics [11, 12]. Various photoactive metal oxides such as WO_3, TiO_2, MnO_2, ZnO, Fe_2O_3, NiO, etc., have been employed as photocatalysts and photoelectrocatalysts for the degradation of pollutants [7, 12-21]. Ag-ZnO doped reduced graphene oxide composite have been fabricated as photoanode for degrading orange II dye [11]. TiO_2-RuO_2/Ti electrode was modified with WO_3 and applied for the electrochemical and photoelectrochemical degradation of acid orange 7 dye using UV and visible light. Results from the work suggested that modification with 6% content of WO_3 gave the highest degradation of the dye [7]. Titanium dioxide nanotube arrays have been reported as photoanodes for the photoelectrochemical oxidation of salicylaldehyde [22]. Yu et al. reported the photoelectrochemical property of expanded graphite-TiO_2 composite photoanode by using titanium mesh as a substrate for the degradation of phenol [23]. Cerium, nitrogen and sulphur co-doped TiO2 composite was prepared and its photoelectrochemical and photocatalytic properties were tested on volatile organic compounds [24]. Kim et al., reported the simultaneous removal of heavy metals and organic pollutant from wastewater using WO_3 photoanode in a Pt and Ti cells [25]. WO_3 thin films have been deposited on glass and fluorine tin oxide coated glass as substrates as photoelectrodes. Their photoelectrochemical properties were investigated for the degradation of methyl red and methyl blue dyes [16, 26]. The photoelectrocatalytic property of BiO nanoplate-ZnO nanorod has been studied for its water splitting and pollutant degradation performance [27]. Titanium nanotube arrays functionalised with reduced graphene oxide have been used as photo-anode for the simultaneous removal of chromium and organic pollutants in water treatment [28]. The enhanced photocatalytic activity of AgI/WO_3 nanocomposites has been reported for the degradation of tetracycline [29]. In addition, WO_3 thin films were deposited on platinum gauze substrate as photoelectrodes for the degradation of orange II dye [30]. Furthermore, bismuth tungstate that was co-doped with samarium and nitrogen was synthesised with enhanced photocatalytic activity under visible light [31].

Tungsten trioxide (WO_3), an n-type semiconductor having a band gap around 2.8 eV, has recovery ability from photocorrosion, physicochemical properties stability and visible light sensitivity which makes it a good photocatalyst [16]. It is an inexpensive photocatalyst with different applications such as in gas sensing, photocatalysis, energy renewal and storage, and electrochromic devices [32-35]. Nevertheless, like other semiconductor, there are limitations associated to its utilisation such as recombination of photo-generated holes and electrons upon the irradiation with a light source. Hence there is need to minimise the recombination by doping with other materials such as exfoliated graphite, and the use of electricity to remove the photogenerated electrons from the semiconductor surface.

Exfoliated graphite (EG), a carbonaceous material, possesses low density, large surface area, compressibility, high temperature resistance, high electrical conductivity and good electron transport capacity [12, 23]. In addition, it has high thermal conductivity, good mechanical property and can bear very high current density. Also, it can be produced using several methods such as the direct exfoliation of graphite, etc. [36-40]. Due to its high electron transport nature, the photo-generated holes and electrons of the WO_3 can be transferred to the exfoliated graphite. As a result, the recombination process of the electron-hole pair would become minimal and the photoactivity of the WO_3 in the composite would be improved, thus producing more hydroxyl radicals for the breaking down of the organics. Moreover, the porous nature of the exfoliated graphite enhances the trapping of photocatalyst. Consequently, it will help in immobilising the powdered WO_3 and hence it reduces losses in recovery process [9, 12, 23, 41]. In addition, EG has been reported for its electrocatalytic property which made it viable for electrochemical sensing and electrochemical oxidation of pollutants [9, 41, 42].

Motivated by the combined properties of WO_3 and EG discussed above, it can be supposed that WO_3-EG composite is attractive and beneficial as photoelectrocatalyst for the photo-assisted electrochemical degradation of 2-nitrophenol and orange II dye.

There are several reports on the removal or degradation of 2-nitrophenols using ozone [1], electron fenton [2], and cerium doped WO_3 photocatalyst in photocatalysis [13]. However, to the best of the authors' knowledge, WO_3-EG composite electrode has not been employed for the photo-assisted electrochemical degradation of 2-nitrophenol and orange II dye for water treatment process. Thus, in this work, WO_3 was trapped on exfoliated graphite to form a composite, constructed into an electrode and employed for the

electrochemical and photo-assisted electrochemical degradation of 2-nitrophenol as a model pollutant in wastewater. It was further employed for degrading orange II dye.

6.2 EXPERIMENTAL PROCEDURES

6.2.1 Materials and apparatus

Ammonium metatungstate hydrate, sulphuric acid (98%), nitric acid, natural graphite flakes, sodium sulphate, potassium hexacyanoferrate (II), potassium hexacyanoferrate (III), potassium chloride, 2-nitrophenol and orange II dye. All reagents used for this work were purchased from Sigma Aldrich, Germany.

6.2.2 Preparation of WO_3 nanoparticles

WO_3 nanoparticles were prepared by a precipitation method in the presence of citric acid [43]. Precisely, 6.9079 g of ammonium metatungstate hydrate was dissolved in 30% v/v, nitric acid solution (50ml) at 70 ºC while stirring. The temperature was maintained while the solution was being stirred until a yellow precipitate was formed. Heating was continued at that temperature until the water was completed evaporated. The solid obtained was subjected to thermal treatment at 600 ºC for 3 h to produce the WO_3 nanoparticles.

6.2.3 Preparation of WO_3-EG composite

Natural graphite was sieved using a 300 µm sieve mesh and intercalated by being soaked in concentrated nitric acid and sulphuric acid mixture in a ratio of 1:3 by volume for 48 hours at room temperature. The intercalated material was then washed to pH 7 and air-dried. It was further exfoliated by subjecting it to temperature of 800 ºC for about a minute to obtained a puffed up exfoliated graphite material.

For the preparation of the WO_3-EG composite, 2g of the as-prepared WO_3 was dispersed in absolute ethanol and sonicated for 30 min to obtain uniformity of suspension of the nanoparticles. Then, 2g of EG was added and further sonicated for 10 min after which the mixture was put in an oven to dry at 100 ºC overnight to achieve complete evaporation of the ethanol.

6.2.4 Fabrication of WO_3-EG composite electrode

The as-prepared WO_3-EG composite was compacted into a pellet that is 1.3 cm in diameter by a hydraulic press at a high pressure of 10000 psi. The pellet was employed for the construction of an electrode with the use of a copper wire, non-conductive epoxy resin and conductive silver paint. The WO_3-EG composite pellet was placed on the coiled part of the copper wire with the assistance of the conductive silver paint and allowed to dry. The edge of the composite pellet was sealed with the resin to allow the flow of electricity from only the basal plane. Furthermore, it was put in a glass rod before being used for the experiment.

6.2.5 Characterisation of WO_3-EG composite

Characterisation was done on exfoliated graphite, tungsten trioxide (WO_3) and WO_3-EG composites with X-ray diffractometer (Rigagu Ultima IV, Japan). This was done using Cu Kα radiation (λ=0.15406) with K-beta filter at 40 kV and 30 mA. It was conducted using scintillation counter at a range of 5 to 90º and the speed is 2º /min. Surface morphological studies were carried out on the as-prepared materials with the aid of scanning electron microscopy (SEM) (TESCAN, Vega 3 XMU, Czech Republic). The elemental composition of the materials was investigated with the aid of energy-dispersive x-ray spectrometer (EDS) (TESCAN, Czech Republic) coupled to the scanning electron microscope. Furthermore, Raman and FTIR studies were done with the help of Perkin Elmer Raman microscope (Raman micro 200, USA) and Perkin Elmer FTIR spectrometer (Spectrum 100, USA) respectively. UV-Visible spectrophotometer (Cary 60, Agilent technologies, Australia) was used to obtain the removal efficiency (decolourisation) of 2-nitrophenol and orange II dye. The light source was Oriel LCA-100 Solar Simulator having 100 W xenon lamp and AM1.5G filter which produces 100mWcm^{-2}.

6.2.6 Photoelectrochemical properties

Photoelectrochemical properties of the materials were studied using 5 mM potassium ferricynanide and ferrocyanide in a 0.1 M KCl solution which was used as a redox probe. Also, 0.1 M Na_2SO_4 solution was utilised as the supporting electrolyte. Cyclic voltammetry (CV), linear sweep voltammetry (LSV) and photocurrent response in the presence of a light source (Oriel LCA-100 Solar Simulator) were carried out on an electrochemical work station with three electrodes (Autolab (302N)

potentiostat/galvanostat) having WO_3-EG (1.3 cm in diameter), Ag/AgCl (3.0 M KCl) and platinum foil as the working electrode, reference electrode and counter electrode respectively.

6.2.7 Electrochemical and photo-assisted electrochemical experiments

The photo-assisted electrochemical degradation of the organics was carried out in a 100 mL reactor containing 20 ppm of 2-nitrophenol in 0.1 M Na_2SO_4 solution. The EG or WO_3-EG electrodes were fixed vertically facing the incident light of the simulator. The power supply for the photo-assisted electrochemical degradation of the 2-nitrophenol experiment was the potentiostat/galvanostat electrochemical station. The light source was Oriel LCA-100 Solar Simulator having a 100 W xenon lamp and AM1.5G filter which produces a power beam of 100 $mWcm^{-2}$ (1.0 sun equivalence), at a distance of 8 cm from the reactor. For the electrochemical degradation of the 2-nitrophenol, only current density/potential was applied without the use of light. An aliquot of the solution was collected at certain intervals from the reactor with the aid of a disposable syringe and filtered over a period 180 min. The concentration decay of the 2-nitrophenol was investigated using the UV-Visible spectrophotometer and the absorption bands of λ = 270 - 450 nm were used. The mineralisation extent was done with total organic carbon (TOC) analyzer (Teledyne Tekmar TOC fusion). The effect of current density, pH, and initial concentration on the removal of 2-nitrophenol were investigated. Furthermore, the photo-assisted electrochemical nature of the electrode was tested on the degradation of orange II dye.

6.3 RESULTS AND DISCUSSION

6.3.1 Raman spectroscopy

Raman spectroscopic technique was employed for the structural investigation of the prepared WO_3-EG sample. Fig. 6.1a shows the spectrum of EG before the addition of the WO_3 having peaks around 1590 and 1353 cm^{-1}, which correspond to the G band and D band of the graphite. The G band results from the in-plane mode of vibration of the sp^2-bonded carbon of the prepared EG. The D band which normally results from vibration of the disorder or defect-induced carbon to carbon bonds in the graphite is observed with a lower intensity. This confirms the production of a highly crystalline EG. Upon the addition of the WO_3 to the EG, there was a slight increase in the low intensity peak that appeared at

1354 cm^{-1} corresponding to the D band of EG [44]. Also, there was a shift in the peak from 1590 to 1598 cm^{-1} and a sharp reduction in the intensity of the G band. This is as a result of disorder in the graphitic sheets because of the presence of sp^3 bonding caused by the presence of WO_3 as shown in Fig. 6.1b [33]. Additional characteristic peaks of WO_3 with different intensities are displayed at 806.7, 716.7, 326.8, 269.3, 131.8 and 74.3 cm^{-1}. This indicates the interaction between the EG and the WO_3. The peaks at 326.8 and 269.3 could be attributed to the bending vibrations of WO_3 monoclinic structure while the peaks at 131.8 and 74.3 cm^{-1} can be allotted to the lattice modes [16, 45]. The high intensity peaks at 806.7 and 716.7 cm^{-1} result from the stretching of O-W-O of a monoclinic structure of WO_3, respectively.

6.3.2 X-ray diffractometry

Fig. 6.1c displays the X-ray diffraction patterns of EG, WO_3 and WO_3-EG. In Fig. 6.1c(iii), the characteristic diffraction peak of EG is observed at $2\theta = 26.6^{o}$ (002) crystal plane, with an interlayer spacing of 0.345 nm [12, 23], however, the observed peak around 37.5º is as a result of cosmic rays. The diffraction peaks of a typical monoclinic polymorph of WO_3 (JPCDS Card number 01-083-0950) were observed at $2\theta = 23.2^{o}$ (002), 23.7 (020), and 24.4 (200) with high intensities. Additional smaller peaks were obtained at 26.7 (120), 29.1 (112), 33.4 (202), 34.2 (202) and 42.1 (220) as shown in Fig. 6.1c (i). Furthermore, the increase in intensity observed at 26.7º in Fig. 6.1c (ii) for the WO_3-EG composite material is due to the diffraction peak resulting from the presence of EG in the WO_3 material. This indicates the co-existence of EG and WO_3 in the as-prepared WO_3-EG material. The estimated crystallite size of the prepared material has an average value of 24.69 nm. This was estimated by employing the Debye-Scherrer's equation: $D = K\lambda / \beta \cos\theta$; K is a constant (0.9), λ is x-ray wavelength (nm), β is the full width of half maximum of the diffraction peak (radian), and θ is the angle of diffraction (radian).

6.3.2 FTIR analysis

The presence of functional groups and chemical interactions between the prepared WO_3 and EG materials were investigated using FTIR analysis. The FTIR spectra of EG and WO_3-EG are presented in Fig. 6.Id (I and II). The peak at 3420 - 3550 cm^{-1} could be assigned to O-H vibrations of the chemisorbed water on the EG surface. Weak bands at 2850 and 2920 cm^{-1} could be due to C-H mode. The aromatic C=C vibration of the EG are

observed at 1628 cm^{-1} (strong) and 1468 cm^{-1} (weak). The absorption band at 1100 cm^{-1} could be allocated to C-O mode. Moreover, the observed small band at 1378 cm^{-1} is linked to C-O-H bending mode which occurs around 1440-1220 cm^{-1} [46]. The additional peak at 750 and 830 cm^{-1} (Fig. 6.1d (II)) can be assigned to W-O-W out of plane deformation mode and W-O-W bridging mode respectively [33, 47]. This is an indication of the presence of the WO_3 in the WO_3-EG material.

6.3.3 UV-Visible spectroscopy

Optical studies were carried out on the WO_3 and WO_3-EG samples using UV-Vis diffuse reflectance (Fig. 6.1e). It is clear that the WO_3-EG portrayed a stronger photoabsorbance in the visible region relatively to WO_3 from λ = 430-800 nm. This results from the addition of the photosensitizing EG. The solar light harvesting can be ascribed to the formation of W-O-C bonds between the WO_3 and EG interfaces. In addition, it has been reported that there is electron transfer (electronic conjugation) from WO_3 to graphene due to the closeness of the conduction band edge of WO_3 (-4.15 eV below vacuum level) to that of graphene (work function is -4.66 eV) [33, 48]. Thus, the electronic conjugation between WO_3 and EG can help in enhancing the absorption of visible light by the composite. Consequently, the capability of the WO_3-EG to absorb visible light is of importance for its improved photoelectrochemical degradation efficiency in the presence of solar energy.

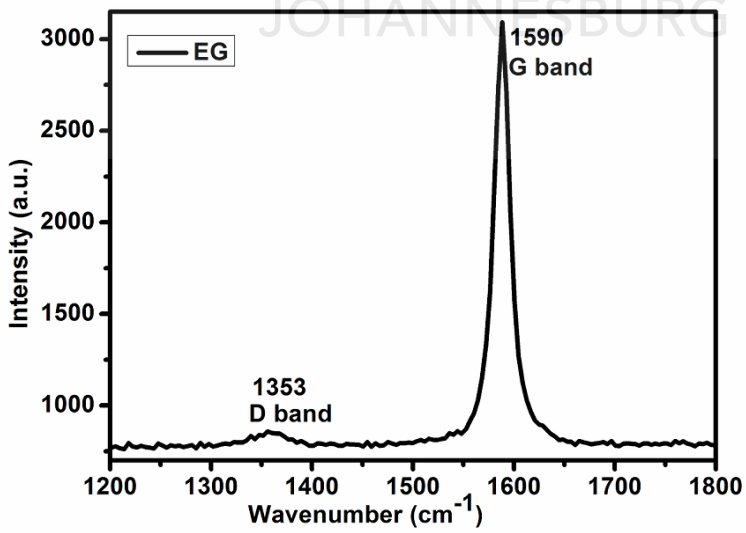

a)

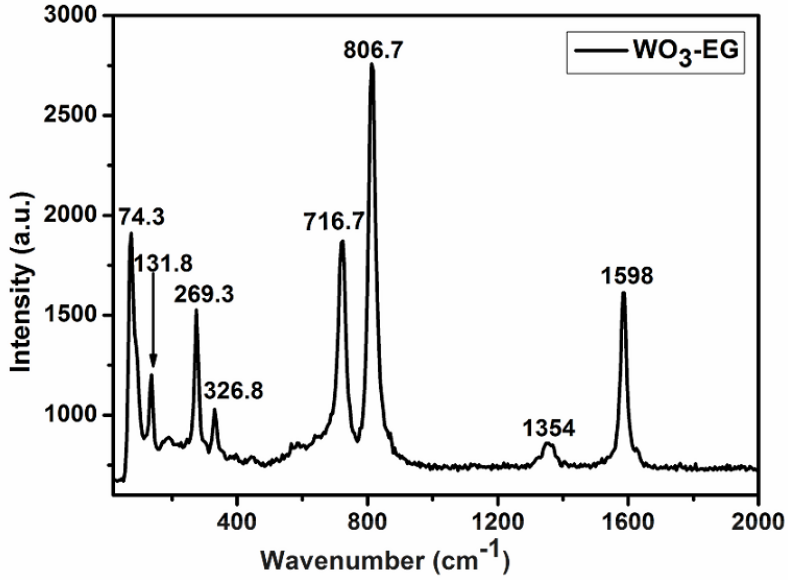

b)

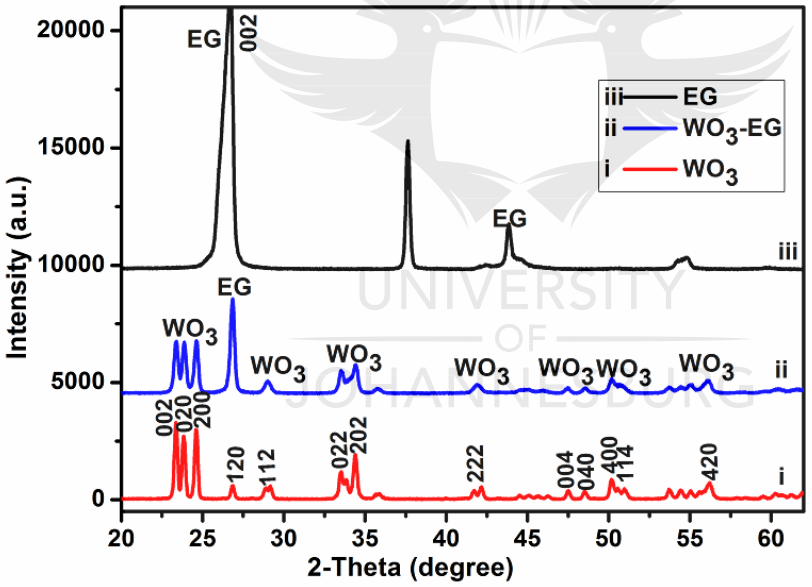

c)

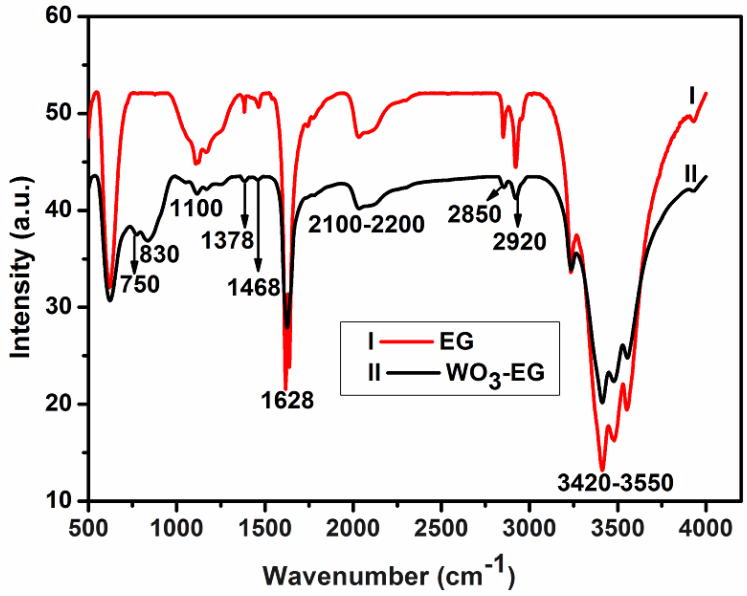

d)

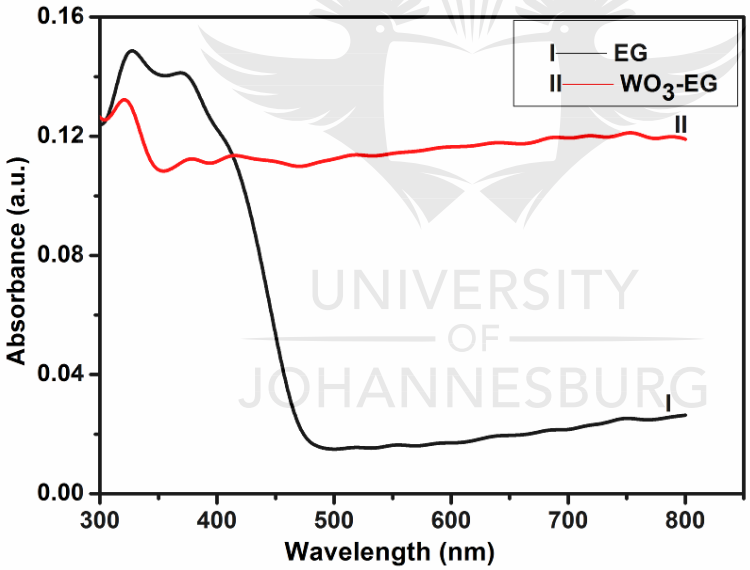

e)

Figure 6.1: Raman results of (a) EG; and (b) WO_3-EG; (c) X-ray diffraction patterns of EG; (i) WO_3, (ii) WO_3-EG and (iii) EG; (c) FTIR results of (I) EG and (II) WO_3-EG composite; and (e) UV-Visible diffuse reflectance spectra of (I) EG and (II) WO_3-EG

6.3.4 Morphological studies of EG, WO_3 and WO_3-EG

The surface morphology of EG, WO_3 and WO_3-EG samples was investigated by SEM joined to EDX spectroscopy. Figure 6.2a depicted the WO_3 nanoparticles with irregular rhombic structures. The graphitic sheets of the EG can be observed with open pore-like cavities for the entrapment of the WO_3 nanostructures (Fig. 6.2b). In Fig. 6.2c, it can be observed that the WO_3 nanoparticles are well distributed in the interlayers and edges of the graphitic sheets, thus, minimising aggregation of the WO_3 particles. This indicated that WO_3 nanoparticles were uniformly dispersed in the WO_3-EG composite material. The presence of W and O in the synthesised material was confirmed by EDS spectrum, indicating the presence of WO_3 in the EG (Fig 6.2d).

a)

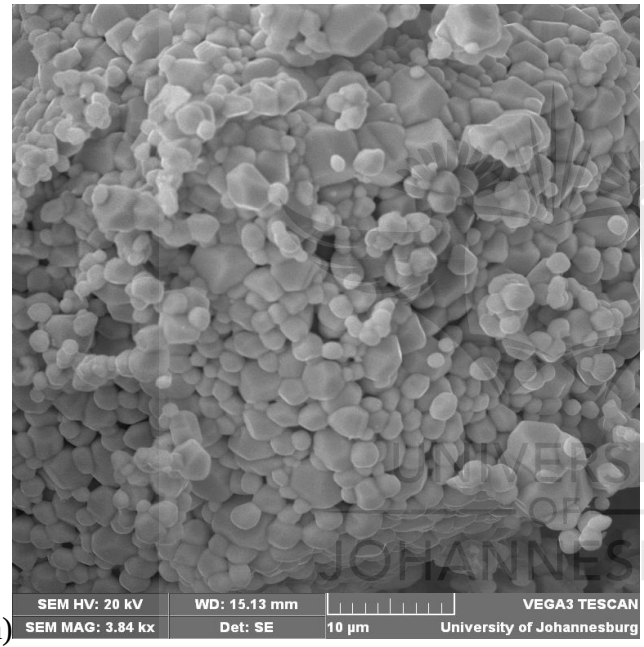

b)

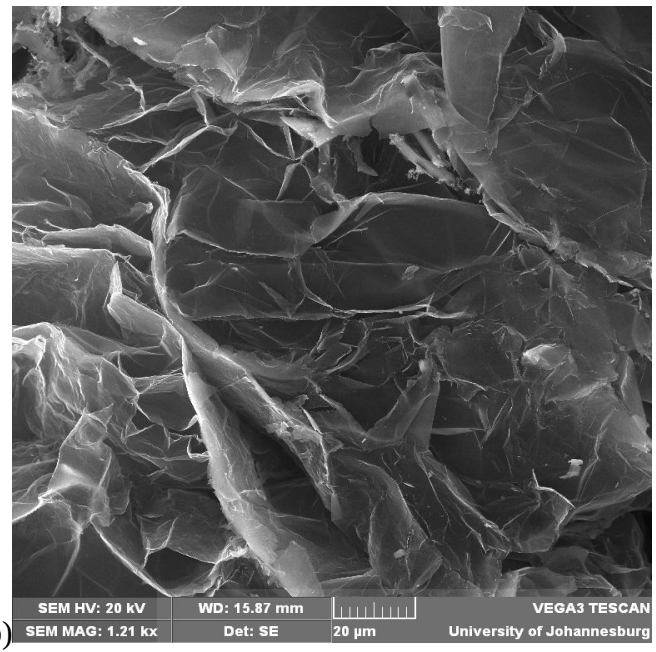

c)

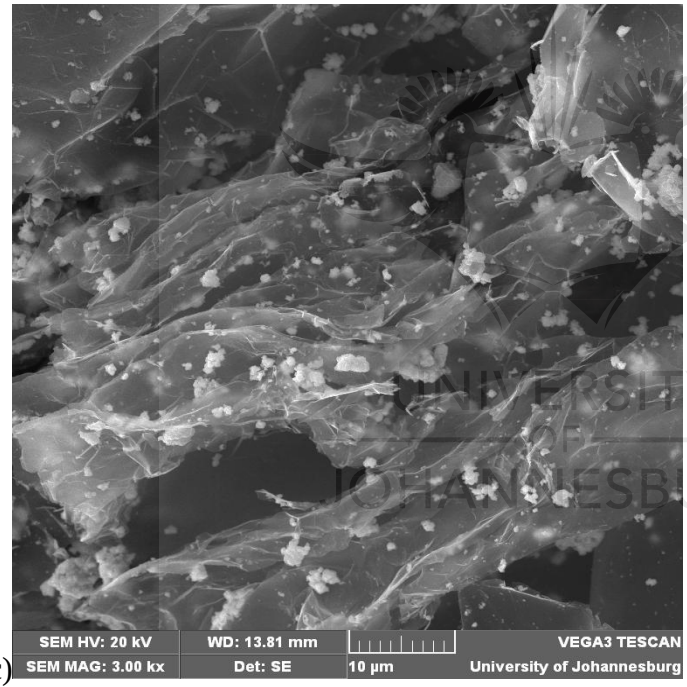

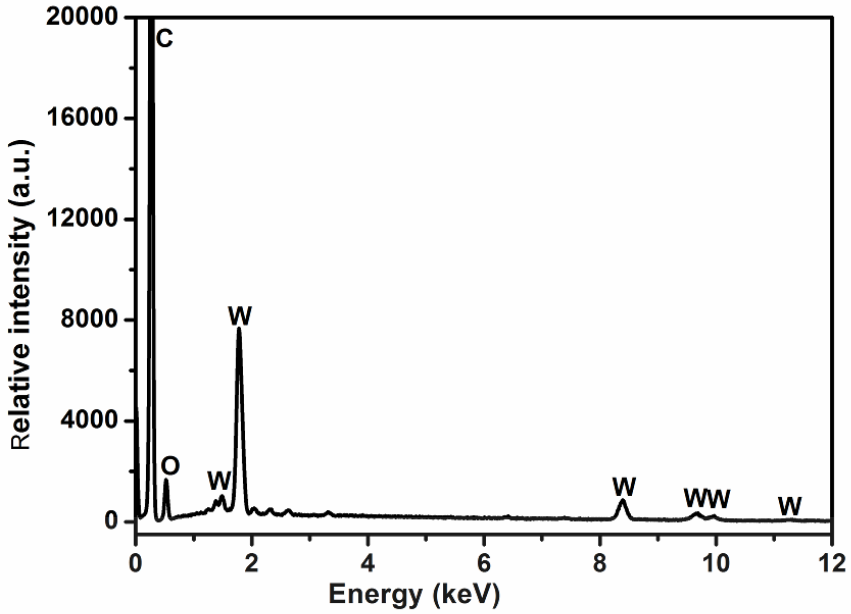

d)

Figure 6.2: (a) WO_3; (b) EG and (c) WO_3-EG composite images of SEM. (d) EDS spectrum of WO_3-EG composite

6.3.6 Electrochemical and photoelectrochemical studies of EG and WO_3-EG

Electrochemical studies were carried on the EG and WO_3-EG electrodes in a redox probe which contains a solution of 0.5 mM $[Fe(CN)_6]^{-3/-4}$ in 0.1 M KCl, and the cyclic voltammograms were recorded at a scan rate of 20 mVs^{-1} (Fig. 6.3a). It was noted that the WO_3-EG electrode displayed an increment in peak current when compared to that of the EG electrode. The increased faradaic current observed from the redox probe showed that the electrode reaction rate is higher [7]. This is due to increase in the electrode active surface area which enhanced the conductivity of the WO_3-EG electrode due to the presence of WO_3 in the EG. The electroactive surface area was calculated using the Randles–Sevcik equation, $ip = kn^{3/2}AD^{1/2}\ v^{1/2}C$; where k is a constant, 2.69×10^5, n is the number of exchanged electrons, D is the diffusion co-efficient (7.6×10^{-6} for ferrocyanide), C is the solution concentration, v is the scan rate and A is the electrode active surface area [49]. The electrode active surface area was calculated to be 0.035 and 0.085mm^2 for the EG and WO_3-EG electrodes respectively. This indicates an increment in the electrochemical active sites in the WO_3-EG electrode compared to the EG electrode [50]. A kinetic study on ferrocyanide was conducted using different scan rates. It was observed that the plot of the

peak currents versus the square root of the scan rates was linear (Fig. 6.3b), suggesting that the process of the electrochemical kinetics of the ferrocyanide was diffusion controlled [50]. Linear sweep voltammetry in the presence and absence of light was used to test the photoelectrochemical behaviour of the electrodes in the presence of 30 ppm of orange II dye in 0.1 M Na_2SO_4. Figure 6.3c showed the linear voltammograms of the EG and WO_3-EG electrodes with and without irradiation. The anodic photocurrent was seen to start around 0.23V vs RHE, and the photocurrent response increased. It was observed that the intensity of the current generated by the WO_3-EG electrode under the xenon lamp irradiation was higher than that of EG electrode without the xenon lamp irradiation. This implied that there was a flow of photogenerated electrons in the WO_3 under irradiation, and the electron transport was enhanced by the conductivity of the EG, indicating the photoactivity of the electrode [51]. The photocurrent response of EG and WO_3-EG was studied (Fig. 6.3d). The magnitude of the photogenerated current by an electrode under irradiation is an indication of the charge separation efficiency of the photogenerated holes and electrons [23, 52]. The sharp increment in the photocurrent response of the WO_3-EG electrode during irradiation suggested that the electrode is photoelectrochemically active. The photogenerated electrons from the WO_3 can be accepted and transported by the EG to the external circuit [23]. This observation is corroborated by the results obtained from the linear sweep voltammetry. Consequently, the WO_3-EG can be employed as a photoanode due to its higher photoelectrocatalytic activity for the degradation of organics in water treatment process.

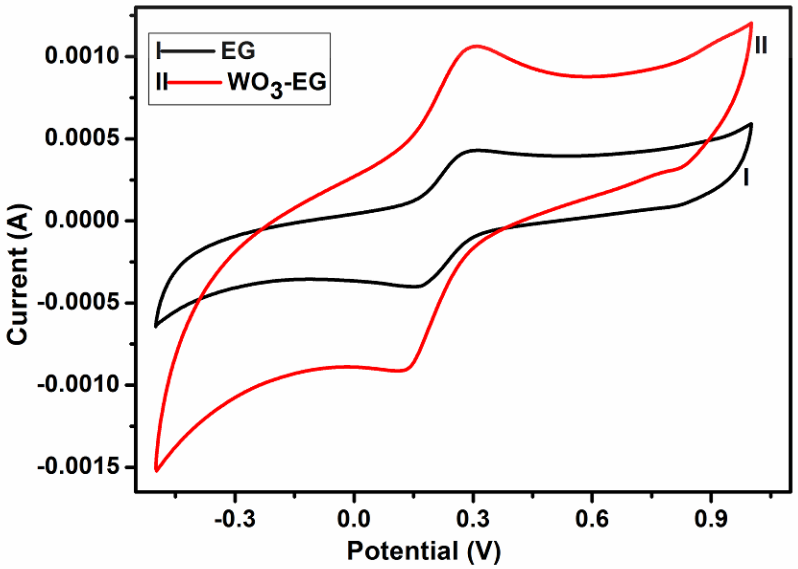

a)

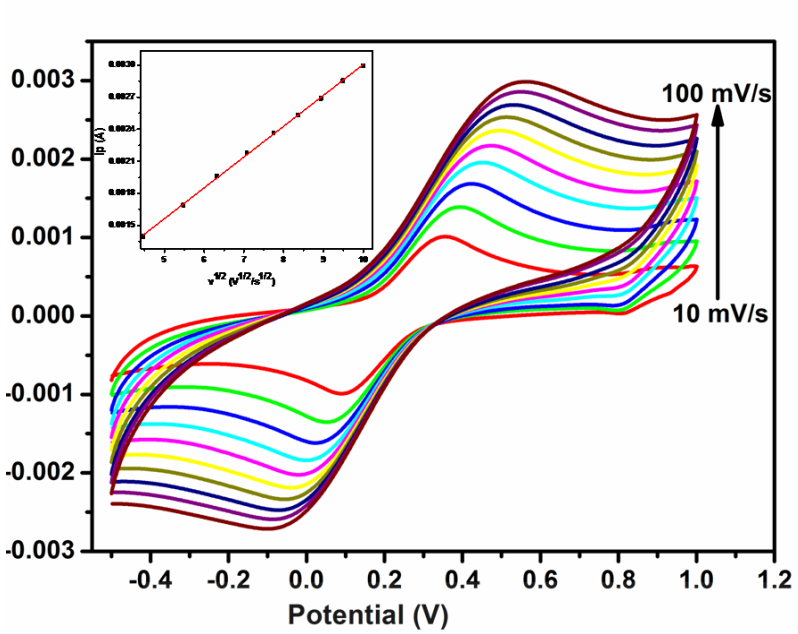

b)

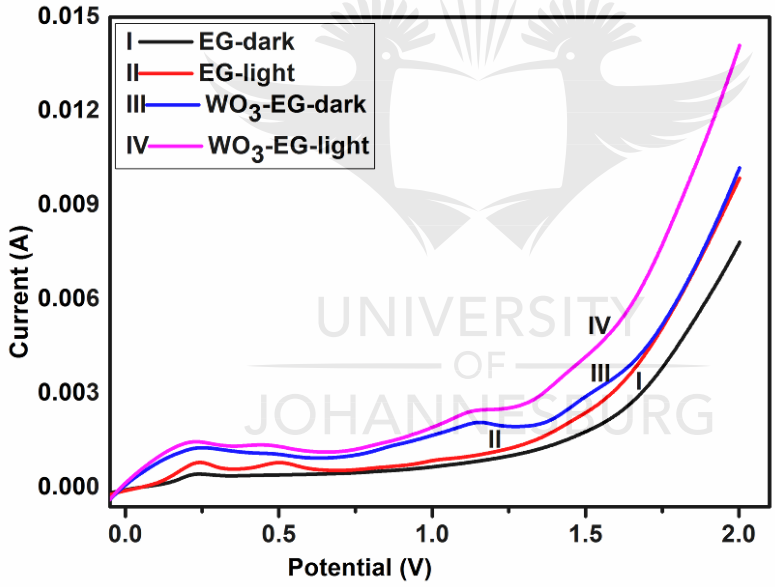

c)

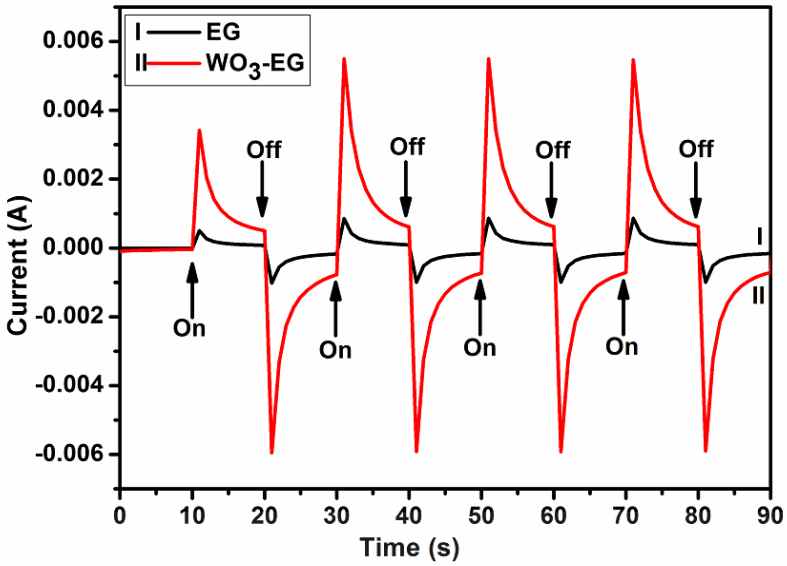

d)

Figure 6.3: (a) CVs of (I) EG and (II) WO_3-EG composite electrodes using 5mM $[Fe(CN)_6]^{-3/-4}$ in 0.1 M KCl solution at a scan rate of 20 mVs^{-1}; (b) CVs of WO_3-EG composite electrodes at different scan rate and the plot of peak currents vs square root of scan rates. (c) Linear sweep voltammograms of EG and WO_3-EG composite electrodes with (light) and without (dark) xenon lamp; and (d) responses from photocurrent of EG ((I) black) and WO_3-EG ((II) red) composite electrodes in the dark (off) and under irradiation (on)

6.3.7 Photo-assisted electrochemical degradation of 2-nitrophenol

The performance of the EG and WO_3-EG electrodes were tested on the degradation of 2-nitrophenol. It was found that WO_3-EG electrode showed a higher removal efficiency in the electrochemical degradation of 2-nitrophenol (52%) in comparison with the EG electrode (39%). Furthermore, WO_3-EG electrode gave a better removal in the photo-assisted electrochemical degradation process (82%) than the EG electrode (54%) as seen in Fig. 6.4a. This can be construed to result from the low electron transfer resistance of the WO_3-EG composite electrode which could enhance its charge separation efficiency [23]. As shown in Fig. 6.4b, the WO_3-EG composite electrode showed an enhanced removal performance in the photo-assisted electrochemical degradation process than the electrochemical degradation. This is attributed to the photosensitive nature of WO_3, leading to a flow of photogenerated holes and electrons upon irradiation, and the electron

transport was enhanced due to the presence of EG that is very conductive. This argument can be buttressed with the results from the LSV and photocurrent responses of the electrodes. Thus, it suggests there is a synergistic combination of EG and WO_3 in the composite electrode which aided the degradation process.

It is evident from Figure 6.4f that the two absorption peaks at 351 and 278 nm of the 2-nitrophenol shifted to 425 nm, with the application of the WO_3-EG electrode. Hence the 2-nitrophenol curve at 0 min before the application of the electrode for electrolysis is different from the other curves during electrolysis. Also, the faint yellow colour of the 2-Nitrophenol became deeper as a result of 2-nitrophenolate ions that are formed after 30mins of electrolysis. Furthermore, there was gradual fading of the yellow colour of the 2-nitrophenol solution which finally disappears after 180 min. In addition, the gradual disappearance of the peak at 425 nm from 30 to 180 min indicates the removal of the 2-nitrophenol using the WO_3-EG photo-electrode.

The experimental conditions were optimised by investigating the effect of current density, pH, and initial concentration of the 2-nitrophenol. The degradation of 2-nitrphenol was pH independent using the WO_3-EG composite electrode as displayed in the concentration decay plots (Fig. 6.4c). However, the removal efficiency at pH 3, 6 and 8.3 are 80, 82 and 77% respectively. It is generally known that the pKa of 2-nitrophenol is 7.2 and the phenolate anion ($C_6H_4NO_3^-$) is dominant in a solution whose pH is greater than the pKa while the neutral molecule is dominant at pH below its pKa. The higher removal of 2-nitrophenol at pH lower than its pKa could be as a result of electrostatic interactions between the neutral molecule and the tungstate ion. The lower removal could be attributed to the repulsion between the tungstate ion and the negatively-charged phenolate anion which could be in competition with hydroxyl radicals for sites on the electrode surface [12, 23]. Thus, the experiments were carried out at pH 6 as the optimum. Figure 6.4d showed the effect that current density had on the degradation efficiency of 2-nitrophenol. There was an increase in the removal efficiency from 55% to 82% with increase in current density from 5 $mAcm^{-2}$ to 10 $mAcm^{-2}$. The increased in current density aided in enhanced separation of photo-generated holes and electrons in addition to the conductivity or electron transport capacity of the EG in the composite electrode. Nevertheless, there was no significant increase as the current density was increased to 15 $mAcm^{-2}$ which gave a removal efficiency of 83%. This could be due to the production of more intermediates which tend to form a film on the electrode surface, thereby, reducing its activity. Hence 10

$mAcm^{-2}$ was taken to be the optimum which is energy cost effective for the photo-assisted electrochemical degradation of 2-nitrophenol. Furthermore, the impact of initial concentration on the photo-assisted electrochemical degradation of 2-nitrophenol was investigated. It was noticed that there was an increase in the removal efficiency as the initial concentration was increased, but it reduced with further increment. This can be ascribed to insufficient sites of degradation on the electrode surface. As the concentration of the 2-nitrophenol is increased, more molecules are absorbed and degraded on the electrode surface until there is saturation on the available sites. Also, more generated electrons are being utilized for the degradation of the molecules and may not be sufficient as the concentration was increasing. Thus, 20 ppm was used as the optimum initial concentration throughout the experiment.

The effect of content of WO_3 in the EG was investigated (Fig. 6.4e). Ratios 0.75:1, 1:1 and 1.25:1 of WO_3:EG were investigated using 0.2 g of EG in all the composites (a typical ratio of WO_3:EG is 0.2 g WO_3 to 0.2 g EG). There was an increase in the removal percentage of 2-nitrophenol from 67.5 to 82 % as the ratio of WO_3:EG was increased from 0.75:1 to 1:1. Further increment to ratio 1:1.25 of WO_3:EG led to a slight reduction in the removal percentage to 72 %. This could be due to the production of holes and electrons which generated more hydroxyl radicals for the degradation of the 2-nitrophenol. Nevertheless, there was no increase in the removal efficiency as the WO_3 content was further increased. This can be ascribed to the shielding of some of the WO_3 nanoparticles from the simulated light, making them less active due to lack of light [12, 53]. In order to test the extent of mineralisation of the 2-nitrophenol after 180 min using the WO_3-EG electrode, the total organic carbon removal was conducted which resulted in 34.6% and 69% removal for electrochemical and photo-assisted electrochemical degradation of 2-nitrophenol respectively. This result is comparable to the reports of other scientists having TOC removal of 2-nitrophenol around 31, 70 and 92 % after 60, 180 and 300 min respectively [1, 13].

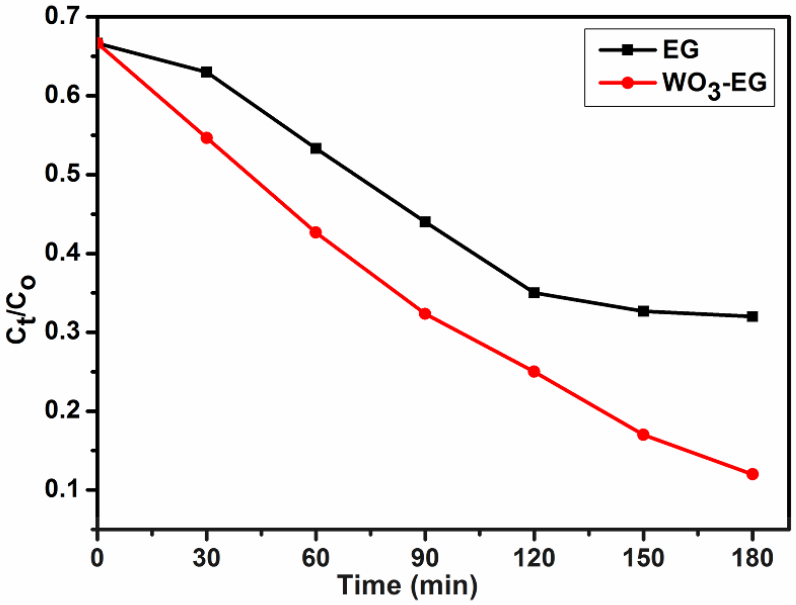

a)

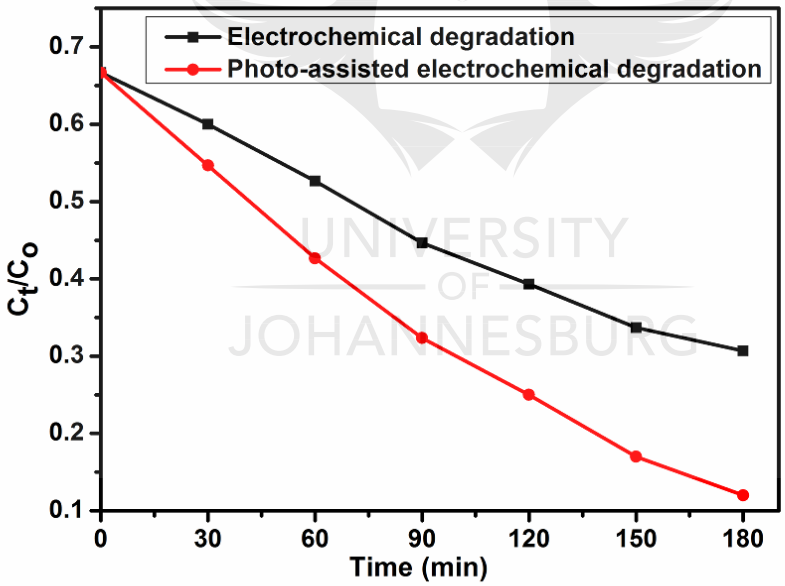

b)

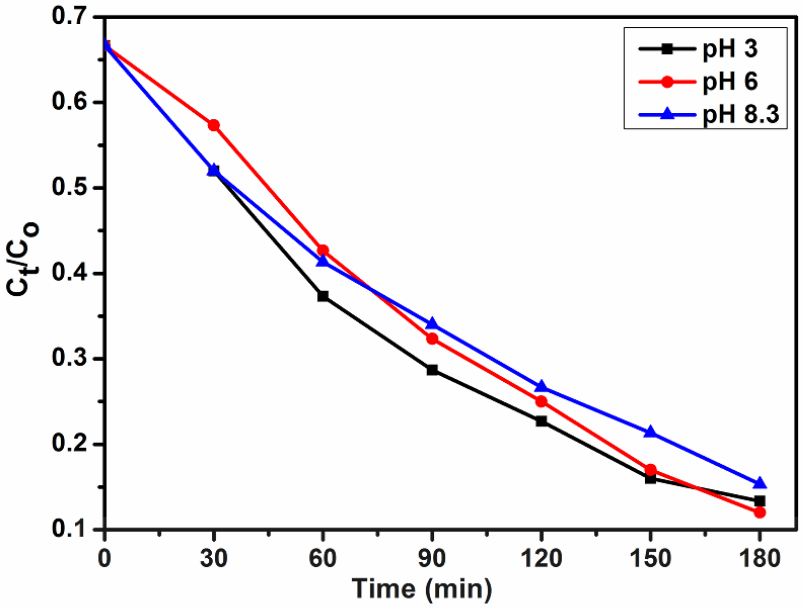

c)

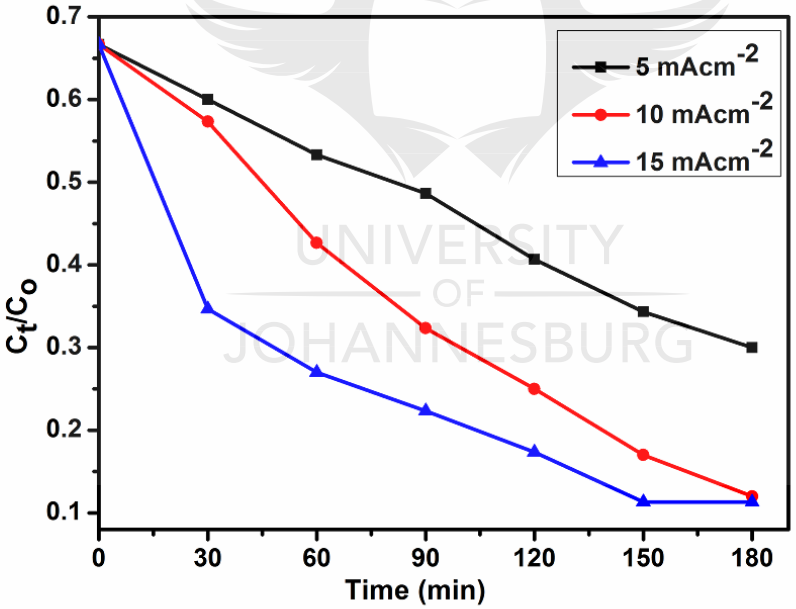

d)

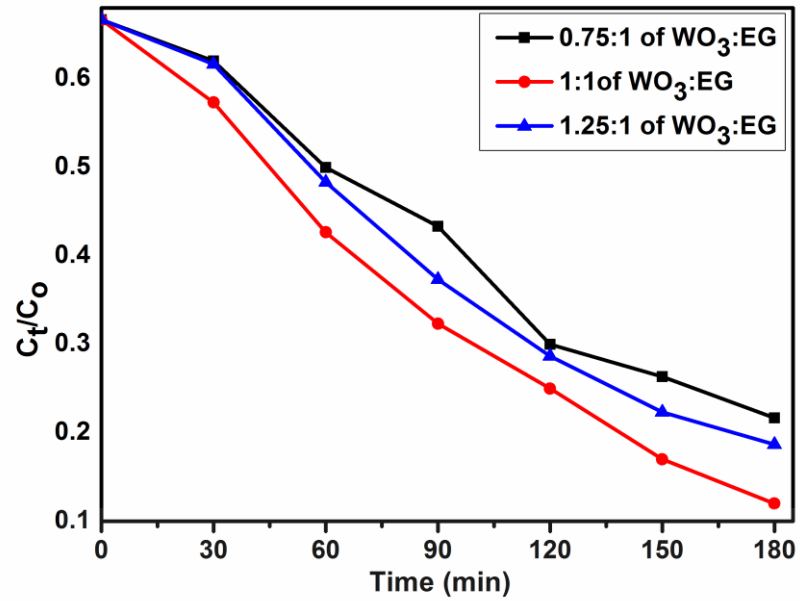

e)

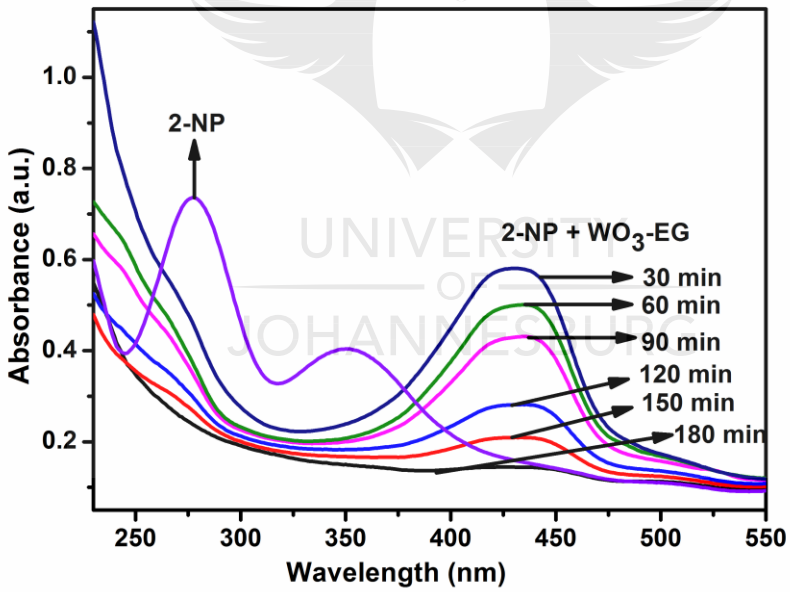

f)

Figure 6.4: Normalised concentration decay versus time plots of the photo-assisted electrochemical degradation of 2-nitrophenol (a) at EG and WO_3-EG composite electrodes, (b) under electrochemical and photo-assisted electrochemical degradation processes, (c) at different pH values, (d) at different current densities and (e) effect of content of WO_3 in WO_3-EG composite in ratios 0.75:1, 1:1 and 1.25:1 of WO_3:EG. (f) UV-Visible spectra

showing the removal of 2-nitrophenol at WO_3-EG composite electrode using photo-assisted electrochemical process.

6.3.8 Degradation kinetics and mechanism of 2-nitrophenol

In order to study the kinetics of the degradation process using WO_3-EG composite electrode, the obtained data from the electrochemical and photo-assisted electrochemical degradation of 2-nitrophenol and orange II dye was subjected to pseudo-first order kinetic equation, $\ln C_o/C_t = k_{app}t$, where C_o is given as the initial concentration of 2-nitrophenol, C_t is its concentration at a specific time, and k is the apparent reaction rate constant. The plots of $\ln C_o / C_t$ versus t were linear (Fig. 6.5a) which indicated that the degradation kinetics followed the pseudo-first order kinetics. The obtained k_{app} for the electrochemical and photo-assisted electrochemical degradation of 2-nitrophenol are; 4.5×10^{-3} min^{-1} and 9.54×10^{-3} min^{-1}, having correlation coefficients values (R^2) of 0.9958 and 0.9871 respectively.

A proposed underlying mechanism for the degradation activity of WO_3-EG electrode due to the application of bias potential and visible light is presented in Fig. 6.5b. The needful reactions that are involved in the generation of the hydroxyl (•OH) radicals at the surface of the electrode for the degradation of the organics are presented in equations [6.1 – 6.13] [54, 55].

$$M + H_2O \rightarrow M(\bullet OH) + H^+ + e^- \text{ (at the anode)} \quad [6.1]$$

Where M is the electrode

$$M(\bullet OH) \rightarrow MO + H^+ + e^- \quad [6.2]$$

$$MO + \text{organics} \rightarrow M + CO_2 + H_2O \quad [6.3]$$

Where MO is a higher oxide formed due to the interaction between the electrode and •OH.

$$\bullet OH + \text{organics} \rightarrow CO_2 + H_2O \quad [6.4]$$

However, there may be oxygen evolution resulting from the decomposition of the higher oxide which may be in competition with the oxidation of the organics, thus, causing an incomplete oxidation of the organics [11, 12].

$$WO \rightarrow W + \tfrac{1}{2} O_2 \quad [6.5]$$

Upon irradiation with visible light;

$$hv + WO_3 \rightarrow WO_3 (h^+ + e^-) \quad [6.6]$$

$$(WO_3\ h^+) + H_2O \rightarrow H^+ + (WO_3 \bullet OH) \quad [6.7]$$

$$e^- + O_2 \rightarrow \bullet O_2^- \quad [6.8]$$

$$\bullet O_2^- + H^+ + H_2O \rightarrow 3 \bullet OH \quad [6.9]$$

$$\bullet OH + \text{2-nitrophenol} \rightarrow CO_2 + H_2O \quad [6.10]$$

$$h^+ + \text{2-nitrophenol} \rightarrow CO_2 + H_2O \quad [6.11]$$

The applied bias potential drives the photo-generated electrons from the conduction band of WO_3 to the exfoliated graphite sheets which enhanced the transport of the generated electrons. As a result, the phenomenal recombination of the hole and electron pairs is minimised [14, 56]. The holes and electrons react with absorbed species such as water and oxygen on the electrode surface through series of steps as shown in eqns [6.1-6.11] to generate hydroxyl radicals. Furthermore, these generated radicals and holes react with the 2-nitrophenol molecules to break them down into compounds like CO_2 and H_2O that are less toxic [10, 57].

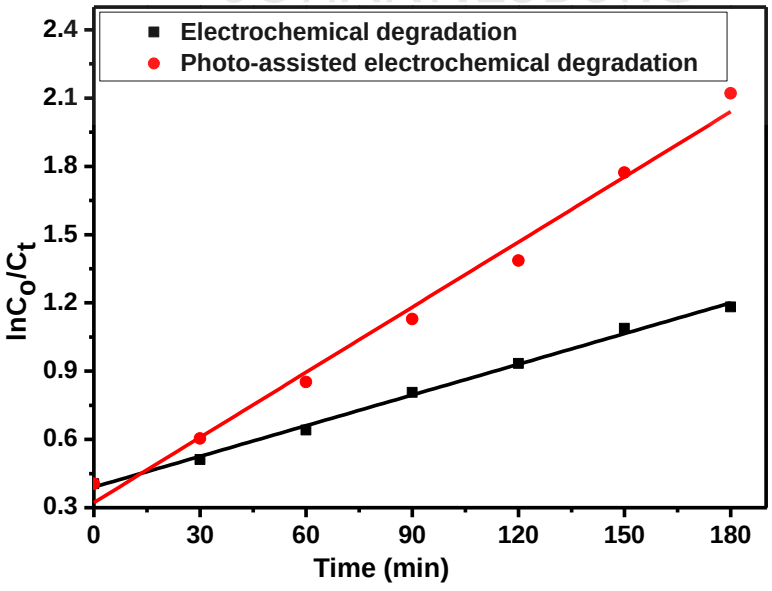

a)

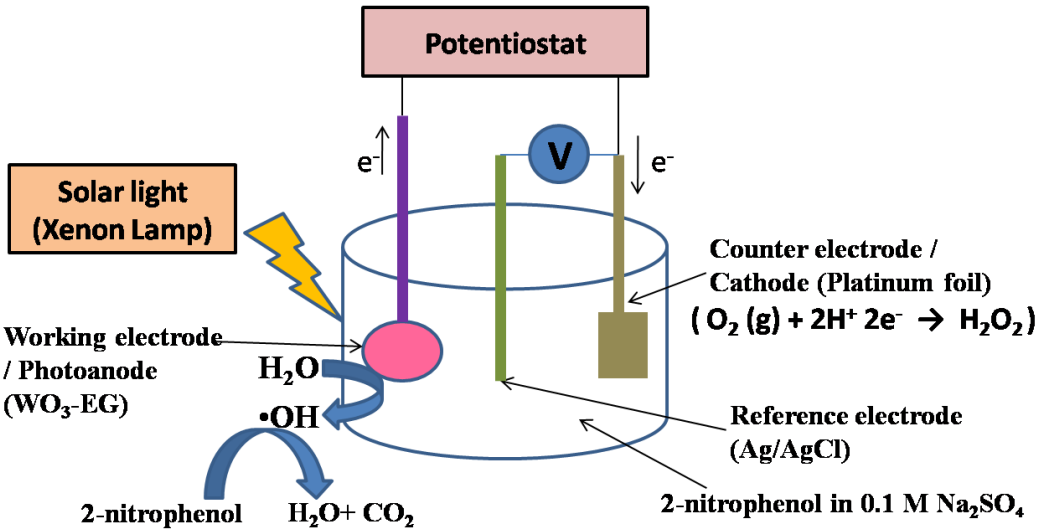

b)

Figure 6.5: (a) Degradation kinetics graphs of electrochemical and photo-assisted electrochemical degradation of 2-nitrophenol dye at pH 6 and 10 $mAcm^{-2}$ using WO_3-EG composite electrode; (b) Proposed underlying charge transfer mechanism of the photo-assisted activity of WO_3-EG composite electrode for the degradation of 2-nitrophenol.

6.3.9 Suitability of WO_3-EG electrode on Orange II dye degradation

To investigate the versatile nature of the WO_3-EG composite electrode in photo-assisted electrochemical degradation process, it was further employed in the degradation of orange II dye. The removal efficiency obtained (Fig. 6.6) were 70.7% (electrochemical degradation) and 95% (photo-assisted electrochemical degradation) after 120 minutes of electrolysis of 30 ppm of orange II dye, current density of 10 $mAcm^{-2}$ and pH 5.5 (pH of the dye solution) under illumination. The mineralisation extent obtained using TOC resulted in 49% and 67% for electrochemical and photo-assisted electrochemical degradation processes respectively. This result is in agreement with literatures [58]

For orange II dye, the k_{app} values for the electrochemical and photo-assisted electrochemical degradation processes are; 6.89×10^{-3} min^{-1} and 16.87×10^{-3} min^{-1}, having correlation coefficients values (R^2) of 0.9849 and 0.9921 respectively.

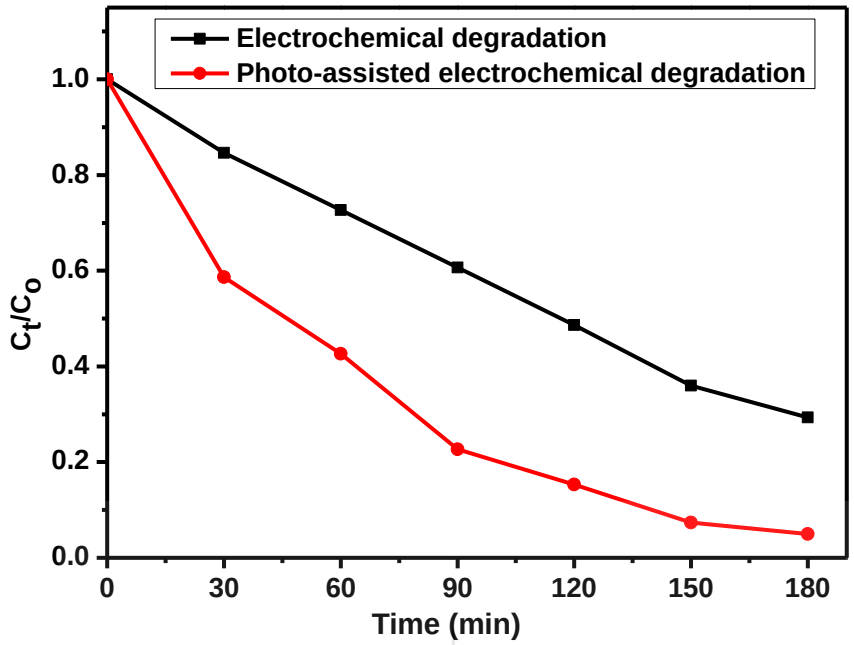

a)

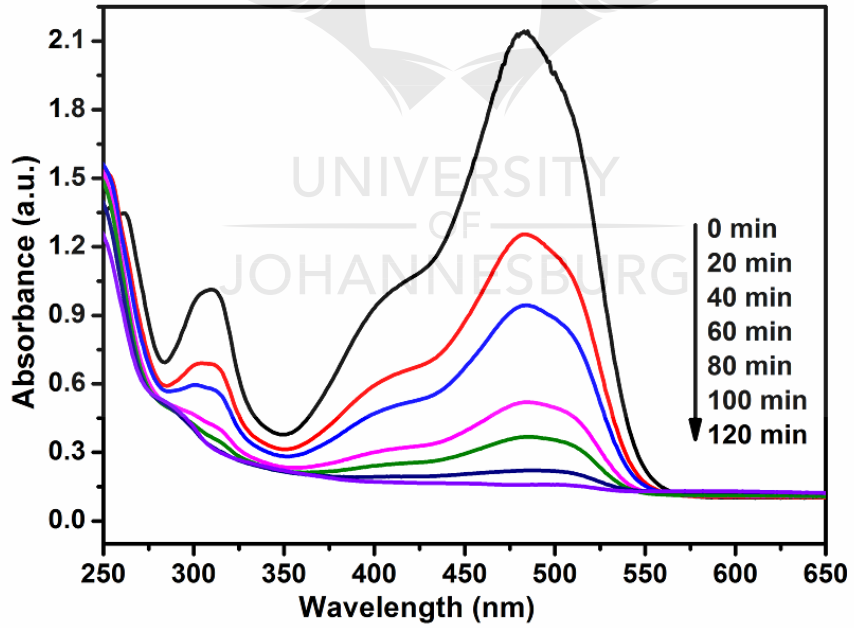

b)

Figure 6.6: (a) Normalised concentration decay versus time plots of the photo-assisted electrochemical degradation of orange II dye, and (b) UV-Visible spectra showing the removal of orange II dye at WO_3-EG composite as photoelectrode.

6.3.10 Evaluation of the degradation intermediates

The 2-nitrophenol solutions were further analysed for the qualitative evaluation of the degradation intermediates using FTIR spectroscopy [54]. In the spectrum of 2-nitrophenol at 0 min, the absorption peaks at 3240 cm^{-1} can be assigned to the O-H stretching vibration, while the weak peak at 3090 cm^{-1} can be allocated to the sp^2 C-H (=C-H). The absorption bands at 1533 and 1308 cm^{-1} can be linked to the asymmetric and symmetric stretching vibrations of aromatic nitro (NO_2) group, while the C=C absorption bands appeared around 1605 and 1470 cm^{-1}. The C-O-H bending vibration occurred around 1360 cm^{-1}, while the peak at 1230 cm^{-1} can be attributed to the C-O stretch band of the 2-nitrophenol as seen in Fig. 6.7a(i). After 60 min of photo-assisted electrochemical treatment of the 2-nitrophenol solution, there was a disappearance of C=C, NO_2 and =C-H vibration bands, and a shift in the O-H band from 3240 cm^{-1} was observed (Fig.6.7b). This suggests the degradation of the 2-nitrophenol compound to other intermediates. The absorption bands at 1652 and 1730 cm^{-1} can be assigned to C=O vibration bands. The appearance of a broad O-H band around 3000-3600 $cm^{-1}$and the C=O band around 1730 cm^{-1} indicates the formation of carboxylic acids [54]. After 120 min, the appearance of weak peaks at 2960 and 1370 cm^{-1} for C-H stretching and bending vibrations was observed. Also, there was a reduction in the intensity of the broad O-H band, while the band at 1730 cm^{-1} increased in intensity. This suggests the degradation of the 2-nitrophenol into carboxylic acids and further plausible mineralisation into CO_2, H_2O and NO_3 which are less toxic. These suggestions are corroborated by the findings of Aslam et at., and Nei C. et al [13, 59].

Additionally, the solutions of the orange II dye were further analysed using the FTIR spectroscopy (Fig.6.7c). Generally, the peaks 1509, 1610 cm^{-1} are the vibration stretching of C=C of the benzene and naphthalene ring of orange II dye, while the band at 1451cm^{-1} can be assigned to its -N=N. Also, the peaks at 1308 and 1205 cm-1 can be linked to the SO_3H of the benzene sulphonic acid of the orange II dye [58]. After 30 min of photo-assisted electrochemical treatment, it was noticed that there was a reduction in the number of bands especially in the fingerprint region. There was a disappearance of the band at 1509 cm^{-1} of the naphthalene ring, suggesting that the orange II dye was broken down into intermediates. After 180 min, there was a complete decolourisation of the dye, indicating the complete removal of the dye. This is supported by the UV visible spectroscopy showing the disappearance of the absorbance peak of the dye at 483 nm. The sharp absorption bands at 1090 and 610 are assigned to SO_4^{2-} of the sodium sulphate that was

used as the supporting electrolyte. Moreover, new absorption bands appeared at 1650 and 1735 cm-1 which suggested the formation of C=O compounds. Also, a broad O-H stretching vibration appeared around 3100-3530 which could indicate the formation of carboxylic acids and other carbonyl groups as intermediates [60]. These intermediates were further degraded by hydroxyl radicals to CO_2, H_2O and NO_3^-. These results and indications are comparable with other works in literatures [58, 60].

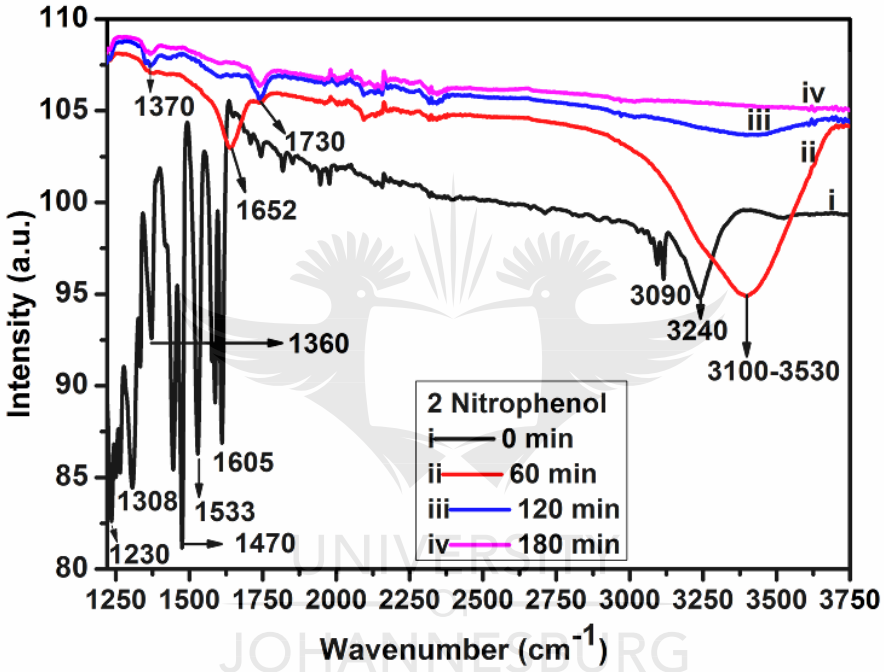

a)

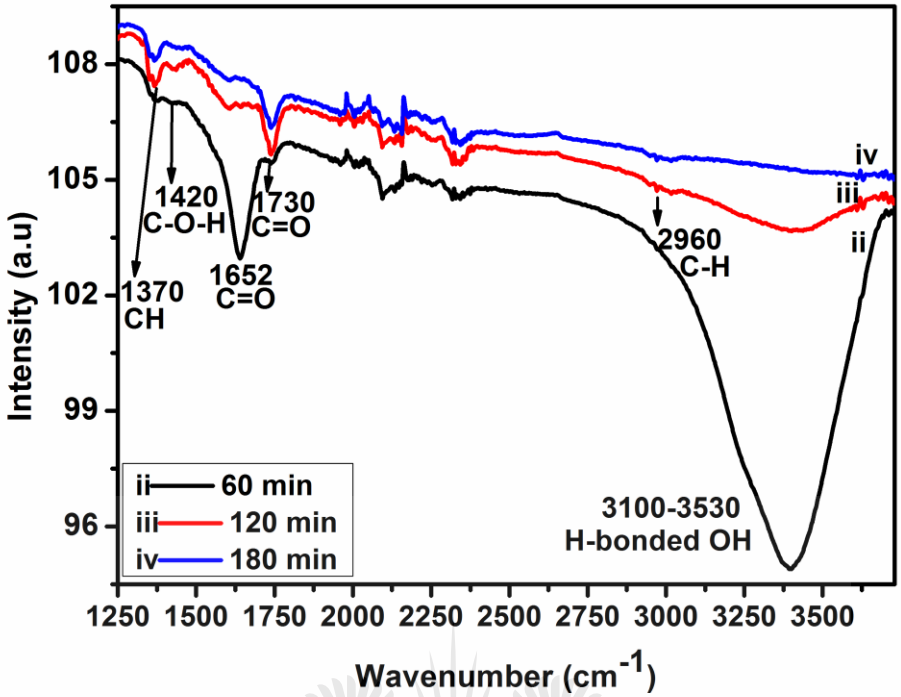
Intensity (a.u)
Wavenumber (cm-1)
1420
C-O-H
1730
C=O
1370
CH
1652
C=O
2960
C-H
3100-3530
H-bonded OH
ii 60 min
iii 120 min
iv 180 min

b)

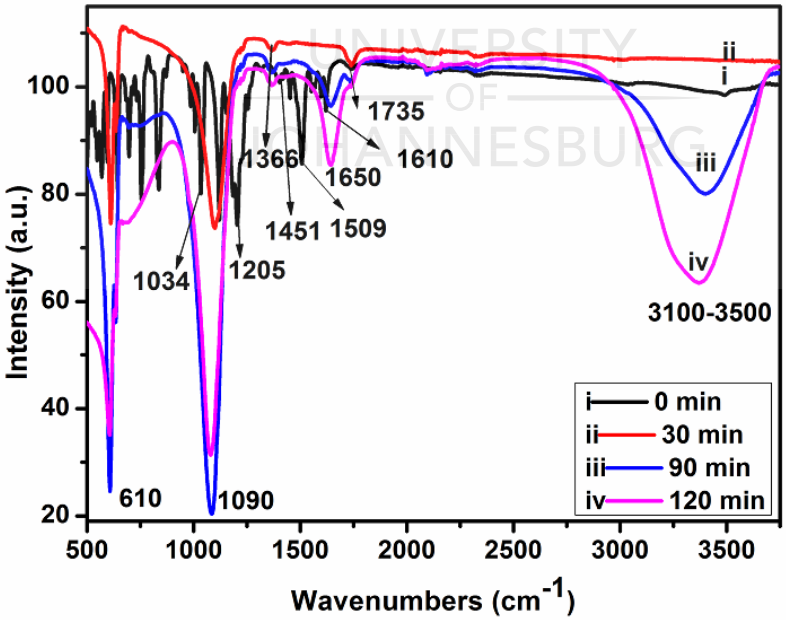
Intensity (a.u.)
Wavenumbers (cm-1)
1735
1610
1366
1650
1451
1509
1034
1205
610
1090
3100-3500
i 0 min
ii 30 min
iii 90 min
iv 120 min

Figure 6.7: FTIR spectrum of the photo-assisted electrochemical degradation of (a) 2-nitrophenol solution at 0, 60, 120 and 180 min, (b) expanded spectrum at 60, 120 and 180 min treatment of 2-nitrophenol, and (c) orange II dye at 0 min, 30, 90 and 120 min.

6.4 SUB CONCLUSION

In this work, WO_3-EG nanocomposite electrode was fabricated and employed successfully for the electrochemical and photo-assisted electrochemical degradation of 2-nitrophenol and orange II dye in water treatment. The WO_3 nanoparticles with different average sizes were uniformly dispersed on the exfoliated graphite sheets. The removal efficiencies were 82% and 95% for the photo-assisted electrochemical degradation of 2-nitrophenol and orange II dye after 180 and 120 minutes respectively. The utilisation of a low current density (10 $mAcm^{-2}$) by the WO_3-EG composite electrode for the photo-assisted electrochemical degradation process is an indication of energy cost effectiveness. The synergy between WO_3 and EG in the WO_3-EG composite is obvious from the improved photo-assisted electrochemical performance portrayed by WO_3-EG electrode compared to its electrochemical performance. Thus, WO_3-EG composite electrode renders itself a good photoanode in water treatment process due to its higher degradation efficiency.

6.5 REFERENCE

[1] A. Shokri, Degradation of 2-nitrophenol from petrochemical wastewater by ozone, Russian Journal of Applied Chemistry, 88 (2015) 2038-2043.

[2] S. Ammar, N. Oturan, M.A. Oturan, Electrochemical oxidation of 2-nitrophenol in aqueous medium by electro-Fenton technology, Journal of Environmental Engineering and Management, 17 (2007) 89.

[3] P. Gharbani, M. Khosravi, S. Tabatabaii, K. Zare, S. Dastmalchi, A. Mehrizad, Degradation of trace aqueous 4-chloro-2-nitrophenol occurring in pharmaceutical industrial wastewater by ozone, International Journal of Environmental Science & Technology, 7 (2010) 377-384.

[4] A. Karimi-Jashni, R.M. Narbaitz, Impact of pH on the adsorption and desorption kinetics of 2-nitrophenol on activated carbons, Water Research, 31 (1997) 3039-3044.

[5] A.K. Verma, R.R. Dash, P. Bhunia, A review on chemical coagulation/flocculation technologies for removal of colour from textile wastewaters, Journal of Environmental Management, 93 (2012) 154-168.

[6] P. Gharbani, S. Tabatabaii, A. Mehrizad, Removal of Congo red from textile wastewater by ozonation, International Journal of Environmental Science & Technology, 5 (2008) 495-500.

[7] E. Kusmierek, E. Chrzescijanska, Application of TiO_2–RuO_2/Ti electrodes modified with WO_3 in electro-and photoelectrochemical oxidation of Acid Orange 7 dye, Journal of Photochemistry and Photobiology A: Chemistry, 302 (2015) 59-68.

[8] E. Brillas, C.A. Martínez-Huitle, Decontamination of wastewaters containing synthetic organic dyes by electrochemical methods. An updated review, Applied Catalysis B: Environmental, 166 (2015) 603-643.

[9] B. Ntsendwana, B.B. Mamba, S. Sampath, O.A. Arotiba, Synthesis, characterisation and application of an exfoliated graphite–diamond composite electrode in the electrochemical degradation of trichloroethylene, RSC Advances, 3 (2013) 24473-24483.

[10] S.H.S. Chan, T. Yeong Wu, J.C. Juan, C.Y. Teh, Recent developments of metal oxide semiconductors as photocatalysts in advanced oxidation processes (AOPs) for treatment of dye wastewater, Journal of Chemical Technology and Biotechnology, 86 (2011) 1130-1158.

[11] E.H. Umukoro, M.G. Peleyeju, J.C. Ngila, O.A. Arotiba, Photoelectrochemical degradation of orange II dye in wastewater at a silver–zinc oxide/reduced graphene oxide nanocomposite photoanode, RSC Advances, 6 (2016) 52868-52877.

[12] B. Ntsendwana, S. Sampath, B. Mamba, O. Arotiba, Photoelectrochemical oxidation of p-nitrophenol on an expanded graphite–TiO_2 electrode, Photochemical & Photobiological Sciences, 12 (2013) 1091-1102.

[13] M. Aslam, M.T. Qamar, M.T. Soomro, I.M. Ismail, Z.A. Rehan, M.W. Ashraf, A. Hameed, The effect of cerium alteration on the photocatalytic performance of WO_3 in sunlight exposure for water decontamination, RSC Advances, 6 (2016) 2436-2449.

[14] F. Chen, F. Yan, Q. Chen, Y. Wang, L. Han, Z. Chen, S. Fang, Fabrication of Fe_3O_4@SiO_2@TiO_2 nanoparticles supported by graphene oxide sheets for the repeated adsorption and photocatalytic degradation of rhodamine B under UV irradiation, Dalton Transactions, 43 (2014) 13537-13544.

[15] A. Fakhri, S. Behrouz, Photocatalytic properties of tungsten trioxide (WO_3) nanoparticles for degradation of Lidocaine under visible and sunlight irradiation, Solar Energy, 112 (2015) 163-168.

[16] Y. Hunge, M. Mahadik, V. Mohite, S. Kumbhar, N. Deshpande, K. Rajpure, A. Moholkar, P. Patil, C. Bhosale, Photoelectrocatalytic degradation of methyl blue using sprayed WO3 thin films, Journal of Materials Science: Materials in Electronics, 27 (2016) 1629-1635.

[17] F. Motahari, M.R. Mozdianfard, F. Soofivand, M. Salavati-Niasari, NiO nanostructures: synthesis, characterization and photocatalyst application in dye wastewater treatment, RSC Advances, 4 (2014) 27654-27660.

[18] W. Mu, X. Xie, X. Li, R. Zhang, Q. Yu, K. Lv, H. Wei, Y. Jian, Characterizations of Nb-doped WO 3 nanomaterials and their enhanced photocatalytic performance, RSC Advances, 4 (2014) 36064-36070.

[19] E.H. Umukoro, M.G. Peleyeju, J.C. Ngila, O.A. Arotiba, Photocatalytic degradation of acid blue 74 in water using Ag–Ag_2O–ZnO nanostuctures anchored on graphene oxide, Solid State Sciences, 51 (2016) 66-73.

[20] S. Wu, W. Chen, L. Yan, Fabrication of a 3D MnO_2/graphene hydrogel for high-performance asymmetric supercapacitors, Journal of Materials Chemistry A, 2 (2014) 2765-2772.

[21] A. Zhu, Q. Zhao, X. Li, Y. Shi, $BiFeO_3$/TiO_2 nanotube arrays composite electrode: Construction, characterization, and enhanced photoelectrochemical properties, ACS applied materials & interfaces, 6 (2013) 671-679.

[22] M. Tian, B. Adams, J. Wen, R.M. Asmussen, A. Chen, Photoelectrochemical oxidation of salicylic acid and salicylaldehyde on titanium dioxide nanotube arrays, Electrochimica Acta, 54 (2009) 3799-3805.

[23] X. Yu, Y. Zhang, X. Cheng, Preparation and photoelectrochemical performance of expanded graphite/TiO_2 composite, Electrochimica Acta, 137 (2014) 668-675.

[24] C.-H. Lee, J.-L. Shie, Y.-T. Yang, C.-Y. Chang, Photoelectrochemical Characteristics, Photodegradation and Kinetics of Metal and Non-Metal Elements Co-Doped Photocatalyst for Pollution Removal, Chemical Engineering Journal, (2016).

[25] G. Kim, E.T. Igunnu, G.Z. Chen, A sunlight assisted dual purpose photoelectrochemical cell for low voltage removal of heavy metals and organic pollutants in wastewater, Chemical Engineering Journal, 244 (2014) 411-421.

[26] Y. Hunge, V. Mohite, S. Kumbhar, K. Rajpure, A. Moholkar, C. Bhosale, Photoelectrocatalytic degradation of methyl red using sprayed WO_3 thin films under visible light irradiation, Journal of Materials Science: Materials in Electronics, 26 (2015) 8404-8412.

[27] P.Y. Kuang, J.R. Ran, Z.Q. Liu, H.J. Wang, N. Li, Y.Z. Su, Y.G. Jin, S.Z. Qiao, Enhanced Photoelectrocatalytic Activity of BiOI Nanoplate–Zinc Oxide Nanorod p–n Heterojunction, Chemistry–A European Journal, 21 (2015) 15360-15368.

[28] C. Liu, Y. Ding, W. Wu, Y. Teng, A simple and effective strategy to fast remove chromium (VI) and organic pollutant in photoelectrocatalytic process at low voltage, Chemical Engineering Journal, 306 (2016) 22-30.

[29] T. Wang, W. Quan, D. Jiang, L. Chen, D. Li, S. Meng, M. Chen, Synthesis of redox-mediator-free direct Z-scheme AgI/WO_3 nanocomposite photocatalysts for the degradation of tetracycline with enhanced photocatalytic activity, Chemical Engineering Journal, 300 (2016) 280-290.

[30] J. Luo, J. Yartym, M. Hepel, Photoelectrochemical degradation of Orange II textile dye on nanostructured WO_3 film electrodes, Journal of New Materials for Elect Systems, 5 (2002) 315-321.

[31] F. Wang, W. Li, S. Gu, H. Li, X. Wu, X. Liu, Samarium and Nitrogen Co-Doped Bi_2WO_6 Photocatalysts: Synergistic Effect of Sm^{3+}/Sm^{2+} Redox Centers and N-Doped Level for Enhancing Visible Light Photocatalytic Activity, Chemistry-A European Journal, 22 (2016) 12859-12867.

[32] S. Bai, Y. Ma, R. Luo, A. Chen, D. Li, Room temperature triethylamine sensing properties of polyaniline–WO_3 nanocomposites with p–n heterojunctions, RSC Advances, 6 (2016) 2687-2694.

[33] M.E. Khan, M.M. Khan, M.H. Cho, Fabrication of WO_3 nanorods on graphene nanosheets for improved visible light-induced photocapacitive and photocatalytic performance, RSC Advances, 6 (2016) 20824-20833.

[34] L. Yin, D. Chen, M. Feng, L. Ge, D. Yang, Z. Song, B. Fan, R. Zhang, G. Shao, Hierarchical Fe_2O_3@WO_3 nanostructures with ultrahigh specific surface areas: microwave-assisted synthesis and enhanced H_2S-sensing performance, RSC Advances, 5 (2015) 328-337.

[35] J. Zhou, Y. Wei, G. Luo, J. Zheng, C. Xu, Electrochromic properties of vertically aligned Ni-doped WO_3 nanostructure films and their application in complementary electrochromic devices, Journal of Materials Chemistry C, 4 (2016) 1613-1622.

[36] M. Yi, J. Li, Z. Shen, X. Zhang, S. Ma, Morphology and structure of mono-and few-layer graphene produced by jet cavitation, Applied Physics Letters, 99 (2011) 123112.

[37] M. Yi, Z. Shen, Kitchen blender for producing high-quality few-layer graphene, Carbon, 78 (2014) 622-626.

[38] M. Yi, Z. Shen, A review on mechanical exfoliation for the scalable production of graphene, Journal of Materials Chemistry A, 3 (2015) 11700-11715.

[39] M. Yi, Z. Shen, Fluid dynamics: an emerging route for the scalable production of graphene in the last five years, RSC Advances, 6 (2016) 72525-72536.

[40] M. Yi, Z. Shen, J. Zhu, A fluid dynamics route for producing graphene and its analogues, Chinese science bulletin, 59 (2014) 1794-1799.

[41] M. Peleyeju, E. Umukoro, J. Babalola, O. Arotiba, Electrochemical Degradation of an Anthraquinonic Dye on an Expanded Graphite-Diamond Composite Electrode, Electrocatalysis, 7 (2016) 132-139.

[42] T. Ndlovu, O.A. Arotiba, S. Sampath, R.W. Krause, B.B. Mamba, Electrochemical detection and removal of lead in water using poly (propylene imine) modified re-compressed exfoliated graphite electrodes, Journal of Applied Electrochemistry, 41 (2011) 1389-1396.

[43] D. Sánchez-Martínez, A. Martínez-de la Cruz, E. López-Cuéllar, Synthesis of WO_3 nanoparticles by citric acid-assisted precipitation and evaluation of their photocatalytic properties, Materials Research Bulletin, 48 (2013) 691-697.

[44] M.P. Kumar, M. Nidhi, C. Srivastava, Electrochemical exfoliation of graphite to produce graphene using tetrasodium pyrophosphate, RSC Advances, 5 (2015) 24846-24852.

[45] B. Grbić, N. Radić, S. Stojadinović, R. Vasilić, Z. Dohčević-Mitrović, Z. Šaponjić, P. Stefanov, TiO_2/WO_3 photocatalytic composite coatings prepared by spray pyrolysis, Surface and Coatings Technology, 258 (2014) 763-771.

[46] M. Tang, X. Xu, T. Wu, S. Zhang, X. Li, Y. Li, Polyacrylamide grafting of modified graphene oxides by in situ free radical polymerization, Materials Research Bulletin, 60 (2014) 576-583.

[47] J. Díaz-Reyes, V. Dorantes-García, A. Pérez-Benítez, J. Balderas-López, Obtaining of films of tungsten trioxide (WO_3) by resistive heating of a tungsten filament, Superficies y vacío, 21 (2008) 12-17.

[48] X. An, C.Y. Jimmy, Y. Wang, Y. Hu, X. Yu, G. Zhang, WO_3 nanorods/graphene nanocomposites for high-efficiency visible-light-driven photocatalysis and NO_2 gas sensing, Journal of Materials Chemistry, 22 (2012) 8525-8531.

[49] Y.S. Grewal, M.J. Shiddiky, S.A. Gray, K.M. Weigel, G.A. Cangelosi, M. Trau, Label-free electrochemical detection of an Entamoeba histolytica antigen using cell-free yeast-scFv probes, Chemical Communications, 49 (2013) 1551-1553.

[50] T. Ndlovu, B.B. Mamba, S. Sampath, R.W. Krause, O.A. Arotiba, Voltammetric detection of arsenic on a bismuth modified exfoliated graphite electrode, Electrochimica Acta, 128 (2014) 48-53.

[51] O. Monfort, S. Sfaelou, L. Satrapinskyy, T. Plecenik, T. Roch, G. Plesch, P. Lianos, Comparative study between pristine and Nb-modified $BiVO_4$ films employed for photoelectrocatalytic production of H_2 by water splitting and for photocatalytic degradation of organic pollutants under simulated solar light, Catalysis Today, 280 (2017) 51-57.

[52] N. Yang, J. Zhai, D. Wang, Y. Chen, L. Jiang, Two-dimensional graphene bridges enhanced photoinduced charge transport in dye-sensitized solar cells, Acs Nano, 4 (2010) 887-894.

[53] T. Das, P.K. Boruah, M.R. Das, B.K. Saikia, Formation of onion-like fullerene and chemically converted graphene-like nanosheets from low-quality coals: application in photocatalytic degradation of 2-nitrophenol, RSC Advances, 6 (2016) 35177-35190.

[54] H.M. Nguyen, C.M. Phan, T. Sen, Degradation of sodium dodecyl sulfate by photoelectrochemical and electrochemical processes, Chemical Engineering Journal, 287 (2016) 633-639.

[55] O. Scialdone, Electrochemical oxidation of organic pollutants in water at metal oxide electrodes: A simple theoretical model including direct and indirect oxidation processes at the anodic surface, Electrochimica Acta, 54 (2009) 6140-6147.

[56] P. Wang, Y. Tang, Z. Dong, Z. Chen, T.-T. Lim, Ag–AgBr/TiO_2/RGO nanocomposite for visible-light photocatalytic degradation of penicillin G, Journal of Materials Chemistry A, 1 (2013) 4718-4727.

[57] H. Hua, Y. Xi, Z. Zhao, X. Xie, C. Hu, H. Liu, Gram-scale wet chemical synthesis of Ag_2O/TiO_2 aggregated sphere heterostructure with high photocatalytic activity, Materials Letters, 91 (2013) 81-83.

[58] J.-X. Chen, L. Zhu, Degradation mechanism of Orange II in UV-Fenton process with hydroxyl-Fe-pillared bentonite as heterogeneous catalyst, Advances in Energy Engineering (ICAEE), 2010 International Conference on, IEEE, 2010, pp. 281-284.

[59] C. Nie, N. Shao, B. Wang, D. Yuan, X. Sui, H. Wu, Fully solar-driven thermo-and electrochemistry for advanced oxidation processes (STEP-AOPs) of 2-nitrophenol wastewater, Chemosphere, 154 (2016) 604-612.

[60] N. Riaz, F. Chong, Z. Man, R. Sarwar, U. Farooq, A. Khan, M. Khan, Preparation, characterization and application of Cu–Ni/TiO_2 in Orange II photodegradation under visible light: effect of different reaction parameters and optimization, RSC Advances, 6 (2016) 55650-55665.

CHAPTER 7

PHOTOCATALYTIC APPLICATION OF Pd-ZnO-EXFOLIATED GRAPHITE NANOCOMPOSITE FOR THE ENHANCED REMOVAL OF ACID ORANGE 7 DYE IN WATER[1]

7.1 INTRODUCTION

Scarcity of clean water which results from the pollution of water bodies by the discharge of industrial wastewaters into the environment has been a global challenge. This has made the provision of clean and safe water of great concern as population and industrialisation are increasing worldwide [1, 2]. Therefore, there is need for proper water treatment to make clean water accessible. Several factors contribute to the water pollution and these include heavy metals and organic pollutants such as pesticides, herbicides, crude oil, pharmaceuticals and dyes [3, 4]. These pollutants are harmful and degradation resistant in nature [5, 6]. The textile industry has been found to consume the largest part of dye manufactured. During the process of colouration, a large percentage of the dye is lost as effluent since some of the dye do not effectively bind to the products [7]. The dye effluents generated from paper, pulp, paint, and textile industries are a treat to the environment because they can be toxic and carcinogenic to aquatic and human lives [8]. Several techniques have been used for wastewater treatment. These include adsorption, precipitation, ion exchange, reverse osmosis, filtration, etc. Most of these techniques have not been very effective. They have partially aided and also presented a set of drawbacks. Therefore, some of these organic pollutants that are degradation resistant require alternative treatment methods apart from the conventional methods that have been previously practiced for many years [9].

However, advanced oxidation processes (OAPs) are being introduced and found as alternative techniques to these conventional techniques. Photocatalysis is a type of AOP which has gained much attention in recent years. It has been found to be an efficient technique for the removal of organic pollutants from industrial waste water [10]. It is economical and has potential to degrade and mineralise recalcitrant organic pollutants [6].

[1] This chapter has been published in Umukoro, E.H.; Madyibi, S.S. ; Peleyeju, M.G.; Tshwenya, L.; Viljoen, E.H.; Ngila, J.C.; Arotiba, O.A. Photocatalytic application of Pd-ZnO-exfoliated graphite nanocomposite for the enhanced removal of acid orange 7 dye in water. *Solid State Sciences*, **2017**, 74, 118–124

A number of photocatalysts have been employed which include; TiO_2 [11] , ZnO [12], ZrO_2 [13] and WO_3 [14].

Zinc oxide is a promising photocatalyst for solar energy conversion and wastewater treatment because of its low toxicity, photocatalytic efficiency, high abundance, optical and chemical stabilities [15, 16]. ZnO is also economically friendly, inexpensive, easily available, and has good catalytic properties [10, 17, 18]. At the nanoscale, the crystal microstructure and morphologies of ZnO nanocrystals strongly influence their photocatalytic performance [19-22]. It is preferred over TiO_2 because it has higher quantum efficiency and it is photoactive under sunlight [4, 23]. The main drawbacks of ZnO are its wide band gap and photocorrosion [24]. Its wide band gap causes narrow light absorption range, and the photo-generated holes and electrons tend to recombine. In order to reduce electron and hole recombination and to improve light absorption, doping of the ZnO with metals such as Ag, Au, Pd is required [4, 25-29]. Doping is the adding of impurities or other materials to a semi-conductor in order to modify its properties and increase photocatalytic activity [30].

Exfoliated graphite (EG) has excellent properties such as low density, compressibility, resilience, thermal stability and corrosion resistant. EG has the ability to capture and shuttle electrons, thus, acting as an electron sink [31] which can aid to minimise recombination of the photogenerated electron and hole when added to the zinc oxide semiconductor for photocatalysis. Also, the addition of palladium as a dopant would act as a scavenger for the electrons that are photogenerated, reducing the electron-hole recombination, thereby enhancing the visible light absorption of ZnO [3].

Thus, this study focuses on the development of palladium and exfoliated graphite doped ZnO nanocomposite for the photocatalytic removal of acid orange 7 dye in water treatment process.

7.2 EXPERMENTAL PROCEDURES

7.2.1 Materials and apparatus

Natural graphite flakes, zinc acetate dihydrate ($Zn(CH_3COO)_2.2H_2O$), ammonium hydroxide (NH_4OH), palladium acetate ($Pd(CH_3COO)_2$), acid orange 7 dye, sulphuric acid

(H_2SO_4), nitric acid (HNO_3) and polyethylene glycol were obtained from Sigma Aldrich, Germany.

7.2.2 Characterisation

Characterisation of the ZnO and ZnO-based nanocomposites were done with X-ray diffractometry (XRD (Rigagu Ultima IV, Japan) to study the crystal and particle size of the materials. Fourier transform infrared spectroscopy (Perkin Elmer FTIR spectrometer (Spectrum 100, USA)) was used to ascertain the effect of doping on the ZnO nanoparticles (functional groups present). Scanning electron microscopy (TESCAN, Vega 3 XMU, Czech Republic) in conjunction with energy dispersive x-ray spectroscopy (EDX, TESCAN, Czech Republic) was employed for studying of surface morphology of the different synthesised nanocomposites and for elemental determination. All characterisation were conducted at the University of Johannesburg, South Africa.

7.2.3 Preparation of EG

Natural graphite was immersed in a mixture containing a 3:1 ratio of concentrated sulphuric acid (H_2SO_4) and concentrated nitric acid (HNO_3), and it was kept at room temperature for 24 hours. The material was washed using deionised water until a neutral pH was achieved. The graphite intercalated compound formed was dried and put in a microwave oven which was operated at 900W for 60s. Under irradiation in the microwave, there was a rapid expansion of the precursor accompanied by lightning, which gives a puffed-up material known as exfoliated graphite (EG) which is sometimes called expanded graphite [32].

7.2.4 Synthesis of Pd-ZnO-EG nanocomposite

Pd-ZnO-EG nanocomposite was prepared by a facile one pot solvothermal method. Briefly, zinc acetate dihydrate (10.97 g), palladium acetate (0.274 g) and EG (0.274 g) were dispersed in a mixture of de-ionised water (50 mL), ethylene glycol (5 mL), ammonia solution (10 mL) and stirred magnetically. The mixture was then transferred into a 70 mL Teflon-lined stainless steel autoclave and heated at 160^{o}C for 12 hours. The obtained product was allowed to cool to room temperature, centrifuged and washed with ethanol and de-ionized water to remove any ions that might be remaining in the product. Then, it was dried at 60^{o}C in an oven overnight. ZnO was prepared using the same method without the

addition of palladium acetate and EG while Pd-ZnO was prepared using the same method without the addition of EG. Also, ZnO-EG was likewise prepared without adding the palladium acetate to the mixture.

7.2.5 Degradation studies

Degradation studies were carried out using ZnO, Pd-ZnO, ZnO-EG and Pd-ZnO-EG nanocomposites as photocatalysts for the degradation of acid orange 7 dye in water. The as-prepared nanocomposite (0.1 g) was dispersed in 100 mL aqueous solution (20ppm) of the dye. The suspension was stirred in the dark for 30 min to reach adsorption – desorption equilibrium. Then it was exposed to visible light irradiation. At intervals of 30 min, 3 ml of the suspension was extracted using a syringe and then filtered to remove the photocatalyst with the aid of 0.45 µm PVDF filter. Then the filtrate was analysed using UV spectrophotometry (Cary 60, Agilent).

7.3 RESULTS AND DISCUSSION

7.3.1 FTIR studies

FTIR studies were conducted to characterise the functional groups which are present in the prepared materials, and the obtained FTIR spectra of ZnO and Pd-ZnO-EG are shown in Figure 7.1. The absorption peak at 3437cm^{-1} is due to the vibration of O-H stretching of the water absorbed on the (Figure 7.1a). The weak band around 519cm^{-1} is due to Zn—O bond. Figure 7.1b shows the absorption peaks of Pd-ZnO-EG. The band at 3382cm^{-1} accounts for the vibration of O—H stretching from the hydroxyl groups on the EG, and the water absorbed on both the EG and ZnO. The peaks at 1616cm^{-1} and 1400cm^{-1} could be attributed to the C=C bond and C—O—H vibration (1220-1440cm^{-1}). The peaks at 2927 and 2848cm^{-1} can be allocated to sp^3 and sp^2 C—H stretching vibrations in EG. The pronounced absorption band at 519cm^{-1} could be associated with the presence of the Zn—O bond. However, the palladium peak was not obviously seen due to its low content in the nanocomposite [10, 33].

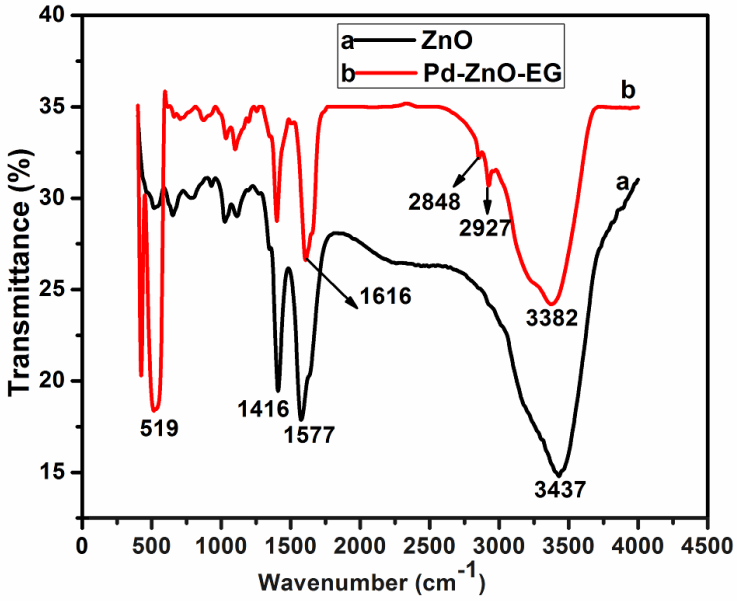

Figure 7.1: FTIR spectra of the (a) ZnO and (b) Pd-ZnO-EG

7.3.2 UV- Vis studies

UV-Visible studies were carried out to investigate the optical behaviour of the material (Fig. 7.2). It was observed that the ZnO-EG displayed a better absorbance of light in the visible region than the synthesized ZnO. This is as a result of the photosensitizing role played by the EG which was added to the ZnO as presented in Fig. 7.2b. In Fig. 7.2c, the as-prepared Pd-ZnO showed a higher absorbance intensity in comparison with the as-prepared ZnO and ZnO-EG from $\lambda = 390 - 800$ nm which is the visible region. This is due to the Pd incorporated into the nanocomposite which aided the separation and transportation of the photogenerated charge carriers [34]. Also, the surface plasmon resonance property of Pd played a role in enhancing the light absorption [35]. Furthermore, Pd-ZnO-EG exhibited a better and higher intensity of absorption in the visible region in relation to the ZnO, ZnO-EG and Pd-ZnO. This can be attributed to photosensitizing property and charge transfer capability of the EG as well as the SPR property of the Pd which resulted in a synergistic process that enhanced the photoactivity of the Pd-ZnO-EG nanocomposite [34, 36], thereby, showing a better photocatalytic ability compared to the prepared ZnO, ZnO-EG and Pd-ZnO materials.

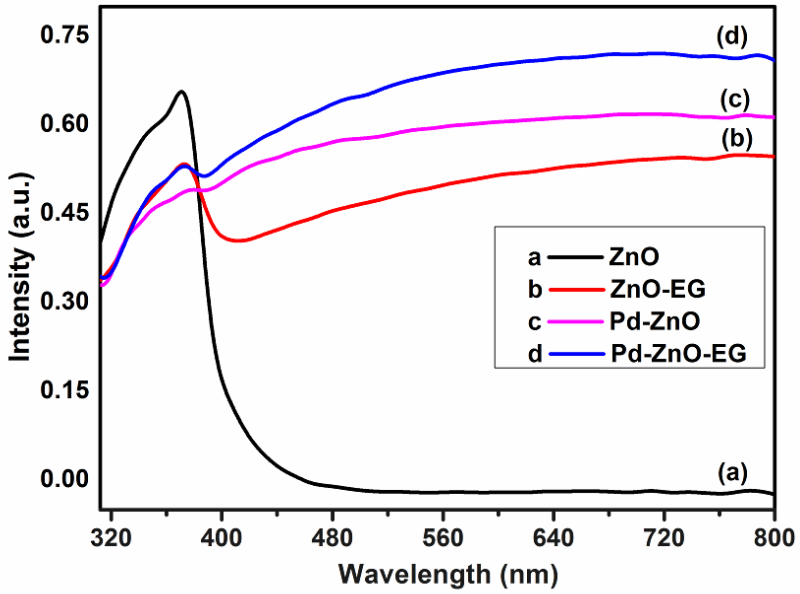

Figure 7.2: UV-Vis results of ZnO and Pd-ZnO-EG nanocomposite

7.3.3 Raman studies

Raman studies were carried out on the as-prepared ZnO and Pd-ZnO-EG materials. Fig. 7.3a presents the Raman spectrum of the prepared ZnO without Pd and EG. The peak observed at 100 cm^{-1} is the E_2 (Low) mode, 336 cm^{-1} originates from E_2(High) – E_2 (Low) which is Raman active frequency phonons, 388 cm^{-1} is known as the A_{1T} mode and the peak at 588 cm^{-1} corresponds to the E_{1L} mode. In addition, the sharp and very intense peak at 441 cm^{-1} corresponds to E_2 (high). It is considered the Raman active optical phonon mode, indicating that the ZnO has a wurtzite hexagonal phase [37-39]. In Fig. 7.3b, additional new peaks were seen around 1353 and 1587 cm^{-1} which are the D and G bands of the EG respectively. They result from the in-plane phonon vibration of the graphitic or sp^2-bonded carbon atoms (G band) and defects introduced in the graphitic sheets (D band) due to the formation of sp^3 bonding caused by the presence of oxygen groups in the EG. Also, the peaks at 388 and 588 cm^{-1} are absent, while there are shifts observed at 330 and 439 cm^{-1} which could be due to the introduction of the Pd and EG [40, 41]. Thus, indicating the formation of the Pd-ZnO-EG nanocomposite.

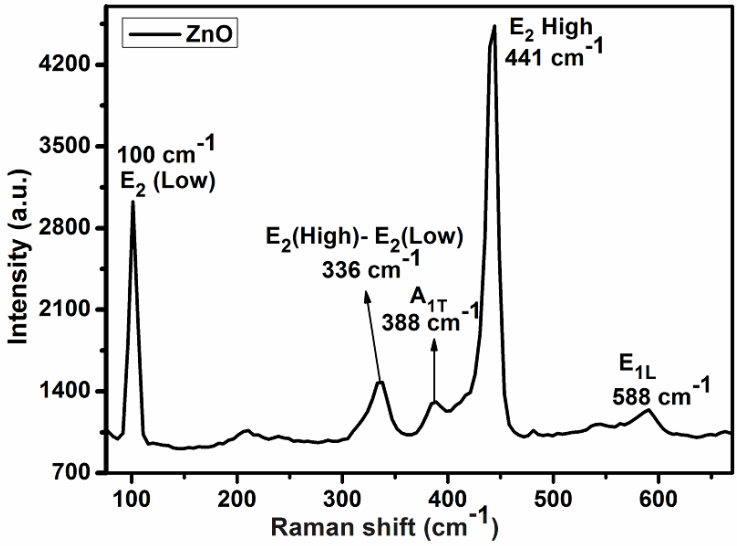

a)

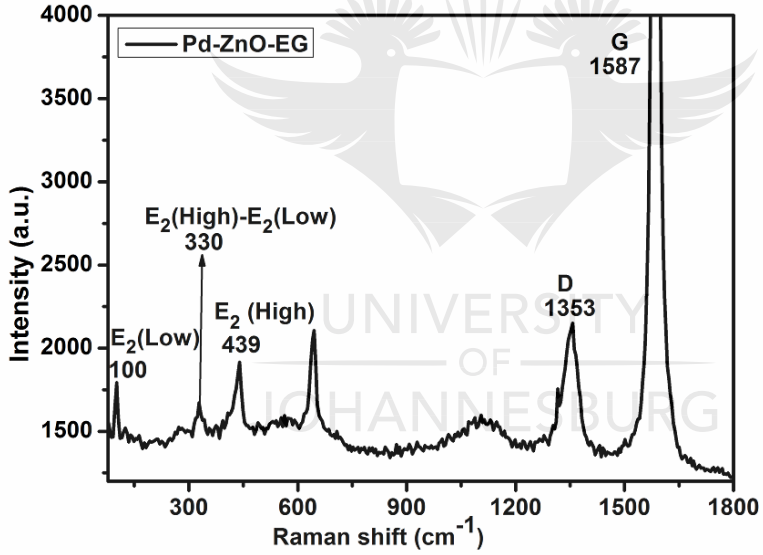

b)

Figure 7.3: Raman spectra of the (a) ZnO and (b)Pd-ZnO-EG materials

7.3.4 XRD studies

XRD studies were conducted on the prepared materials as shown in Fig. 7.4. ZnO has the hexagonal wurzite structure, with the diffraction peaks observed at 32°, 36°, 39°, 51°, 63° and 69° as shown in Figure 7.4a. In Figure 7.4b, the peaks for ZnO appeared with an additional low intensity peak around 42° corresponding to the crystal plane (111) of Pd (JCPDS no. 87-0639) which confirming the presence of Pd in the Pd-ZnO material [42,

43]. Figure 7.4c shows the XRD pattern for the ZnO-EG having the conspicuous characteristic peak of EG in addition to those of ZnO which indicated the preparation of ZnO-EG material. Figure 7.4d displayed that the peaks at 32°, 36° and 39° became lowered in their intensities because of the destruction resulting from distortions caused by Pd and EG. The conspicuous peak around 26° which is the characteristic of EG confirms the presence of EG, indicating the successful preparation of the Pd-ZnO-EG composite. The intensity of this peak resulted in the lowered intensity of other components. However, the EDS result (Fig 7.5e) confirms the presence of Pd which is not obvious in Fig 7.4d.

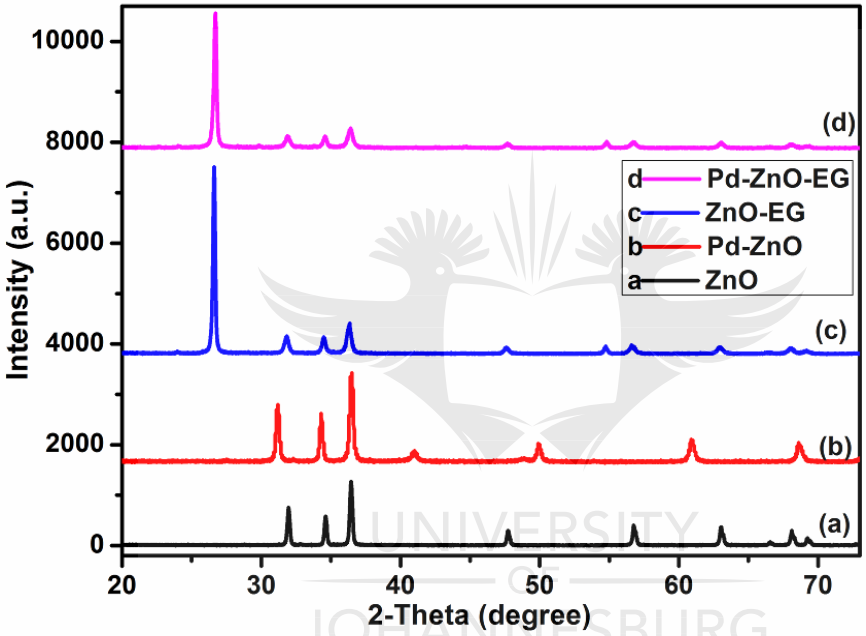

Figure 7.4: XRD patterns of (a) ZnO, (b) Pd-ZnO, (c) ZnO-EG, and (d) Pd-ZnO-EG

7.3.5 Morphological studies

The surface morphology and elemental composition of the prepared materials were done with the aid of transmission emission and scanning electron microscopy in addition to an energy dispersive X-ray spectroscopy. Figure 7.5a shows that the as prepared ZnO are flower-like structures. Figure 7.5b shows that the EG has several layers of graphitic sheets which can trap the ZnO and Pd nanoparticles. Figure 5c clearly displays the Pd-ZnO nanoparticles on the EG sheets. The TEM result shows the as-prepared Pd-ZnO-EG nanocomposites with different sizes, and the Pd anchored on the ZnO and EG (Figure 7.5d).

The EDS studies were done to find the elemental composition of the Pd-ZnO-EG material. As seen in Figure 7.5e, the EDS spectrum reveals the presence of C, O, Zn and Pd in the Pd-ZnO-EG composite, indicating the successful synthesis of the Pd-ZnO-EG material [10, 33]. Table 7.1 shows the percentage composition of the Pd-ZnO-EG as determined by EDS, and the final amount or content of Pd in the composite was found to be approximately 1% by weight, which is very minute.

a)

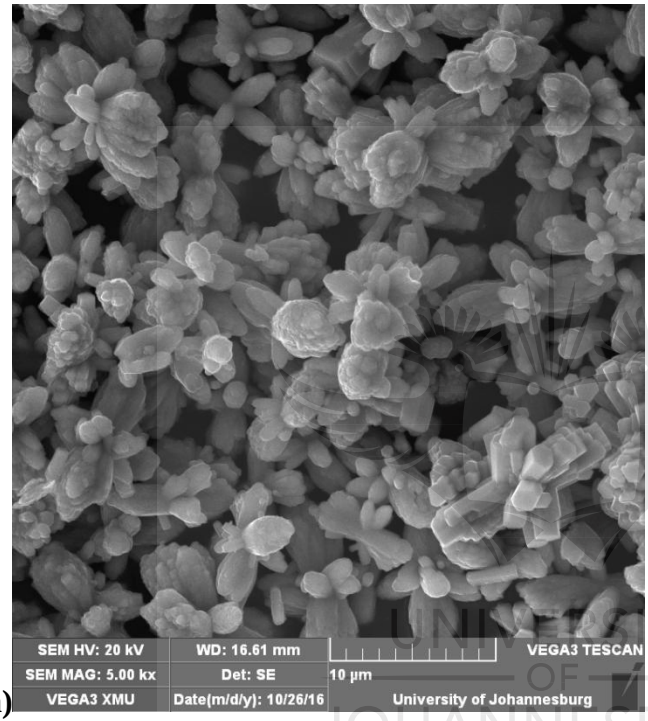

b)

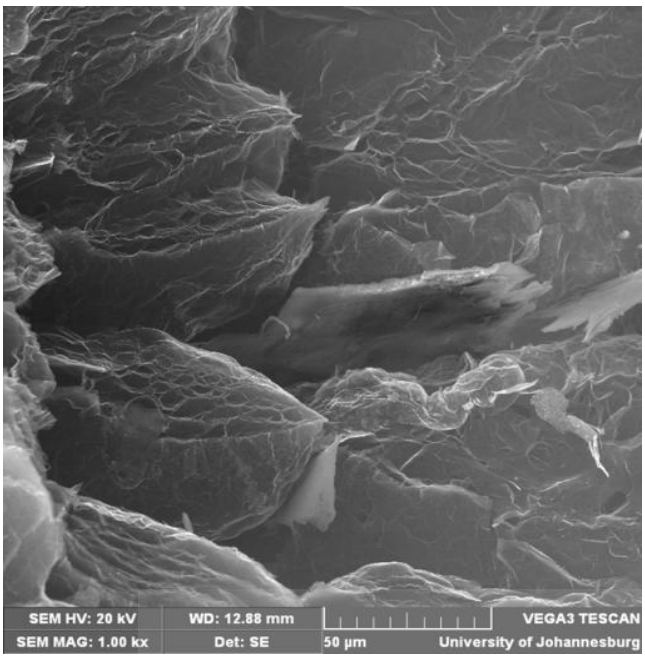

c)

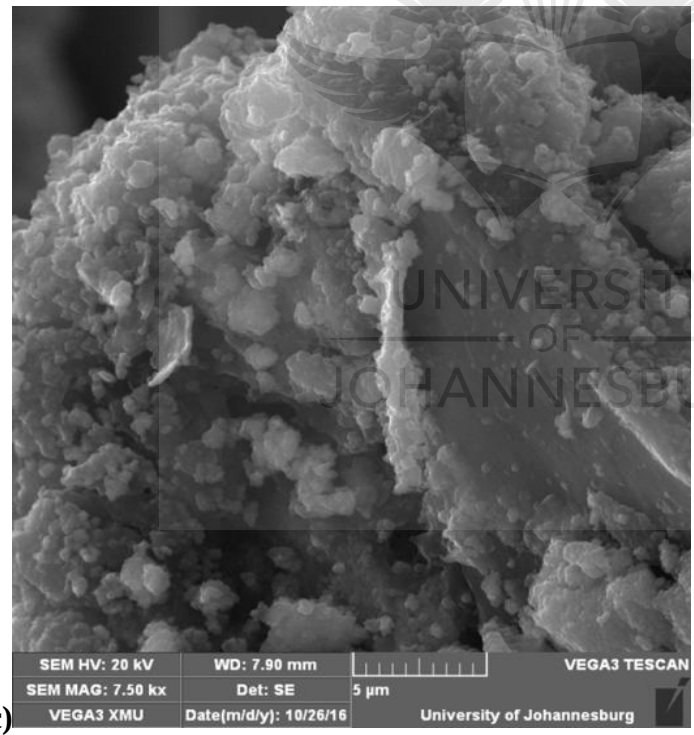

d)

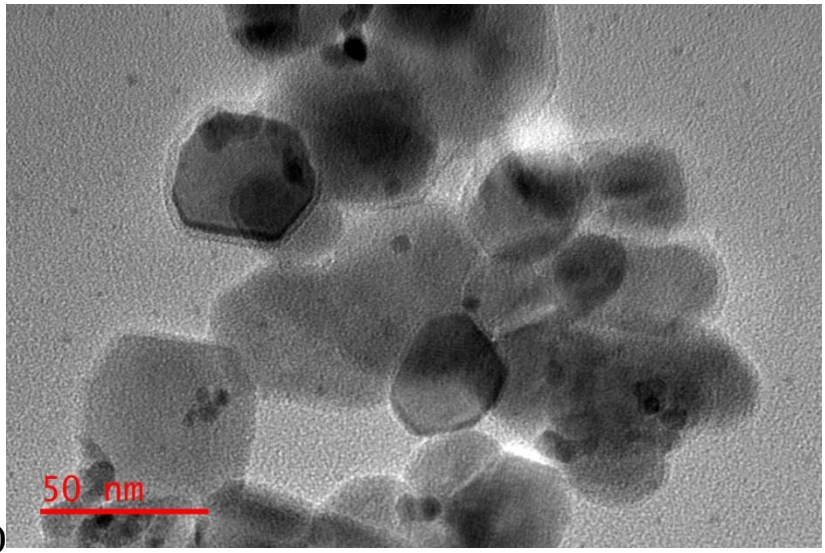

e)

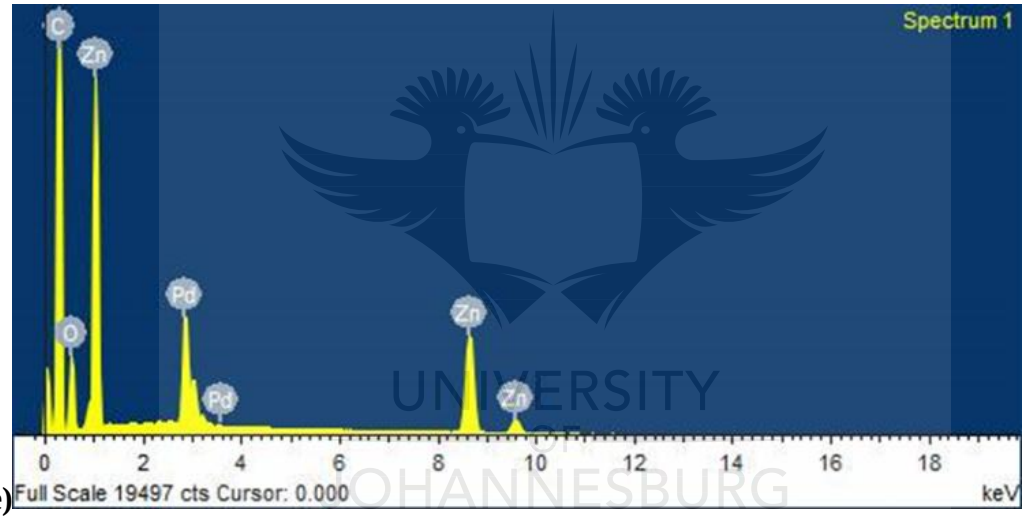

Figure 7.5: SEM images of (a) ZnO, (b) EG and (c) Pd-ZnO-EG; (d) TEM image and (e) EDX spectrum of the as prepared Pd-ZnO-EG

Table 7.1: Percentage composition of Pd-ZnO-EG

Element	Weight%	Atomic%	Compd%	Formula
C K	22.33	30.91	81.83	CO2
Zn K	13.67	3.48	17.02	ZnO
Pd L	1.00	0.16	1.15	PdO
O	62.99	65.46		
	100.00			

7.3.6 Braunauer-Emmett-Teller (BET) surface area analysis

The surface area, pore size and pore volume of the materials were determined using nitrogen adsorption-desorption (BET) analyses. The results obtained are presented in Table 7.2. Figure 7.6 shows the nitrogen adsorption-desorption isotherms of the as-prepared Pd-ZnO-EG material. It was found that the Pd-ZnO-EG exhibited a larger BET surface area, pore volume and pore size when compared to ZnO. This implies that the addition of the Pd and EG resulted in an increase in surface area which invariably enhanced the photocatalytic degradation of the acid orange 7 dye by the Pd-ZnO-EG.

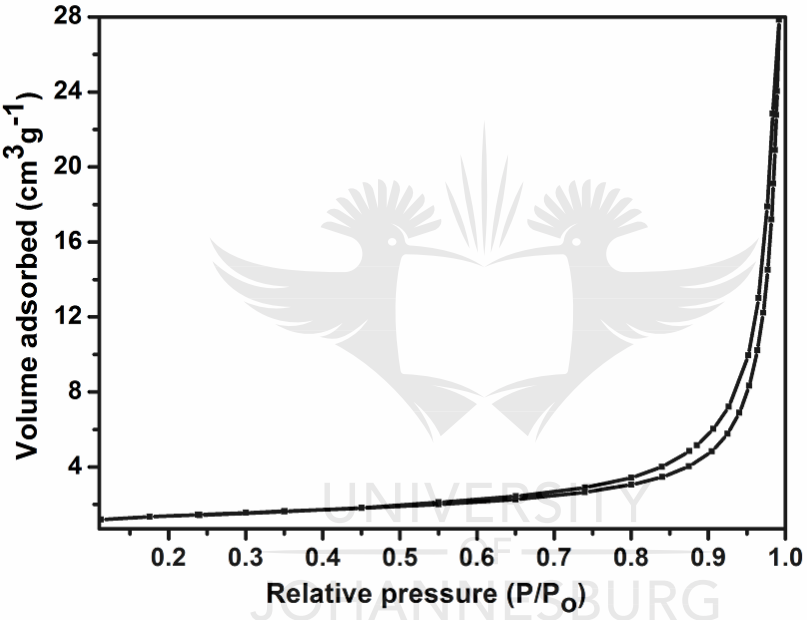

Figure 7.6: The Nitrogen adsorption-desorption isotherms of the as-prepared Pd-ZnO-EG

Table 7.2: The BET surface area, pore volume and pore size of the as-prepared ZnO and Pd-ZnO-EG materials

Material	BET Surface area (m^2g^{-1})	Pore volume (cm^3g^{-1})	Pore size (nm)
ZnO	3.2959	0.010482	12.72152
Pd-ZnO-EG	4.9329	0.035344	28.66022

7.3.7 Photocatalytic activity

Figure 7.7 shows the plots of the normalized concentration with time at an initial concentration of 20 ppm of the dye solution using ZnO, Pd-ZnO and Pd-ZnO-EG. The degradation of the dye was carried out at pH 7. The photocatalytic capabilities of the materials were evaluated for the removal of acid orange 7 dye as a model organic pollutant. The degradation of the dye using the ZnO as a photocatalyst was very little, close to nothing as shown in Figure 7.7a, and the percentage removal obtained was 3%. In Figure 7.7b, the ZnO-EG gave a removal percentage of 22.5% while the as prepared Pd-ZnO yielded a 25% percentage removal of the acid orange 7 dye due to the presence of palladium in the ZnO composite (Figure 7.7c). Figure 7.7d shows that the Pd-ZnO-EG composite gave a higher percentage removal of 87%, displaying the highest photodegradation efficiency compared to ZnO and Pd-ZnO. This is due to the integration of Pd which acted as an electron sink as well as improving the light absorption of the ZnO. In addition, the electron transport ability of the EG aided in the transfer of the electrons from the ZnO, thereby, reducing the electron-hole recombination process on the ZnO semiconductor. Consequently, there was generation of more hydroxyl radicals for the photodegradation of the acid orange 7 dye in the solution. Since ZnO is generally known to suffer photocorrosion, a photo-stability test was carried out on the as-prepared Pd-ZnO-EG material for the degradation of the acid orange 7 dye. The Pd-ZnO-EG was recycled and used three times for the degradation of the dye. The test results revealed there was a decreased in the percentage removal from 87 to 77% showing a good stability of the material.

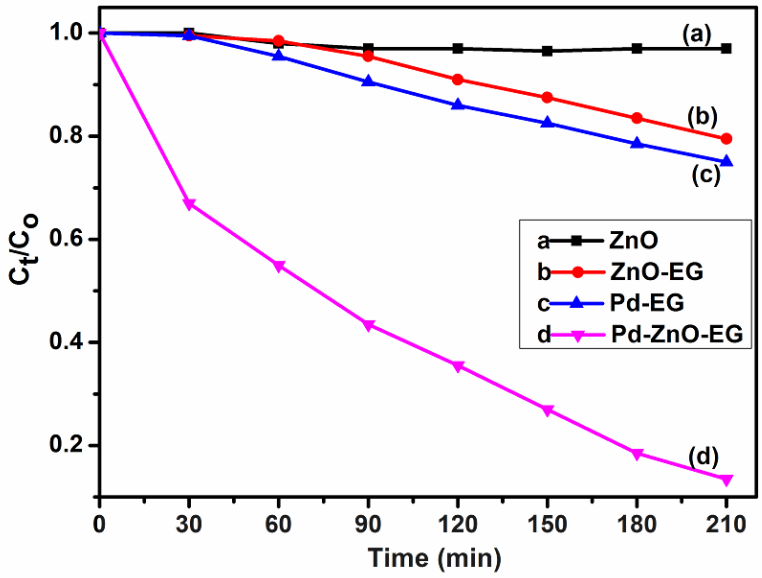

Figure 7.7: Photocatalytic activities of the (a) ZnO, (b) ZnO-EG, (c) Pd-ZnO and (d) Pd-ZnO-EG for the removal of acid orange 7 dye using 20 ppm as initial dye concentration

A mechanism was proposed for the photocatalytic activity which results from visible light absorption by Pd-ZnO-EG is presented in Figure 7.8, and the reactions necessary for the generation of the •OH radicals are shown in equations [7.1] –[7.10]

$hv + ZnO \rightarrow ZnO + h^+ + e^-$ [7.1]

$hv + H_2O \rightarrow H^+ + \bullet OH$ [7.2]

$2\ h^+ + 2\ H_2O \rightarrow 2\ H^+ + H_2O_2$ [7.3]

$H_2O_2 \rightarrow HO\bullet + \bullet OH$ [7.4]

$e^- + O_2 \rightarrow \bullet O_2^-$ [7.5]

$\bullet O_2^- + H^+ \rightarrow HO_2\bullet$ [7.6]

$\bullet O_2^- + HO_2\bullet + H^+ \rightarrow H_2O_2 + O_2$ [7.7]

$HOOH \rightarrow HO\bullet + \bullet OH$ [7.8]

$\bullet OH$ + acid orange 7 dye $\rightarrow CO_2 + H_2O$ [7.9]

h^+ + acid orange 7 dye → CO_2 + H_2O [7.10]

During irradiation, the EG attracts and transfer the photo-generated electrons because of its charge transfer / electrical conducting ability [44-46]. EG aids in extending the photoresponse of semiconductors such as TiO_2, ZnO, etc. and reduces electron-hole recombination rate [44-46]. Also, its porous nature assists in trapping the Pd-ZnO nanoparticles, thereby reducing loss in the photocatalyst recovery process [44]. The electrons and holes generated under irradiation migrate to the nanocomposite surface to create a reduction-oxidation environment which enabled the degradation of the acid orange 7 dye. The holes combine with the water molecules forming protons and hydroxyl radicals (•OH). The electron reacts with the O_2 from the wastewater to form superoxide radical $•O_2^-$. Then the radicals react with the protons to form hydroperoxide radicals, $HO_2•$. The radicals generated react repeatedly with the acid orange 7 dye to degrade them into less harmful substances such as CO_2 and H_2O [10, 30].

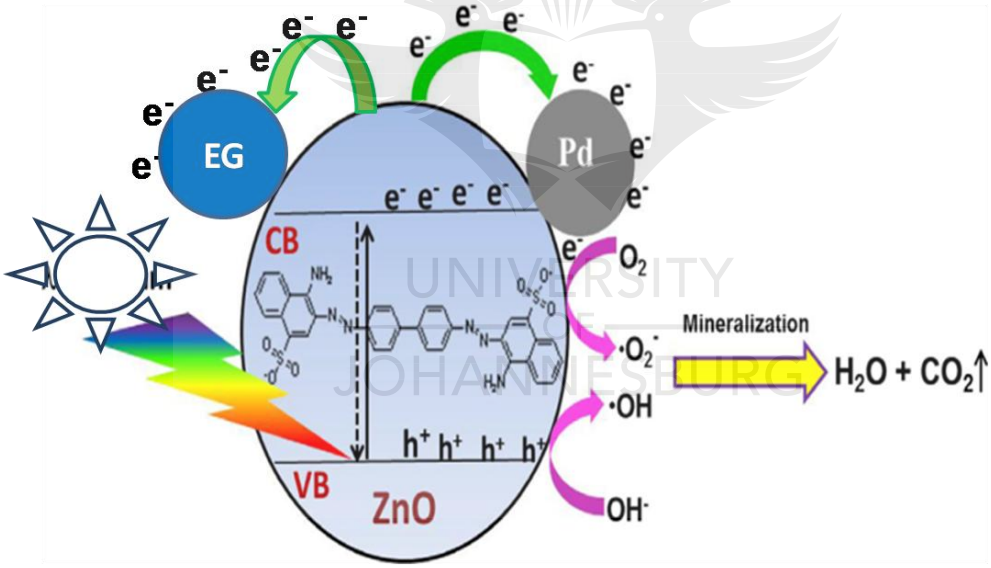

Figure 7.8: Possible mechanism for the photocatalytic activity of Pd-ZnO-EG for the degradation of acid orange 7 dye

7.4 SUB CONCLUSION

A composite of Pd-ZnO-EG was synthesised, characterised and applied for the photocatalytic removal of acid orange 7 dye as a model pollutant. The SEM results showed flower-like structures of the prepared ZnO nanoparticles, and the successful incorporation of the Pd-ZnO on the layers of the EG sheets. The EDS revealed the presence of Pd, Zn, O

and C in the prepared sample and the percentage of Pd present was 1% by weight. Doping the ZnO with Pd and EG resulted in improved degradation efficiency and the removal of acid orange 7 dye in the water treatment process when compared to the pristine ZnO. The better photocatalytic response of the Pd-ZnO-EG makes it attractive and beneficial for the treatment of industrial wastewater especially in industries where dye is utilised.

7.5 REFERENCES

[1] W.J. Cosgrove, F.R. Rijsberman, World water vision: making water everybody's business, Routledge2014.

[2] X. Qu, P.J. Alvarez, Q. Li, Applications of nanotechnology in water and wastewater treatment, Water research, 47 (2013) 3931-3946.

[3] N. Güy, S. Çakar, M. Özacar, Comparison of palladium/zinc oxide photocatalysts prepared by different palladium doping methods for congo red degradation, Journal of colloid and interface science, 466 (2016) 128-137.

[4] V.C. Srivastava, Photocatalytic oxidation of dye bearing wastewater by iron doped zinc oxide, Industrial & Engineering Chemistry Research, 52 (2013) 17790-17799.

[5] I. Oller, S. Malato, J.A. Sánchez-Pérez, Combination of Advanced Oxidation Processes and biological treatments for wastewater decontamination—A review, Science of The Total Environment, 409 (2011) 4141-4166.

[6] R. Khan, M.S. Hassan, L.-W. Jang, J.H. Yun, H.-K. Ahn, M.-S. Khil, I.-H. Lee, Low-temperature synthesis of ZnO quantum dots for photocatalytic degradation of methyl orange dye under UV irradiation, Ceramics International, 40 (2014) 14827-14831.

[7] B. Padhi, Pollution due to synthetic dyes toxicity & carcinogenicity studies and remediation, International Journal of Environmental Sciences, 3 (2012) 940.

[8] X. Cai, Y. Cai, Y. Liu, S. Deng, Y. Wang, Y. Wang, I. Djerdj, Photocatalytic degradation properties of $Ni(OH)_2$ nanosheets/ZnO nanorods composites for azo dyes under visible-light irradiation, Ceramics International, 40 (2014) 57-65.

[9] N. Tripathy, R. Ahmad, J.E. Song, H.A. Ko, Y.-B. Hahn, G. Khang, Photocatalytic degradation of methyl orange dye by ZnO nanoneedle under UV irradiation, Materials Letters, 136 (2014) 171-174.

[10] E.H. Umukoro, M.G. Peleyeju, J.C. Ngila, O.A. Arotiba, Photocatalytic degradation of acid blue 74 in water using Ag–Ag_2O–Zno nanostuctures anchored on graphene oxide, Solid State Sciences, 51 (2016) 66-73.

[11] D. Dolat, S. Mozia, B. Ohtani, A. Morawski, Nitrogen, iron-single modified (N-TiO_2, Fe-TiO_2) and co-modified (Fe, N-TiO_2) rutile titanium dioxide as visible-light active photocatalysts, Chemical Engineering Journal, 225 (2013) 358-364.

[12] M.W. Kadi, D. McKinney, R.M. Mohamed, I.A. Mkhalid, W. Sigmund, Fluorine doped zinc oxide nanowires: Enhanced photocatalysts degrade malachite green dye under visible light conditions, Ceramics International, 42 (2016) 4672-4678.

[13] A.T. Ezhil Vilian, M. Rajkumar, S.-M. Chen, In situ electrochemical synthesis of highly loaded zirconium nanoparticles decorated reduced graphene oxide for the selective determination of dopamine and paracetamol in presence of ascorbic acid, Colloids and Surfaces B: Biointerfaces, 115 (2014) 295-301.

[14] W. Shen, J. Tang, D. Wang, R. Yang, W. Chen, X. Bao, Y. Wang, J. Jiao, Y. Wang, Z. Huang, L. Huang, J. Liu, W. Wang, P. Wu, L.A. Belfiore, Enhanced efficiency of polymer solar cells by structure-differentiated silver nano-dopants in solution-processed tungsten oxide layer, Materials Science and Engineering: B, 206 (2016) 61-68.

[15] H. Moussa, E. Girot, K. Mozet, H. Alem, G. Medjahdi, R. Schneider, ZnO rods/reduced graphene oxide composites prepared via a solvothermal reaction for efficient sunlight-driven photocatalysis, Applied Catalysis B: Environmental, 185 (2016) 11-21.

[16] A. Valour, F. Cheviré, F. Tessier, F. Grasset, B. Dierre, T. Jiang, E. Faulques, L. Cario, S. Jobic, Preparation of nitrogen doped zinc oxide nanoparticles and thin films by colloidal route and low temperature nitridation process, Solid State Sciences, 54 (2016) 30-36.

[17] J. bo Zhong, J. zhang Li, X. yang He, J. Zeng, Y. Lu, W. Hu, K. Lin, Improved photocatalytic performance of Pd-doped ZnO, Current Applied Physics, 12 (2012) 998-1001.

[18] S. Muthulingam, I.-H. Lee, P. Uthirakumar, Highly efficient degradation of dyes by carbon quantum dots/N-doped zinc oxide (CQD/N-ZnO) photocatalyst and its compatibility on three different commercial dyes under daylight, Journal of colloid and interface science, 455 (2015) 101-109.

[19] A. Mclaren, T. Valdes-Solis, G. Li, S.C. Tsang, Shape and size effects of ZnO nanocrystals on photocatalytic activity, Journal of the American Chemical Society, 131 (2009) 12540-12541.

[20] C. Yu, K. Yang, Y. Xie, Q. Fan, C.Y. Jimmy, Q. Shu, C. Wang, Novel hollow Pt-ZnO nanocomposite microspheres with hierarchical structure and enhanced photocatalytic activity and stability, Nanoscale, 5 (2013) 2142-2151.

[21] C. Yu, K. Yang, W. Zhou, Q. Fan, L. Wei, C.Y. Jimmy, Preparation, characterization and photocatalytic performance of noble metals (Ag, Pd, Pt, Rh) deposited on sponge-like ZnO microcuboids, Journal of Physics and Chemistry of Solids, 74 (2013) 1714-1720.

[22] C. Yu, W. Zhou, H. Liu, Y. Liu, D.D. Dionysiou, Design and fabrication of microsphere photocatalysts for environmental purification and energy conversion, Chemical Engineering Journal, 287 (2016) 117-129.

[23] Z.S. Seddigi, S.A. Ahmed, A. Bumajdad, E.Y. Danish, A.M. Shawky, M.A. Gondal, M. Soylak, The Efficient Photocatalytic Degradation of Methyl Tert-butyl Ether Under Pd/ZnO and Visible Light Irradiation, Photochemistry and photobiology, 91 (2015) 265-271.

[24] N. Daneshvar, D. Salari, A.R. Khataee, Photocatalytic degradation of azo dye acid red 14 in water on ZnO as an alternative catalyst to TiO_2, Journal of Photochemistry and Photobiology A: Chemistry, 162 (2004) 317-322.

[25] S. Balachandran, N. Prakash, M. Swaminathan, Heteroarchitectured Ag–Bi_2O_3–ZnO as a bifunctional nanomaterial, RSC Advances, 6 (2016) 20247-20257.

[26] S. Balachandran, M. Swaminathan, Facile fabrication of heterostructured Bi_2O_3–ZnO photocatalyst and its enhanced photocatalytic activity, The Journal of Physical Chemistry C, 116 (2012) 26306-26312.

[27] S. Balachandran, M. Swaminathan, Superior photocatalytic activity of bimetallic Cd-Ag-ZnO for the degradation of azo dyes under UV light, Emerging Materials Research, 1 (2012) 157-163.

[28] L. Deng, Z. Zhu, L. Liu, H. Liu, Synthesis of Ag_2O and Ag co-modified flower-like SnS_2 composites with enhanced photocatalytic activity under solar light irradiation, Solid State Sciences, 63 (2017) 76-83.

[29] K. Thirumalai, S. Balachandran, M. Shanthi, M. Swaminathan, Heterostructured dysprosium vanadate–ZnO for photo-electrocatalytic and self-cleaning applications, Materials Science in Semiconductor Processing, 71 (2017) 84-92.

[30] K.M. Lee, C.W. Lai, K.S. Ngai, J.C. Juan, Recent developments of zinc oxide based photocatalyst in water treatment technology: a review, Water research, 88 (2016) 428-448.

[31] T. Ndlovu, A.T. Kuvarega, O.A. Arotiba, S. Sampath, R.W. Krause, B.B. Mamba, Exfoliated graphite/titanium dioxide nanocomposites for photodegradation of eosin yellow, Applied Surface Science, 300 (2014) 159-164.

[32] M. Peleyeju, E. Umukoro, J. Babalola, O. Arotiba, Electrochemical Degradation of an Anthraquinonic Dye on an Expanded Graphite-Diamond Composite Electrode, Electrocatalysis, 7 (2016) 132-139.

[33] S. Anas, S. Rahul, K.B. Babitha, R.V. Mangalaraja, S. Ananthakumar, Microwave accelerated synthesis of zinc oxide nanoplates and their enhanced photocatalytic activity under UV and solar illuminations, Applied Surface Science, 355 (2015) 98-103.

[34] L. Hao, W. Gao, Y. Liu, Y. Liu, Z. Han, Q. Xue, J. Zhu, Self-powered broadband, high-detectivity and ultrafast photodetectors based on Pd-MoS_2/Si heterojunctions, Physical Chemistry Chemical Physics, 18 (2016) 1131-1139.

[35] P. Zuppella, E. Pasqualotto, S. Zuccon, F. Gerlin, A.J. Corso, M. Scaramuzza, A. De Toni, A. Paccagnella, M.G. Pelizzo, Palladium on plastic substrates for plasmonic devices, Sensors, 15 (2015) 1138-1147.

[36] E.H. Umukoro, M.G. Peleyeju, J.C. Ngila, O.A. Arotiba, Towards wastewater treatment: Photo-assisted electrochemical degradation of 2-nitrophenol and orange II dye at a tungsten trioxide-exfoliated graphite composite electrode, Chemical Engineering Journal, 317 (2017) 290-301.

[37] A. Khan, Raman spectroscopic study of the ZnO nanostructures, J. Pak. Mater. Soc, 4 (2010) 5-9.

[38] A. Khan, M.E. Kordesch, Synthesis of novel zinc oxide microphone-like microstructures, Materials Letters, 62 (2008) 230-234.

[39] A. Umar, B. Karunagaran, E. Suh, Y. Hahn, Structural and optical properties of single-crystalline ZnO nanorods grown on silicon by thermal evaporation, Nanotechnology, 17 (2006) 4072.

[40] K.-W. Park, J.H. Jung, Spectroscopic and electrochemical characteristics of a carboxylated graphene–ZnO composites, Journal of Power Sources, 199 (2012) 379-385.

[41] P. Wang, Y. Tang, Z. Dong, Z. Chen, T.-T. Lim, Ag–AgBr/TiO_2/RGO nanocomposite for visible-light photocatalytic degradation of penicillin G, Journal of Materials Chemistry A, 1 (2013) 4718-4727.

[42] A.T. Kuvarega, R.W. Krause, B.B. Mamba, Nitrogen/palladium-codoped TiO_2 for efficient visible light photocatalytic dye degradation, The Journal of Physical Chemistry C, 115 (2011) 22110-22120.

[43] S. Navaladian, B. Viswanathan, T. Varadarajan, R. Viswanath, A rapid synthesis of oriented palladium nanoparticles by UV irradiation, Nanoscale research letters, 4 (2009) 181.

[44] X. Yu, Y. Zhang, X. Cheng, Preparation and photoelectrochemical performance of expanded graphite/TiO_2 composite, Electrochimica Acta, 137 (2014) 668-675.

[45] Y. Yu, N. Zhao, C. Shi, C. He, E. Liu, J. Li, Electrochemical hydrogen storage of expanded graphite decorated with TiO_2 nanoparticles, International journal of hydrogen energy, 37 (2012) 5762-5768.

[46] X. Yue, R. Zhang, F. Zhang, L. Wang, Decomposition of crude oil absorbed into expanded graphite/TiO_2/NiO composites, Desalination, 252 (2010) 163-166.

CHAPTER 8

PHOTO-ELECTROCATALYTIC APPLICATION OF PALLADIUM DECORATED ZINC OXIDE-EXPANDED GRAPHITE ELECTRODE FOR THE REMOVAL OF 4-NITROPHENOL: EXPERIMENTAL AND COMPUTATIONAL STUDY[1]

8.1 INTRODUCTION

The efficient and effective disposal of organic pollutants in the environment is a necessity for sustainable development in the society. However, this is a major challenge due to the growth of industrialisation [1]. Nitrophenol and its derivatives are organic pollutants which are mostly used in agricultural, textile, paper, explosives and pharmaceutical industries [2, 3]. They are potentially hazardous and mutagenic to humans and the general ecosystem [2, 4]. Among the derivatives of nitrophenols, 4-nitrophenol is found to be highly toxic, stable and biorefactory in nature [2, 4]. Therefore, the removal of 4-nitrophenol from industrial wastewaters is essential. Several traditional methods have been utilised for the treatment of these 4-nitrophenol-containing wastewaters, but the poor removal rate is still a general concern due to its high resistance to biodegradation [5-8].

In recent years, electrochemical methods have been successfully developed as alternatives to the conventional methods for the removal of organic pollutants. This is mainly due to the generation of highly reactive hydroxyl radical for the non-selective oxidation of these pollutants [9-11]. This process entails the electrochemical production of hydroxyl radical at the surface of the electrode which is followed by its reaction with the organic pollutants [9, 11]. The advantages of electrocatalytic degradation technique include the immobilisation of the catalyst (electrode) which helps in minimising catalyst separation from the reaction system, controlled reaction conditions and the relatively low equipment cost [10, 12]. However, some drawbacks have also been reported such as the oxygen evolution which takes place simultaneously with the oxidation of the pollutant resulting from the application of high voltage, the low concentration of the pollutant raises the problem of mass transfer and the processes can be time consuming [10, 13, 14]. Thus, it is important to improve this technique by the concurrent use of visible light irradiation (photolysis), leading to a process known as photoelectrocatalysis. In this process, a photoanode is constructed by mounting a semiconductor material that is photoactive on a conducting support with the simultaneous application of light and a bias voltage. This leads to the production of non-selective oxidants

[1] This chapter has been reviewed and accepted with corrections: Royal Society of Chemistry Advances, RSC Adv.

such as hydroxyl radical by the semiconductor and the conducting support for the degradation of the pollutants [9, 15]. In recent years, the most widely used TiO_2 semiconductor photoanode [14-20] has been substituted by ZnO due to its nontoxicity, availability, low cost, chemical and thermal stability, good catalytic efficiency and optoelectronic nature [21-24]. ZnO has also found applications in photovoltaic devices, water splitting and organic pollutants degradation [25, 26]. However, the fundamental problem of ZnO is the recombination rate of the photoexcited holes and electrons which hinders its photocatalytic efficiency. Generally, the kinetics of the recombination rate is faster than that of the surface reduction-oxidation reactions, and this results in a decrease of the quantum efficiency of photocatalysis [23, 24]. Different techniques have been used to reduce the electron-hole recombination rate and these include the introduction of semiconductor oxides, carbonaceous materials and noble metals [23, 24, 27]. Noble metals nanoparticles such as Au, Ag, Pt and Pd have been reported to enhance the photocatalytic activity of ZnO [28-30]. In comparison with Pt and Au, Pd is cheaper and it has been employed in catalytic processes [24]. Pd nanoparticles can act as collectors for the photoexcited electrons and these aid the charge transfer and transportation processes, thereby creating more active sites for the catalytic reaction [31]. The use of expanded graphite (EG) can also help in reducing the recombination rate of ZnO. EG is a carbonaceous material consisting of two dimensional bonded carbons which possesses excellent electrical conductivity, large surface area, good porosity, compressibility, low density and excellent electron transfer and transport properties. In addition, it possesses good mechanical and thermal stability, good resistance to high temperature, and can withstand high voltage [15, 32-34]. The inclusion of EG in Pd-ZnO-EG can result in the EG acting as an electron sink for photoexcited electrons from ZnO due to the unique electron transport capability of EG [19]. As a result, the problem of electron-hole recombination rate of ZnO would be minimised. Thus, the photoactivity of ZnO in the Pd-ZnO-EG nanocomposite would be enhanced by forming more oxidants such as hydroxyl radical for the degradation of organic pollutants. The EG can also be used as a conducting support for the immobilisation and trapping of the ZnO and Pd, therefore, minimising the losses from the recovery of these photocatalysts [15].

Considering the unique properties of Pd, ZnO and EG, it can be hypothesised that Pd-ZnO-EG nanocomposite can act as a promising photoeletrocatalytic material for the degradation of 4-nitrophenol. In this novel study, Pd-ZnO supported on EG was synthesised, fabricated into a photoanode and used for the photoelectrocatalytic removal of 4-nitrophenol as a model organic pollutant. Of importance is the understanding of the degradation pattern and products

during the photoelectrocatalytic process because it can be used to estimate the toxicity of the product in comparison with the initial organic pollutants, the time of reaction, the kinetics and mechanism of reaction. To better understand the degradation mechanism, we have employed density functional theory (DFT) method to predict the degradation products and the different possible degradation pathways for the 4-nitrophenol degradation which is in agreement with experimental findings reported in literature.

8.2 EXPERIMENTAL PROCEDURES

8.2.1 Materials and apparatus

Nitric acid, sulphuric acid, natural graphite, sodium sulphate, zinc acetate dehydrate, potassium hexacyanoferrate (II), sodium hydroxide, potassium chloride, 4-nitrophenol and potassium hexacyanoferrate (III). These were bought from Sigma Aldrich, Germany and used for the experiment without further purification.

8.2.2 Synthesis of expanded graphite (EG)

The expanded graphite was prepared by employing our previous technique [35, 36]. Sifted flakes of natural graphite (300 μm) were immersed in a 1:3 (vol/vol) mixture of concentrated nitric and sulphuric acids for 48 h at ambient conditions for the intercalation of the graphite material. The intercalated graphitic material was washed properly to achieve a pH value close to 7, and dried in the air. Then, the expansion of the graphitic material was done by heating the material at about 800 ºC to form a puffed-up material called expanded graphite.

8.2.3 Synthesis and construction of Pd-ZnO-EG nanocomposite

Zinc acetate dehydrate (3.29 g), 2.4 g of sodium hydroxide and 2 g of the prepared EG were mixed in 70 mL of ethanol solution and stirred for 30 min. The mixture was poured into a Teflon-lined autoclave and thermally treated at 160 ºC for 24 h. The autoclave was left to cool to ambient temperature. The ZnO-EG formed was centrifuged, washed several times with water and ethanol, and dried overnight at 60 ºC in an oven. In order to prepare the Pd-ZnO-EG, a certain amount of the ZnO-EG was weighed and dispersed in ethanol, followed by ultrasonication for 30 min. Palladium (II) acetate in ethanol solution was added and ultrasonicated further for 20 min. The resulting mixture was put in a water bath and kept at 70 ºC for 3 h. The mixture was filtered and dried at 60 ºC overnight. The amount of Pd in the composite was 5 % by weight of the Pd-ZnO-EG nanocomposite.

8.2.4 Construction of EG, ZnO-EG and Pd-ZnO-EG electrodes

The construction of the electrodes was done using a technique described in our previous studies [11, 15, 19, 37]. The as-prepared EG, ZnO-EG and Pd-ZnO-EG nanocomposites were used to make pellets using a hydraulic press at a pressure of about 10000 psi. These pellets were utilised for fabricating the electrodes. Copper wire, conductive silver paint and epoxy sealer were also used. These pellets were placed on the coiled copper wire with the assistance of the conductive silver paint. This was left out in ambient air overnight. The pellets edges were then sealed with the epoxy sealer in order for electricity to flow only from the basal plane. This was placed in a glass rod before further use.

8.2.5 Characterisation of EG, ZnO-EG and Pd-ZnO-EG nanocomposites

X-ray diffractometer (Philips PAN Analytical X'Pert powder, Netherlands) with Cu-Kα radiation (λ = 0.15418) was used to determine the crystallinity of the as-prepared materials. The Raman spectra were measured with Witec alpha300 R confocal Raman microscope (Germany). The spectra from the UV absorbance were done at a wavelength of 200–800 nm with Shimadzu UV-2450 (Japan). Morphological images of the as-prepared samples were taken with scanning electron microscopy (TESCAN, VEGA 3 XMU, Czech Republic) and transmission electron microscopy (JEOL JEM-2100, USA) at 200 kV accelerating voltage. Energy-dispersive X-ray spectrometer (TESCAN, Czech Republic) connected to the SEM was employed in measuring the samples' elemental composition. The extent of mineralisation was measured with Teledyne Tekmar TOC Analyzer (USA). Cary 60 UV-Visible spectrophotometer (Agilent technologies, USA) was utilised in determining the removal efficiency of the 4-nitrophenol. The source of visible light irradiation was Oriel LCA-100 Solar Simulator (USA) which was equipped with 100 W xenon lamp and AM1.5G filter.

8.2.6 Photoelectrochemical measurements

Electrochemical and photoelectrochemical behaviours of the EG, ZnO-EG and Pd-ZnO-EG nanocomposite electrodes were investigated in a redox probe of 5 mM of potassium ferrocyanide and ferricynanide in 0.1 M KCl solution. Cyclic voltammetry (CV) and chronoamperometry photocurrent responses under visible light (Oriel LCA-100 Solar Simulator) were investigated in a three-electrode electrochemical configuration with Autolab 302N potentiostat (The Netherlands), while the working electrodes (with diameter of 1.3 cm

and geometric area of 1.33 cm^2) were the as-prepared materials, platinum foil was used as counter electrode and the reference electrode was Ag/AgCl (3.0 M KCl).

8.2.7 Electrochemical and photoelectrocatalytic experiments

The photoelectrocatalytic activity of the materials were determined by the degradation of 4-nitrophenol. This was carried out in a reactor (100 mL) with 20 ppm of 4-nitrophenol. A solution of 0.1 M Na_2SO_4 was used as supporting electrolyte. The electrodes were positioned to face the irradiation from the solar simulator. The source of power was the potentiostat, while Oriel LCA-100 Solar Simulator was the source of irradiation. In order to achieve a power beam of 1 sun which is equivalent to a 100 $mWcm^{-2}$, an AM1.5G filter was placed in the simulator and the reactor was 8 cm away from the irradiation source. A bias potential was applied without making use of the visible light for the electrocatalytic removal of the 4-nitrophenol. At 30 min intervals, an aliquot of 4-nitrophenol was withdrawn from the reactor with disposable syringe over a period of 2 h 30 min. The aliquot was then filtered and the removal efficiency of the 4-nitrophenol was measured on a UV-Visible spectrophotometer. The total organic content was investigated on a TOC analyser (Teledyne Tekmar TOC fusion). Furthermore, the influence of pH, current density and percentage of Pd in the nanocomposite were studied.

8.2.8 Computational details

Quantum chemical calculations based on density functional theory (DFT) method were used to study the different possible pathways for the degradation of 4-nitrophenol. Full geometry optimisations were carried out in the gas phase with the B3LYP [38, 39] functional with the 6-31G(d) basis set [40]. The optimisations were followed by frequency computations at the same level of theory to confirm that the stationary points are minima (no imaginary frequencies) and that each of the transition state (TS) structures has only one imaginary frequency. The reaction pathways were subjected to intrinsic reaction coordinate (IRC) [41, 42] analysis in order to trace their paths and to confirm that the optimised TS connects the correct reactant and product. Zero-point energy (ZPE) correction is included in all the reported electronic energies. All the computations were carried out using the Gaussian 09 software suite [43] running on the GridChem Science Gateway [44-46].

8.3 RESULTS AND DISCUSSION

8.3.1 Raman studies

The Raman spectra of the EG and Pd-ZnO-EG materials are illustrated in Figs 8.1a and 8.1b. The band observed at 100 cm^{-1} of the Raman spectrum of ZnO (Fig 1a) corresponds to the E_2 (Low) mode while the peak at 336 cm^{-1} results from the Raman active frequency phonons, E_2 (High) – E_2 (Low). The peak around 388 cm^{-1} can be assigned to the A_{1T} mode, while the low intensity peak at 588 cm^{-1} can be ascribed to the E_{1L} mode. In addition, the very intense and characteristic peak at 441 cm^{-1} is attributed to E_2 (high), considered as the Raman active optical phonon mode. This is an indication that the as-prepared ZnO possesses a wurtzite hexagonal phase [47-49]. The peak at 639 cm^{-1} is exhibited by Pd nanoprticles which is a Raman active vibrational mode and characteristic feature of PdO [50, 51]. In Fig. 8.1b, it is clear that additional new peaks appeared near 1353 and 1587 cm^{-1} which are the D and G bands of the EG, respectively (Inset). These are due to the in-plane phonon vibration of the sp^2-bonded carbon atoms of the graphite material (G band) and the defects produced in the graphite sheets (D band) due to the formation of sp^3 carbon bonding caused by the oxygen groups present in the EG. However, a disappearance of the two peaks at 388 and 588 cm^{-1} was observed. In addition, shifts were noticed in the peaks at 330 and 439 cm^{-1} and this could be due to the incorporation of the Pd and EG [52, 53]. This indicates the successful preparation of the Pd-ZnO-EG nanocomposite.

8.3.2 XRD analysis

The crystallinity and phase of the samples were examined by conducting XRD analysis. The XRD patterns of ZnO and Pd-ZnO-EG are presented in Fig. 8.1c. the XRD pattern of ZnO shows peaks at 2θ = 31.8º, 34.6º, 36.4º, 47.7º, 56.7º, 63.0º, 66.5º and 68.1º which correspond to the crystal plane of (100), (002), (101), (102), (110), (103), (200) and (112). These confirm that the hexagonal wurzite structure of ZnO was prepared (JCPDS Card no. 36-1451). The conspicuous peak observed at 2θ =26.46° is allocated to the (002) crystal plane of EG, confirming the presence of EG. However, due to the small amount of Pd added, the peaks for Pd were not observed [24].

8.3.3 UV- visible analysis

The optical behaviour of the materials was determined using UV-Visible analysis. The ZnO-EG exhibited a better photo-absorbance than the ZnO in the region of visible light from λ = 430 – 800 nm (Fig. 8.1d). This can be attributed to the presence of EG which is photosensitizing in nature [54]. It can also be observed that Pd-ZnO-EG displayed a better photo-response in the visible light region with a higher intensity relative to the as-prepared ZnO-EG. Firstly, this better photoresponse is an indication of the addition of Pd to the ZnO-EG material. Secondly, the decoration of the ZnO-EG with Pd aided in effective separation and transport of the photogenerated charge carriers [55]. In the same vein, the surface plasmon resonance behaviour of Pd played a role in improving the light absorption [56]. It can be deduced that the photosensitizing nature and charge transfer ability of the EG as well as the surface plasmon resonance behaviour of the Pd resulted in a synergic enhancement of the photoactivity observed in the Pd-ZnO-EG nanocomposite [15, 55].

8.3.4 Braunauer-Emmett-Teller (BET) analysis

The determination of the surface area, pore volume and pore size of the ZnO and Pd-ZnO-EG was carried out with the aid of nitrogen adsorption-desorption (BET) analysis. Table 8.1 shows the obtained results from the analysis. The nitrogen adsorption-desorption isotherms of the prepared Pd-ZnO-EG sample are presented (Fig. 8e). It was observed that the Pd-ZnO-EG displayed bigger pore size, pore volume and BET surface area in comparison with the bare ZnO. This is an indication that the incorporation of the Pd and EG led to an increase in surface area which can improve the photoelectrocatalytic degradation of the 4-nitrophenol by the Pd-ZnO-EG electrode.

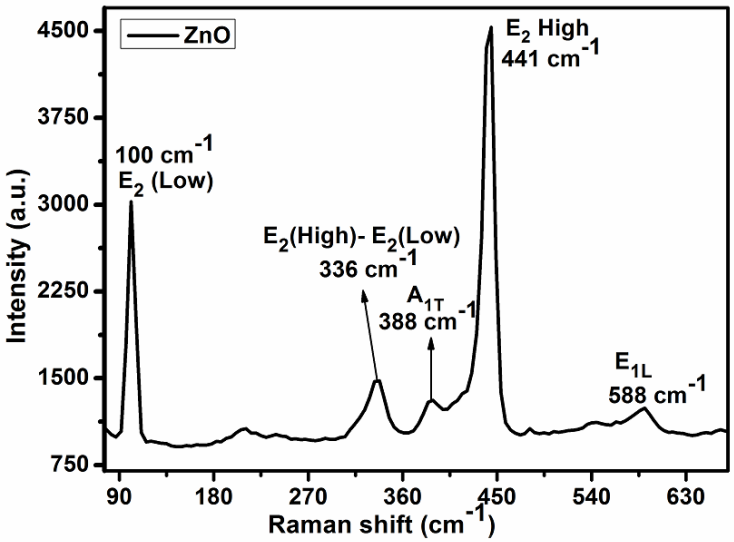

a)

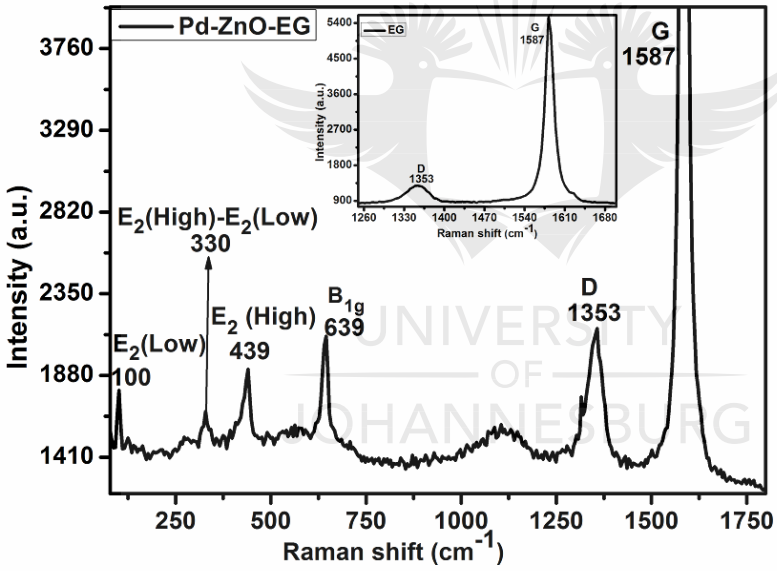

b)

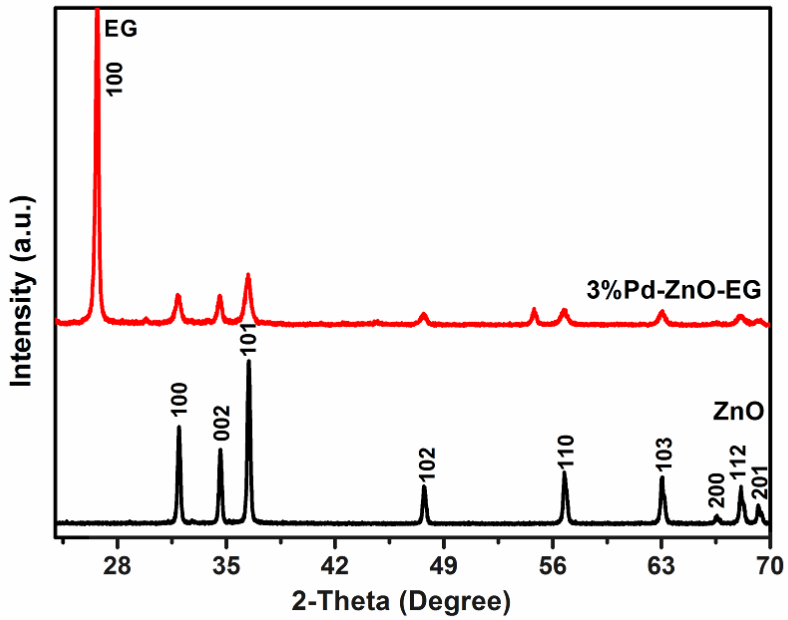

c)

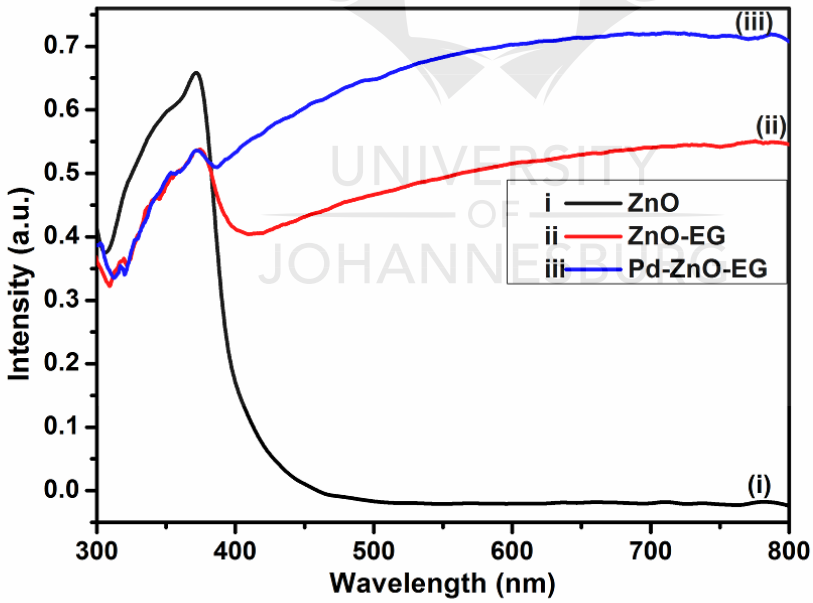

d)

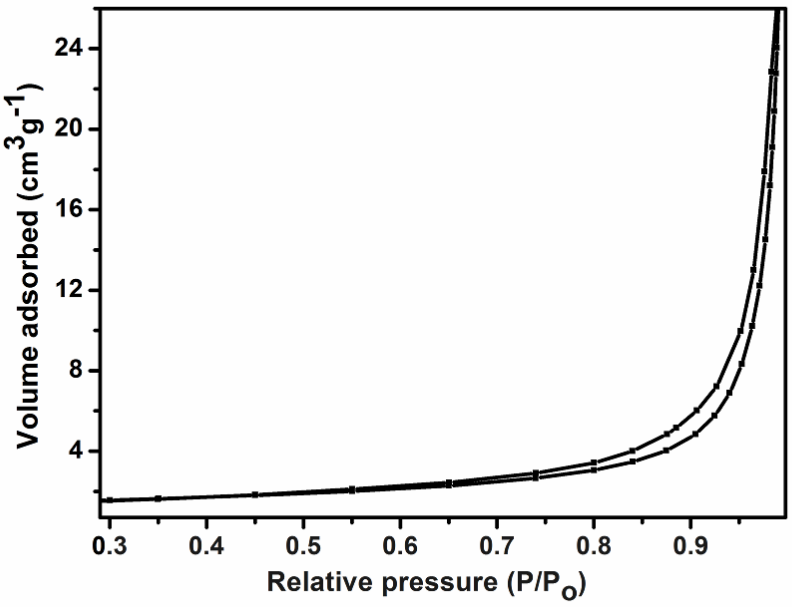

e)

Figure 8.1: Raman spectra of (a) ZnO and (b) Pd-ZnO-EG and EG (inset); (c) X-ray diffractograms of ZnO and 3% Pd-ZnO-EG; (d) UV-Visible absorbance spectra of (i) ZnO, (ii) ZnO-EG and (iii) Pd-ZnO-EG. (e) Nitrogen adsorption-desorption isotherms of Pd-ZnO-EG sample.

Table 8.1: The BET surface area, pore volume and pore size of the bare ZnO and Pd-ZnO-EG samples

Material	BET Surface area (m^2g^{-1})	Pore volume (cm^3g^{-1})	Pore size (nm)
ZnO	3.2959	0.0105	12.7215
Pd-ZnO-EG	4.9329	0.0354	28.6602

8.3.5 Morphological studies

The morphological images of the as-prepared ZnO, EG, and Pd-ZnO-EG were taken on SEM and TEM, while the elemental composition were determined using an energy dispersive X-ray spectroscopy joined to the TEM. Figure 8.2a shows the different layers of graphitic sheets and pores of the EG for the immobilisation of the Pd and ZnO nanoparticles. In Fig. 8.2b, the ZnO

nanoparticles are supported within the layers of the EG sheets. Figures 8.2c and 8.2d illustrate the TEM results of the ZnO and the Pd-ZnO-EG respectively. The Pd nanoparticles (smaller nanoparticles) aredistributed on the ZnO nanoparticles (larger particles) within the graphitic sheets/layers of the EG In Fig. 8.2e, the EDS spectrum shows the elemental composition of the Pd-ZnO-EG to be C, O, Zn and Pd, confirming the successful preparation of the Pd-ZnO-EG nanocomposite [24].

a)

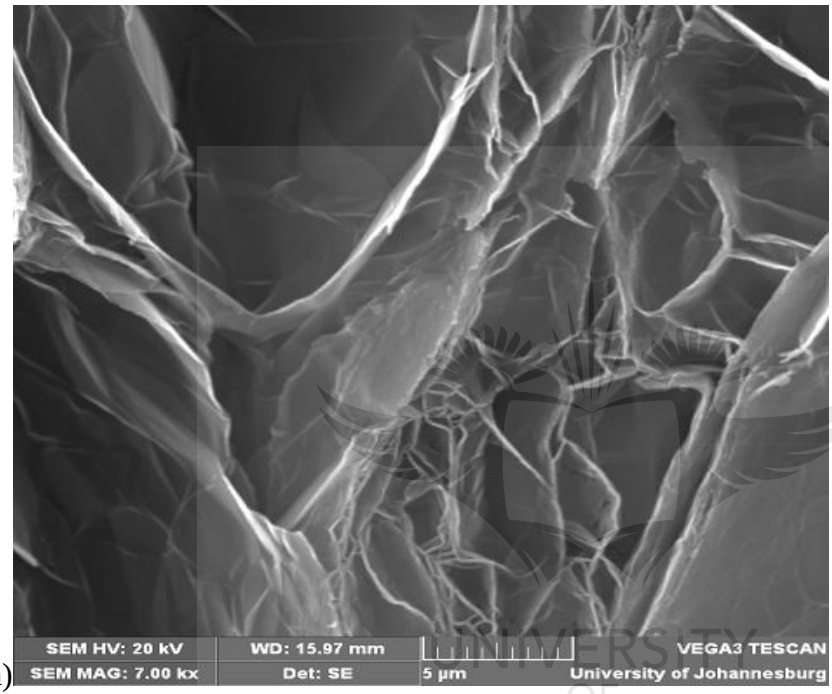

b)

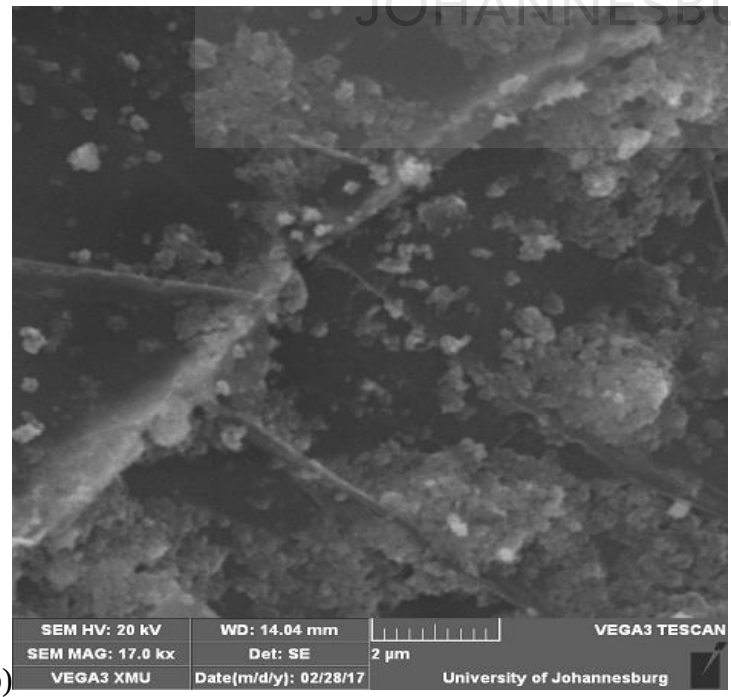

c) 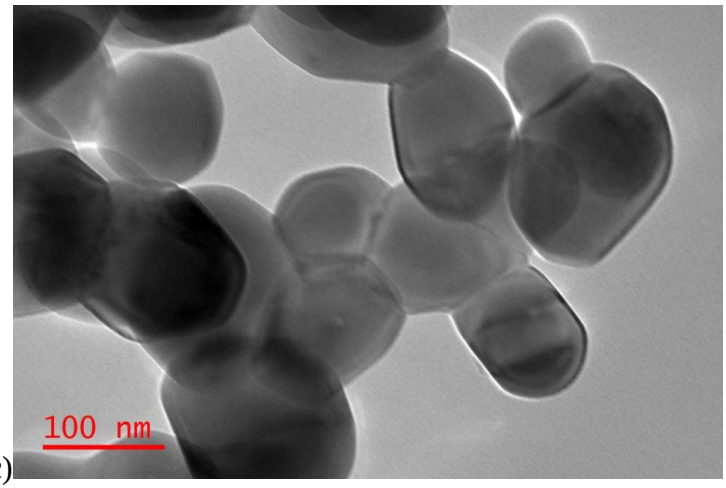

d) 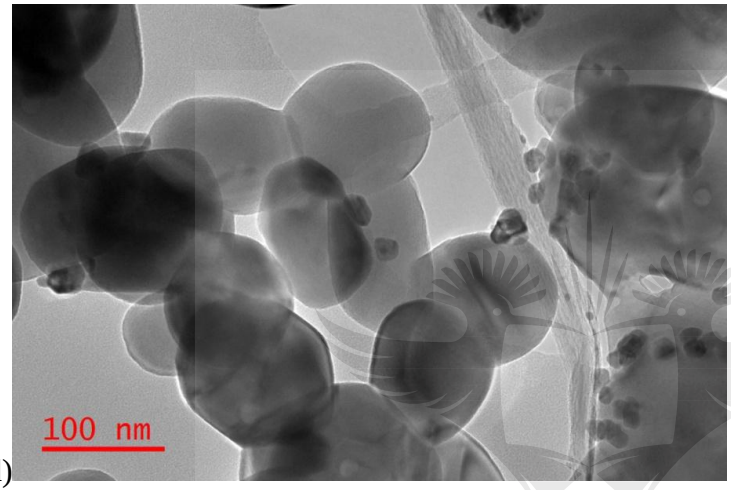

e) 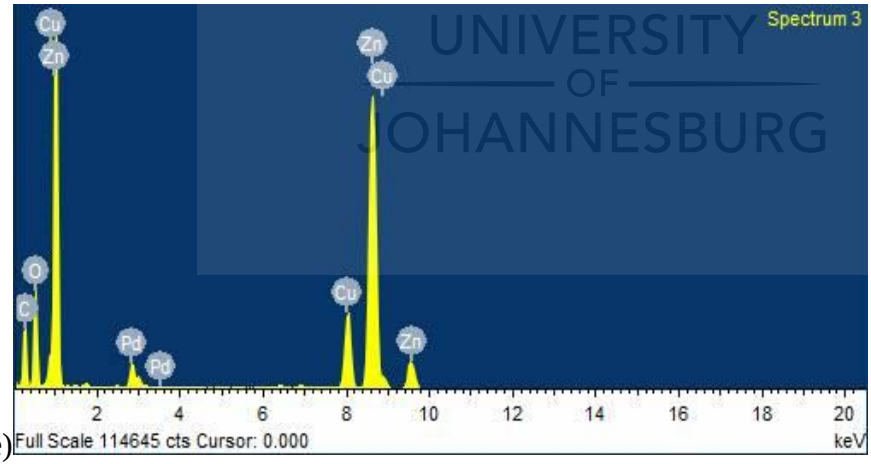

Figure 8.2: SEM images of (a) Expanded graphite, (b) Pd-ZnO nanoparticles trapped in EG sheets. TEM images of (c) ZnO and (d) Pd nanoparticles anchored on ZnO immobilised on the EG. (e) EDX spectra showing the presence of Pd, Zn, O and C in the Pd-ZnO-EG samples

8.3.6 Photoelectrochemical characterisation

The cyclic voltammetry of the Pd-ZnO-EG displayed a much higher current in relation to EG and ZnO-EG electrodes (Fig. 8.3a). Lower faradaic currents of the $[Fe(CN)_6]^{-3/-4}$ were observed from the EG and ZnO-EG when compared to that generated from Pd-ZnO-EG. This could be as a result of the increase in the surface area of the Pd-ZnO-EG after the addition of Pd nanoparticles to the ZnO-EG as showed by the results of the BET. This might lead to increase in the electroactive surface area of the electrode, thus the Pd-ZnO-EG is seen to exhibit a higher rate of electrode reaction.[24, 35, 55]. The electrode active surface area of the Pd-ZnO-EG could also be responsible for the increased current, thus, the electrode active surface areas were determined using the Randles–Sevcik equation;

$$ip = kn^{3/2}AD^{1/2}v^{1/2}C \qquad [8.1]$$

Where *D*, diffusion co-efficient, is 7.6×10^{-6} for ferrocyanide, *k* is 2.69×10^{5}, *A* is the area of the electrode active surface, *n* is the number of electrons involved in the reaction process, *C* is concentration of the electrochemical probe and *v* is the scan rate [57, 58]. The calculated electroactive surface areas of the EG, ZnO-EG and Pd-ZnO-EG electrodes are 1.60, 2.27 and 10.91 mm^2 respectively. These suggest that there was a considerable increase in the electrochemical active sites after the addition of the Pd nanoparticle [35]. Chronoamperometry technique was employed to study the photocurrent responses of the EG, ZnO-EG and Pd-ZnO-EG materials. The efficiency of charge carriers separation and transfer is proportional to the photocurrent response of the material [17, 59, 60]. It is observed from Fig. 8.3c that the Pd-ZnO-EG exhibited a stronger photoresponse in comparison to the ZnO-EG and EG materials. This suggests that the Pd nanoparticles could effectively retard the recombination of the photo-generated electrons and holes, and thereby improving the photoelectrocatalytic activity of the Pd-ZnO-EG, thus, making it a promising photoelectrode for photoelectrocatalytic processes especially in water treatment process.

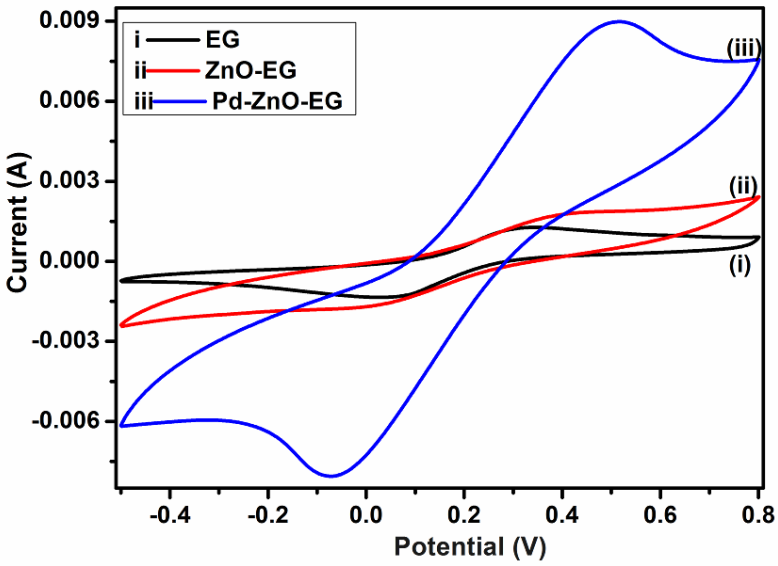

a)

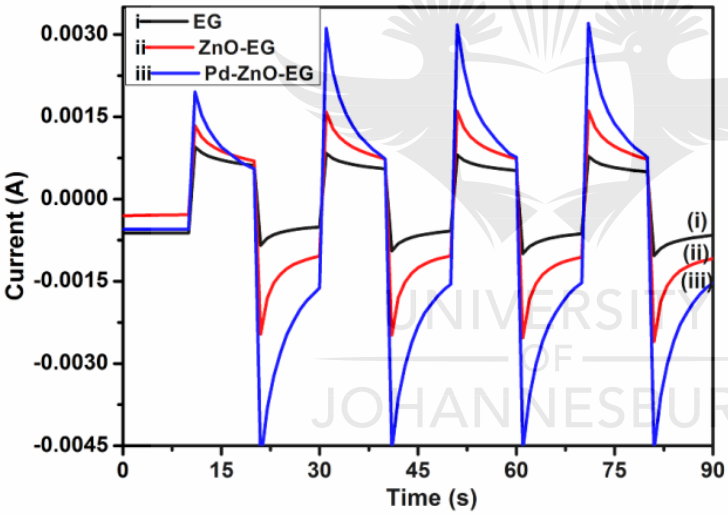

b)

Figure 8.3: (a) Cyclic voltammograms of (i) EG, (ii) ZnO-EG and (iii) Pd-ZnO-EG electrodes in 5mM $[Fe(CN)_6]^{-3/-4}$, 0.1 M KCl solution, at 50 mVs^{-1} scan rate (b) Photocurrent responses of (i) EG, (ii) ZnO-EG and (iii) Pd-ZnO-EG electrodes in the dark and under light

8.3.7 Photoelectrocatalytic experiments

The photoelectrocatalytic activities of the EG, ZnO-EG and Pd-ZnO-EG electrodes were evaluated by the rate of removal of 4-nitrophenol as a target organic pollutant. The removal rate was monitored using UV-Visible spectroscopy and total organic carbon (TOC) analysis. The results revealed that the Pd-ZnO-EG electrode exhibited a 94% photoelectrocatalytic

removal and a 69% electrocatalytic removal of 4-nitrophenol (Fig. 8.4a). The EG and ZnO-EG electrodes were used as control experiments for the photoelectrocatalytic removal of 4-nitrophenol. As presented in Fig. 8.4b, the kinetics curves show that the ZnO-EG electrode gave a better removal efficiency compared to that of the EG electrode. This is attributed to the photoactive nature of ZnO in the ZnO-EG material. Moreover, after the addition of Pd to the ZnO-EG material, an enhanced photoelectrocatalytic removal performance (94%) was found. The improved removal efficiency is as a result of the photoactive nature of ZnO and the enhanced absorption of visible light caused by the surface plasma resonance ability of Pd in the composite. The Pd can also behave as electron sink for the photoinduced electrons, thereby minimising the recombination of the electron-hole pairs generated [24, 61]. In addition, the ability of the EG to act as electron sink as well as its electron transport nature must have aided in inhibiting the recombination of the photoinduced holes and electrons which led to the improved photoelectrocatalytic performance of the Pd-ZnO-EG electrode.The synergic combination of ZnO, EG and Pd that led to improved photocatalytic degradation can be buttressed with photocurrent responses in Fig. 8.3b which was highest for the Pd-ZnO-EG electrode. The extent of mineralisationof the 4-nitrophenol was evaluated on a TOC analyser after a period of 150 min. The TOC results showed a removal percentage of 58% for Pd-ZnO-EG electrode which is better in comparison with that of EG (32%) and ZnO-EG (40%) electrodes.

Optimisation of the reaction conditions was carried out by evaluating the influence of change in pH, current density and Pd content in the nanocomposite. The photoelectrocatalytic removal of the 4-nitrophenol using Pd-ZnO-EG was found to be pH dependent as presented in the kinetics curves in Fig. 8.4c. The results obtained at pH 4, 7 and 10 are 60, 94 and 64%, respectively. With a pKa of 7.2, 4–nitrophenol is expected to be neutral at pH 7. The highest degradation rate obtained from pH 7 may be as a result of the prevailing neutral 4-nitrophenol which is not poised to or less likely to compete with the OH radical. The influence of current density, which is generally proportional to the production of hydroxyl radical [62], on the removal efficiency of 4-nitrophenol on the Pd-ZnO-EG electrode was investigated (Fig. 8.4d). As the current density was increased from 2.5 to 5 $mAcm^{-2}$, the removal efficiency increased from 73 to 94%. However, no significant increase in the removal efficiency was observed when the current density was increased to 7.5 $mAcm^{-2}$. This could be attributed to increase in oxygen evolution which tends to compete with the oxidation of the organic pollutant [62]. The production of intermediates during the degradation process can constitute a film on the surface of the electrode and reduce its activity. Consequently, increasing the current density

would not lead to effectiveness of cost and energy for the photoelectrocatalytic removal of the 4-nitrophenol. Thus, a current density of 5 $mAcm^{-2}$ was employed for the experiments for energy efficiency.

An increase in the percentage removal was noticed as the Pd content by mass was increased from 1% to 3%. However, further increase in the content to 5% weight of Pd in the nanocomposite did not give a considerable change in the percentage removal of the 4-nitrophenol using the Pd-ZnO-EG electrode. As the Pd content was increased, more hydroxyl radicals were produced for the breaking down of the 4-nitrophenol, but further increase in the Pd content led to the ZnO being shielded from the irradiated light, thereby reducing the photoactive capability of the material [63].

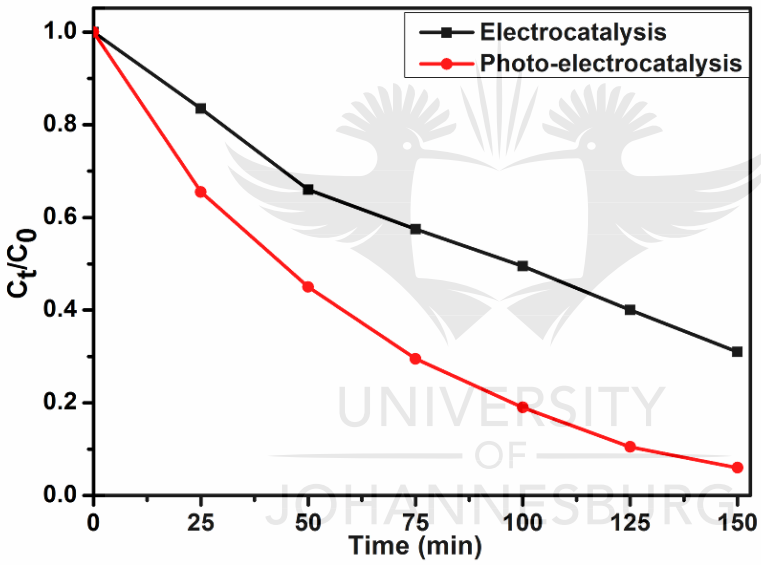

a)

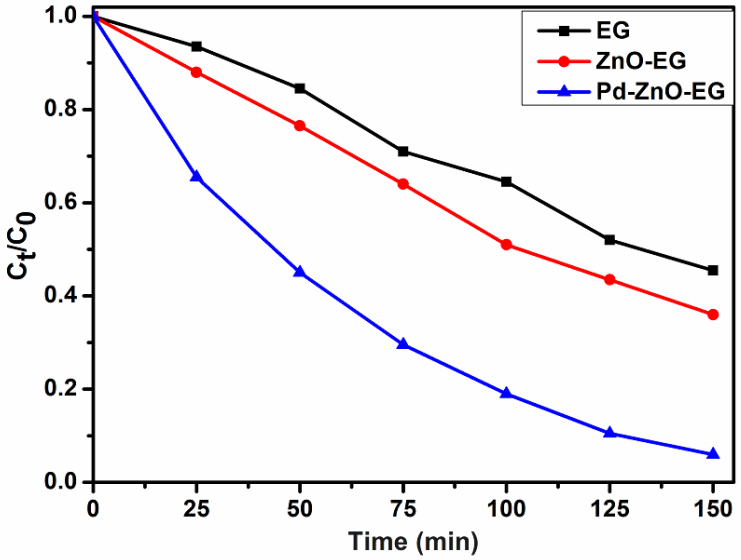

b)

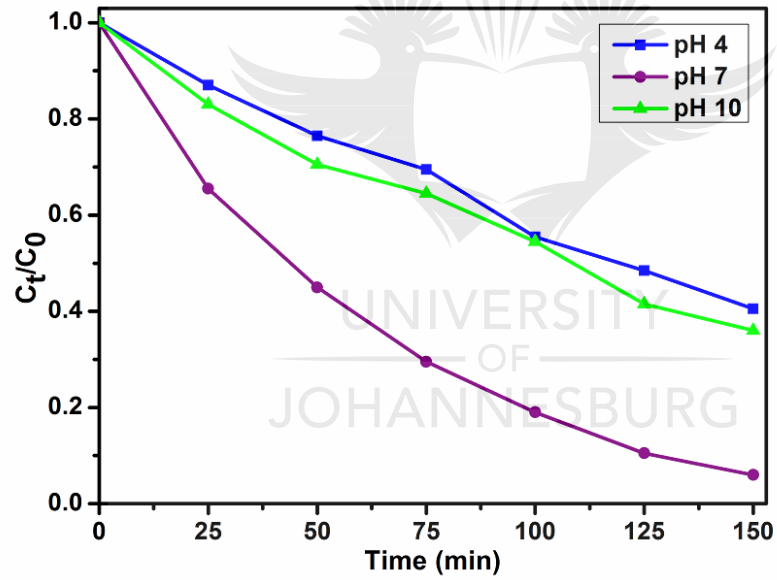

c)

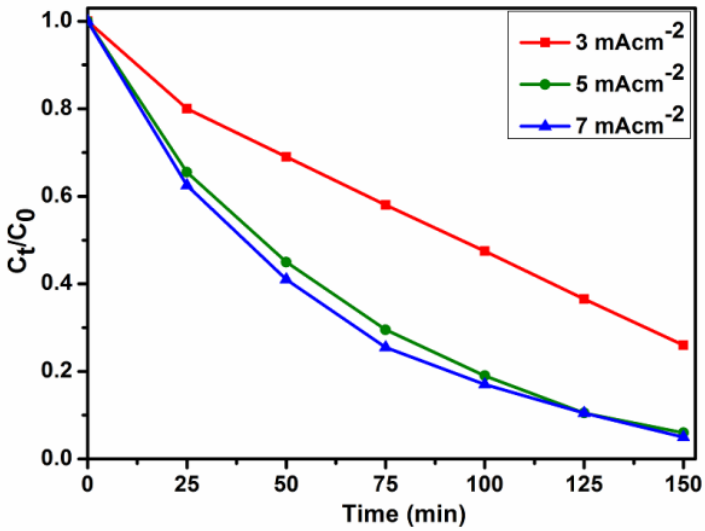

d)

Figure 8.4: Kinetics curves of (a) electrochemical and photoelectrocatalytic removal of 4-nitrophenol at Pd-ZnO-EG electrode. (b) Photoelectrocatalytic removal of 4-nitrophenol at EG, ZnO-EG and Pd-ZnO-EG electrodes. Effect of various (c) pH conditions and (d) different current densities at Pd-ZnO-EG electrode.

8.3.8 Photoelectrocatalytic degradation kinetics and mechanism

The rate of reaction of the degradation of 4-nitrophenol at the EG, ZnO-EG and Pd-ZnO-EG electrode were investigated by modelling the obtained data with Langmuir-Hinshelwood first-order kinetics equation;

$$r = dC/dt = k_r K_{ad} C/(1+K_{ad}C) \quad [8.2]$$

Where r is the degradation rate, C is the concentration of 4-nitrophenol at a particular time, t, K_{ad} is the reactant adsorption equilibrium constant, and k_r is the rate constant of reaction. At very low initial concentration and relatively weak adsorption, $K_{ad}C$ is << 1, and the equation can be simplified to apparent first-order kinetic having k_{app} as the apparent first-order rate constant;

$$ln\ C_0/C_t = k_r K_{ad} t = k_{app} t \quad [8.3]$$

C_0 is the 4nitrophenol initial concentration, C_t is the its concentration at reaction time, t. Figure 8.5a depicts that the $ln\ C_0/C_t$ versus time curves of the obtained data fitted to give linear kinetics curves with coefficients of correlation greater than 0.95. This implies that

reaction for the photoelectrocatalytic removal of 4-nitrophenol follows the pseudo first-order reaction kinetics model, and it can be seen that the Pd-ZnO-EG electrode displayed a better rate of degradation in comparison to EG and ZnO-EG electrodes. The estimated rate constants and correlation coeficients for the electrodes are are 5.53×10^{-3} min^{-1} and 0.9753 for EG; 6.97×10^{-3} min^{-1} and 0.9928 for ZnO-EG; and 18.52×10^{-3} min^{-1} and 0.9913 for Pd-ZnO-EG.

A plausible mechanism was proposed to describe the photoelectrocatalytic process and the reactions taking place for the 4-nitrophenol removal are presented in equations [8.4] – [8.9];

$$hv + ZnO \rightarrow ZnO\ (h^{+}_{VB} + e^{-}_{CB}) \quad [8.4]$$

$$e^{-} + O_2 \rightarrow \bullet O_2^{-} \quad [8.5]$$

$$h^{+} + H_2O \rightarrow H^{+} + \bullet OH \quad [8.6]$$

$$\bullet O_2^{-} + 2H^{+} \rightarrow \bullet OH + \bullet OH \quad [8.7]$$

$$\bullet OH + \text{4-nitrophenol} \rightarrow \text{intermediates} \rightarrow CO_2 + H_2O \quad [8.8]$$

$$\bullet O_2^{-} + \text{4-nitrophenol} \rightarrow \text{intermediates} \rightarrow CO_2 + H_2O \quad [8.9]$$

The difference in the photoelectrocatalytic performance of the different electrodes can be explained using the difference in the work function of ZnO (5.2 eV) and Pd (5.12 eV). It is generally known that a Schottky junction is formed when two materials having different work functions are connected. Electrons flow from the low work function material to the one with a higher work function [64, 65]. Since the Fermi energy of Pd metal (lower work function) is higher than the Fermi level of ZnO semiconductor (higher work function), electrons tend to transfer from the Pd to the ZnO (Fig. 8.5b) until a new Fermi energy level is achieved at equilibrium. At this new Fermi energy level, an Ohmic-type junction which is a metal-semiconductor Schottky barrier is formed under equilibrium [24, 64, 65]. Upon irradiation with visible light, electrons and holes are photoexcited in the ZnO and the photoinduced electrons in the conduction band of the ZnO are transferred to the Pd under the influence of the static electric field at the Schottky junction [24, 65], thus, an effective charge separation is facilitated. The separated and the remaining electrons on the ZnO conduction band react with dissolved oxygen molecules to generate superoxide radicals which react with water molecules to give hydroxyl radicals. The photoinduced holes can migrate to the surface of the ZnO and react with water on the semiconductor surface to form hydroxyl radicals. Based on equations

[8.4] – [8.9], these generated radicals further react with the 4-nitrophenol pollutant to give intermediates which undergo mineralisation to produce CO_2 and H_2O.

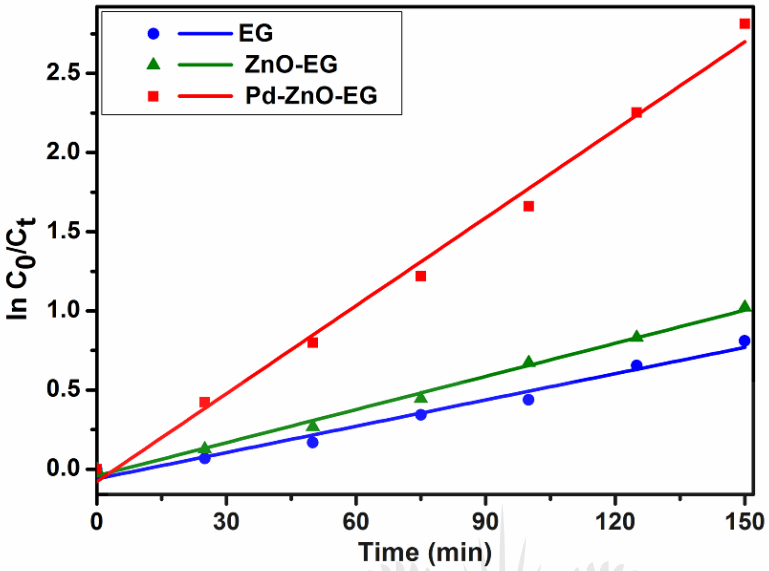

a)

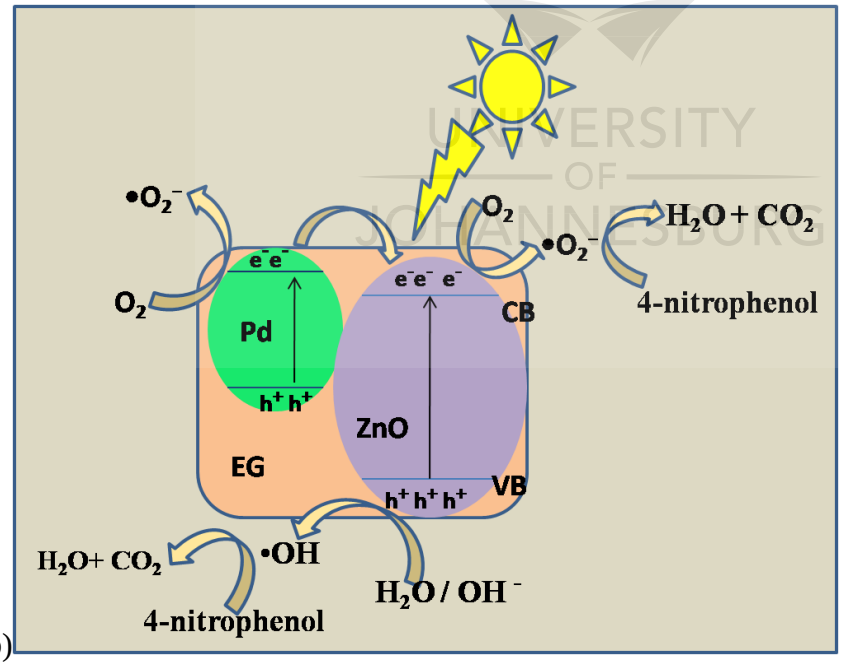

b)

Figure 8.5: (a) Removal kinetics plots of EG, ZnO-EG and Pd-ZnO-EG for the photo-electrocatalytic removal of 4-nitrophenol at neutral pH and 7 $mAcm^{-2}$ at Pd-ZnO-EG electrode. (b) Proposed mechanism for the charge transfer involved in the photo-electrocatalytic activity of Pd-ZnO-EG electrode for the removal of 4-nitrophenol.

8.3.9 Computational modelling of the degradation of 4-nitrophenol

The degradation reaction mechanisms of the oxidation of 4-nitrophenol were studied using the B3LYP/6-31G(d) method in the gas phase based on the reaction between 4-nitrophenol and hydroxyl radical [38, 39]. The reaction pathways for the attack at different positions of 4-nitrophenol by hydroxyl radical were considered and these are represented in Fig 8.6a. The optimized geometries of the transition states are illustrated in Fig 8.6b. The intrinsic reaction coordinates are provided in Fig. 8.6c. It is found from previous reports that molecular oxygen which is evolved at the cathode in an electrochemical system plays an important role in the degradation process and therefore, subsequent reactions with molecular oxygen were also investigated [66, 67].

It was found that the reaction of hydroxyl radical with the 4-nitrophenol has low activation energy and pathway D is barrierless. The addition of hydroxyl radical at position C-4 leads to the formation of hydroquinone and NO_2 radical, having activation energy of 5.83 kJ mol^{-1} for the forward reaction and 115.05 kJ mol^{-1} for the reverse reaction (Fig. 8.6a).

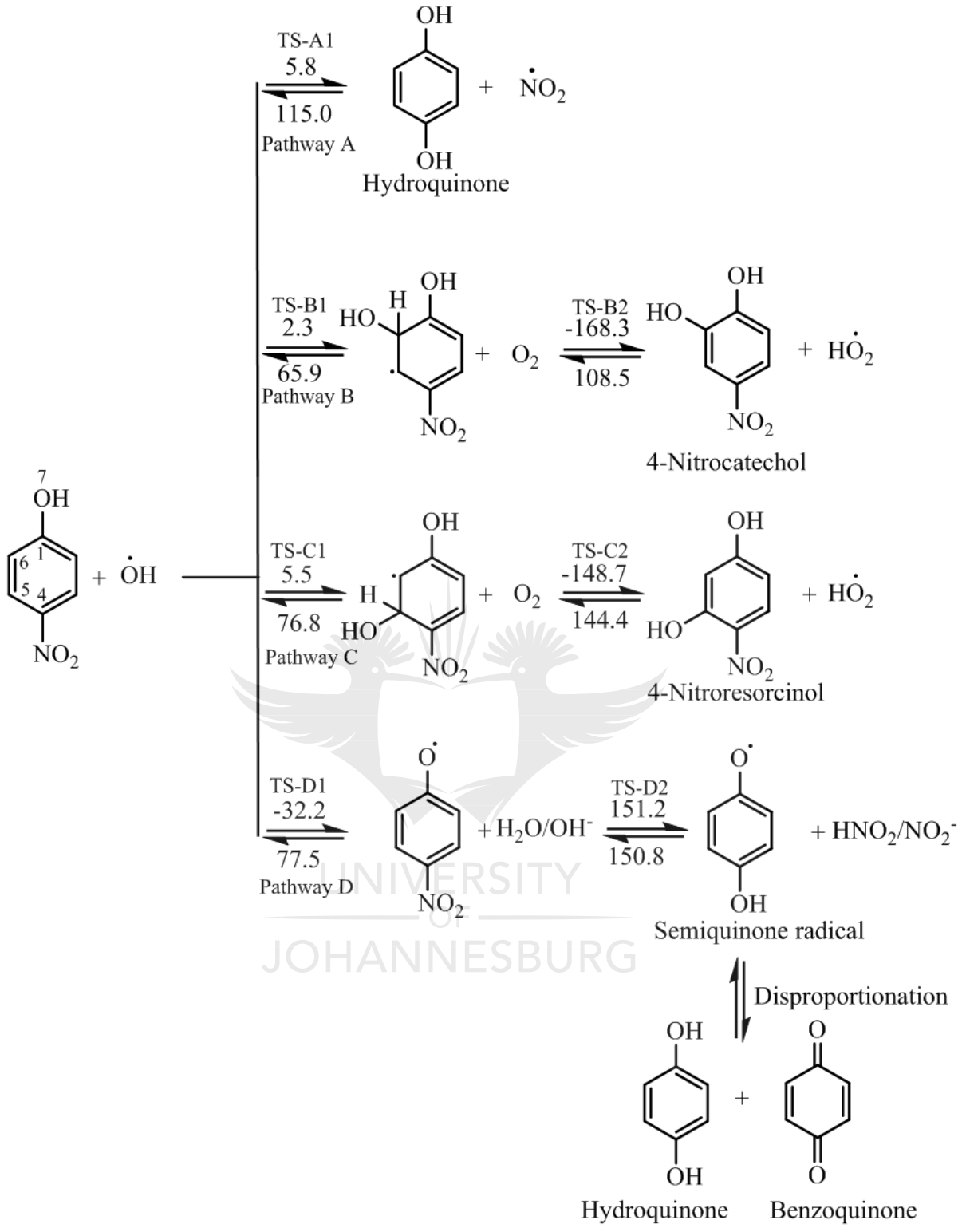

a)

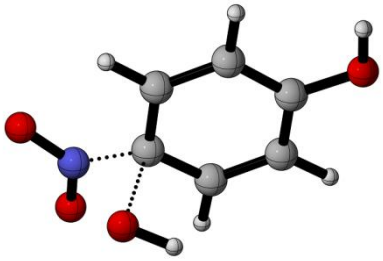

TS-A1

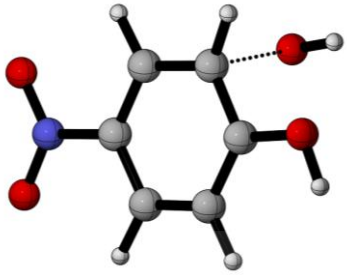

TS-B1

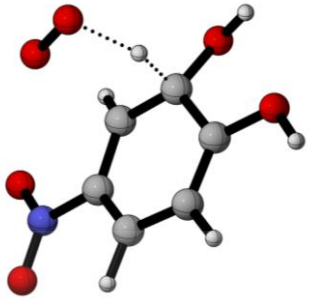

TS-B2

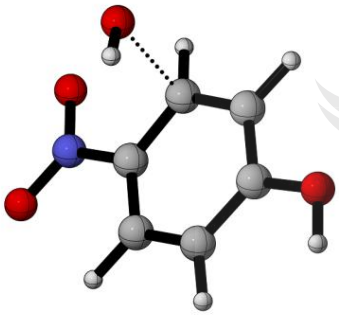

TS-C1

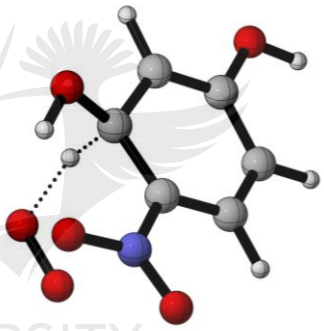

TS-C2

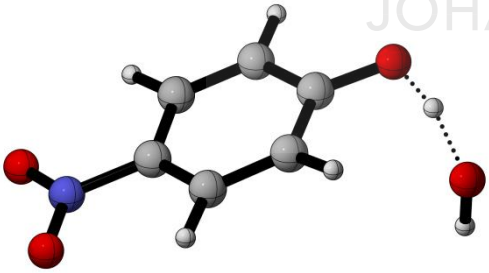

TS-D1

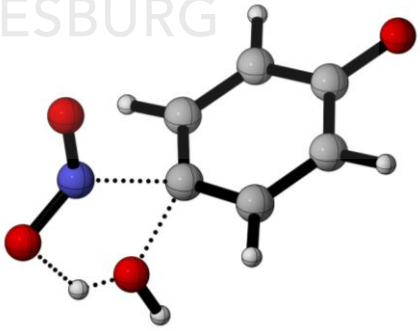

TS-D2

b)

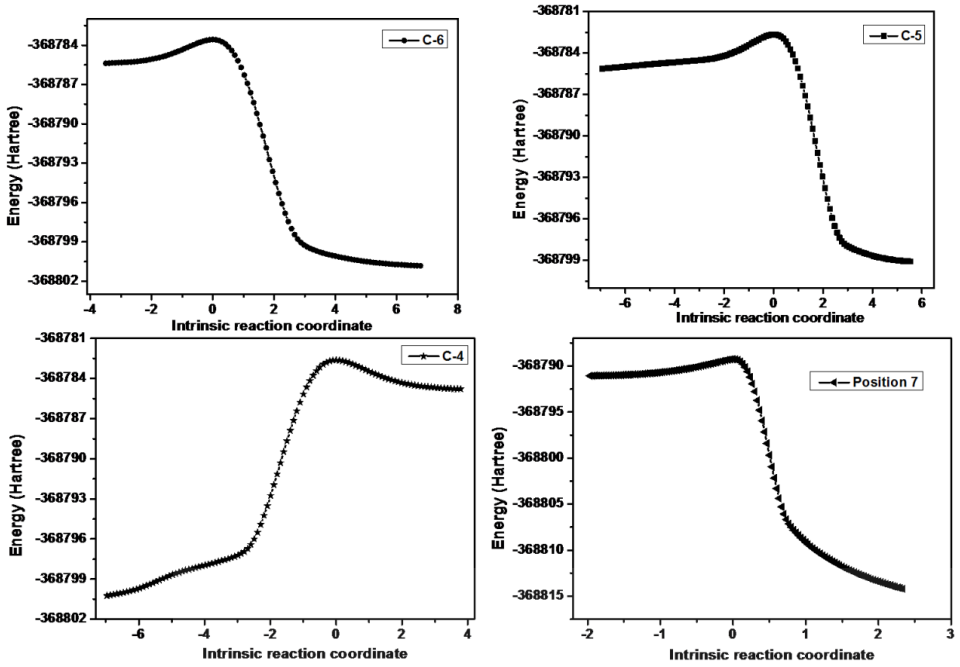

c)

Figure 8.6: (a) Oxidative degradation reaction pathways for the hydroxyl attack and hydrogen abstraction on 4-nitrophenol to give 4-nitrocatechol, 4-nitroresorcinol and semiquinone radical which eventually disproportionate into hydroquinone and benzoquinone (activation energies (numbers on arrows) for the forward and backward reactions are given in kJ mol-1). (b) Optimized geometries of the transition states. (c) Various reaction coordinates for the hydroxyl attacks on the various positions of the 4-nitrophenol

The pathways (A and B) of the hydroxyl radical attack on the ortho and meta positions of 4-nitrophenol have low activation energies of 2.3 and 5.5 kJ mol^{-1}, respectively. Subsequently, the substitution reaction was accompanied by proton abstraction by molecular oxygen produced in the electrochemical system/solution. This leads to the production of 4-nitrocatechol, 4-nitroresorcinol and hydroperoxyl radical (HO_2•). 4-Nitrocatechol and 4-nitroresorcinol are some of the oxidation products of 4-nitrophenol reported in literature, where 4-nitrocatechol is preferentially formed as this pathway is kinetically favoured [68-71]. These results are also in agreement with the products obtained for the computational studies for the degradation of 4-chlorophenol leading to 4-chlorocatechol and hydroperoxyl radical [66]. In addition, the molecular oxygen can also react with the ortho- OH adduct to form peroxyl radicals and eventually, leads to the ring opening and release hydroperoxyl radical (Fig. 8.7). The ring opening gives rise to intermediates that are oxidised by OH radical and mineralised into carbon dioxide, water and nitrates [66, 70].

Another possible degradation pathway is the abstraction of proton from the hydroxyl group on 4-nitrophenol (pathway D). This pathway is found barrierless and can occur spontaneously, leading to the production of 4-nitrophenoxyl radical and water. The nitrophenoxyl radical and water react further to generate a semiquinone radical which was found to be endothermic and slow due to the large activation energy computed (151.2 kJ mol^{-1}). Semiquinone radicals are generally known to break down into hydroquinone and 1,4-benzoquinone which are other oxidation products of 4-nitrophenol which were determined in several experimental studies [66, 68-70, 72]. The energy profile for the pathway A is found in Fig. 8.7c.

It can be deduced from the DFT study that for the photoelectrocatalytic degradation of 4-nitrophenol by hydroxyl radical generated in the system led to the formation of benzoquinone, hydroquinone, 4-nitrocatechol and 4-nitroresorcinol. Reaction with the ortho OH adduct can also cause ring opening which would be further oxidised or mineralised to less harmful products. In addition, there is generation of hydroperoxyl radical and hydroxyl radical in the system which can initiate more attacks.

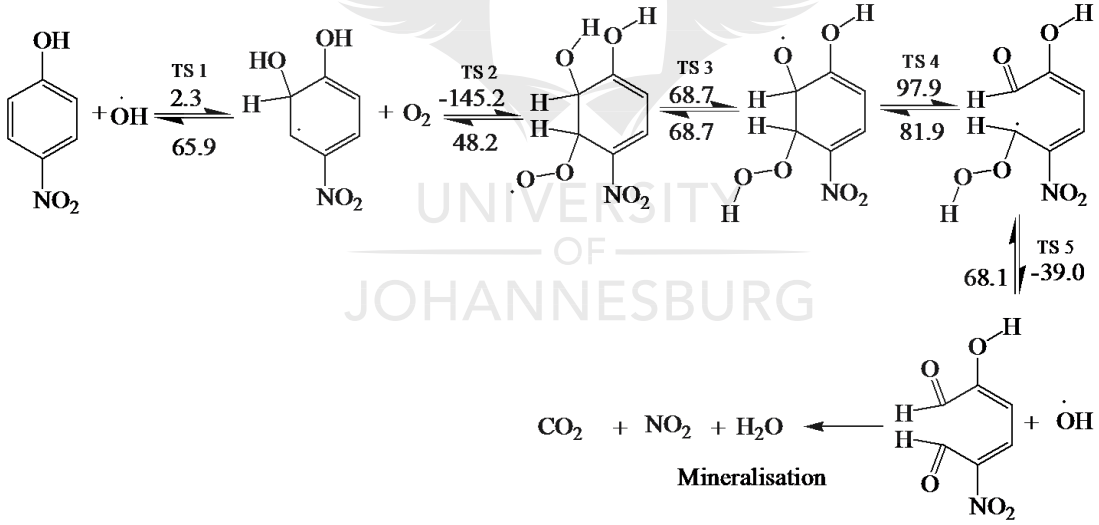

a)

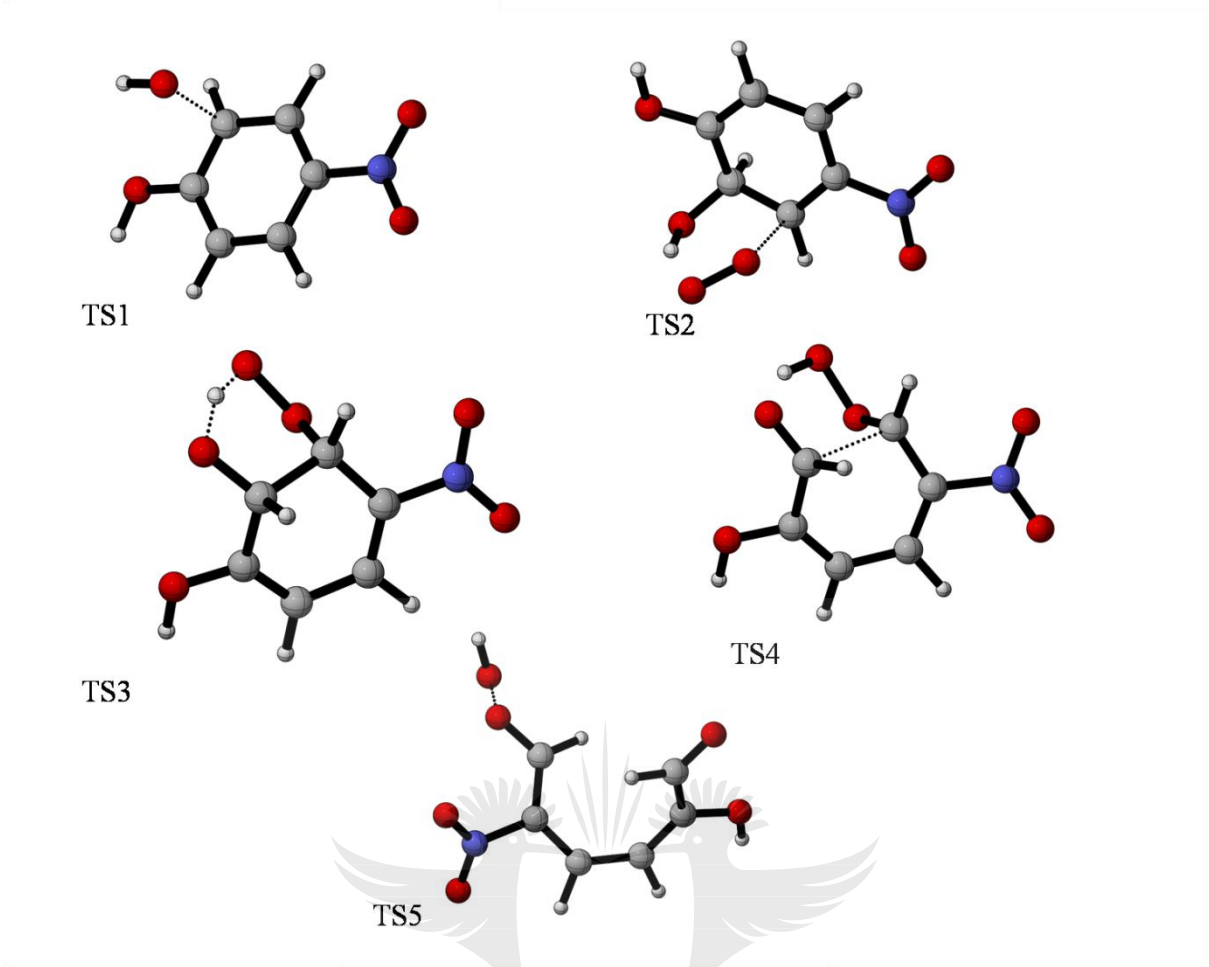

b)

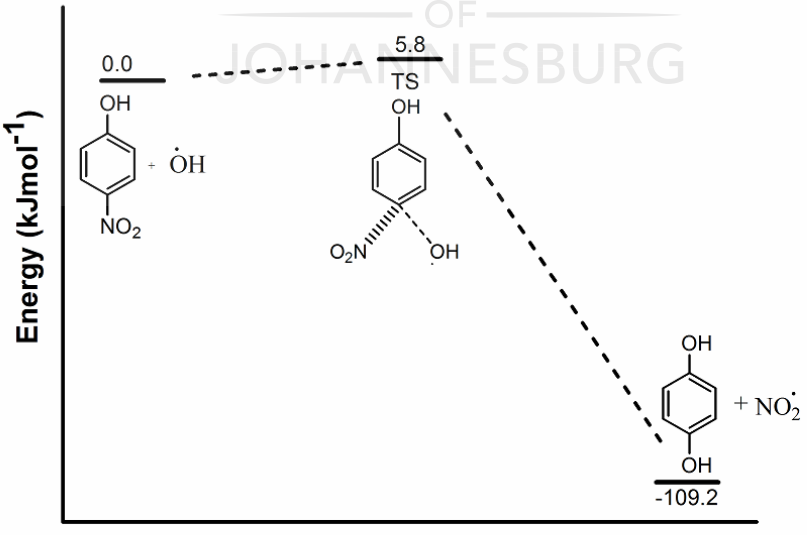

(c)

Figure 8.7: (a) Plausible mechanism for the 4-nitrophenol oxidative degradation reaction leading to the ring opening of the molecule (activation energies (numbers on arrows) for the forward and backward reactions are given in $kJmol^{-1}$), (b) transitions states at various steps of the ring opening of 4-nitrophenol molecule, (c) Energy profile diagram for the nitrophenol degradation pathway (A) leading to the formation hydroquinone from the hydroxyl attack on position 4

8.4 SUB CONCLUSION

In summary, Pd-ZnO-EG electrode was constructed from a Pd-ZnO-EG nanocomposite, synthesised by a hydrothermal method and characterised using various techniques. The Pd-ZnO-EG nanomaterials have large surface area, pore size and volume, and strong absorption in the visible light region. The electrode was used for the photoelectrocatalytic removal of 4-nitrophenol as a target water pollutant. The Pd-ZnO-EG electrode showed improved photoelectrocatalytic activity in relation to ZnO-EG and EG electrodes for the removal of the 4-nitrophenol. This is as a result of the Pd nanoparticles and the conducting EG acting as collectors for the photoexcited electrons, thereby aiding charge transfer and reducing recombination of charges. In addition, the photocurrent responses showed that the Pd-ZnO-EG nanocomposite electrode could be employed as a good photo-electrode for the benefits of photoelectrocatalytic processes and environmental remediation such as treatment of industrial wastewaters. The oxidative degradation of 4-nitrophenol by hydroxyl radical was predicted using DFT method which led to the generation of hydroquinone, benzoquinone, 4-nitrocatechol, 4-nitroresorcinol and the ring opening of the 4-nitrophenol. This was obtained by DFT computations of plausible reaction mechanism and pathways resulting from hydroxyl radical attacks on different positions on the molecule of 4-nitrophenol, accompanied by hydrogen abstraction by ground state oxygen reactions. Furthermore, hydroxyl radical was regenerated which can further oxidise the ring structure and initiate a new degradation process.

8.5 REFERENCES

[1] Z. Wu, Y. Zhang, X. Wang, Z. Zou, Ag@ $SrTiO_3$ nanocomposite for super photocatalytic degradation of organic dye and catalytic reduction of 4-nitrophenol, New Journal of Chemistry, 41 (2017) 5678-5687.

[2] J. Ding, Q. Li, L. Zhao, X. Li, Q. Yue, B. Gao, A wheat straw cellulose based semi-IPN hydrogel reactor for metal nanoparticles preparation and catalytic reduction of 4-nitrophenol, RSC Advances, 7 (2017) 17599-17611.

[3] N. Sahiner, H. Ozay, O. Ozay, N. Aktas, New catalytic route: hydrogels as templates and reactors for in situ Ni nanoparticle synthesis and usage in the reduction of 2-and 4-nitrophenols, Applied Catalysis A: General, 385 (2010) 201-207.

[4] R. Zhu, Q. Chen, Q. Zhou, Y. Xi, J. Zhu, H. He, Adsorbents based on montmorillonite for contaminant removal from water: a review, Applied Clay Science, 123 (2016) 239-258.

[5] S. Ammar, N. Oturan, M.A. Oturan, Electrochemical oxidation of 2-nitrophenol in aqueous medium by electro-Fenton technology, Journal of Environmental Engineering and Management, 17 (2007) 89.

[6] P. Gharbani, S. Tabatabaii, A. Mehrizad, Removal of Congo red from textile wastewater by ozonation, International Journal of Environmental Science & Technology, 5 (2008) 495-500.

[7] L.-Z. Huang, H.C.B. Hansen, M.J. Bjerrum, Electrochemical reduction of nitroaromatic compounds by single sheet iron oxide coated electrodes, Journal of hazardous materials, 306 (2016) 175-183.

[8] A.K. Verma, R.R. Dash, P. Bhunia, A review on chemical coagulation/flocculation technologies for removal of colour from textile wastewaters, Journal of Environmental Management, 93 (2012) 154-168.

[9] E. Brillas, C.A. Martínez-Huitle, Decontamination of wastewaters containing synthetic organic dyes by electrochemical methods. An updated review, Applied Catalysis B: Environmental, 166 (2015) 603-643.

[10] G.R. Malpass, D.W. Miwa, S.A. Machado, A.J. Motheo, SnO 2-based materials for pesticide degradation, Journal of hazardous materials, 180 (2010) 145-151.

[11] M. Peleyeju, E. Umukoro, J. Babalola, O. Arotiba, Electrochemical Degradation of an Anthraquinonic Dye on an Expanded Graphite-Diamond Composite Electrode, Electrocatalysis, 7 (2016) 132-139.

[12] K. Jüttner, U. Galla, H. Schmieder, Electrochemical approaches to environmental problems in the process industry, Electrochimica Acta, 45 (2000) 2575-2594.

[13] E. Brillas, C.A. Martínez-Huitle, Decontamination of wastewaters containing synthetic organic dyes by electrochemical methods. An updated review, Applied Catalysis B: Environmental, 166–167 (2015) 603-643.

[14] E. Kusmierek, E. Chrzescijanska, Application of TiO_2–RuO_2/Ti electrodes modified with WO_3 in electro-and photoelectrochemical oxidation of Acid Orange 7 dye, Journal of Photochemistry and Photobiology A: Chemistry, 302 (2015) 59-68.

[15] E.H. Umukoro, M.G. Peleyeju, J.C. Ngila, O.A. Arotiba, Towards wastewater treatment: Photo-assisted electrochemical degradation of 2-nitrophenol and orange II dye at a tungsten trioxide-exfoliated graphite composite electrode, Chemical Engineering Journal, 317 (2017) 290-301.

[16] H.W. Jeong, T.H. Jeon, J.S. Jang, W. Choi, H. Park, Strategic modification of $BiVO_4$ for improving photoelectrochemical water oxidation performance, The Journal of Physical Chemistry C, 117 (2013) 9104-9112.

[17] P.Y. Kuang, J.R. Ran, Z.Q. Liu, H.J. Wang, N. Li, Y.Z. Su, Y.G. Jin, S.Z. Qiao, Enhanced photoelectrocatalytic activity of BiOI nanoplate–zinc oxide nanorod p–n heterojunction, Chemistry–A European Journal, 21 (2015) 15360-15368.

[18] J. Li, S. Lv, Y. Liu, J. Bai, B. Zhou, X. Hu, Photoeletrocatalytic activity of an n-ZnO/p-Cu_2O/n-TNA ternary heterojunction electrode for tetracycline degradation, Journal of hazardous materials, 262 (2013) 482-488.

[19] E.H. Umukoro, M.G. Peleyeju, J.C. Ngila, O.A. Arotiba, Photoelectrochemical degradation of orange II dye in wastewater at a silver–zinc oxide/reduced graphene oxide nanocomposite photoanode, RSC Advances, 6 (2016) 52868-52877.

[20] A. Zhu, Q. Zhao, X. Li, Y. Shi, $BiFeO_3/TiO_2$ nanotube arrays composite electrode: Construction, characterization, and enhanced photoelectrochemical properties, ACS applied materials & interfaces, 6 (2013) 671-679.

[21] J. Becker, K.R. Raghupathi, J. St. Pierre, D. Zhao, R.T. Koodali, Tuning of the crystallite and particle sizes of ZnO nanocrystalline materials in solvothermal synthesis and their photocatalytic activity for dye degradation, The Journal of Physical Chemistry C, 115 (2011) 13844-13850.

[22] X. Chen, Y. He, Q. Zhang, L. Li, D. Hu, T. Yin, Fabrication of sandwich-structured ZnO/reduced graphite oxide composite and its photocatalytic properties, Journal of materials science, 45 (2010) 953-960.

[23] F. Sun, X. Qiao, F. Tan, W. Wang, X. Qiu, One-step microwave synthesis of Ag/ZnO nanocomposites with enhanced photocatalytic performance, Journal of Materials Science, (2012) 1-7.

[24] L. Zhang, L. Du, X. Yu, S. Tan, X. Cai, P. Yang, Y. Gu, W. Mai, Significantly enhanced photocatalytic activities and charge separation mechanism of Pd-decorated ZnO–graphene oxide Nanocomposites, ACS applied materials & interfaces, 6 (2014) 3623-3629.

[25] S. Balachandran, N. Prakash, M. Swaminathan, Heteroarchitectured $Ag–Bi_2O_3–ZnO$ as a bifunctional nanomaterial, RSC Advances, 6 (2016) 20247-20257.

[26] E.H. Umukoro, M.G. Peleyeju, J.C. Ngila, O.A. Arotiba, Photocatalytic degradation of acid blue 74 in water using $Ag–Ag_2O–Zno$ nanostuctures anchored on graphene oxide, Solid State Sciences, 51 (2016) 66-73.

[27] W.W. Wang, Y.J. Zhu, L.X. Yang, $ZnO–SnO_2$ hollow spheres and hierarchical nanosheets: hydrothermal preparation, formation mechanism, and photocatalytic properties, Advanced Functional Materials, 17 (2007) 59-64.

[28] H. Gu, Y. Yang, J. Tian, G. Shi, Photochemical synthesis of noble metal (Ag, Pd, Au, Pt) on graphene/ZnO multihybrid nanoarchitectures as electrocatalysis for H_2O_2 reduction, ACS applied materials & interfaces, 5 (2013) 6762-6768.

[29] S. Ma, J. Xue, Y. Zhou, Z. Zhang, Photochemical synthesis of ZnO/Ag_2O heterostructures with enhanced ultraviolet and visible photocatalytic activity, Journal of Materials Chemistry A, 2 (2014) 7272-7280.

[30] Y. Wang, Q. Wang, X. Zhan, F. Wang, M. Safdar, J. He, Visible light driven type II heterostructures and their enhanced photocatalysis properties: a review, Nanoscale, 5 (2013) 8326-8339.

[31] W. Shi, Y. Yan, X. Yan, Microwave-assisted synthesis of nano-scale $BiVO_4$ photocatalysts and their excellent visible-light-driven photocatalytic activity for the degradation of ciprofloxacin, Chemical engineering journal, 215 (2013) 740-746.

[32] M. Yi, Z. Shen, Kitchen blender for producing high-quality few-layer graphene, Carbon, 78 (2014) 622-626.

[33] M. Yi, Z. Shen, A review on mechanical exfoliation for the scalable production of graphene, Journal of Materials Chemistry A, 3 (2015) 11700-11715.

[34] M. Yi, Z. Shen, J. Zhu, A fluid dynamics route for producing graphene and its analogues, Chinese science bulletin, 59 (2014) 1794-1799.

[35] T. Ndlovu, B.B. Mamba, S. Sampath, R.W. Krause, O.A. Arotiba, Voltammetric detection of arsenic on a bismuth modified exfoliated graphite electrode, Electrochimica Acta, 128 (2014) 48-53.

[36] B. Ntsendwana, B.B. Mamba, S. Sampath, O.A. Arotiba, Synthesis, characterisation and application of an exfoliated graphite–diamond composite electrode in the electrochemical degradation of trichloroethylene, RSC Advances, 3 (2013) 24473-24483.

[37] M.G. Peleyeju, A.O. Idris, E.H. Umukoro, J.O. Babalola, O.A. Arotiba, Electrochemical Detection of 2, 4-Dichlorophenol on a Ternary Composite Electrode of Diamond, Graphene, and Polyaniline, ChemElectroChem, (2017).

[38] A.D. Becke, Density functional thermochemistry. I. The effect of the exchange- only gradient correction, The Journal of chemical physics, 96 (1992) 2155-2160.

[39] C. Lee, W. Yang, R. Parr, Density-functional exchange-energy approximation with correct asymptotic behaviour, Phys. Rev. B, 37 (1988) 785-789.

[40] W.J. Hehre, Ab initio molecular orbital theory, Wiley-Interscience1986.

[41] C. Gonzalez, H. Schelgel, Reaction path following in mass-weighted internal coordinates, Journal of Physical Chemistry, 94 (1990) 5523-5527.

[42] C. Gonzalez, H.B. Schlegel, An improved algorithm for reaction path following, The Journal of Chemical Physics, 90 (1989) 2154-2161.

[43] M. Frisch, G. Trucks, H. Schlegel, G. Scuseria, M. Robb, J. Cheeseman, G. Scalmani, V. Barone, B. Mennucci, G. Petersson, Gaussian 09, Revision E. 01, 2009, Gaussian, Inc., Wallingford CT.

[44] R. Dooley, G. Allen, S. Pamidighantam, Computational chemistry grid: production cyberinfrastructure for computational chemistry, Proceedings of the 13th Annual Mardi Gras Conference, 2005, pp. 83.

[45] R. Dooley, K. Milfeld, C. Guiang, S. Pamidighantam, G. Allen, From proposal to production: Lessons learned developing the computational chemistry grid cyberinfrastructure, Journal of Grid Computing, 4 (2006) 195-208.

[46] K. Milfeld, C. Guiang, S. Pamidighantam, J. Giuliani, Cluster computing through an application-oriented computational chemistry Grid, Proceedings of the 2005 Linux Clusters: The HPC Revolution, 2005.

[47] A. Khan, Raman spectroscopic study of the ZnO nanostructures, J. Pak. Mater. Soc, 4 (2010) 5-9.

[48] A. Khan, M.E. Kordesch, Synthesis of novel zinc oxide microphone-like microstructures, Materials Letters, 62 (2008) 230-234.

[49] A. Umar, B. Karunagaran, E. Suh, Y. Hahn, Structural and optical properties of single-crystalline ZnO nanorods grown on silicon by thermal evaporation, Nanotechnology, 17 (2006) 4072.

[50] A.-S. Mamede, G. Leclercq, E. Payen, J. Grimblot, P. Granger, Surface Raman spectroscopic study of NO transformation over Pd-based catalysts, Physical Chemistry Chemical Physics, 5 (2003) 4402-4406.

[51] X. Yang, M. Zhen, G. Li, X. Liu, X. Wang, C. Shu, L. Jiang, C. Wang, Preparation of Pd-decorated fullerenols on carbon nanotubes with excellent electrocatalytic properties in alkaline media, Journal of Materials Chemistry A, 1 (2013) 8105-8110.

[52] K.-W. Park, J.H. Jung, Spectroscopic and electrochemical characteristics of a carboxylated graphene–ZnO composites, Journal of Power Sources, 199 (2012) 379-385.

[53] P. Wang, Y. Tang, Z. Dong, Z. Chen, T.-T. Lim, Ag–AgBr/TiO_2/RGO nanocomposite for visible-light photocatalytic degradation of penicillin G, Journal of Materials Chemistry A, 1 (2013) 4718-4727.

[54] P. Avetta, M. Sangermano, M. Lopez-Manchado, P. Calza, Use of graphite oxide and/or thermally reduced graphite oxide for the removal of dyes from water, Journal of Photochemistry and Photobiology A: Chemistry, 312 (2015) 88-95.

[55] L. Hao, W. Gao, Y. Liu, Y. Liu, Z. Han, Q. Xue, J. Zhu, Self-powered broadband, high-detectivity and ultrafast photodetectors based on Pd-MoS_2/Si heterojunctions, Physical Chemistry Chemical Physics, 18 (2016) 1131-1139.

[56] P. Zuppella, E. Pasqualotto, S. Zuccon, F. Gerlin, A.J. Corso, M. Scaramuzza, A. De Toni, A. Paccagnella, M.G. Pelizzo, Palladium on plastic substrates for plasmonic devices, Sensors, 15 (2015) 1138-1147.

[57] Y.S. Grewal, M.J. Shiddiky, S.A. Gray, K.M. Weigel, G.A. Cangelosi, M. Trau, Label-free electrochemical detection of an Entamoeba histolytica antigen using cell-free yeast-scFv probes, Chemical Communications, 49 (2013) 1551-1553.

[58] W. Yuan, Y. Zhou, Y. Li, C. Li, H. Peng, J. Zhang, Z. Liu, L. Dai, G. Shi, The edge-and basal-plane-specific electrochemistry of a single-layer graphene sheet, Scientific reports, 3 (2013) 2248.

[59] F. Wang, W. Li, S. Gu, H. Li, X. Wu, X. Liu, Samarium and Nitrogen Co-Doped Bi_2WO_6 Photocatalysts: Synergistic Effect of Sm^{3+}/Sm^{2+} Redox Centers and N-Doped Level for Enhancing Visible Light Photocatalytic Activity, Chemistry-A European Journal, 22 (2016) 12859-12867.

[60] W. Zhao, Y. Liu, Z. Wei, S. Yang, H. He, C. Sun, Fabrication of a novel p–n heterojunction photocatalyst n-$BiVO_4$@p-MoS_2 with core–shell structure and its excellent visible-light photocatalytic reduction and oxidation activities, Applied Catalysis B: Environmental, 185 (2016) 242-252.

[61] J. bo Zhong, J. zhang Li, X. yang He, J. Zeng, Y. Lu, W. Hu, K. Lin, Improved photocatalytic performance of Pd-doped ZnO, Current Applied Physics, 12 (2012) 998-1001.

[62] Y. Wang, C. Shen, M. Zhang, B.-T. Zhang, Y.-G. Yu, The electrochemical degradation of ciprofloxacin using a SnO_2-Sb/Ti anode: Influencing factors, reaction pathways and energy demand, Chemical Engineering Journal, 296 (2016) 79-89.

[63] T. Das, P.K. Boruah, M.R. Das, B.K. Saikia, Formation of onion-like fullerene and chemically converted graphene-like nanosheets from low-quality coals: application in photocatalytic degradation of 2-nitrophenol, RSC Advances, 6 (2016) 35177-35190.

[64] S.A. Ansari, M.M. Khan, M.O. Ansari, J. Lee, M.H. Cho, Biogenic synthesis, photocatalytic, and photoelectrochemical performance of Ag–ZnO nanocomposite, The Journal of Physical Chemistry C, 117 (2013) 27023-27030.

[65] D.R. Hang, S.E. Islam, C.H. Chen, K.H. Sharma, Full Solution Processed Synthesis and Mechanisms of a Recyclable and Bifunctional Au/ZnO Plasmonic Platform for Enhanced UV/Vis Photocatalysis and Optical Properties, Chemistry-A European Journal, 22 (2016) 14950-14961.

[66] V.-M. Guérin, R. Zouzelka, H. Bibova-Lipsova, J. Jirkovsky, J. Rathousky, T. Pauporté, Experimental and DFT study of the degradation of 4-chlorophenol on hierarchical micro-/nanostructured oxide films, Applied Catalysis B: Environmental, 168 (2015) 132-140.

[67] Y.-y. Zhao, E. Tsuchida, Y.-K. Choe, J. Wang, T. Ikeshoji, A. Ohira, Theoretical studies on the degradation of hydrocarbon copolymer ionomers used in fuel cells, Journal of Membrane Science, 487 (2015) 229-239.

[68] S. Chempath, J.M. Boncella, L.R. Pratt, N. Henson, B.S. Pivovar, Density functional theory study of degradation of tetraalkylammonium hydroxides, The Journal of Physical Chemistry C, 114 (2010) 11977-11983.

[69] B. Peters, A. Heyden, A.T. Bell, A. Chakraborty, A growing string method for determining transition states: Comparison to the nudged elastic band and string methods, The Journal of chemical physics, 120 (2004) 7877-7886.

[70] W. Wang, S. Wang, X. Xie, V. Ramani, Density functional theory study of hydroxide-ion induced degradation of imidazolium cations, International Journal of Hydrogen Energy, 39 (2014) 14355-14361.

[71] S. Chaliha, K.G. Bhattacharyya, P. Paul, Oxidation of 4-nitrophenol in water over Fe (III), Co (II), and Ni (II) impregnated MCM41 catalysts, Journal of chemical technology and biotechnology, 83 (2008) 1353-1363.

[72] A. Chauhan, G. Pandey, N.K. Sharma, D. Paul, J. Pandey, R.K. Jain, p-Nitrophenol degradation via 4-nitrocatechol in Burkholderia sp. SJ98 and cloning of some of the lower pathway genes, Environmental science & technology, 44 (2010) 3435-3441.

[73] R. Ding, Z.-Y. Mao, J.-L. Wang, Synergistic effects of 4-nitrophenol degradation using gamma irradiation combined with a advanced oxidation process, Nuclear Science and Techniques, 27 (2016) 4.

[74] V. Kadiyala, B.F. Smets, K. Chandran, J.C. Spain, High affinity p-nitrophenol oxidation by Bacillus sphaericus JS905, FEMS microbiology letters, 166 (1998) 115-120.

[75] J. Li, Q. Liu, Q. qing Ji, B. Lai, Degradation of p-nitrophenol (PNP) in aqueous solution by Fe 0-PM-PS system through response surface methodology (RSM), Applied Catalysis B: Environmental, 200 (2017) 633-646.

CHAPTER 9

EXPANDED GRAPHITE SUPPORTED p-n MoS_2-SnO_2 HETEROJUNCTION NANOCOMPOSITE ELECTRODE FOR ENHANCED PHOTO-ELECTROCATALYTIC DEGRADATION OF A PHARMACEUTICAL POLLUTANT[1]

9.1 INTRODUCTION

Thousands of tons of wastewaters containing pharmaceutical pollutants are being generated annually, and these are emptied into water bodies with little or no proper treatment, making the complexity of wastewater pollution a major challenge especially in developing countries [1, 2]. Specifically, antibiotics can cause problems to the ecosystem due to their capacity to persist in the environment [3-5]. Recently, the persistence of pharmaceutical products, especially antibiotics in water bodies even after treatment, has been reported [6]. This persistence can be attributed to the poor efficiency of the conventional wastewater treatment methods as a result of the recalcitrant nature of these pharmaceuticals. Also, they have attracted global scientific concerns because of their potential capacity to promote the spread of microorganisms having genes that are resistant to antibiotics. Consequently, they can cause serious threats to aquatic and human lives [6, 7]. These challenges thus necessitate the need for adequate and effective treatment techniques for the removal of pharmaceuticals. Example of such antibiotics is ciprofloxacin which is used for the treatment of bacterial infections, and its wide occurrence in the aquatic environment has necessitated the search for effective techniques for its removal [8-10].

Electrocatalytic techniques have been employed for the treatments of organic pollutants in the past few years due to the production of non-selective and active hydroxyl radicals that react with these pollutants to degrade them [11-14]. Electrocatalytic degradation involves either the oxidation of organic pollutants on the surface of the electrode by electron transfer, resulting in poor efficiency or by the oxidation of pollutants by electrochemically produced hydroxyl radicals at the electrode [11, 12]. The advantages of electrocatalytic degradation technique include the incorporation of the catalyst within the electrode which helps in minimising catalyst separation from the reaction system, controlled reaction

[1] This chapter has been submitted and it is under review with: Journal of Electroanalytical Chemistry

conditions and the relatively low equipment cost [12, 15]. Nevertheless, some setbacks are linked with this process such as mass transfer of the organics which results from low concentration and oxygen evolving from the system due to high voltage that is normally applied as well as the long period of time involved in the process [11, 12, 16]. Hence it is important to enhance this technique by combining it with photolysis, resulting in an approach called photo-electrocatalytic process. It involves the fabrication of a photoanode by the immobilisation of a photoactive / semiconductor material on a conducting material, and the concurrent application of visible light and bias potential. This results in the generation of oxidising agents such as hydroxyl radicals by the semiconductor and conducting substrates for the break-down of the pollutants [17, 18].

Several semiconductor metal oxides have been employed as photo-electrode for the degradation of antibiotics. For example, the photoelectrochemical properties of titanium films modified with silver and gold nanoparticles were studied and then utilised for the degradation of tetracycline hydrochloride [19]. The degradation of ciprofloxacin on titania films supported on transparent electrodes has been documented [20]. It was reported that the use of Pt/Ti electrode for the photo-electrochemical degradation of antibiotic, berberine, gave a better removal efficiency and mineralisation when compared to electrochemical and photocatalytic processes [21]. The enhanced photo-electrocatalytic activity of n-ZnO/p-Cu_2O/n-TiO2 nanotube arrays heterojunction used as electrode in degrading antibiotic, tetracycline, was reported [22]. However there is still the search for efficient and novel electro-active materials needed to fabricate photoanodes. In recent years, SnO_2, an n-type semiconductor having a band gap, Eg = 3.6 eV [23, 24], has been utilised as electrode materials in transistors [23, 25], lithium batteries [26, 27], solar cells [28], sensors [23, 29] and supercapacitors [30], as well as in photocatalysis [24]. This is due to its peculiar properties such as its high chemical and electrochemical stability, gas sensitivity and photoelectronic nature [24, 29]. However, like other semiconductor with wide band gap, it is linked with setbacks such as electron-hole recombination and narrow visible light absorption range. Thus, there is need to improve its photoactive performance for effective application by using a p-type semiconductor, MoS_2, to form a p-n heterojunction material with n-type SnO_2 that could aid the separation of the photo-excited holes and electrons [31]. MoS_2 is a 2D and p-type material having a band gap, Eg of 1.9 eV. It has attracted scientific interest due to its high surface area, excellent optical, magnetic, electrocatalytic and mechanical properties [32-36]. As a result of its

advantageous properties, it has been employed for several electrochemical processes such as solar cells, phototransistors, sensors, hydrogen evolution and supercapacitors [33, 34, 37, 38]. A p-n heterojunction formation between p-MoS_2 and n-SnO_2 (MoS_2-SnO_2 nanohybrid) could improve the efficiency of interfacial charge transfer, resulting in the minimisation of electron-hole recombination. Consequently, there would be enhancement in the photoactive capability of SnO_2. In addition, the low band gap and excellent visible light absorption nature of MoS_2, could improve the photoactivity of SnO_2. Also, the use of expanded graphite could aid in minimising the recombination rate of the photogenerated holes and electrons in SnO_2. Expanded graphite (EG) is a 2D carbon material which is porous, compressible, low in density, and can transport electrons effectively. It is electrically and thermally conductive, high temperature resistant, mechanically strong and can withstand high current density [18, 39, 40]. As a result of its high electron mobility nature, the photo-excited holes and electrons of SnO_2 could be transferred to the expanded graphite. Consequently, there would be a minimisation of the recombination of the electron-hole pair and the photoactive property of the SnO_2 in the MoS_2-SnO_2/EG nanocomposite would be improved, thus leading to the production of more oxidising radicals for the removal of pharmaceutical pollutants. Furthermore, the expanded graphite porosity helps in trapping the MoS_2-SnO_2 photocatalyst. As a result, it would help to immobilise the powdered MoS_2-SnO_2 photocatalyst, and thus, leads to reduced losses in the recovery process [18, 41]. EG has been utilised in several electrocatalytic applications such as electrochemical sensing, photo-assisted and electrochemical oxidation of pollutants [18, 42].

It can be hypothesised that the unique properties of SnO_2, MoS_2 and EG stated above can make MoS_2-SnO_2/EG of great benefit as photo-electrode for the removal of ciprofloxacin in water treatment process. To the best of the authors' knowledge, MoS_2-SnO_2 supported on expanded graphite MoS_2-SnO_2/EG electrode for the degradation of antibiotic ciprofloxacin has not been documented. Herein, MoS_2-SnO_2 nanohybrid supported on EG was fabricated as an electrode and utilised for the photo-electrocatalytic removal of ciprofloxacin as a model pharmaceutical pollutant.

9.2 EXPERIMENTAL PROCEDURES

9.2.1 Materials and apparatus

Tin (IV) chloride dehydrate, potassium hydroxide, sulphuric acid (98%), polyethylene glycol, natural graphite flakes, thiourea, nitric acid, ammonium heptamolybdate tetrahydrate, sodium sulphate, potassium hexacyanoferrate (II), potassium chloride, potassium hexacyanoferrate (III), and ciprofloxacin. The reagents used for this experiment were purchased from Sigma Aldrich, Germany.

9.2.2 Preparation of MoS_2 nanosheets

The MoS_2 nanosheets were synthsised by a hydrothermal method [43]. In brief, 3 mM of ammonium heptamolybdate tetrahydrate was dissolved using deionised water and stirred. Then, 5 mL of polyethylene glycol with a molecular weight of approximately 400 was added. The mixture was stirred for 30 min and thiourea (48 mM) was added while stirring for about 10 min. After that, the mixture was put in a stainless teflon-lined autoclave and heated at 200 ºC for 24 h. After, the autoclave was brought out and allowed to cool down. The product formed was washed several times with deoinised water and ethanol using a centrifuge. The obtained product was dried for 12 h at 60 ºC.

9.2.3 Synthesis of expanded graphite (EG)

Expanded graphite, also known as exfoliated graphite, was synthesised using previous reported method [18]. Graphite flakes were sieved with a 300 µm sieve mesh and soaked for 48 h in a 1:3 (vol/vol) mixture of concentrated nitric and sulphuric acids at ambient temperature to intercalate the graphite. The intercalated graphite was washed until a near pH 7 was reached, and then, air-dried. Furthermore, it was expanded by heating it at 800 ºC to produce a puffed-up material known as expanded graphite.

9.2.4 Synthesis of SnO_2 nanosheets

The SnO_2 nanosheets were synthesised hydrothermally. Briefly, 1.5 g of tin (IV) chloride dehydrate was dissolved in 25 mL ethanol and stirred continuously for complete dissolution. Then, a solution of 1 M KOH (30 mL) was added gradually until a milky white precipitate was formed. The mixture was stirred for 1 h and transferred into a Teflon-lined

stainless steel autoclave and heated at 140 ºC for 12 h. The autoclave was left to cool and the precipitate formed was washed using distilled water and ethanol to remove any ions present. Finally, the product obtained was dried at 60 ºC in an oven before it was used.

9.2.5 Synthesis of MoS_2–SnO_2/EG nano-hybrid

MoS_2-SnO_2 nanohybrid was prepared using the procedure for the synthesis of SnO_2 in section 2.4 except that 0.5 g of the as-prepared MoS_2 nanosheets was first dispersed in a 25 mL ethanol and sonicated for 30 min. Then the tin (IV) chloride dehydrate was added to the suspension and stirred continuously following the hydrothermal method described for the preparation of SnO_2 nanosheets.

For the synthesis of MoS_2–SnO_2/EG nanocomposite, the obtained MoS_2-SnO_2 nanohybrid was dispersed uniformly in ethanol by sonication for 30 min. Expanded graphite (1.5 g) was added, followed by sonication for 10 min. The mixture was put in a digital type temperature-controlled oven at 100 ºC for 12 h to dry and for the ethanol to evaporate completely [18]. SnO_2-EG nanocomposite was synthesised in the same way without adding MoS_2 nanosheets, while MoS_2-EG nanocomposite was prepared without adding SnO_2 nanosheets.

9.2.6 Construction of SnO_2-EG, MoS_2-EG and MoS_2–SnO_2/EG nanocomposite electrodes

The EG, SnO_2-EG, MoS_2-EG and MoS_2–SnO_2/EG nanocomposite electrodes were constructed using a method described in our previous works [14, 18, 41, 44]. The as-synthesised EG, SnO_2-EG, MoS_2-EG and MoS_2–SnO_2/EG nanocomposites were compressed, forming pellets with the aid of a hydraulic press at 10000 psi. The pellets were further used for constructing the electrodes by utilizing a copper wire, conductive silver paint and epoxy sealer. These pellets were put on top of the coiled copper wire using the conductive silver paint and left to dry overnight. The pellets edges were sealed using the epoxy sealer in order for electricity to flow from the basal plane only. Then, it was kept in a glass rod and later used.

9.2.7 Characterisation of SnO_2-EG, MoS_2-EG and MoS_2–SnO_2/EG nanocomposites

The as-prepared materials were characterised with the aid of X-ray diffractometer (Philips PAN Analytical X'Pert powder, Netherlands) using a copper x-ray source, Cu-Kα radiation (λ=0.15418) and K-beta filter. The Raman studies were carried out with Witec alpha300 R confocal Raman microscope (Germany). The measurements of the UV absorbance were carried out with the aid of Shimadzu UV-2450. Morphological images of the prepared materials were obtained using scanning electron microscopy (TESCAN, VEGA 3 XMU, Czech Republic) and high resolution transmission electron microscopy (JEOL JEM-2100, USA) at accelerating voltage of 200kV. Energy-dispersive x-ray spectrometer (TESCAN, Czech Republic) linked to the SEM was used in determining the elemental composition of the materials. The extent of mineralisation was determined using Teledyne Tekmar TOC Analyzer (USA). A UV-Visible spectrophotometer (Cary 60, Agilent technologies, USA) was utilised in determining the removal efficiency of the ciprofloxacin while the source of visible light irradiation was Oriel LCA-100 Solar Simulator (USA) which is equipped with 100 W xenon lamp and AM1.5G filter to give 100mWcm^{-2}.

9.2.8 Photoelectrochemical characterisation

Electrochemical and photoelectrochemical behaviours of the SnO_2-EG, MoS_2-EG and MoS_2–SnO_2/EG nanocomposite electrodes were investigated in a redox probe of 5 mM of potassium ferrocyanide and ferricynanide in 0.1 M KCl solution. The geometric area of the each electrode is 1.3 cm^2. Cyclic and linear sweep voltammetric studies (CV and LSV), electrochemical impedance spectroscopy (EIS) and photocurrent measurements under visible light source (Oriel LCA-100 Solar Simulator) were conducted using a three-electrode electrochemical work set-up (Autolab (302N) potentiostat/galvanostat). The prepared electrodes were utilised as the working electrodes (diameter of 1.3 cm), platinum foil as the counter electrode and Ag/AgCl (3.0 M KCl) as the reference electrode.

9.2.9 Electrochemical and photo-electrocatalytic experiments

The photo-electrocatalytic studies on the degradation of a pharmaceutical pollutant, using ciprofloxacin as a model was carried out in a photoreactor (100 mL) with 20 ppm of ciprofloxacin in 0.1 M Na_2SO_4 (supporting electrolyte) solution. These electrodes were placed at a vertical position where they can be best irradiated by the incident light from the

solar simulator. The source of power used for the experiment was a potentiostat/galvanostat electrochemical workstation, and the light source was Oriel LCA-100 Solar Simulator that has a 100 W xenon lamp. Also, it contains an AM1.5G filter producing a power beam of 1 sun (100 $mWcm^{-2}$ equivalence) when the photoreactor is placed 8 cm from the light source. Potential/current density was applied without using any source of visible light in the eletrocatalytic removal of the ciprofloxacin. After every 30 min, an amount was taken from the solution in the photoreactor using a disposable syringe over a time range of 180 min. The aliquot was filtered and the removal efficiency of the ciprofloxacin was determined on a UV-Visible spectrophotometer using an absorption band of λ = 271 nm. The total organic was investigated on the (TOC) analyser (Teledyne Tekmar TOC fusion). In addition, the experimental conditions were optimised at different pH, initial concentration of the ciprofloxacin and current density.

9.3 RESULTS AND DISCUSSION

9.3.1 XRD analysis

XRD studies of the prepared materials were performed to investigate the crystalline structure of the materials and the diffractograms are presented (Fig. 9.1a). The obtained diffraction peaks for the prepared SnO_2 correspond to (110), (101), (200), (211), (220) and (310) planes which are characteristics of tetragonal rutile phase of SnO_2. This agrees with the JCPDS (card no. 72-1147), and indicates a high purity and crystalline structure of the prepared SnO_2 [24, 27]. For the MoS_2, the diffraction peaks at 2θ = 14.1º, 33.14º, 39.4º, 49.58º and 58.9º detected can be indexed to the (002), (101), (103), (105) and (110) planes which are feature peaks of MoS_2 hexagonal structure. This is in line with the reported data (JCPDS card no. 37-1492) and no impurity peaks were seen [29, 43]. The diffractogram for EG gave a characteristic peak at 2θ = 26.6º and a weak peak at 2θ = 55.6º that can be indexed at (002) and (004) crystal planes [14, 18]. After the addition of the MoS_2-SnO_2 to the EG, some of the peaks from MoS_2 and SnO_2 were still observed, but at low intensity because of the large amount of EG present. Also, the intensity of the EG peak at (004) plane increased due to the overlapping of the peak of SnO_2 at (220) plane. This indicates the formation of the MoS_2–SnO_2/EG composite. However, due to the small amounts of MoS_2 and SnO_2 compared to that of EG present in the composite, it was observed that some of the peaks were no more obvious in the MoS_2–SnO_2/EG diffractogram.

9.3.2 Raman studies

Raman spectra for the as-prepared materials were obtained for structural studies. The Raman spectrum for the EG shows two characteristic peaks at 1351 and 1590 cm^{-1} which are allocated to the D and G bands of graphite respectively (Fig. 9.1c inset). The lower intensity D band is the defects or sp^3 bonds formed in the graphitic structure and the higher intensity G band is from the vibration mode of the sp^2 carbon atoms of the as-prepared EG which was crystalline [14, 18, 45]. Figure 9.1b depicts the Raman spectrum of the MoS_2-SnO_2 nanohybrid which exhibits strong peaks of MoS_2 around 380 and 410 cm^{-1}. These correspond to the Raman active modes of E^1_{2g} and A_{1g} which are the in-plane and out-of-plane vibrations of S-Mo-S respectively [29, 43, 46]. Also, a characteristic peak around 634 cm^{-1} (A_{1g}) resulting from the out-of-plane vibration of the SnO_2 was seen [24, 29]. This confirms the successful preparation of the MoS_2-SnO_2 nanohybrid. In Figure 9.1c, the Raman pattern of the MoS_2-SnO_2/EG nanocomposite displays characteristic peaks of EG, MoS_2 and a very weak peak of SnO_2, suggesting the successful synthesis of the nanocomposite material [29].

9.3.3 Optical analysis

UV-Vis diffuse reflectance was performed on the materials to study their optical behaviour. Figure 9.1d shows that the as-prepared SnO_2-EG, MoS_2-EG and MoS_2-SnO_2/EG samples have absorption of visible light with absorbency greater than 400 nm and these correspond to the absorption edges of the materials. The band gap energy was calculated using the equation;

$$E_g = 1240 / \lambda \qquad [9.1]$$

Where λ is the absorbance wavelength [22, 47]. The MoS_2-SnO_2/EG has absorption band around 500 nm, and its estimated band gap energy is about 2.48 eV which is smaller in comparison to SnO_2-EG and MoS_2-EG with estimated band gap energies around 2.99 and 2.76 eV respectively. This can be linked to the formation of the heterojunction between the p-MoS_2 and the n-SnO_2 [31, 48, 49], and the presence of the photosensitising EG in the MoS_2-SnO_2/EG nanohybrid [18]. The narrow band gap of the MoS_2-SnO_2/EG nanohybrid is favourable for the absorption of solar light, thus, making it a potential candidate for photo-electrocatalytic processes.

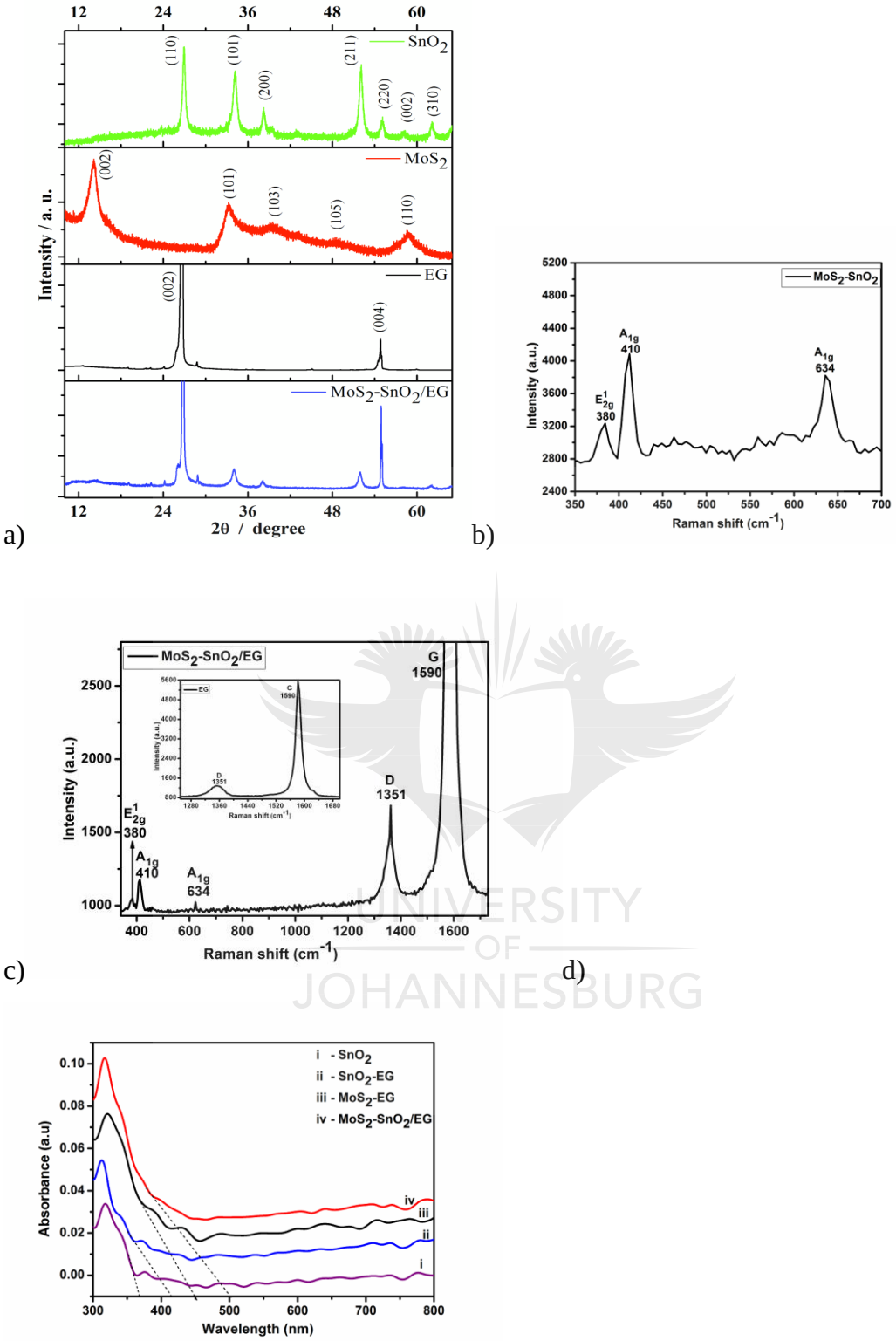

Figure 9.1: (a) XRD patterns of as-synthesised SnO_2 nanosheets, hierarchical microsphers of MoS_2 nanosheets, EG and SnO_2-MoS_2/EG nanohybrid. Raman spectra of (b) SnO_2-MoS_2; (c) SnO_2-MoS_2/EG and EG(inset). (e) UV-Visible diffuse reflectance spectra of (i) SnO_2, (ii) SnO_2-EG; (iii) MoS_2-EG, and (iv) MoS_2- SnO2/EG materials

9.3.4 SEM and TEM studies

The morphologies of the prepared materials were investigated using SEM. Figure 9.2a reveals that the SnO_2 particles are nanosheets. Figure 9.2b depicts the MoS_2 particles are hierarchical microspheres with nanosheets of MoS_2 [43]. Figure 9.2c displays the SnO_2 were entrapped in the graphitic open cavities of the EG. Also, it was observed that the MoS_2-SnO_2 were uniformly anchored in the edges and interlayers of the EG sheets, forming the MoS_2-SnO_2/EG nanocomposite (Fig. 9.2d-f). Furthermore, the TEM images reveal that the SnO_2 nanosheets are about 10 nm in size, with lattice fringe spacing of 0.339 nm which can be attributed to (110) plane of SnO_2 nanostructures (Fig. 9.3a-b). The SAED rings in Fig. 9.3c can be indexed to the planes of the tetragonal rutile SnO_2 structure [24, 29]. Figure 9.3(d-e) reveal the nanosheets of the MoS_2 hierarchical microsphere having lattice fringe spacing of 0.68 nm that corresponds to the (002) plane of MoS_2 nanostructures [29, 43]. Figure 9.3(f-g) display the TEM images of the MoS_2-SnO_2/EG nanocomposite having the MoS_2-SnO_2 supported on the EG sheets. Furthermore, the elemental composition of the MoS_2-SnO_2/EG nanocomposite was investigated using TEM-EDS mapping, indicating the presence of C, Sn, O, Mo and S in the nanocomposite, thus confirming the successful preparation of the MoS_2-SnO_2/EG nanocomposite.

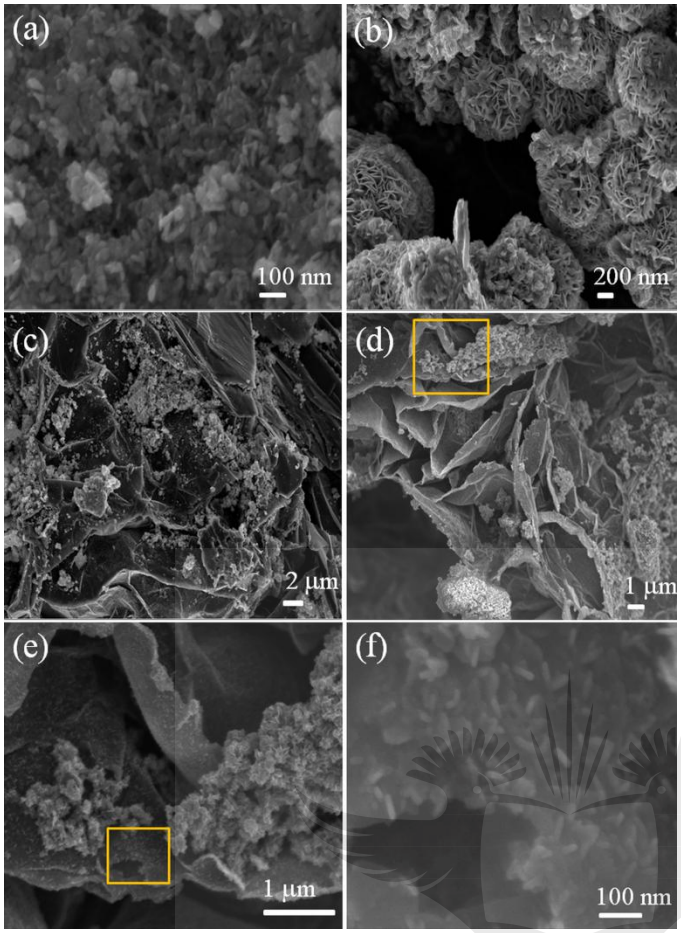

Figure 9.2: SEM images of as-synthesized SnO_2 nanosheets (a), hierarchical microsphers of MoS_2 nanosheets (b), EG-SnO_2 nano-hybrid (c), and EG/SnO_2-MoS_2 nano-hybrid (d-f).

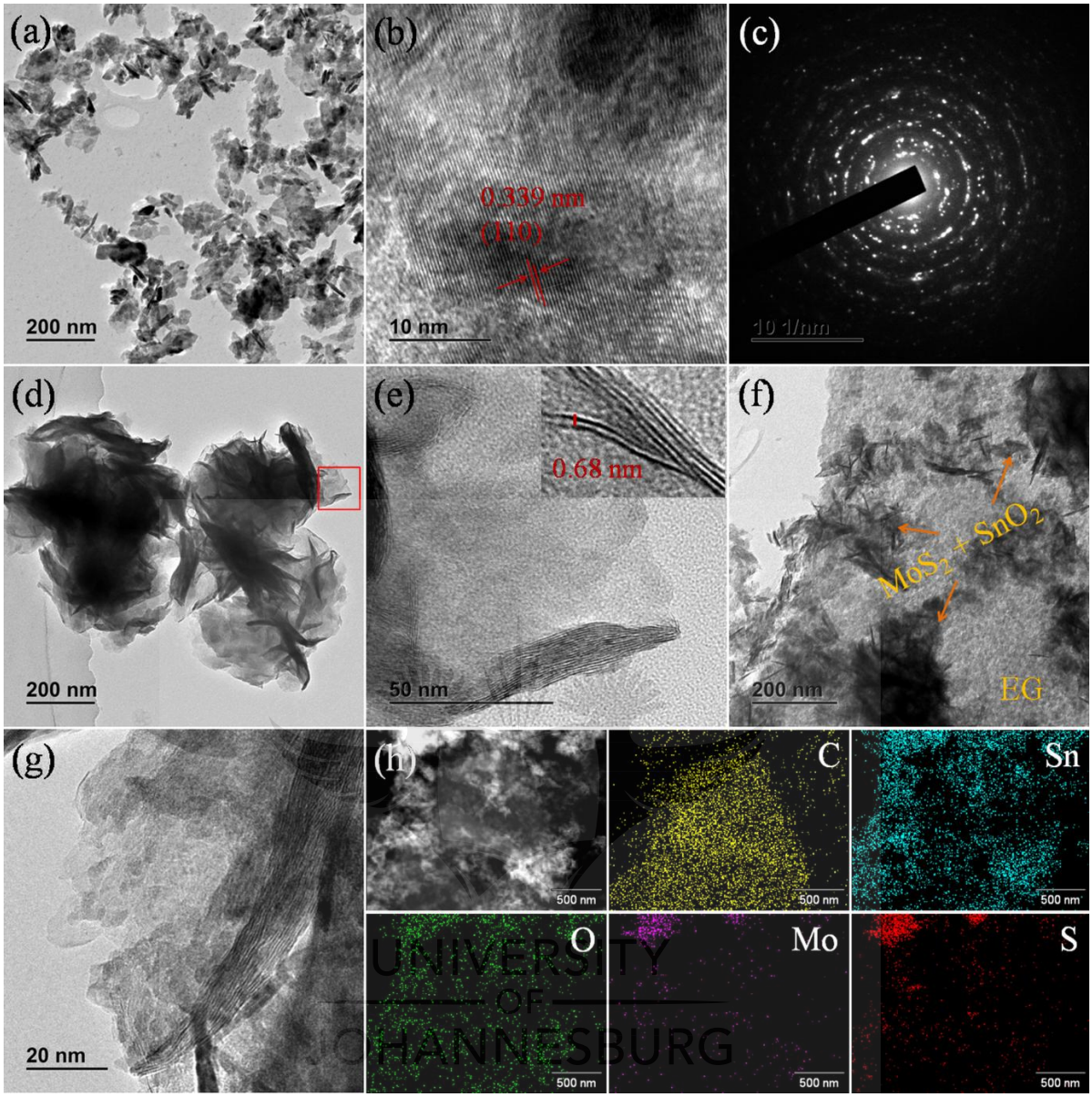

i)

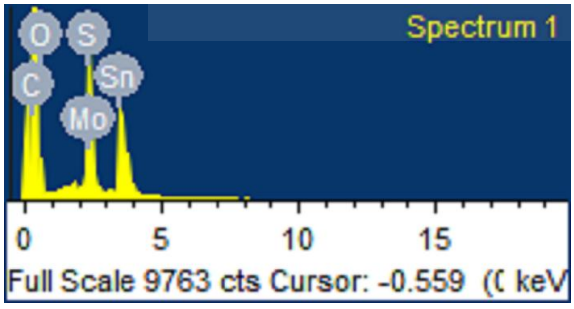

Figure 9.3: TEM images of the (a-b) as-synthesised SnO_2 nanosheets and (c) SAED pattern of SnO_2 nanosheets; (d-e) hierarchical microspheres of MoS_2 nanosheets and the inset of (e) shows the distance between two layers in MoS_2 nanosheets; (f-g) SnO_2-

MoS_2/EG nanocomposite and (h) its TEM-EDX mapping images; (i) EDS of MoS_2-SnO_2/EG

9.3.5 Electrochemical and photoelectrochemical characterisation

The EG, SnO_2-EG, MoS_2-EG and MoS_2-SnO_2/EG electrodes with a geometric area of 1.3 cm^2 were characterised using electrochemical and photoelectrochemical techniques in 0.1 M KCl solution of 0.5 mM $[Fe(CN)_6]^{-3/-4}$ which was the redox or electrochemical probe. Cyclic voltammetry was carried out on the different electrodes at scan rates of 10 mVs^{-1} and 50 mVs^{-1}. As observed in Fig. 9.4a, the MoS_2-SnO_2/EG electrode exhibited an enhancement in the peak current in comparison with the peak current exhibited by the EG, MoS_2-EG and SnO_2-EG electrodes. Thus, the rate of the electrode reaction would be higher because of the large faradaic current displayed by the electrochemical probe using the MoS_2-SnO_2/EG electrode [16, 18]. The addition of SnO_2 and MoS_2 to the EG material increased the electrochemical conductivities of SnO_2-EG and MoS_2-EG electrodes when compared to that of EG electrode. Furthermore, the addition of MoS_2-SnO_2 nanohybrid to the EG material resulted in an enhancement in the current. This can be attributed to the increased electrode active surface area of the MoS_2-SnO_2/EG electrode. Moreover, the p-n heterojunction in the MoS_2-SnO_2 nanhybrid could result in effective charge separation and transfer, and this would lead to an improved peak current and conductivity of the MoS_2-SnO_2/EG electrode. The area of the electroactive surface was estimated by employing the Randles–Sevcik equation;

$$ip = kn^{3/2}AD^{1/2}\,v^{1/2}C \qquad [9.2]$$

Where D is the diffusion co-efficient (7.6×10^{-6} for ferrocyanide), the constant, k is 2.69×10^5, A is the area of the electrode active surface, n is the number of electrons exchanged in the reaction, C is the electrochemical probe concentration, and v is the scan rate [50]. The estimated electroactive surface areas of the electrodes at scan rates of 10 mVs^{-1} were 0.15, 0.23, 0.20 and 0.29 mm^2 for EG, SnO_2-EG, MoS_2-EG and MoS_2-SnO_2/EG electrodes respectively, while the geometric area of each electrode is 1.3 cm^2. These changes in electroactive surface area are due to the addition of SnO_2, MoS_2 and MoS_2-SnO_2 to the EG material [51]. Charge transfer processes taking place at the electrodes were studied on the potassium ferrocyanide using different scan rates (Figure 9.4b). Observation was made that there was a linear increase of the different CVs current

with the square root of the different scan rates (Figure 9.4b inset). This indicates that the electrochemical process/kinetics was diffusion controlled [50, 51]. Furthermore, the photoelectrochemical response of the materials was investigated by performing linear sweep voltammetry in the dark as well as under light [18, 48, 54]. Figure 9.4c presents the current-potential (I-V) plots for EG, MoS_2-EG, SnO_2-EG and MoS_2-SnO_2/EG materials in a potential range of 0.1 – 2.0 V vs Ag/AgCl. As can be clearly seen, there is enhancement in the photoresponse with MoS_2-SnO_2/EG displaying a higher current than EG, MoS_2-EG, SnO_2-EG materials. This enhancement reveals an increase in the transport rate of the photoinduced charge carriers and effective separation of the electron-hole pairs [48, 54]. In addition, chronoamperometry measurement was conducted on the EG, MoS_2-EG, SnO_2-EG materials. Higher photocurrent response implies a more separation efficiency of the photoinduced electron-hole pair efficiency [31, 48, 55]. Figure 9.4d shows that the MoS_2-SnO_2/EG displays a higher photocurrent intensity in comparison with the EG, MoS_2-EG, SnO_2-EG. This further reveals the capability of charge carriers production and improved electron-hole pair separation due to the MoS_2-SnO_2 p-n heterojunction of the MoS_2-SnO_2/EG, indicating its photo-electrocatalytic nature. This result is in line with the results of the LSV. Thus, the as-prepared MoS_2-SnO_2/EG materials can be beneficial as a photoelectrode for the degradation of pharmaceutical pollutants in wastewater treatment.

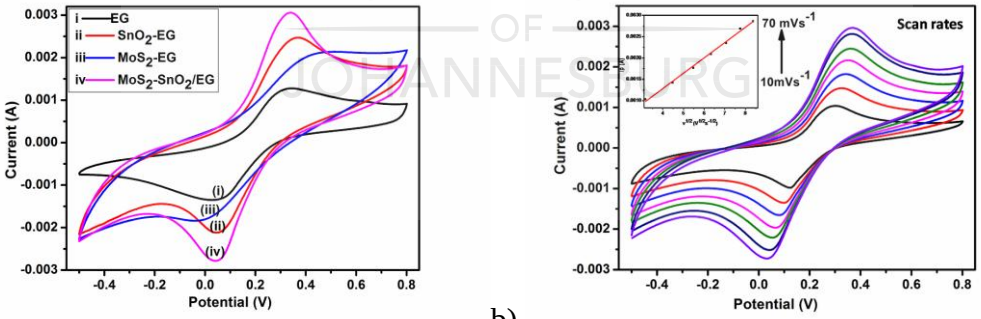

a) b)

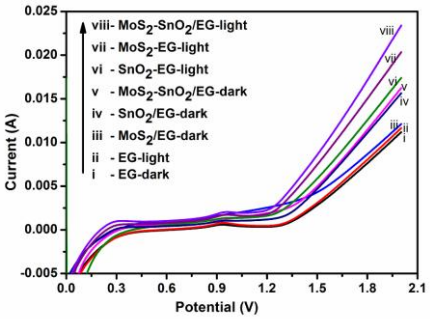

c)

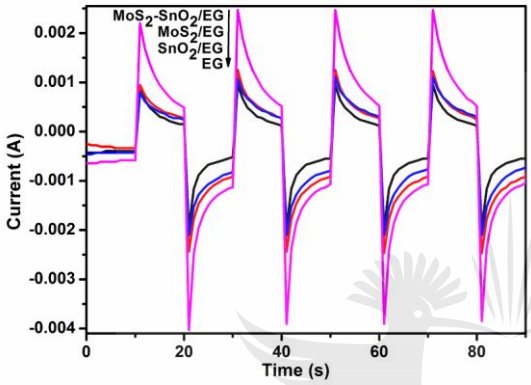

d)

Figure 9.4: (a) Cyclic voltammograms of (i) EG; (ii) SnO_2-EG; (iii) MoS_2-EG; and MoS_2-SnO_2/EG electrodes in 0.1 M KCl solution of 5mM $[Fe(CN)_6]^{-3/-4}$ at 50 mVs^{-1} scan rate; (b) CVs of MoS_2-SnO_2/EG electrode at various scan rates and the linear curve of peak currents verses square roots of the scan rates; (c) LSV of the electrodes in the dark and with light; and (d) Photocurrent responses of the different electrodes with and without irradiation

9.3.6 Photo-assisted electrochemical degradation of ciprofloxacin

The application of the EG, MoS_2-EG, SnO_2-EG and MoS_2-SnO_2/EG electrodes for the photo-electrocatalytic removal of ciprofloxacin as a typical pharmaceutical pollutant was investigated, and this was monitored using UV-Visible spectroscopy and TOC analysis. At a current density of 0.010 Acm^{-2} and a small electrode geometric area of 1.3cm^2, the obtained results showed that the MoS_2-SnO_2/EG electrode displayed a photo-electrocatalytic removal efficiency of 78.5% and an electrocatalytic removal efficiency of 55.5% (Fig. 9.5a). Furthermore, as a control experiment, EG electrode was used for the photo-electrocatalytic removal of ciprofloxacin and it gave a removal efficiency of 50.5 %.

Upon the separate addition of MoS_2 and SnO_2 to the EG, 68.5 and 64.5% were obtained for the MoS_2-EG and SnO_2-EG electrodes respectively. This is due to the photosensitivity of MoS_2 and SnO_2. Moreover, the addition of the MoS_2-SnO_2 nanohybrid to the EG gave 78.5% for the MoS_2-SnO_2/EG electrode. This is due to the light harvesting nature of the nanocomposite and the formation of heterojunction between the MoS_2 and SnO_2 which led to an improved charge separation and transport, thereby resulting in improved photo-electrocatalytic performance of the MoS_2-SnO_2/EG nanocomposite. Thus, as shown in Fig. 9.5b, the kinetic curves revealed a better photo-electrocatalytic removal of the ciprofloxacin compared to the EG, MoS_2-EG and SnO_2-EG electrodes [52, 53]. These can be corroborated by the results from the photocurrent and linear sweep voltammetry measurements of the different fabricated electrodes. TOC analysis was carried out to investigate the mineralisation process of the ciprofloxacin after 2 h 30 min. The conversion of the organic carbon gave a removal of 39.7% for MoS_2-SnO_2/EG nanocomposite electrode which is higher when compared to that of EG (25%), MoS_2-EG (32%) and SnO_2-EG (30%) electrodes. This is in agreement with results obtained for removal efficiency and TOC measurements reported in literatures [1, 6].

Then further experiments were conducted to determine optimised conditions at different pH values, current densities and amount of MoS_2 in the nanocomposite. It was found that the removal efficiency of the ciprofloxacin was better at pH 5.4 in relation to pH 4.0 and 8.0 using the MoS_2-SnO_2/EG nanocomposite electrode as shown in the kinetic curves (Fig. 9.5c). Thus, pH value of 5.4 was used for the experiments [6]. The variation of the current density showed that the experiment was dependent on the current density used (Fig. 9.5d). This is because the current density applied relates to the production of hydroxyl radicals [56]. An enhancement was observed as the current efficiency was increased from 0.0075 Acm^{-2} to 0.0100 Acm^{-2}, increasing the removal efficiency from 49% to 78.5%. Further increment of the current density from 0.0100 to 0.1500 Acm^{-2} resulted in a removal of 86%. However, the percentage increase of the removal efficiency when the current density was increased from 0.0100 to 0.0150 Acm^{-2} was lower compared to that when it was increased from 0.0075 to 0.0100 Acm^{-2}. This implies that further increase of the current density from 0.0150 to 0.0200 Acm^{-2} may not necessarily result in any significant increase in the removal efficiency. This is as a result of the increased oxygen evolution resulting from higher current density which can be in competition with the degradation of the pharmaceutical pollutant [56]. Thus, higher current densities would not result in energy

and cost effectiveness for the photo-electrocatalytic removal of ciprofloxacin. For purpose of energy efficiency, a current density of 0.0100 Acm^{-2} was used for the study. Furthermore, the effect of MoS_2 content in the MoS_2-SnO_2/EG nanocomposite was studied (Fig. 9.5e). The photo-electrocatalytic removal of ciprofloxacin gave 69, 78.5 and 65% for the introduction of 0.1, 0.3 and 0.5 g of MoS_2 in the nanocomposite. This implies that there was an improvement in the removal as the content of MoS_2 was increased, but further increase led to a decrease in the removal of the ciprofloxacin. This increased removal could be attributed to the production and separation of photoinduced holes and electrons which led to the generation of more oxidising radicals for the removal of the ciprofloxacin. However, a recorded reduction in removal with further MoS_2 content increase could be due to the prevention of SnO_2 nanoparticles from harvesting visible light by the increased amount of MoS_2, rendering them less photoactive due to the limited amount of light reaching the SnO_2 [18, 57].

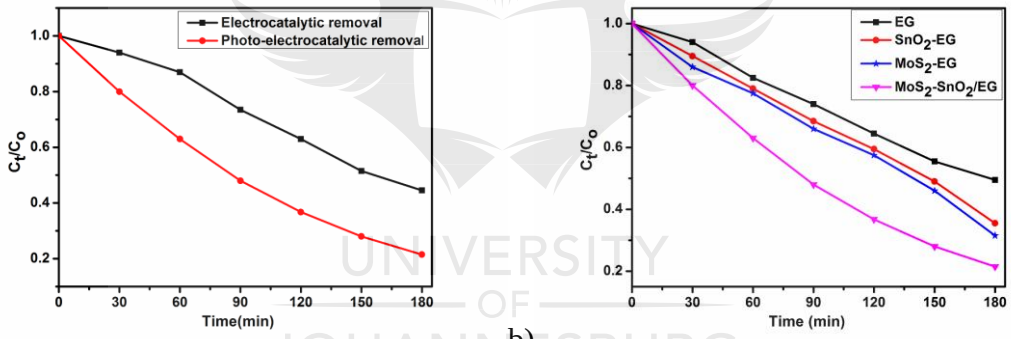

a) b)

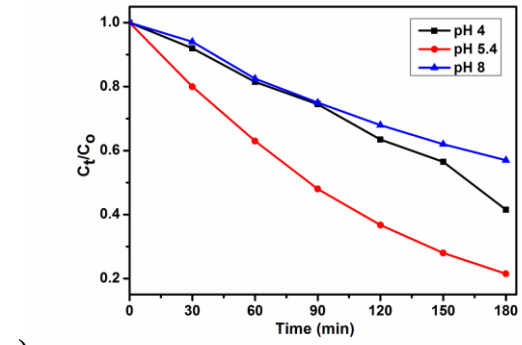

c)

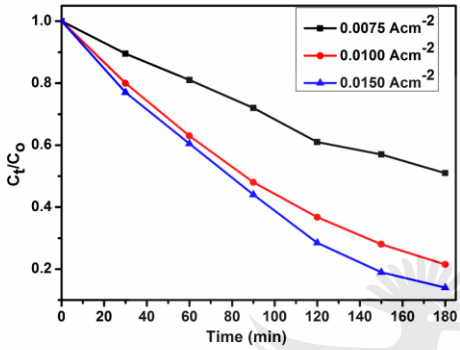

d)

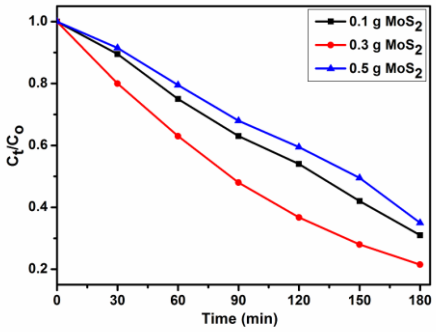

e

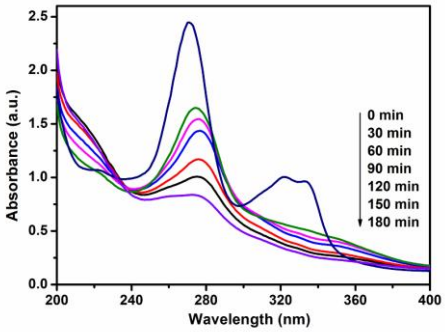

f)

Figure 9.5: Degradation kinetics curves of ciprofloxacin of (a) Electrocatalytic and photo-electrocatalytic on MoS_2-SnO_2/EG electrode, and (b) photo-electrocatalytic removal on

EG, SnO_2-EG, MoS_2-EG and MoS_2-SnO_2/EG electrodes. Effects of (c) pH; (d) current density and (e) MoS_2 content in the nanocomposite. (f) UV-Vis spectra for the photo-electrocatalytic removal of ciprofloxacin on MoS_2-SnO_2/EG electrode.

9.3.7 Degradation kinetics and underlying mechanism

Investigation of the degradation rates of the different electrode reactions was carried out by fitting the degradation data using pseudo-first order kinetic model;

$$\ln C_o/C_t = k_{app}t, \qquad [9.3]$$

Where k is the reaction rate constant; C_o is the ciprofloxacin concentration before the reaction process; C_t is the ciprofloxacin concentration at a particular reaction time, t. Figure 9.6a illustrates clearly that the MoS_2-SnO_2/EG electrode exhibited a better degradation rate than the other electrodes. The calculated rate constant values and correlation coeficients for the different electrodes are 4.06×10^{-3} min^{-1} and 0.9905 for EG; 5.47×10^{-3} min^{-1} and 0.9571 for SnO_2-EG; 5.97×10^{-3} min^{-1} and 0.9440 for MoS_2-EG; and 8.63×10^{-3} min^{-1} and 0.9987 for MoS_2-SnO_2/EG electrodes.

To understand the underlying mechanism of the photo-electrocatalytic process, the band edge potential of the materials was determined which is necessary for the flow and separation of the photoinduced holes and electrons. The valence and conduction band edge potential were evaluated using the empirical equations [53];

$$E_{VB} = X - E_C + 0.5g \qquad [9.4]$$

$$E_{CB} = E_{VB} - E_g \qquad [9.5]$$

Here, E_{VB} and E_{CB} are the valence and conduction bands of the semiconductor where E_C is the energy of free electrons vs hydrogen, given as 0.45 eV. X is known as the absolute electronegativity of the semiconductor. It is the geometric mean of the electron affinity and first ionisation energy of the individual atoms that constitute the semiconductor. The estimated E_{CB} and E_{VB} for MoS_2 are -0.12 eV and 1.78 eV while those of SnO_2 are -0.09 eV and 3.51 eV. When the SnO_2 nanoparticles are in contact with the surface of the MoS_2, a p-n heterojunction is established and electrons transfer from the SnO_2 to the MoS_2 until there is an alignment of their Fermi levels, reaching equilibrium state [53, 54, 58] as shown

in Fig. 9.6b. At this state, the SnO_2 is positively charged while the MoS_2 is negatively charged, creating an inner electric field at the junction interface. From the band gap energy position, the CB and VB energies of MoS_2 are higher than the CB and VB energies of SnO_2 (Fig. 9.6c). Upon irradiation, the photoinduced electrons are transferred from the CB of the p-type MoS_2 to the CB of the n-type SnO_2, whereas the holes are transferred from the VB of n-type SnO_2 to the VB of the p-type MoS_2 because of the force of the electric field that was created [54, 58-60]. This results in enhanced separation of the photo-induced holes and electrons at the p-n heterojunction interface [31]. These charge carriers move to the nanocomposite surface where the electrons are trapped by dissolved oxygen and water to form superoxide ($\bullet O_2^-$) and hydroxyl (•OH) radicals which eventually react with the ciprofloxacin to give CO_2, NH_3 and H_2O [59]. The plausible mechanism for these reactions is given as follows;

$$hv + MoS_2 \rightarrow MoS_2 (h_{VB}^+ + e_{CB}^-) \quad (6)$$

$$MoS_2 (e_{CB}^-) \rightarrow SnO_2 (e_{CB}^-) \quad (7)$$

$$e_{CB}^- + O_2 \rightarrow \bullet O_2^- \quad (8)$$

$$h^+ + H_2O \rightarrow H^+ + \bullet OH \quad (9)$$

$$\bullet OH + \text{ciprofloxacin} \rightarrow CO_2 + H_2O \quad (10)$$

$$\bullet O_2^- + \text{ciprofloxacin} \rightarrow CO_2 + H_2O \quad (11)$$

$$h^+ + \text{ciprofloxacin} \rightarrow CO_2 + H_2O \quad (12)$$

a)

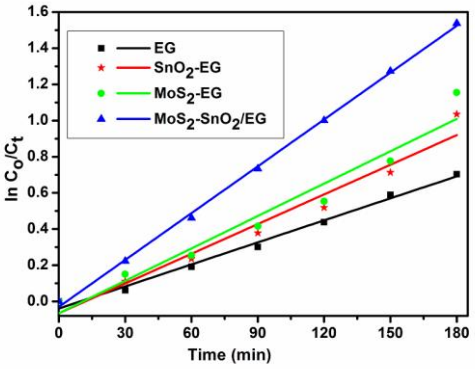

b)

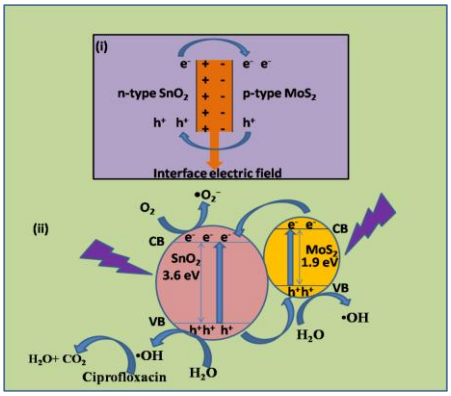

c)

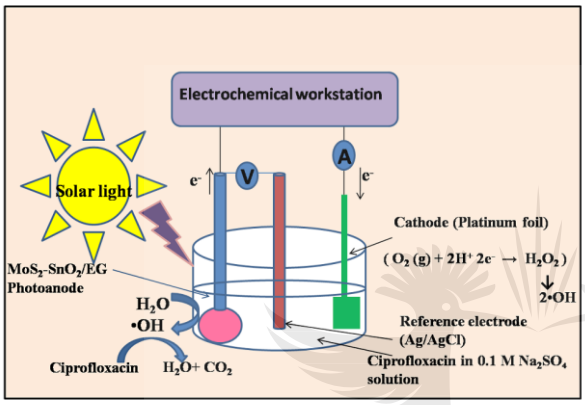

Figure 9.6: (a) Plots of $\ln(C_0/C_t$ versus reaction time for the different electrodes. (b) Proposed plausible charge transfer mechanism and (c) the photo-electrocatalytic behaviour MoS_2-SnO_2/EG electrode.

9.4 SUB CONCLUSION

This work reports the synthesis and characterisation of a novel photo-electrode consisting of a p-n MoS_2-SnO_2 heterojunction anchored on an expanded graphite (EG). This was applied in the photo-electrocatalytic degradation of ciprofloxacin as a target pharmaceutical pollutant in water. The fabricated electrode exhibited a better photo-electrocatalytic performance compared to MoS_2-EG, SnO_2-EG and EG electrodes for the removal of the ciprofloxacin. This is attributed to the formation of the MoS_2-SnO_2 p-n heterojunction in the nanocomposite which aided charge separation and transfer, thereby resulting in the diminution of the recombination rate of the photoinduced electrons and holes. Furthermore, the linear sweep voltammetry and photocurrent measurements revealed that the nanocomposite electrode is rendered a good photo-electrode which can be

beneficial for photo-electrocatalytic treatment of industrial waste waters and other photo-electrocataytic reactions.

9.5 REFERENCES

[1] A.S. Giri, A.K. Golder, Ciprofloxacin degradation from aqueous solution by Fenton oxidation: reaction kinetics and degradation mechanisms, RSC Advances, 4 (2014) 6738-6745.

[2] D.J. Larsson, C. de Pedro, N. Paxeus, Effluent from drug manufactures contains extremely high levels of pharmaceuticals, Journal of hazardous materials, 148 (2007) 751-755.

[3] I. Cesarino, R.P. Simões, F.C. Lavarda, A. Batagin-Neto, Electrochemical oxidation of sulfamethazine on a glassy carbon electrode modified with graphene and gold nanoparticles, Electrochimica Acta, 192 (2016) 8-14.

[4] A. El-Ghenymy, P.L. Cabot, F. Centellas, J.A. Garrido, R.M. Rodríguez, C. Arias, E. Brillas, Electrochemical incineration of the antimicrobial sulfamethazine at a boron-doped diamond anode, Electrochimica Acta, 90 (2013) 254-264.

[5] M. Pérez-Moya, M. Graells, G. Castells, J. Amigó, E. Ortega, G. Buhigas, L.M. Pérez, H.D. Mansilla, Characterization of the degradation performance of the sulfamethazine antibiotic by photo-Fenton process, Water Research, 44 (2010) 2533-2540.

[6] Y. Ji, C. Ferronato, A. Salvador, X. Yang, J.-M. Chovelon, Degradation of ciprofloxacin and sulfamethoxazole by ferrous-activated persulfate: implications for remediation of groundwater contaminated by antibiotics, Science of the total environment, 472 (2014) 800-808.

[7] K. Kümmerer, Antibiotics in the aquatic environment–a review–part I, Chemosphere, 75 (2009) 417-434.

[8] M. El-Kemary, H. El-Shamy, I. El-Mehasseb, Photocatalytic degradation of ciprofloxacin drug in water using ZnO nanoparticles, Journal of Luminescence, 130 (2010) 2327-2331.

[9] P. Huo, Z. Lu, H. Wang, J. Pan, H. Li, X. Wu, W. Huang, Y. Yan, Enhanced photodegradation of antibiotics solution under visible light with Fe^{2+}/Fe^{3+} immobilized on

TiO_2/fly-ash cenospheres by using ions imprinting technology, Chemical engineering journal, 172 (2011) 615-622.

[10] W. Shi, Y. Yan, X. Yan, Microwave-assisted synthesis of nano-scale $BiVO_4$ photocatalysts and their excellent visible-light-driven photocatalytic activity for the degradation of ciprofloxacin, Chemical engineering journal, 215 (2013) 740-746.

[11] E. Brillas, C.A. Martínez-Huitle, Decontamination of wastewaters containing synthetic organic dyes by electrochemical methods. An updated review, Applied Catalysis B: Environmental, 166–167 (2015) 603-643.

[12] G.R. Malpass, D.W. Miwa, S.A. Machado, A.J. Motheo, SnO_2-based materials for pesticide degradation, Journal of hazardous materials, 180 (2010) 145-151.

[13] C.A. Martinez-Huitle, S. Ferro, Electrochemical oxidation of organic pollutants for the wastewater treatment: direct and indirect processes, Chemical Society Reviews, 35 (2006) 1324-1340.

[14] M. Peleyeju, E. Umukoro, J. Babalola, O. Arotiba, Electrochemical Degradation of an Anthraquinonic Dye on an Expanded Graphite-Diamond Composite Electrode, Electrocatalysis, 7 (2016) 132-139.

[15] K. Jüttner, U. Galla, H. Schmieder, Electrochemical approaches to environmental problems in the process industry, Electrochimica Acta, 45 (2000) 2575-2594.

[16] E. Kusmierek, E. Chrzescijanska, Application of TiO_2–RuO_2/Ti electrodes modified with WO_3 in electro-and photoelectrochemical oxidation of Acid Orange 7 dye, Journal of Photochemistry and Photobiology A: Chemistry, 302 (2015) 59-68.

[17] E. Brillas, C.A. Martínez-Huitle, Decontamination of wastewaters containing synthetic organic dyes by electrochemical methods. An updated review, Applied Catalysis B: Environmental, 166 (2015) 603-643.

[18] E.H. Umukoro, M.G. Peleyeju, J.C. Ngila, O.A. Arotiba, Towards wastewater treatment: Photo-assisted electrochemical degradation of 2-nitrophenol and orange II dye

at a tungsten trioxide-exfoliated graphite composite electrode, Chemical Engineering Journal, 317 (2017) 290-301.

[19] N. Smirnova, V. Vorobets, O. Linnik, E. Manuilov, G. Kolbasov, A. Eremenko, Photoelectrochemical and photocatalytic properties of mesoporous TiO_2 films modified with silver and gold nanoparticles, Surface and Interface Analysis, 42 (2010) 1205-1208.

[20] I. Tantis, L. Bousiakou, G.-A. Karikas, P. Lianos, Photocatalytic and photoelectrocatalytic degradation of the antibacterial agent ciprofloxacin, Photochemical & Photobiological Sciences, 14 (2015) 603-607.

[21] S. Xiao, Y. Song, Z. Tian, X. Tu, X. Hu, L. Ruixia, Enhanced mineralization of antibiotic berberine by the photoelectrochemical process in presence of chlorides and its optimization by response surface methodology, Environmental Earth Sciences, 73 (2015) 4947-4955.

[22] J. Li, S. Lv, Y. Liu, J. Bai, B. Zhou, X. Hu, Photoeletrocatalytic activity of an n-ZnO/p-Cu_2O/n-TNA ternary heterojunction electrode for tetracycline degradation, Journal of hazardous materials, 262 (2013) 482-488.

[23] Q. Kuang, C. Lao, Z.L. Wang, Z. Xie, L. Zheng, High-sensitivity humidity sensor based on a single SnO_2 nanowire, Journal of the American Chemical Society, 129 (2007) 6070-6071.

[24] S. Wu, H. Cao, S. Yin, X. Liu, X. Zhang, Amino acid-assisted hydrothermal synthesis and photocatalysis of SnO_2 nanocrystals, The Journal of Physical Chemistry C, 113 (2009) 17893-17898.

[25] E.N. Dattoli, Q. Wan, W. Guo, Y. Chen, X. Pan, W. Lu, Fully transparent thin-film transistor devices based on SnO2 nanowires, Nano letters, 7 (2007) 2463-2469.

[26] P. Lian, X. Zhu, S. Liang, Z. Li, W. Yang, H. Wang, High reversible capacity of SnO_2/graphene nanocomposite as an anode material for lithium-ion batteries, Electrochimica Acta, 56 (2011) 4532-4539.

[27] L. Yu, D. Cai, H. Wang, M.-M. Titirici, Hydrothermal synthesis of SnO_2 and SnO_2@C nanorods and their application as anode materials in lithium-ion batteries, RSC Advances, 3 (2013) 17281-17286.

[28] M. Moreno, A. Varela, L. Otero-Díaz, Cation nonstoichiometry in tin-monoxide-phase Sn 1− δ O with tweed microstructure, Physical Review B, 56 (1997) 5186.

[29] D. Zhang, Y.e. Sun, P. Li, Y. Zhang, Facile fabrication of MoS_2-modified SnO_2 hybrid nanocomposite for ultrasensitive humidity sensing, ACS applied materials & interfaces, 8 (2016) 14142-14149.

[30] J. Yan, E. Khoo, A. Sumboja, P.S. Lee, Facile coating of manganese oxide on tin oxide nanowires with high-performance capacitive behavior, ACS nano, 4 (2010) 4247-4255.

[31] W. Zhao, Y. Liu, Z. Wei, S. Yang, H. He, C. Sun, Fabrication of a novel p–n heterojunction photocatalyst n-$BiVO_4$@p-MoS_2 with core–shell structure and its excellent visible-light photocatalytic reduction and oxidation activities, Applied Catalysis B: Environmental, 185 (2016) 242-252.

[32] S.K. Balasingam, J.S. Lee, Y. Jun, Few-layered $MoSe_2$ nanosheets as an advanced electrode material for supercapacitors, Dalton Transactions, 44 (2015) 15491-15498.

[33] S.K. Balasingam, A. Thirumurugan, J.S. Lee, Y. Jun, Amorphous MoS_x thin-film-coated carbon fiber paper as a 3D electrode for long cycle life symmetric supercapacitors, Nanoscale, 8 (2016) 11787-11791.

[34] L. Hao, W. Gao, Y. Liu, Y. Liu, Z. Han, Q. Xue, J. Zhu, Self-powered broadband, high-detectivity and ultrafast photodetectors based on Pd-MoS_2/Si heterojunctions, Physical Chemistry Chemical Physics, 18 (2016) 1131-1139.

[35] Q. Ji, Y. Zhang, T. Gao, Y. Zhang, D. Ma, M. Liu, Y. Chen, X. Qiao, P.-H. Tan, M. Kan, Epitaxial monolayer MoS_2 on mica with novel photoluminescence, Nano letters, 13 (2013) 3870-3877.

[36] Y. Yoon, K. Ganapathi, S. Salahuddin, How good can monolayer MoS_2 transistors be?, Nano letters, 11 (2011) 3768-3773.

[37] R. Bose, S.K. Balasingam, S. Shin, Z. Jin, D.H. Kwon, Y. Jun, Y.-S. Min, Importance of hydrophilic pretreatment in the hydrothermal growth of amorphous molybdenum sulfide for hydrogen evolution catalysis, Langmuir, 31 (2015) 5220-5227.

[38] H. Xu, J. Wu, Q. Feng, N. Mao, C. Wang, J. Zhang, High responsivity and gate tunable graphene-MoS_2 hybrid phototransistor, Small, 10 (2014) 2300-2306.

[39] M. Yi, Z. Shen, Kitchen blender for producing high-quality few-layer graphene, Carbon, 78 (2014) 622-626.

[40] M. Yi, Z. Shen, A review on mechanical exfoliation for the scalable production of graphene, Journal of Materials Chemistry A, 3 (2015) 11700-11715.

[41] E.H. Umukoro, M.G. Peleyeju, J.C. Ngila, O.A. Arotiba, Photoelectrochemical degradation of orange II dye in wastewater at a silver–zinc oxide/reduced graphene oxide nanocomposite photoanode, RSC Advances, 6 (2016) 52868-52877.

[42] T. Ndlovu, O.A. Arotiba, S. Sampath, R.W. Krause, B.B. Mamba, Electrochemical detection and removal of lead in water using poly (propylene imine) modified re-compressed exfoliated graphite electrodes, Journal of Applied Electrochemistry, 41 (2011) 1389-1396.

[43] N. Kumar, B.P.A. George, H. Abrahamse, V. Parashar, J.C. Ngila, Sustainable one-step synthesis of hierarchical microspheres of PEGylated MoS_2 nanosheets and MoO_3 nanorods: Their cytotoxicity towards lung and breast cancer cells, Applied Surface Science, 396 (2017) 8-18.

[44] M.G. Peleyeju, A.O. Idris, E.H. Umukoro, J.O. Babalola, O.A. Arotiba, Electrochemical Detection of 2, 4-Dichlorophenol on a Ternary Composite Electrode of Diamond, Graphene, and Polyaniline, ChemElectroChem, (2017).

[45] M.P. Kumar, M. Nidhi, C. Srivastava, Electrochemical exfoliation of graphite to produce graphene using tetrasodium pyrophosphate, RSC Advances, 5 (2015) 24846-24852.

[46] L. Chen, F. Xue, X. Li, X. Huang, L. Wang, J. Kou, Z.L. Wang, Strain-gated field effect transistor of a MoS_2–ZnO 2D–1D hybrid structure, ACS nano, 10 (2015) 1546-1551.

[47] Y. Wu, X. Zhang, G. Zhang, W. Guan, Visible light-assisted synthesis of Pt/Bi_2WO_6 and photocatalytic activity for ciprofloxacin, IET Micro & Nano Letters, 9 (2014) 119-122.

[48] P.Y. Kuang, J.R. Ran, Z.Q. Liu, H.J. Wang, N. Li, Y.Z. Su, Y.G. Jin, S.Z. Qiao, Enhanced photoelectrocatalytic activity of BiOI nanoplate–zinc oxide nanorod p–n heterojunction, Chemistry–A European Journal, 21 (2015) 15360-15368.

[49] E.H. Umukoro, M.G. Peleyeju, J.C. Ngila, O.A. Arotiba, Photocatalytic degradation of acid blue 74 in water using Ag–Ag_2O–Zno nanostuctures anchored on graphene oxide, Solid State Sciences, 51 (2016) 66-73.

[50] W. Yuan, Y. Zhou, Y. Li, C. Li, H. Peng, J. Zhang, Z. Liu, L. Dai, G. Shi, The edge- and basal-plane-specific electrochemistry of a single-layer graphene sheet, Scientific reports, 3 (2013) 2248.

[51] T. Ndlovu, B.B. Mamba, S. Sampath, R.W. Krause, O.A. Arotiba, Voltammetric detection of arsenic on a bismuth modified exfoliated graphite electrode, Electrochimica Acta, 128 (2014) 48-53.

[52] J. Ke, J. Liu, H. Sun, H. Zhang, X. Duan, P. Liang, X. Li, M.O. Tade, S. Liu, S. Wang, Facile assembly of Bi_2O_3/Bi_2S_3/MoS_2 np heterojunction with layered n-Bi_2O_3 and p-MoS_2 for enhanced photocatalytic water oxidation and pollutant degradation, Applied Catalysis B: Environmental, 200 (2017) 47-55.

[53] J. Yan, Z. Chen, H. Ji, Z. Liu, X. Wang, Y. Xu, X. She, L. Huang, L. Xu, H. Xu, Construction of a 2D Graphene-Like MoS_2/C_3N_4 Heterojunction with Enhanced Visible-Light Photocatalytic Activity and Photoelectrochemical Activity, Chemistry–A European Journal, (2016).

[54] S.A. Ansari, M.M. Khan, M.O. Ansari, J. Lee, M.H. Cho, Biogenic synthesis, photocatalytic, and photoelectrochemical performance of Ag–ZnO nanocomposite, The Journal of Physical Chemistry C, 117 (2013) 27023-27030.

[55] F. Wang, W. Li, S. Gu, H. Li, X. Wu, X. Liu, Samarium and Nitrogen Co-Doped Bi2WO6 Photocatalysts: Synergistic Effect of Sm3+/Sm2+ Redox Centers and N-Doped Level for Enhancing Visible Light Photocatalytic Activity, Chemistry-A European Journal, 22 (2016) 12859-12867.

[56] Y. Wang, C. Shen, M. Zhang, B.-T. Zhang, Y.-G. Yu, The electrochemical degradation of ciprofloxacin using a SnO_2-Sb/Ti anode: Influencing factors, reaction pathways and energy demand, Chemical Engineering Journal, 296 (2016) 79-89.

[57] T. Das, P.K. Boruah, M.R. Das, B.K. Saikia, Formation of onion-like fullerene and chemically converted graphene-like nanosheets from low-quality coals: application in photocatalytic degradation of 2-nitrophenol, RSC Advances, 6 (2016) 35177-35190.

[58] S. Ma, J. Xue, Y. Zhou, Z. Zhang, Photochemical synthesis of ZnO/Ag_2O heterostructures with enhanced ultraviolet and visible photocatalytic activity, Journal of Materials Chemistry A, 2 (2014) 7272-7280.

[59] A. Habibi-Yangjeh, M. Shekofteh-Gohari, Novel magnetic Fe_3O_4/ZnO/$NiWO_4$ nanocomposites: Enhanced visible-light photocatalytic performance through pn heterojunctions, Separation and Purification Technology, 184 (2017) 334-346.

[60] L.-P. Zhu, N.-C. Bing, D.-D. Yang, Y. Yang, G.-H. Liao, L.-J. Wang, Synthesis and photocatalytic properties of core–shell structured α-Fe_2O_3@SnO_2 shuttle-like nanocomposites, CrystEngComm, 13 (2011) 4486-4490.

CHAPTER 10

GENERAL CONCLUSIONS AND RECOMMENDATIONS

10.1 CONCLUSIONS

The research work has achieved all the objectives outlined for this work.

In this research we have carried out successful

- synthesis of photo-electrocatalytic materials for the removal of organic pollutants from aqueous solutions;
- synthesis/production of carbon materials such as graphene/ reduced graphene oxide and their use in fabricating electrodes;
- use of reduced graphene oxide (RGO) and Exfoliated/Expanded graphite (EG) to immobilize metal oxides and semiconductor photocatalysts including ZnO, WO_3, SnO_2, MoS_2, and Ag-Ag_2O;
- characterization of synthesized and fabricated materials using various techniques including XRD, UV, FTIR, BET surface area determination, TEM, SEM, EDS, CV, LSV and photo current measurements;
- degradation of Acid Blue 74 dye, Orange II dye, 2-nitrophenol, Acid Orange 7 dye and 4-nitrophenol using the synthesized and fabricated materials by the electrochemical and photo-electrochemical/photo-electrocatalytic processes; and
- kinetic analysis of degradation data and proposition of plausible degradation mechanism.

The following conclusions were drawn based on the results obtained from the study:

- The electrochemical application of carbon materials such as graphene and exfoliated graphite as electrode materials showed that they can be beneficial for electrochemical processes.
- This study has shown the scientific relevance of graphene and exfoliated graphite in the field of advance oxidation processes. It is found that novel electrodes could be developed for photo-electrocatalytic processes using graphene and exfoliated graphite because their photoelectrochemical properties can easily be tuned and improved by incorporating metal oxides such as ZnO, Ag_2O, WO_3 and SnO_2. Also,

the setbacks of narrow light absorption range and rate of recombination of photogenerated holes and electrons could be minimised by the incorporation of noble metals such as silver and palladium as well as the formation a heterojunction using other photocatalysts. For instance, the incorporation of silver and ZnO into reduced graphene oxide to form a composite electrode displayed enhanced electrochemical stability and degradation efficiency when compared to the reduced graphene oxide electrode. To the best of our knowledge, the use of Ag-ZnO-reduced graphene oxide had not been reported as electrode for the degradation of organics such as dyes.

- The exfoliated graphite based-WO_3 electrode could degrade 2-nitrophenol and orange II dye at low current densities with the assistance of visible light. This renders this photoelectrode a potential candidate for water treatment and photo-electrocatalytic processes where organics are important.
- The carbon-metal oxide composite electrodes have been rendered beneficial and cost effective for electrochemical applications due to their ease of preparation, low cost, non-toxicity and their capability to degrade organic pollutants such as nitrophenols, dyes and pharmaceuticals at low current densities and visble light.

- Finally, this study was able to demonstrate the application of carbon materials such as graphene and exfoliated graphite as potential and suitable electrode materials for the degradation of different organic pollutants in wastewater treatment using advance oxidation processes. The scientific and technological demonstrations in this study could be employed for wastewater treatment process. These AOPs can be grouped under green chemistry since the methods utilise visible light and electron which are regarded as“clean reagents”. Thus, photo-electrochemical process can be incorporated in wastewater treatment operation units. It can be used for industrial applications in the treatment of wastewater using graphene or exfoliated graphite composites for the treatment of wastewater or industries effluent prior to discharge into the environment. This can help in the reduction of the organic pollutant loadings. Furthermore, the high degradation efficiencies obtained from the carbon-metal oxides systems show that AOPs are cost effective and efficient water treatment methods which could help in reducing health problems that are linked to polluted and contaminated water.

10.2 RECOMMENDATIONS FOR FURTHER WORK

Though the study was successfully conducted, there are some works that need to be carried out. Some of the recommendations for future research include:

- The graphene/EG-metal oxide electrode was applied for the photoelectrochemical degradation of organic pollutants in synthetic water samples. It is recommended that this technique should be further applied to real wastewater samples.
- Since the carbon-metal oxide composite electrodes displayed enhanced degradation efficiencies, it is recommended that these electrodes be applied in wastewater treatment plants.
- Further studies should be carried out on the reaction mechanisms to understand the pathways and intermediate products formed during the degradation process. This can be done by the use of other characterisation techniques such as GC-MS to analyse the reaction mixtures and products with a view to identifying the reaction intermediates and products. This could give better insight and understanding on the toxicity of the intermediates and products formed and they can be compared with the toxicity of the initial organics
- Investigation of the photocatalytic, electrocatalytic and photoelectrocatalytic degradation of the studied pollutants in a flow system which is more suitable for industrial processes.
- In order to save time and energy, computational modelling of the reaction processes should be further conducted to predict feasibility of the synthesis of new and potential electrode materials as well as the degradation kinetics and intermediates of these and other organic pollutants.